Comptes Rendus
de l'Académie des sciences

Chimie

Volume 27, Special Issue S1, 2024

Special issue / *Numéro spécial*

French/Nordic Special Issue on Materials and Coordination Chemistry / *Numéro spécial franco-nordique sur les matériaux et la chimie de coordination*

Guest editors / *Rédacteurs en chef invités*

Claude P. Gros, Abhik Ghosh

ACADÉMIE
DES SCIENCES
INSTITUT DE FRANCE

Académie des sciences — Paris

ISSN: 1878-1543 (electronic)

CENTRE
MERSENNE

Comptes Rendus
Chimie

Objective of the journal

Comptes Rendus Chimie is an international peer-reviewed electronic journal, covering all areas of chemistry.

It publishes special issues, original research articles, review articles, accounts, historical perspectives, pedagogical texts or conference proceedings, without length limit, in English or in French and in a format as flexible as necessary (figures, associated data, etc.).

Comptes Rendus Chimie is published since 2020 with the centre Mersenne pour l'édition scientifique ouverte (Mersenne Center for open scientific publishing), according to a virtuous Diamond Open Access policy, free for authors (no author processing charges nor publishing fees) as well as for readers (immediate and permanent open access).

About the journal

Comptes Rendus Chimie is published exclusively in electronic format.

All information on the journal, as well as the full text of all articles, is available on its website at: https://comptes-rendus.academie-sciences.fr/chimie/.

Author enquiries

For any inquiries about submitting a manuscript, please refer to the journal's website: https://comptes-rendus.academie-sciences.fr/chimie/.

Contact

Académie des sciences
23 quai de Conti
75006 Paris (France)
cr-chimie@academie-sciences.fr

Comptes Rendus
Chimie
2024, 27, nº S1

Contents / *Sommaire*

ACADÉMIE
DES SCIENCES
INSTITUT DE FRANCE

Comptes Rendus. Chimie
2024, Vol. 27, Special issue S1, p. 1
`https://doi.org/10.5802/crchim.355`

French/Nordic Special Issue on Materials and Coordination Chemistry

Guest Editors

Claude P. Gros has been a Full Professor of Organic Chemistry at the medicinal/pharmaceutical school of the Université de Bourgogne since 2009. He obtained his PhD from the same University in 1995 under the supervision of Prof. Roger Guilard, following up with a one-year postdoctoral position at the University of California Davis with Prof. Kevin M. Smith, working on chlorins and pyrroloporphyrins. His research interests include the synthesis and reactivity of porphyrins, corroles, BODIPYs and dipyrrins and their metal complexes, along with their applications in energy and electron transfers, gas sensors and medicinal chemistry. In 2021, he was elected as a National Foreign Expert of the People's Republic of China, where he served at the University of Nanjing. He is also the actual Director of the National Research Network GDR Mapyro: https://mapyro.chimie.unistra.fr. Claude P. Gros has organized and co-chaired numerous international conferences, especially in France and China, and was also awarded several international programs, most notably the Åsgård programs of the Institut Français de Norvège. Over May 30–31, 2024, he hosted a highly successful 1st Åsgård Horizon French-Norwegian Inorganic and Materials Chemistry Symposium in Dijon.

Abhik Ghosh is a professor of inorganic and materials chemistry at UiT The Arctic University of Norway. He grew up in Kolkata, India, and did his B.Sc. (Honours) at Jadavpur University. He did his Ph.D. at the University of Minnesota under the supervision of Paul G. Gassman, while also extensively collaborating with Jan Almlöf. After postdoctoral stints in bioinorganic chemistry with Larry Que and David Bocian, he joined UiT as Associate Professor in 1996, rising to full professor in 2000. He was a Senior Fellow of the San Diego Supercomputer Center (1997–2004) and a Visiting Professor at the University of Auckland (on several occasions) and at the University of Rome Tor Vergata (2024). Since 2021, he has led UiT's Center for Sustainable STEM Education. He edited the popular science book *Letters to a Young Chemist* (Wiley, 2011) and coauthored the textbook *Arrow Pushing in Inorganic Chemistry: A Logical Approach to the Chemistry of the Main Group Elements* (Wiley, 2014); the latter won the 2015 PROSE Award for Best Textbook in the Mathematical and Physical Sciences. A fluent Sanskrit speaker, he coauthored an influential essay "The Grammar of the Elements: Did the Sanskrit alphabet influence Mendeleev's periodic table?" with Stanford University linguist Paul Kiparsky. Ghosh is an elected member of several academies and learned societies including the European Academy of Sciences and Academia Europaea. In 2022, he received the Hans Fischer Career Award for Lifetime Achievements in Porphyrin Chemistry. In June 2025, Ghosh plans to host the 2nd Åsgård Horizon French-Norwegian Inorganic and Materials Chemistry Symposium in Tromsø.

ISSN (electronic): 1878-1543

ACADÉMIE
DES SCIENCES
INSTITUT DE FRANCE

Comptes Rendus. Chimie
2024, Vol. 27, Special issue S1, p. 3-4
`https://doi.org/10.5802/crchim.358`

Foreword

French/Nordic Special Issue on Materials and Coordination Chemistry

Foreword to the French/Nordic special issue on materials and coordination chemistry

Claude P. Gros [a] **and Abhik Ghosh** [b]

[a] Institut de Chimie Moléculaire de l'Université de Bourgogne (ICMUB), UMR CNRS 6302, Université de Bourgogne, 9 Avenue Alain Savary, BP 47870, 21078 Dijon Cedex, France

[b] Department of Chemistry, UiT – The Arctic University of Norway, Tromsø N-9037, Norway

E-mails: claude.gros@u-bourgogne.fr (C. P. Gros), abhik.ghosh@uit.no (A. Ghosh)

French–Nordic relations have long been characterized by deep mutual admiration, wide-ranging cultural exchange, and collaboration in the scientific-technological arena. The nations in question dedicate substantial amounts of funds annually to international collaboration and to French–Nordic collaboration in particular. Both France and the Nordic countries are home to unique large-scale facilities such as the ESRF and MAXLAB, historic and legendary universities, as well as world-class research groups at smaller universities in spectacular settings. The world's northernmost university UiT—The Arctic University of Norway at 70° N, home base of one of the guest editors (in Tromsø), is an example of the latter. This Special Issue of *Comptes Rendus Chimie* celebrates French–Nordic collaboration in coordination chemistry and materials chemistry and/or research groups interested or engaged in such collaboration.

Herein, Piligkos et al. (doi:10.5802/crchim.282) describe the influence of long aliphatic side chains on the magnetic properties of tris(salen)-type lanthanide (Tb-Tm and Y) complexes.

Cattey and Plasseraud (doi:10.5802/crchim.260) investigate the reactivity of the hydroxo di-*n*-butyltin-trifluoromethanesulfonato dimer complex towards 1,10-phenanthroline leading to novel 1,10-phenanthroline-complexed, mono- and binuclear organotin(IV) derivatives.

Henrichsen, Bendix, and Weihe (doi:10.5802/crchim.266) present and interpret the parallel-mode X-band EPR spectra of the hexaaquamanganese(II) ion, assisted by the species' exact T_d (tetrahedral) crystallographic symmetry.

Abou-Fayssal, Poli, Philippot, Riisager, and Manoury (doi:10.5802/crchim.301) review polymeric nanoreactors for catalytic applications, including a recent nanoreactor used in biphasic catalysis.

Pascal, Zaborova, and Siri (doi:10.5802/crchim.292) report the synthesis and characterization of two nickel complexes based on 1,2,4-triamino-5-nitrobenzene as air-stable aromatic polyamines, highlighting the importance of intramolecular hydrogen-bonding interactions and the influence of the nitro group on the stability of the complexes.

Devillers and coworkers (doi:10.5802/crchim.307) describe a synthesis of *meso*-(pyridin-2-ylmethyl)-porphyrins based on the nucleophilic attack by (pyridin-2-ylmethyl)lithium on a porphyrin with one free *meso*-position.

Lioret and Decréau (doi:10.5802/crchim.335) present a proof of concept of a novel approach to in vivo imaging involving Cherenkov Radiation Energy Transfer (CRET) from ^{18}F-fluorodeoxyglucose to subphthalocyanine fluorophores.

Using relativistic DFT calculations, Ghosh and Conradie (doi:10.5802/crchim.264) shed new light on gold(II) porphyrins, rare mononuclear Au(II) species that were isolated and structurally characterized only a few years ago. A key feature of these complexes is a wave deformation of the porphyrin, a reflection of a noninnocent porphyrin macrocycle.

Also focusing on gold complexes, Orthaber et al. (doi:10.5802/crchim.328) describe the use of the semi-rigid *cis*-1,2-bis(diphenylphosphino)ethene ligand, which favors the formation of mononuclear, as opposed to binuclear, Au(I) complexes.

Finally, guest editors Ghosh and Gros and their coworkers (doi:10.5802/crchim.299) introduce hypsochlorins, named by analogy with hypsoporphyrins, which exhibit blue-shifted optical spectra relative to their normal counterparts.

It is worth mentioning that this special issue is being published shortly after the 1st Åsgard Horizon French-Norwegian Inorganic and Materials Chemistry Symposium, which took place May 30–31, 2024, in Dijon, France. The second edition of this symposium will be held in Tromsø, Norway, in June, 2025. Both events were organized under the auspices of the *Institut Français de Norvège*, whose support we deeply appreciate.

We are also grateful to the French *Académie des Sciences* and to Dr Pierre Braunstein, Editor-in-Chief of the *Comptes Rendus Chimie*, as well as to Mr. Julien Desmarets for his efficient handling of the submitted manuscripts. We trust that this issue will encourage many others, from exchange students to senior scientists, to take advantage of the wide-ranging opportunities afforded by French–Nordic collaboration.

ACADÉMIE
DES SCIENCES
INSTITUT DE FRANCE

Comptes Rendus. Chimie
2024, Vol. 27, Special issue S1, p. 5-16
`https://doi.org/10.5802/crchim.282`

Research article

French/Nordic Special Issue on Materials and Coordination Chemistry

Derivatives of trigonal lanthanide complexes by reaction with long aliphatic chain amines

Yiwei Zhou [#, a], **Christian Dirk Buch** [#, a], **Steen Hansgaard Hansen** [a] **and Stergios Piligkos** [*, a]

[a] Department of Chemistry, University of Copenhagen, Universitetsparken 5,
DK-2100 Copenhagen Ø, Denmark

E-mail: piligkos@chem.ku.dk (S. Piligkos)

Abstract. We present the synthesis and characterisation of a novel series of lanthanide complexes bearing long aliphatic chains, obtained by post-functionalisation of LnL (Ln = Tb–Tm and Y, H_3L = tris(((3-formyl-5-methylsalicylidene)amine)ethyl)amine) via Schiff-base reaction with 1-octadecylamine. Crystal structures show that the first coordination sphere is not radically perturbed by the post-functionalisation although the trigonal symmetry is lost. Post-derivatisation influences the static magnetic properties of the Kramers and non-Kramers ions differently, with the non-Kramers ions most sensitive to derivatisation. The observed differences likely stem from changes in eigenvector composition as luminescence spectra showed minor modifications of the energy spectra upon derivatisation.

Keywords. Lanthanide complexes, Aliphatic chains, Magnetic properties, Crystal structure, Crystal field.

Funding. Novo Nordisk Foundation (Grant agreement no. NNF20OC0065610).

Manuscript received 31 May 2023, revised 3 October 2023, accepted 13 December 2023.

1. Introduction

Lanthanide complexes coordinated to organic ligands have attracted significant attention in many different fields due to the special optical, electronic, and magnetic properties of the lanthanide ions. These lanthanide-containing complexes exhibit various applications ranging from luminescent thermometers [1–4], and MRI contrast agents [5–7] for medical imaging to quantum information processing [8–14], and single molecule magnets (SMMs) [15–19]. Understanding the electronic structure in lanthanide complexes is important for optimising their performance and designing new functional materials [20]. Lanthanide-containing complexes that can be modified with various chemical groups to tune their properties or give new features, such as functionalisation for deposition on different surfaces or solubility in diverse media, offer promising prospects. It is still challenging to synthesise lanthanide complexes where the first coordination sphere remains constant upon post-derivatisation.

Recently, we studied the magnetic properties of a new family of trigonal lanthanide complexes LnL (H_3L = tris(((3-formyl-5-methylsalicylidene)amine) ethyl)amine) with Ln ranging from Gd to Lu [21]. These complexes have three pendant carbonyl groups that are non-coordinating to the lanthanide ion. Therefore, these carbonyl groups can be used to react with primary amines via a Schiff-base reaction

---

[#] Contributed equally

[*] Corresponding author

ISSN (electronic): 1878-1543

to form imines. This post-derivatisation conserves the number and nature of atoms in the first coordination sphere. We have previously performed studies focusing on the derivatisation of YbL, for example by reacting YbL with benzylamine to obtain complexes suitable for deposition on graphene [21], or by reacting YbL with 1-octadecylamine to form new complexes [22] that have potential in making lanthanide-containing micelles [23–28] and Langmuir–Blodgett film [29–32].

Herein, we present the synthesis and characterisation of a novel series of lanthanide complexes **LnL^{18}** (**H$_3$L^{18}** = tris(((3-(1-octadecylimine)-5-methylsalicylidene)amine)ethyl)amine) with Ln = Tb–Tm and Y. We investigate the crystal field splitting of **LnL^{18}** by luminescence measurements and the static magnetic properties by SQUID magnetometry. Additionally, the dynamic magnetic properties were examined through alternating current SQUID magnetometry. The results were compared to **YbL^{18}** and (Tb–Tm)L to get an understanding of the impact of the post-derivatisation on the electronic and magnetic properties of the Ln ions.

2. Experimental

2.1. *Materials and physical measurements*

All solvents and chemicals used for the syntheses of the complexes herein were purchased from commercial sources and used as received. All syntheses were made without any attempt to exclude moisture or oxygen. No attempt was made to dry any of the solvents used. The Ln(OTf)$_3$·xH$_2$O salts, 2,6-diformyl-*p*-cresol (dfmp) and LnL were prepared as described in literature [21].

Positive-ion mode MALDI mass spectrometry was performed on a Bruker Solarix XR 7T ESI/MALDI FT-ICR MS instrument at the Department of Chemistry, University of Copenhagen. Infrared (IR) spectra were measured on an Agilent Technologies Cary 630 FTIR spectrometer. Powder X-ray diffraction (PXRD) was recorded on a BRUKER D8 ADVANCE powder diffractometer using a Cu Kα radiation (λ = 1.5418 Å) source. ^{1}H NMR was obtained using a Bruker 500 MHz instrument equipped with a cryoprobe. For ^{1}H NMR, calibration was done against solvent signals from the deuterated solvent. Elemental (C, H, and N) analyses were performed on a FlashEA 1112 instrument at The Microanalytical Laboratory at the Department of Chemistry, University of Copenhagen. Direct current (d.c.) and alternating current (a.c.) magnetic susceptibility measurements were recorded using a Quantum-Design MPMS-XL SQUID magnetometer. The measurements were done on polycrystalline samples immobilised in a small amount of n-hexadecane to avoid orientation of the sample in the magnetic field. The magnetic susceptibility measurements were corrected for the diamagnetism of n-hexadecane (186×10^{-6} cm^3/mol) [33] and of the sample using the approximation ($M_{\text{sample}}/2) \times 10^{-6}$ cm^3/mol [34]. Luminescence spectra of polycrystalline samples of **TbL^{18}**, **HoL^{18}** and **ErL^{18}** were obtaining from a Horiba-Jobin Yvon Fluorolog fluorimeter equipped with an InGaAs near-infrared (NIR) detector and a photomultiplier detector for the UV/Vis range. Additionally, an Oxford Instruments cryostat was used for the cryogenic measurements. UV/Vis absorption spectroscopy was measured on a Lambda 2 UV/Vis spectrometer manufactured by Perkin Elmer. The measurement was performed with a scan rate of 120 nm/min and with a background correction to the pure solvent.

2.2. *Synthesis of LnL^{18} (H$_3$L^{18} = Tris(((3-(1-octadecylimine)-5-methylsalicylidene) amine)ethyl)amine))*

TbL^{18}. TbL (0.052 g; 0.070 mmol) and 1-octadecylamine (0.189 g; 0.70 mmol) were dissolved in a MeOH:CHCl$_3$ 1:1 mixture (20 ml). The mixture was boiled until it became clear. Then the solution was kept at 50 °C until a yellow precipitate formed. The solution was left to slowly cool down to room temperature. The precipitate was washed with MeCN and diethyl ether.

Yield: 0.076 g (86%). Anal. Calcd for C$_{87}$H$_{144}$N$_7$O$_3$Tb: C, 69.89; H, 9.71; N: 6.56. Found: C, 69.86; H, 9.82; N: 6.58. MALDI mass spectrum: 1496.07 *m/z* [TbL^{18}H]$^+$ (Figure S2). IR ν(C–H): 2917 cm^{-1}, 2849 cm^{-1}, $\nu_{C=N}$: 1634 cm^{-1}, 1619 cm^{-1} (Figure S8).

The remaining **LnL^{18}** complexes (Ln = Dy–Tm) and **YL^{18}** were synthesised analogously to **TbL^{18}**.

DyL^{18}. Yield: 0.071 g (73%). Anal. Calcd for C$_{87}$H$_{144}$N$_7$O$_3$Dy: C, 69.73; H, 9.69; N: 6.54. Found: C, 69.59; H, 9.76; N: 6.58. MALDI mass spectrum: 1499.07 *m/z* $[DyL^{18}H]^+$ (Figure S3). IR ν(C–H): 2918 cm^{-1}, 2850 cm^{-1}, ν(C=N): 1633 cm^{-1}, 1619 cm^{-1} (Figure S9).

HoL^{18}. Yield: 0.055 g (62%). Anal. Calcd for $C_{87}H_{144}N_7O_3Ho$: C, 69.61; H, 9.67; N: 6.53. Found: C, 69.12; H, 9.68; N: 6.59. MALDI mass spectrum: 1502.08 *m/z* $[HoL^{18}H]^+$ (Figure S4). IR ν(C–H): 2919 cm^{-1}, 2851 cm^{-1}, ν(C=N): 1634 cm^{-1}, 1619 cm^{-1} (Figure S10).

ErL^{18}. Yield: 0.069 g (80%). Anal. Calcd for $C_{87}H_{144}N_7O_3Er$: C, 69.51; H, 9.65; N: 6.52. Found: C, 69.04; H, 9.76; N: 6.88. MALDI mass spectrum: 1504.08 *m/z* $[ErL^{18}H]^+$ (Figure S5). IR ν(C–H): 2919 cm^{-1}, 2851 cm^{-1}, ν(C=N): 1634 cm^{-1}, 1619 cm^{-1} (Figure S11).

TmL^{18}. Yield: 0.064 g (73%). Anal. Calcd for $C_{87}H_{144}N_7O_3Tm$: C, 69.43; H, 9.64; N: 6.51. Found: C, 68.05; H, 9.45; N: 6.52. MALDI mass spectrum: 1506.08 *m/z* $[TmL^{18}H]^+$ (Figure S6). IR ν(C–H): 2918 cm^{-1}, 2850 cm^{-1}, ν(C=N): 1634 cm^{-1}, 1620 cm^{-1} (Figure S12).

YL^{18}. Yield: 0.05 g (56%). Anal. Calcd for $C_{87}H_{144}N_7O_3Y$: C, 73.33; H, 10.19; N: 6.88. Found: C, 72.81; H, 10.29; N: 6.73. MALDI mass spectrum: 1426.03 *m/z* $[YL^{18}H]^+$ (Figure S7). IR ν(C–H): 2916 cm^{-1}, 2850 cm^{-1}, ν(C=N): 1634 cm^{-1}, 1620 cm^{-1} (Figure S13) ^1H NMR (500 MHz, $CDCl_3$) δ/ppm 8.23 (s, 3 H), 8.17(s, 3 H), 7.76 (s, 3 H), 7.01 (s, 3 H), 4.30 (t, 3 H, $J = 13.3$ Hz), 3.40 (d, 3 H, $J = 14.1$ Hz), 3.15 (m, 6 H), 3.09 (m, 3 H), 2.84 (d, 3 H, $J = 12.7$ Hz), 2.21 (s, 9 H), 1.26 (m, 96 H), 0.88 (t, 9 H, $J = 6.9$ Hz) (Figure S1).

The complexes diluted in a diamagnetic host (**Gd@YL^{18}**, **Dy@YL^{18}** and **Er@LuL^{18}**) were synthesised analogously to **TbL^{18}**, but using a 5:95 mixture of either GdL, DyL or ErL and YL or LuL as the diamagnetic host.

Gd@YL^{18} at 5% dilution. Yield: 0.09 g (62%). Calcd for $C_{87}H_{144}N_7O_3Y_{0.95}Gd_{0.05}$: C, 73.33; H, 10.19; N, 6.88. Found: C, 72.05; H, 10.13; N, 6.73. The PXRD was checked for phase purity of the sample (Figure S22). IR ν(C–H): 2917 cm^{-1}, 2850 cm^{-1}, ν(C=N): 1633 cm^{-1}, 1619 cm^{-1} (Figure S15).

Dy@YL^{18} at 5% dilution. Yield: 0.07 g (47%). Calcd for $C_{87}H_{144}N_7O_3Y_{0.95}Dy_{0.05}$: C, 73.33; H, 10.19; N, 6.88. Found: C, 72.23; H, 10.14; N, 6.51. The PXRD was checked for phase purity of the sample (Figure S22). IR ν(C–H): 2916 cm^{-1}, 2850 cm^{-1}, ν(C=N): 1633 cm^{-1}, 1619 cm^{-1} (Figure S16).

Er@LuL^{18} at 5% dilution. Yield: 0.07 g (51%). Calcd for $C_{87}H_{144}N_7O_3Lu_{0.95}Er_{0.05}$: C, 69.15; H, 9.61; N, 6.49. Found: C, 68.81; H, 9.64; N, 6.39. The PXRD was checked for phase purity of the sample (Figure S22). IR ν(C–H): 2917 cm^{-1}, 2850 cm^{-1}, ν(C=N): 1634 cm^{-1}, 1620 cm^{-1} (Figure S17).

2.3. *Crystal structure determination*

Crystals suitable for single-crystal X-ray diffraction were obtained in different manners for the complexes depending on the metal ion. For **TbL^{18}** and **DyL^{18}**, single crystals were obtained through slow evaporation of a MeCN:chloroform 1:1 solution. For **HoL^{18}**, single crystals were obtained by dissolving the complex in chloroform and then adding the solution to acetone (approximately five times the volume). Upon evaporation of the solvents, single crystals of **HoL^{18}** formed.

Single-crystal X-ray diffraction on single crystals of **TbL^{18}**, **DyL^{18}**, and **HoL^{18}** was performed at 100 K using a Bruker D8 VENTURE diffractometer equipped with a Mo Kα high-brilliance I μS S3 radiation source (λ = 0.71073 Å), a PHOTON 100 CMOS detector, and an Oxford Cryosystems cooling system. Data reduction was performed using SAINT, and the absorption corrections was handled by SADABS using the multi-scan method. The structures were recorded using APEX3 and solved by SHELXT [35,36] using intrinsic phasing and refined using SHELXL [37] (Least Squares). Visualisation of the crystallographic data during the refinement was obtained using the OLEX2 program package [38,39]. All atoms were refined anisotropically except for hydrogen. Hydrogen atoms were placed at calculated positions in OLEX2 using the "Add H" command. In the structure of **TbL^{18}**, additional electron density was found next to the molecule. This electron density could not be modelled as solvent and a solvent mask (SQUEEZE) in OLEX2 was thus used. The electron density amounted to 9 electrons which could stem from a disordered water molecule.

3. Results and discussion

3.1. *Synthesis and characterisation*

The complexes **LnL^{18}** (Ln = Tb–Tm, Y) were synthesised using a one-pot Schiff-base reaction between the corresponding LnL complex and

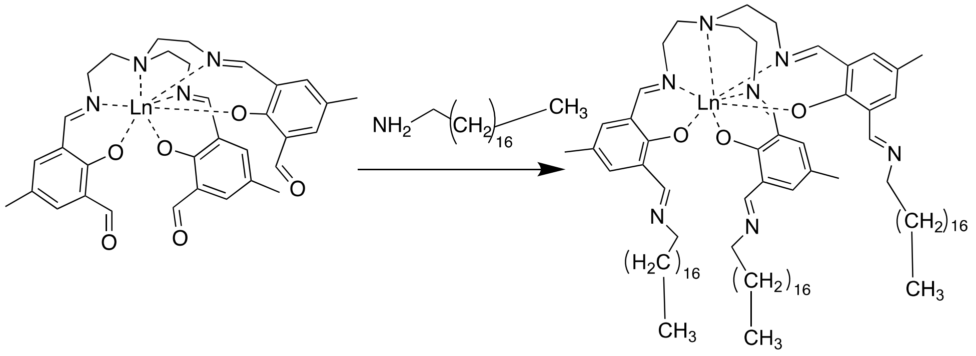

LnL

LnL^{18}

Scheme 1. Schiff-base reaction forming the **LnL^{18}** complexes.

1-octadecylamine (Scheme 1). In order to ensure that all aldehyde groups of the complex were transformed to 1-octadecylimine groups, a 1:10 ratio between LnL and 1-octadecylamine was used. MALDI mass spectra show signals from all [LnL^{18}H]$^+$, confirming that the complexes have been formed (Figure S2–S7). The isotope pattern of each complex matches with the experimental spectrum further strengthening that the observed signals come from the intended product. IR spectra of the **LnL^{18}** complexes show no trace of the aldehyde stretch (1668–1669 cm^{-1}) found in the parent complex LnL (Figure S8–S14) confirming the complete reaction of all aldehyde groups with 1-octadecylamine. Additionally, the C–H stretches between 2850–2919 cm^{-1} for **LnL^{18}** are much more intense than those for LnL (Figure S14), as anticipated from the larger amount of C–H units in **LnL^{18}** compared to LnL.

The polycrystalline samples of **LnL^{18}** (Ln = Tb–Tm, Y) are phase-pure and of the same structure as the one determined for the **LnL^{18}** single crystals (*vide infra*). This is confirmed by a PXRD simulation from a single crystal studied by X-ray diffraction at room temperature (Figure S21).

In **LnL^{18}** all Ln(III) ions except for Y(III) are paramagnetic. The paramagnetism of these ions complicates the recording of NMR spectra and hence only ^{1}H NMR on **YL^{18}** has been performed. The ^{1}H NMR spectrum of **YL^{18}** shows the expected signals and integrals of these signals (Figure S1). As anticipated by the structure of the complexes, most of the protons in the octadecyl chains have almost identical chemical shifts with only the two protons next to the imine group and the protons on the terminal methyl group of each chain showing markedly different chemical shifts than the rest of the chain. The NMR spectrum shows no signs of the starting materials confirming that the complexes are formed purely as also indicated by the above analyses.

The CHN elemental analyses also agree with the expected values for the **LnL^{18}** complexes indicating that the complexes have been obtained pure.

The complexes containing the larger Ln ions (La(III), Pr(III), Nd(III), Sm(III), Eu(III) and Gd(III)) were also synthesised following a similar procedure as for **(Tb–Tm, Y)L^{18}**. However, the PXRD revealed that they were difficult to get phase-pure or in the same phase as the complexes containing the smaller Ln ions **(Tb–Tm, Y)L^{18}**. This was also seen for (La–Eu)L and is likely the result of solvent coordination to the Ln ion. It is common that the greater size of the early Ln ions leads to higher coordination numbers through solvent coordination [40]. By doping **GdL^{18}** into the **YL^{18}** diamagnetic host it was possible to obtain **GdL^{18}** in the same phase as the complexes **LnL^{18}** (Ln = Tb–Tm, Y, Figure S22).

Last, it should be mentioned that introduction of long aliphatic chains makes the post-derivatised **LnL^{18}** much more soluble in organic solvents than their parent complexes. Hence, these complexes are readily soluble in, for example chloroform and dichloromethane, but remain insoluble in alkanes.

3.2. *Crystal structure*

Single crystals large enough for single-crystal X-ray diffraction were obtained for **TbL^{18}**, **DyL^{18}** and

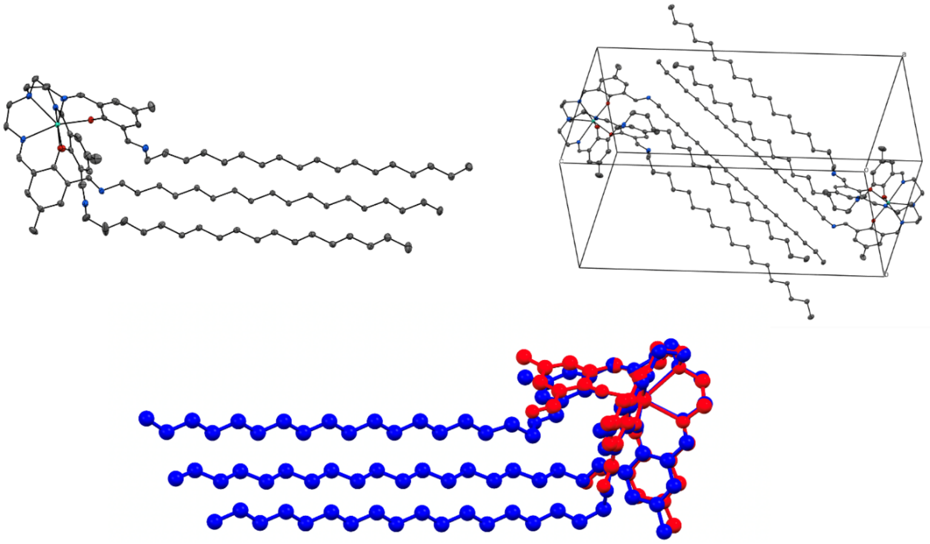

Figure 1. Solid state structure (upper left) and unit cell (upper right) of $\mathbf{TbL^{18}}$. Colour code: Tb, green; N, blue; O, red; C, grey. All hydrogen atoms have been omitted for clarity. Thermal ellipsoids are set to 50% probability. Structural overlay of the solid state structures of $\mathbf{TbL^{18}}$ (blue) and TbL (red) viewed from the side (bottom).

$\mathbf{HoL^{18}}$. The complexes crystallise in the triclinic space group $P\bar{1}$ with two complexes contained in the unit cell. The complexes contain three octadecyl chains which extend from the metal-containing part of the complex (Figure 1). The alkyl chains do not extend in a straight line away from the metal centre but instead form a bend thereby lowering the symmetry of the complex from C_3, as in the parent complex LnL, to C_1. This bend is likely a consequence of both crystal-packing effects and van der Waals interactions between neighbouring complexes (Figure 1). In fact, extended networks of van der Waals interactions are found throughout the crystal structure, with these networks forming large arrays of hydrocarbon stackings (Figure S26). Similar extended networks have been found for $\mathbf{YbL^{18}}$ [22]. The large amount of van der Waals interactions in the crystal structure is also reflected in the unit cell dimensions. The side lengths of the unit cell are for instance 12.5 Å × 12.5 Å × 30.0 Å in $\mathbf{TbL^{18}}$ with the *c* directions clearly being much longer than the two other dimensions which are equivalent in size (Table S1).

As in $\mathbf{YbL^{18}}$, the newly formed imine groups point away from the Ln ion and are therefore non-coordinating.

The post-derivatisation of LnL with 1-octadecylamine leads to small structural changes to the first coordination sphere of the complexes. For instance Tb–$\mathrm{N_{imine}}$ in $\mathbf{TbL^{18}}$ is on average 2.474(17) Å compared to 2.490(1) Å in TbL, and Tb–$\mathrm{N_{apical}}$ in $\mathbf{TbL^{18}}$ is 2.6346(17) Å compared to 2.647(2) Å in TbL. The other bond lengths also remain very similar to the parent complexes, as do the bond angles (Table 1). Still the bond angles do vary more than the bond lengths as is clearly visible when the two structures are overlaid (Figure 1).

Although the trigonal symmetry of the complexes is lost upon post-derivatisation, the first coordination sphere around the Ln centre remains approximately trigonal. The Ln–O bond varies between 2.195(1)–2.203(1) Å for $\mathbf{TbL^{18}}$, 2.187(2)–2.199(2) Å for $\mathbf{DyL^{18}}$, and 2.179(2)–2.192(2) for $\mathbf{HoL^{18}}$, while Ln–$\mathrm{N_{imine}}$ bond varies between 2.468(2)–2.479(2) Å for $\mathbf{TbL^{18}}$, 2.461(2)–2.462(2) Å for $\mathbf{DyL^{18}}$, and 2.453(2)–2.454(2) for $\mathbf{HoL^{18}}$ (Table S3). Additionally, the three angles in the triangle defined by the three phenoxides remain close to the expected 60° for trigonal symmetry, while the angles involving the three coordinating imines deviate more (Table 1).

Moving from $\mathbf{TbL^{18}}$ to $\mathbf{HoL^{18}}$, a slight contraction in the bond lengths between the Ln ion and the ligand is observed (Tables 1 and S3). This is to be expected as the Ln(III) ions shrink in size through the series. The contraction in the bond lengths is even

Table 1. Average bond lengths and angles in **TbL^{18}**, TbL, **DyL^{18}**, DyL, **HoL^{18}**, HoL, and **YbL^{18}**

	TbL^{18}	**TbL**	**DyL^{18}**	**DyL**	**HoL^{18}**	**HoL**	**YbL^{18}**
Bond length (Å)							
Ln–O	2.200(1)	2.208(1)	2.192(2)	2.196(2)	2.184(2)	2.191(2)	2.156(1)
Ln–$\mathrm{N}_{\text{imine}}$	2.474(2)	2.490(1)	2.462(1)	2.473(2)	2.453(1)	2.462(2)	2.418(2)
Ln–$\mathrm{N}_{\text{apical}}$	2.635(2)	2.647(2)	2.631(2)	2.628(3)	2.631(2)	2.626(3)	2.612(2)
Bond angle (°)							
$\angle\ \mathrm{N}_{\text{imines}}$	57.26(4)–61.44(4)	60	57.35(5)–61.44(5)	60	57.48(5)–61.40(5)	60	57.62(5)–61.34(5)
$\angle\ \mathrm{O}_{\text{phenoxides}}$	59.22(4)–60.5(4)	60	59.19(5)–61.07(5)	60	59.07(5)–61.02(5)	60	59.15(5)–61.11(3)

The data for TbL, DyL, HoL and **YbL^{18}** were taken from literature [21,22].

more visible when comparing the aforementioned complexes to **YbL^{18}**. As the bond lengths shrink, the previously mentioned angles between the coordinating imine groups come closer to 60°, and the complexes thereby become closer to trigonal with smaller Ln ions.

Like for the previously studied **YbL^{18}** [22], the differences in the first coordination sphere between the post-derivatised **LnL^{18}** and their parent LnL remain minor. The biggest difference between the post-derivatised complexes **LnL^{18}** and their parent complexes LnL is seen in the length of the complexes and the distances to neighbouring Ln centres. The addition of the three octadecyl chains extends the longest distance within one complex (r_1) from 13.2 Å to 32.8 Å (Figures S24 and S28). Consequently, the distance between two Ln(III) ions within a unit cell (r_2) also increases from 7.8 Å to 30.0 Å (Figures S24 and S29). Because the aliphatic chains stack inside a unit cell (Figure 1), r_2 gets elongated quite significantly; however, the distances to the nearest neighbours or the next nearest neighbours remain very similar between **LnL^{18}** and LnL (Table S2 and Figures S25–S26 and S30–S31).

3.3. *Influence of the post-derivatisation on the crystal field splitting*

In an effort to understand the influence of the octadecyl chains on the electronic structure of the ground multiplets of **TbL^{18}**–**TmL^{18}**, the complexes were studied using variable-temperature-variable-field (VTVB) measurements, luminescence spectroscopy and d.c. magnetic susceptibility measurements, and compared to those of their parent complexes.

3.3.1. *Luminescence spectroscopy*

Luminescence spectroscopy was measured on polycrystalline samples of **TbL^{18}**, **HoL^{18}**, and **ErL^{18}** as well as TbL, HoL, and ErL (Figure 2). To eliminate possible hot bands and decrease the bandwidth, the measurements were carried out at low temperature (4 K). All the compounds share an intense absorption around 400 nm from the phenyl rings as seen in the UV/Vis absorption spectrum (Figure S66). All the luminescence spectra were measured by exciting the ligand in this absorption region (400–425 nm). Following absorption by the ligand, energy is then transfered to the lanthanide. The excitation wavelength was adjusted to avoid higher order diffractions from the excitation monochromator in the emission spectrum.

The emission spectra of **LnL^{18}** and of the parent complex LnL are very similar, as expected from the close structural resemblance of the first coordination spheres (Figure 2). For **TbL^{18}** the signal to noise ratio is much lower than seen for the parent complex TbL. We suspect this to be due to the additional Schiff-base of the post-functionalisation which could lead to a fast quenching of the emitting $^5\mathrm{D}_4$ state of Tb due to the very large amount of additional high-energy C–H stretches being introduced, which is clearly seen from IR spectroscopy (Figure S8).

The number of observed bands is very similar between **TbL^{18}** and TbL, **HoL^{18}** and HoL, and **ErL^{18}** and ErL. **TbL^{18}** and TbL have 10 and 11 observable bands, respectively, while **HoL^{18}** and HoL have 8 and

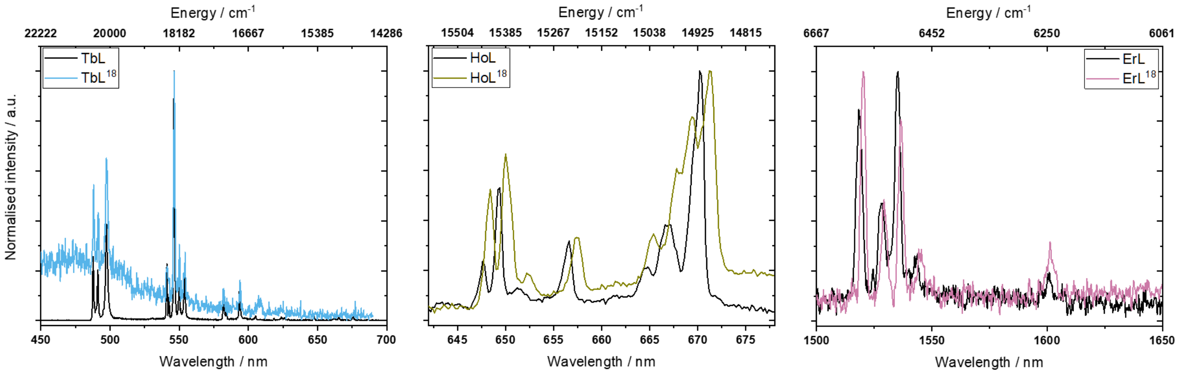

Figure 2. Luminescence spectra of: $\mathbf{TbL^{18}}$ and TbL (left) measured at 4 K, with excitation at 400 nm; $\mathbf{HoL^{18}}$ and HoL (middle) measured at 4 K, with excitation at 400 nm; $\mathbf{ErL^{18}}$ and ErL (right) measured at 4 K, with excitation at 425 nm.

7, respectively, and $\mathbf{ErL^{18}}$ and ErL have both 5 bands. In the case of the Ho and Er complexes, the bands stem from the $^5F_5 \rightarrow {}^5I_8$ and $^4I_{13/2} \rightarrow {}^4I_{15/2}$ transitions, respectively. Thus, these luminescence spectra only give information about the splitting of the ground multiplet. For the Tb complexes the situation is different with luminescence transitions observed for $^5D_4 \rightarrow {}^7F_6$, $^5D_4 \rightarrow {}^7F_5$ and $^5D_4 \rightarrow {}^7F_4$. Here the 3 observed bands between 480–500 nm ($^5D_4 \rightarrow {}^7F_6$) provide information on the ground multiplet splitting. The available experimental data (Figure 2 and Table S9) do not allow to unambiguously assign the observed bands as of electronic or vibrational origin. Therefore, for the sake of simplicity, we assume for all complexes that all the observed transitions are of electronic origin. In each spectrum, the highest energy band is assigned as the zero-phonon line; these are at 20492 cm^{-1}, 15423 cm^{-1}, 6578 cm^{-1} for $\mathbf{TbL^{18}}$, $\mathbf{HoL^{18}}$, and $\mathbf{ErL^{18}}$, respectively, and 20500 cm^{-1}, 15442 cm^{-1} and 6587 cm^{-1} for TbL, HoL and ErL, respectively. The energies of the various ground term sublevels can be found in Table 2. We note there are fewer emission bands observed in the luminescence spectra of $\mathbf{LnL^{18}}$ and LnL than what is expected based on the number of energy levels in the ground multiplet. The remaining energy levels may be hidden in the linewidth of the peaks. For instance, the three bands originating from $^5D_4 \rightarrow {}^7F_6$ in TbL have linewidths of 91–186 cm^{-1}.

Table 2. The observed energies (cm^{-1}) of the ground term sublevels of $\mathbf{TbL^{18}}$, TbL; $\mathbf{HoL^{18}}$, HoL; and $\mathbf{ErL^{18}}$, ErL

$\mathbf{TbL^{18}}$	**TbL**	$\mathbf{HoL^{18}}$	**HoL**	$\mathbf{ErL^{18}}$	**ErL**
0	0	0	0	0	0
138	142	38	43	39	45
383	395	90	86	70	73
		211	212	102	104
		394	400	333	341
		448	440		
		484	–		
		524	521		

The energy level splitting of the ground multiplet is essentially unchanged upon post-derivatisation of TbL, HoL or ErL to $\mathbf{TbL^{18}}$, $\mathbf{HoL^{18}}$ or $\mathbf{ErL^{18}}$. The energies of the ground term sublevels (Table 2) indicate small changes of 2–13 cm^{-1}, however, considering the step size of 0.2–0.3 nm used in the measurements, the uncertainties of the energies are comparable to these numbers, being ±25 cm^{-1} for $\mathbf{TbL^{18}}$, ±9 cm^{-1} $\mathbf{HoL^{18}}$ and ±2 cm^{-1} for $\mathbf{ErL^{18}}$. This is also expected from the close structural resemblance of the first coordination spheres. In our previous study on $\mathbf{YbL^{18}}$ we also saw very small changes in the energy level structure of the ground multiplet [22]. However, when the derivatisation is made on the phenyl rings, changes in the energy level splitting of up to 45% have been observed between Er(trensal) derivatives (H_3trensal = 2,2′,2″-tris(salicylideneimino)trimethylamine) [41]. The larger shifts in the energy levels moving between

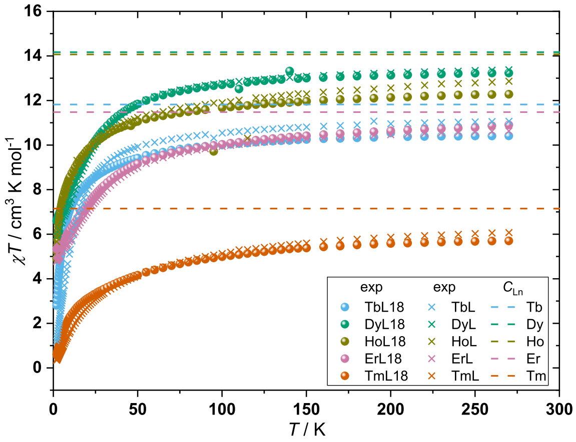

Figure 3. Temperature dependence of the χT product of **TbL^{18}–TmL^{18}** and TbL–TmL. The χT data of LnL are obtained from literature [21]. Curie constants (C_{Ln}) of Tb(III), Dy(III), Ho(III), Er(III), and Tm(III) are shown as dashed lines.

different Ln(trensal) derivatives are likely due to the substitution groups being placed directly on the phenyl rings rather than an aldehyde being changed into an imine.

3.3.2. *Static magnetic properties*

The static magnetic properties of **TbL^{18}–TmL^{18}** were studied by d.c. magnetic susceptibility measurements and VTVB measurements. The d.c. magnetic susceptibility measurements (Figure 3) were recorded in the temperature range 2–270 K in a static magnetic field B of 1000 Oe.

The d.c. susceptibility data are plotted as the χT product, where $\chi = M/B$, with χ being the molar magnetic susceptibility and M being the magnetisation, and B being the magnetic field.

TbL^{18}–TmL$_{18}$ reach their lowest χT value at 2 K being 2.80, 6.59, 4.91, 5.33, 0.60 cm^3·K·mol^{-1}, respectively. Upon increasing the temperature, the χT products continuously increase, which is due to the population of excited levels in the ground multiplets of the complexes as there are negligible magnetic couplings to neighbouring complexes (the nearest paramagnetic centre is about 7 Å away). At 270 K, the χT products of **TbL^{18}–TmL^{18}** reach their highest values at 10.41 (C_{Tb} = 11.82), 13.23 (C_{Dy} = 14.17), 12.28 (C_{Ho} = 14.07), 10.90 (C_{Er} = 11.48), and 5.70 (C_{Tm} = 7.15) cm^3·K·mol^{-1}, respectively. These χT products are smaller than the values expected for the isolated Ln(III), known as the Curie constants (C_{Ln}). This suggests that the total energetic splitting of their ground states is larger than the thermal energy available at 270 K. This is corroborated by the luminescence spectra and has also been observed for other complexes with a similar coordination sphere such as the Ln(trensal) [42,43], Ln(trenovan) (H_3 trenovan = tris(((3-methoxysaliclidene)amino) ethyl)amine) [44], and LnL [21].

Comparing the temperature dependence of the χT products of **TbL^{18}–TmL^{18}** to TbL–TmL the Kramers ion (Dy and Er)-containing complexes show almost no difference between the post-derivatised and parent complexes, as expected from the very subtle changes in the first coordination sphere and the similar energy level splitting of the ground multiplet found between **ErL^{18}** and ErL. This was also observed for the χT products of the Kramers ion complexes **YbL^{18}** and YbL [22]. In terms of the non-Kramers ion (Tb, Ho and Tm) complexes, larger deviations between the post-derivatised complexes and the parent complexes are found. Emission spectroscopy showed very similar energy level splittings of the ground multiplets of **TbL^{18}** and TbL as well as for **HoL^{18}** and HoL, leading us to believe that the change in the temperature dependence of the χT products between post-derivatised complexes and their parent complexes likely stems from different eigenvector compositions. This also explains why the χT product at 2 K for **TbL^{18}** is 2.80 cm^3·K·mol^{-1} while it is 1.20 cm^3·K·mol^{-1} for TbL. The large difference in the eigenvector compositions is also corroborated by VTVB measurements (*vide infra*).

VTVB measurements were conducted with applied magnetic fields of 500, 5000, 10,000, 20,000, 30,000, 40,000, and 50,000 Oe and with temperatures in the range 2–10 K (Figures S32–S36).

For all complexes the maximum magnetisation value is reached at 2 K and 50,000 Oe. The reduced magnetisation of **TbL^{18}–TmL^{18}** does not superimpose, suggesting that the ground state is not thermally isolated from excited states. This is similar to the parent complexes LnL, where only the GdL and YbL complexes show superimposable reduced magnetisation curves [21]. Comparing the VTVB measurements of the post-derivatised complexes **TbL^{18}–TmL^{18}** with the parent complexes TbL–TmL, the difference between the Kramers and non-Kramers ion-containing complexes becomes more apparent. The VTVB measurements of the Kramers ion-containing complexes **DyL^{18}** and DyL as well as **ErL^{18}** and ErL are almost identical (Figures S33 and S35), suggesting very similar eigenvector compositions of the ground energy levels for the post-derivatised and parent complexes. On the contrary, the non-Kramers ion-containing complexes show different VTVB magnetisation for **LnL^{18}** and LnL (Figures S32, S34 and S36). The difference between magnetisation curves for the Kramers and non-Kramers ion complexes upon derivatisation is likely due to the difference in the degeneracy of the energy levels of the Kramers and non-Kramers ions and the loss of crystallographic trigonal symmetry upon derivatisation, with the latter leading to additional off-diagonal terms in the crystal field Hamiltonian, causing more mixings of the states. Unlike in the case of Kramers ions, the energy levels of non-Kramers ions are not forced to be degenerate in pairs at zero magnetic field. Previous measurements on TbL, HoL and TmL indicated that the ground state is likely a singlet but with an excited doublet very close to the ground state for TbL and HoL [21]. If the degeneracy of this doublet is lifted due to the loss of trigonal symmetry, this may lead to much different magnetisation curves.

3.3.3. *Influence of the post-derivatisation on the dynamic magnetic properties*

A.c. susceptibility measurements were performed on **TbL^{18}**–**TmL^{18}** within the frequency range 1–1500 Hz of an oscillating magnetic field of 3.5 Oe, and with an applied static magnetic field H of 0 to 5000 Oe (Figures S37–S46). When no static magnetic field is applied, none of the complexes show any out-of-phase a.c. signal (χ'') with respect to the available frequency range. This suggests that a large degree of quantum tunnelling of magnetisation (QTM) is present in the complexes, similar to the parent complexes and other complexes with the Ln(trensal) motif [21,44,45]. In an attempt to quench the QTM, the a.c. susceptibility was measured in static magnetic fields. When applying a static magnetic field, an out-of-phase signal emerged for the complexes containing Kramers ions (Dy and Er). This was not observed for the complexes containing non-Kramers ions. The difference between the Kramers and non-Kramers ion complexes is likely due to the non-Kramers complexes having a singlet instead of a doublet as the ground state. In three-fold symmetry, only Kramers ions are required to have a degenerate ground state in zero magnetic field. This difference between the Kramers and non-Kramers ions has also been observed in the parent complexes LnL and for the similar Ln(trensal) complexes [21,44].

The field dependence of the χ'' for **DyL^{18}** and **ErL^{18}** show similar features (Figures S40 and S44). At low magnetic fields a peak in the χ'' is found at high frequencies. Upon increasing the magnetic field this process disappears from the measurement window, and instead a very broad signal emerges at low frequencies. The same behaviour was observed in the parent complexes DyL and ErL, where the broad relaxation process was found to be temperature-independent [21]. Unfortunately the relaxation process at high frequencies has its maximum outside our measurement window preventing an investigation of its temperature dependence.

In an effort to slow the relaxation dynamics of the process found at high frequencies the complexes **DyL^{18}** and **ErL^{18}** were diluted at 5% into the diamagnetic hosts **YL^{18}** and **LuL^{18}**, respectively. The dilution into the diamagnetic host limits the dipolar interactions between neighbouring magnetic centres, thereby limiting the effect of dipolar couplings on the spin-lattice relaxation. The field dependence of the χ" of **Dy@YL^{18}** and **Er@LuL^{18}** show a single peak with a maximum around 100 Hz (Figures S54 and S60). At 1000 Oe the χ'' signal is most intense and at the lowest frequency for both **Dy@YL^{18}** and **Er@LuL^{18}**, presenting the optimal field to study the temperature dependence. Upon increasing the temperature, the signal quickly moves outside our measurement window with the maximum of the signal moving past the measurement window already at 3 K (Figures S56 and S62). Using CC-FIT2 [46], the temperature dependence of the a.c. susceptibility data was fitted to a generalised Debye model. The limited temperature interval that could be extracted from the measurements prevents a detailed analysis of the results. To compare the relaxation dynamics of the post-derivatised complexes to those of the parent complexes, DyL and ErL were diluted into their diamagnetic hosts YL and LuL at 5%, respectively. However, the dilution into a diamagnetic host did not result to observation of a maximum within the available frequency range (Figures S58 and S64). This shows that the spin-lattice relaxation of the Dy and Er ions is slowed down upon the derivatisation, a feature which was also observed for **YbL^{18}** [22].

As previously mentioned, **GdL^{18}** could not be obtained phase-pure. However, when **GdL^{18}** is diluted at 5% into the diamagnetic host **YL^{18}**, it adopts the same phase as the other members of the **LnL^{18}** family presented herein. Having obtained the Gd complex phase-pure we decided to compare its relaxation dynamics to those of the parent complex GdL. For this, GdL was diluted at 5% into the diamagnetic host YL. Field dependence measurements of the a.c. susceptibility for **Gd@YL^{18}** showed an optimal relaxation at 3000 Oe (Figure S48). Temperature dependence was subsequently measured with a static magnetic field of 3000 Oe for both Gd complexes (Figures S49–S52). Using CC-FIT2 [46], the relaxation times were obtained for each complex. Contrary to the Dy and Er containing complexes, relaxation times for **Gd@YL^{18}** and Gd@YL could be obtained over a large temperature interval (Figure 4 and Tables S5 and S6). Both complexes show very similar relaxation times up to 5 K. Going to higher temperatures, **Gd@YL^{18}** starts to relax faster, which may be attributed to the increased amount of vibrations from the octadecyl chains. In a double logarithmic plot the temperature dependence of the relaxation time of Gd@YL is fully linear with a slope of 1.5, which indicates that the relaxation could be governed by a direct process in this temperature regime (Figure S65). In the case of **Gd@YL^{18}**, the temperature dependence of the relaxation shows a slight curvature, suggesting that at least two different relaxation processes are present within the studied temperature interval.

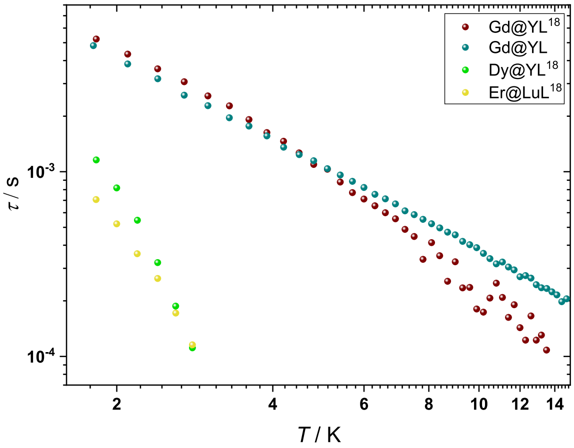

Figure 4. Temperatue dependence of the relaxation time (τ) of **Gd@YL^{18}** at 5% dilution, **Gd@YL** at 5% dilution, **Dy@YL^{18}** at 5% dilution, and **Er@LuL^{18}** at 5% dilution. τ was obtained by fitting the generalised Debye model using CC-FIT2 [46] to the temperature dependence of the a.c. magnetic susceptibility of these complexes at a fixed applied static magnetic field.

4. Conclusion

A novel series of aliphatic chain containing lanthanide complexes **(Tb–Tm, Y)L^{18}** have been obtained through Schiff-base reaction post-derivatisation of LnL with 1-octadecylimine chains. Single-crystal X-ray diffraction revealed that upon post-derivatisation the first coordination sphere of **LnL^{18}** shows great similarities to the one of the parent complex. However, due to van der Waals interactions between the octadecyl chains in the solid state, the trigonal symmetry of the parent complex (LnL) was lost upon post-functionalisation. Emission spectra of **(Tb, Ho, Er)L^{18}** and (Tb, Ho, Er)L showed little change in the energetic splitting of the ground multiplet upon post-derivatisation. The changes in the energy level splitting were much smaller than what has been observed between different Er(trensal) derivatives, suggesting that changes in the second coordination sphere that do not change the electron density on the phenyl rings of the complexes have very little effect on the energy levels of the Ln ions in this type of complexes. Although the energy level splitting seems to be little perturbed by the post-derivatisation, the static magnetic properties were found to change significantly upon post-derivatisation for the non-Kramers ion complexes. The effect was largest for the magnetisation measurements at low temperature and is likely the result of a large change in the eigenvector compositions because of non-diagonal terms induced by the low symmetry. This large difference in the static magnetic properties of the non-Kramers ions upon post-derivatisation was not observed for the Kramers ions. It is surprising that post-derivatisation influences the static magnetic properties of the LnL complexes differently depending on whether they contain Kramers or non-Kramers ions. This is important to the future integration of Ln complexes into devices, where bulk properties are wished to be retained upon device integration. If LnL complexes are to be integrated into such devices the focus should be on integrating the Kramers ion-containing complexes which seem less susceptible to small perturbations.

Further studies will investigate how different chain lengths of the amines affect the electronic and magnetic properties of the Ln ions to get a better understanding of the relationship between the static and dynamic properties of the systems as well as between the Kramers and non-Kramers ion complexes. Moreover, Langmuir–Blodgett films formed with these complexes will be studied, to see how the static magnetic and electronic properties change upon organisation in a 2D structure.

Declaration of interests

The authors do not work for, advise, own shares in, or receive funds from any organization that could benefit from this article, and have declared no affiliations other than their research organizations.

Funding

We thank the Novo Nordisk Foundation for research grant NNF20OC0065610.

Accession codes

CCDC 2222267, 2222268 and 2263962 contain the supplementary crystallographic data for this paper. These data can be obtained free of charge via www.ccdc.cam.ac.uk/data_request/cif, or by emailing data_request@ccdc.cam.ac.uk, or by contacting The Cambridge Crystallographic Data Centre, 12 Union Road, Cambridge CB2 1EZ, UK; fax: +44 1223 336033.

Supplementary data

Supporting information for this article is available on the journal's website under https://doi.org/10.5802/crchim.282 or from the author.

References

[1] H. Liang, K. Yang, Y. Yang, Z. Hong, S. Li, Q. Chen, J. Li, X. Song, H. Yang, *Nano Lett.*, 2022, **22**, 9045-9053.

[2] C. D. S. Brites, S. Balabhadra, L. D. Carlos, *Adv. Opt. Mater.*, 2018, **7**, article no. 1801239.

[3] S. Goderski, M. Runowski, P. Wozny, V. Lavin, S. Lis, *ACS Appl. Mater. Interfaces*, 2020, **12**, 40475-40485.

[4] R. M. Diaz-Rodriguez, D. A. Galico, D. Chartrand, E. A. Suturina, M. Murugesu, *J. Am. Chem. Soc.*, 2022, **144**, 912-921.

[5] J. Wahsner, E. M. Gale, A. Rodriguez-Rodriguez, P. Caravan, *Chem. Rev.*, 2019, **119**, 957-1057.

[6] E. Kanal, *Magn. Reson Imaging*, 2016, **34**, 1341-1345.

[7] H. Li, T. J. Meade, *J. Am. Chem. Soc.*, 2019, **141**, 17025-17041.

[8] K. S. Pedersen, A. M. Ariciu, S. McAdams, H. Weihe, J. Bendix, F. Tuna, S. Piligkos, *J. Am. Chem. Soc.*, 2016, **138**, 5801-5804.

[9] D. Aguila, L. A. Barrios, V. Velasco, O. Roubeau, A. Repolles, P. J. Alonso, J. Sese, S. J. Teat, F. Luis, G. Aromi, *J. Am. Chem. Soc.*, 2014, **136**, 14215-14222.

[10] D. Maniaki, D. Garay-Ruiz, L. A. Barrios, D. Martins, D. Aguila, F. Tuna, D. Reta, O. Roubeau, C. Bo, G. Aromi, *Chem. Sci.*, 2022, **13**, 5574-5581.

[11] B. E. Bode, E. Fusco, R. Nixon, C. D. Buch, H. Weihe, S. Piligkos, *J. Am. Chem. Soc.*, 2023, **145**, 2877-2883.

[12] C. D. Buch, K. Kundu, J. J. Marbey, J. van Tol, H. Weihe, S. Hill, S. Piligkos, *J. Am. Chem. Soc.*, 2022, **144**, 17597-17603.

[13] M. D. Jenkins, Y. Duan, B. Diosdado, J. J. García-Ripoll, A. Gaita-Ariño, C. Giménez-Saiz, P. J. Alonso, E. Coronado, F. Luis, *Phys. Rev. B*, 2017, **95**, article no. 064423.

[14] J. J. Le Roy, J. Cremers, I. A. Thomlinson, M. Slota, W. K. Myers, P. H. Horton, S. J. Coles, H. L. Anderson, L. Bogani, *Chem. Sci.*, 2018, **9**, 8474-8481.

[15] S. T. Liddle, J. van Slageren, *Chem. Soc. Rev.*, 2015, **44**, 6655-6669.

[16] N. Ishikawa, M. Sugita, T. Ishikawa, S. Y. Koshihara, Y. Kaizu, *J. Am. Chem. Soc.*, 2003, **125**, 8694-8695.

[17] D. N. Woodruff, R. E. Winpenny, R. A. Layfield, *Chem. Rev.*, 2013, **113**, 5110-5148.

[18] C. A. P. Goodwin, F. Ortu, D. Reta, N. F. Chilton, D. P. Mills, *Nature*, 2017, **548**, 439-442.

[19] F. S. Guo, B. M. Day, Y. C. Chen, M. L. Tong, A. Mansikkamaki, R. A. Layfield, *Science*, 2018, **362**, 1400-1403.

[20] J. D. Rinehart, J. R. Long, *Chem. Sci.*, 2011, **2**, 2078-2085.

[21] C. D. Buch, S. H. Hansen, C. M. Tram, D. Mitcov, S. Piligkos, *Inorg. Chem.*, 2020, **59**, 16328-16340.

[22] Y. Zhou, C. D. Buch, S. H. Hansen, S. Piligkos, *Dalton Trans.*, 2023, **52**, 8792-8799.

[23] C. S. Bonnet, L. Pellegatti, F. Buron, C. M. Shade, S. Villette, V. Kubicek, G. Guillaumet, F. Suzenet, S. Petoud, E. Toth, *Chem. Commun.*, 2010, **46**, 124-126.

[24] E. M. Surender, S. Comby, S. Martyn, B. Cavanagh, T. C. Lee, D. F. Brougham, T. Gunnlaugsson, *Chem. Commun.*, 2016, **52**, 10858-10861.

[25] S. Kaščáková, A. Giuliani, S. Lacerda, A. Pallier, P. Mercère, É. Tóth, M. Réfrégiers, *Nano Res.*, 2015, **8**, 2373-2379.

[26] J. Wang, A. Groeneveld, M. Oikonomou, A. Prusova, H. Van As, J. W. van Lent, A. H. Velders, *Soft Matt.*, 2016, **12**, 99-105.

[27] R. J. Ellis, Y. Meridiano, R. Chiarizia, L. Berthon, J. Muller, L. Couston, M. R. Antonio, *Chem. Eur. J.*, 2013, **19**, 2663-2675.

[28] R. Pinol, J. Zeler, C. D. S. Brites, Y. Gu, P. Tellez, A. N. Carneiro Neto, T. E. da Silva, R. Moreno-Loshuertos, P. Fernandez-Silva, A. I. Gallego, L. Martinez-Lostao, A. Martinez, L. D. Carlos, A. Millan, *Nano Lett.*, 2020, **20**, 6466-6472.

[29] J. A. Kitchen, D. E. Barry, L. Mercs, M. Albrecht, R. D. Peacock, T. Gunnlaugsson, *Angew. Chem. Int. Ed. Engl.*, 2012, **51**, 704-708.

[30] D. E. Barry, J. A. Kitchen, L. Mercs, R. D. Peacock, M. Albrecht, T. Gunnlaugsson, *Dalton Trans.*, 2019, **48**, 11317-11325.

[31] A. T. O'Neil, J. A. Harrison, J. A. Kitchen, *Chem. Commun.*, 2021, **57**, 8067-8070.

[32] V. Shul'gin, N. Pevzner, A. Gusev, M. Sokolov, V. Panyushkin, J. Devterova, K. Kirillov, I. Martynenko, W. Linert, *J. Coord. Chem.*, 2018, **71**, 4228-4236.

[33] W. M. Haynes, *CRC Handbook of Chemistry and Physics*, 94th ed., CRC Press, 2014.

[34] G. A. Bain, J. F. Berry, *J. Chem. Educ.*, 2008, **85**, 532-536.

[35] G. M. Sheldrick, *Acta Crystallogr. A*, 2008, **64**, 112-122.

[36] G. M. Sheldrick, *Acta Crystallogr. A*, 2015, **71**, 3-8.

[37] G. M. Sheldrick, *Acta Crystallogr. C*, 2015, **71**, 3-8.

[38] O. V. Dolomanov, L. J. Bourhis, R. J. Gildea, J. A. K. Howard, H. Puschmann, *J. Appl. Crystallogr.*, 2009, **42**, 339-341.

[39] L. J. Bourhis, O. V. Dolomanov, R. J. Gildea, J. A. Howard, H. Puschmann, *Acta Crystallogr. A*, 2015, **71**, 59-75.

[40] M. Woods, K. M. Payne, E. J. Valente, B. E. Kucera, V. G. Young Jr, *Chem. Eur. J.*, 2019, **25**, 9997-10005.

[41] K. S. Pedersen, L. Ungur, M. Sigrist, A. Sundt, M. Schau-Magnussen, V. Vieru, H. Mutka, S. Rols, H. Weihe, O. Waldmann, L. F. Chibotaru, J. Bendix, J. Dreiser, *Chem. Sci.*, 2014, **5**, 1650-1660.

[42] K. S. Pedersen, J. Dreiser, H. Weihe, R. Sibille, H. V. Johannesen, M. A. Sorensen, B. E. Nielsen, M. Sigrist, H. Mutka, S. Rols, J. Bendix, S. Piligkos, *Inorg. Chem.*, 2015, **54**, 7600-7606.

[43] B. M. Flanagan, P. V. Bernhardt, E. R. Krausz, S. R. Luthi, M. J. Riley, *Inorg. Chem.*, 2002, **41**, 5024-5033.

[44] E. Lucaccini, J. J. Baldovi, L. Chelazzi, A. L. Barra, F. Grepioni, J. P. Costes, L. Sorace, *Inorg. Chem.*, 2017, **56**, 4729-4739.

[45] E. Lucaccini, L. Sorace, M. Perfetti, J. P. Costes, R. Sessoli, *Chem. Commun.*, 2014, **50**, 1648-1651.

[46] D. Reta, N. F. Chilton, *Phys. Chem. Chem. Phys.*, 2019, **21**, 23567-23575.

ACADÉMIE
DES SCIENCES
INSTITUT DE FRANCE

Comptes Rendus. Chimie
2024, Vol. 27, Special issue S1, p. 17-34
`https://doi.org/10.5802/crchim.260`

Research article

French/Nordic Special Issue on Materials and Coordination Chemistry

Organotin(IV) trifluoromethanesulfonate chemistry: isolation and characterization of novel 1,10-phenanthroline-based derivatives

Hélène Cattey [a] **and Laurent Plasseraud** [*, a]

[a] Institut de Chimie Moléculaire de l’Université de Bourgogne, UMR-CNRS 6302,
Université de Bourgogne, 9 avenue A. Savary, F-21078 Dijon, France
E-mails: helene.cattey@u-bourgogne.fr (H. Cattey),
laurent.plasseraud@u-bourgogne.fr (L. Plasseraud)

Abstract. The reactivity of the hydroxo di-*n*-butyltin trifluoromethanesulfonato dimer complex [*n*-$Bu_2Sn(\mu\text{-}OH)(H_2O)(CF_3SO_3)]_2$ (**1**) toward 1,10-phenanthroline (phen) has been investigated, leading to the formation of two novel di-*n*-butyltin(IV) trifluoromethanesulfonate complexes [*n*-$Bu_2Sn(\mu\text{-}OH)(phen)]_2[CF_3SO_3]_2$ (**5**) and [*n*-$Bu_2Sn(phen)_2][CF_3SO_3]_2$ (**6**), in which the tin atoms are bis-chelated by one and two bidentate phen ligands, respectively. Salts **5** and **6** were characterized by single crystal X-ray diffraction analysis, elemental analysis, mass spectrometry, and infrared spectroscopy as well as ^{1}H, ^{19}F, $^{13}C\{^{1}H\}$, and $^{119}Sn\{^{1}H\}$ NMR spectroscopy. Monitoring by $^{119}Sn\{^{1}H\}$ NMR spectroscopy in CD_3CN solution of the reaction proceeding with successive addition of phen revealed the *in situ* formation of three organotin(IV) trifluoromethanesulfonate intermediate species. Two of these, namely {[*n*-$Bu_2Sn(H_2O)]_2O\cdot$*n*-$Bu_2Sn(OH)_2\}[CF_3SO_3]_2$ (**2**) and [*n*-$Bu_2Sn_2(OH)(CF_3SO_3)]_2O$ (**4**), were already known and could be clearly identified on the basis of their $^{119}Sn\{^{119}H\}$ NMR chemical shifts. The composition of the third intermediate, **3**, with an unknown chemical shift value, was investigated. A possible structure, especially suggested by electrospray-ionization mass spectrometry, is proposed as [{*n*-$Bu_2Sn(phen)(CF_3SO_3)\}_2(\mu\text{-}CF_3SO_3)][CF_3SO_3]$. Furthermore, from a mixture of **1** and phen in equimolar ratio, in dichloromethane solvent and at –20 °C, temperature-sensitive crystals of a new hydrated di-*n*-butyltin cation, [*n*-$Bu_2Sn(phen)(OH)(H_2O)][CF_3SO_3]$ (**7**), were isolated. Crystals of the organic salt 1,10-phenanthrolinium trifluoromethanesulfonate (phenHOTf) were also obtained from the filtrate of the mother-liquor. The reactivity of **1** toward 2,9-dimethyl-1,10-phenanthroline was also explored (dmphen), leading to the detection of characteristic fingerprints of distannoxanes **2** and **4** by $^{119}Sn\{^{119}H\}$ NMR, and to the crystallization of phenanthrolinium triflate salts, which were characterized by X-ray diffraction analysis as **dmphenHOTf** and **dmphenHOTf·dmphen**.

Keywords. Di-*n*-butyltin(IV) complexes, Trifluoromethanesulfonate anion, Nitrogen-containing heterocyclic compounds, 1,10-Phenanthroline derivatives, $^{119}Sn\{^{1}H\}$ NMR monitoring, Single crystal X-ray diffraction.

Manuscript received 28 April 2023, revised 19 July 2023, accepted 4 September 2023.

---

[*] Corresponding author

ISSN (electronic): 1878-1543

1. Introduction

To the best of our knowledge, the first study describing the synthesis of organotin trifluoromethanesulfonates dates back to the 1970s, led by Schmeißer's group [1]. Since then, this class of compounds has attracted much interest in homogeneous catalysis and synthesis. These compounds are indeed reported to be efficient for specific metal-assisted organic reactions, acting as appropriate *Lewis* acid catalysts. Beneficial effects have been particularly described for the aldol reaction of *Mukaiyama* [2], *Robinson* annulation [3], acetylation of alcohols [4], transesterification of dimethyl carbonate with phenol [5], and direct synthesis of dimethyl carbonate (DMC) from methanol and carbon dioxide [6,7]. From a synthetic point of view, organotin trifluoromethanesulfonates are generally prepared by reacting an organotin oxide with trifluoromethanesulfonic acid (CF_3SO_3H, TfOH) [8,9], or alternatively, from an organotin chloride ($R_{(4-x)}SnCl_x$ with R = alkyl) in the presence of silver trifluoromethanesulfonate ($AgCF_3SO_3$) [8,10]. Several organotin(IV) complexes have been characterized in the solid state by single crystal X-ray analysis. The CF_3SO_3 group can be ionic and behave as a counter anion, or be a ligand directly bound to tin. In the latter case, it can adopt various coordination modes. Examples of mono-, bi-, and tridentate as well as terminal, *pseudo*-terminal, and bridging CF_3SO_3 groups have already been reported in the literature for *p*-block metals and are shown in Scheme 1 [11,12].

The chemistry and structural aspects of organotin trifluoromethanesulfonates were first reviewed by Beckmann in 2005 [13]. Since 2006, our group has also contributed to this field by characterizing several new specimens by X-ray crystallographic analysis: (i) ionic monobenzyltin(IV) trifluoromethanesulfonate clusters exhibiting unprecedented Sn_6, Sn_{11}, and Sn_{12} frameworks [14,15], (ii) a two-dimensional organostannoxane coordination network ${}^{2}_{\infty}\{[n\text{-Bu}_2(\mu\text{-OH})\text{SnOSn}(\mu\text{-}\eta^2\text{–}O_3SCF_3)n\text{-Bu}_2]_2[n\text{-Bu}_2(\eta^1\text{-}O_3SCF_3)\text{SnOSn}(\mu\text{-OH})n\text{-Bu}_2]_2\}$ [12], which was found to be a polymorph of the tetra-*n*-butyldistannoxane trifluoromethanesulfonate cluster, $[n\text{-Bu}_2Sn_2(OH)(CF_3SO_3)]_2O$ (**4**), described initially by Otera [16,17], (iii) a polymeric chain of dimeric hydroxo di-*n*-butyltin(IV) units bridged by trifluoromethanesulfonate ligands, $[Sn_2(CF_3O_3S)_2(C_4H_9)_4(OH)_2]_n$ [10]. More recently, we reported the isolation and characterization of the dihydrated di-*n*-butyltin(IV) trifluoromethanesulfonate salt $\{[n\text{-Bu}_2Sn(H_2O)]_2O\cdot n\text{-Bu}_2Sn(OH)_2\}[CF_3SO_3]_2$ (**2**), which is characterized by a Sn_3O_3 core [18]. **2** was obtained by reacting at room temperature with the dimeric hydroxo di-*n*-butyl trifluoromethanesulfonate $[n\text{-Bu}_2Sn(\mu\text{-OH})(H_2O)(CF_3SO_3)]_2$ (**1**) with a mixture of anthracene and phenazine.

Continuing to explore the reactivity of **1** toward nitrogen-containing heterocyclic compounds, we report herein the synthesis and characterization of two novel diorganotin trifluoromethanesulfonate derivatives, $[n\text{-Bu}_2Sn(\mu\text{-OH})(\text{phen})]_2[CF_3SO_3]_2$ (**5**) and $[n\text{-Bu}_2Sn(\text{phen})_2][CF_3SO_3]_2$ (**6**), resulting from the reaction of **1** with 1,10-phenanthroline (phen), with the latter acting as bidentate ligand. Monitoring of the reaction by $^{119}Sn\{^1H\}$ NMR spectroscopy in solution (CD_3CN) and as a function of the amount of phen added revealed successive *in situ* formation of species **2**, **3**, and **4**. From the three molar equivalents of phen, only the resonance of **5** is visible in the spectrum. Species **2** and **4** have already been reported in the literature; however, to the best of our knowledge, **3** is a new species. Complexes **5** and **6** were fully characterized by IR, ^1H, ^{11}F, ^{13}C, and $^{119}Sn\{^1H\}$ NMR spectroscopy, mass spectrometry, elemental analysis, and X-ray diffraction analysis. Further investigations were conducted to isolate and identify species **3**. By changing the solvent conditions from acetonitrile to dichloromethane and in a 1:1 molar ratio of **1** and phen, the unprecedented mononuclear hydrated di-*n*-butyltin cation, $[n\text{-Bu}_2Sn(\text{phen})(OH)(H_2O)][CF_3SO_3]$ (**7**), was isolated, with the tin center *N,N*-chelated by a bidentate phen ligand and bearing a terminal hydroxyl group. Moreover, the reactivity of **1** was also tested in the presence of 2,9-dimethyl-1,10-phenanthroline (dmphen). From this reaction, only the phenanthrolinium triflates (**dmphenHOTf** and **dmphen·dmphenHOTf**), resulting from the mono-protonation of dmphen, were obtained.

2. Results and discussion

2.1. *Synthesis and isolation of $[n\text{-Bu}_2Sn(\mu\text{-OH})(\text{Phen})]_2[CF_3SO_3]_2$ (5) and $[n\text{-Bu}_2Sn(\text{Phen})_2][CF_3SO_3]_2$ (6)*

The air-stable dinuclear di-*n*-butyltin(IV) trifluoromethanesulfonate salts $[n\text{-Bu}_2Sn(\mu\text{-OH})(\text{phen})]_2$

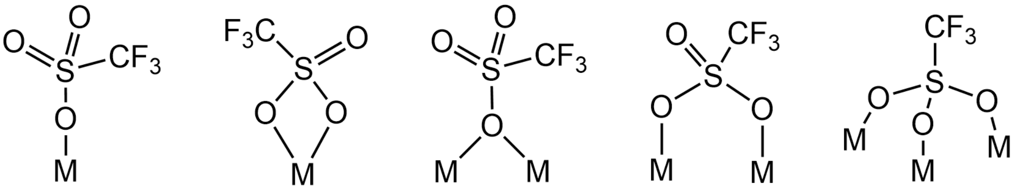

Scheme 1. Molecular representations of known coordination modes involving the trifluoromethanesulfonate ligand and p-block metals (M).

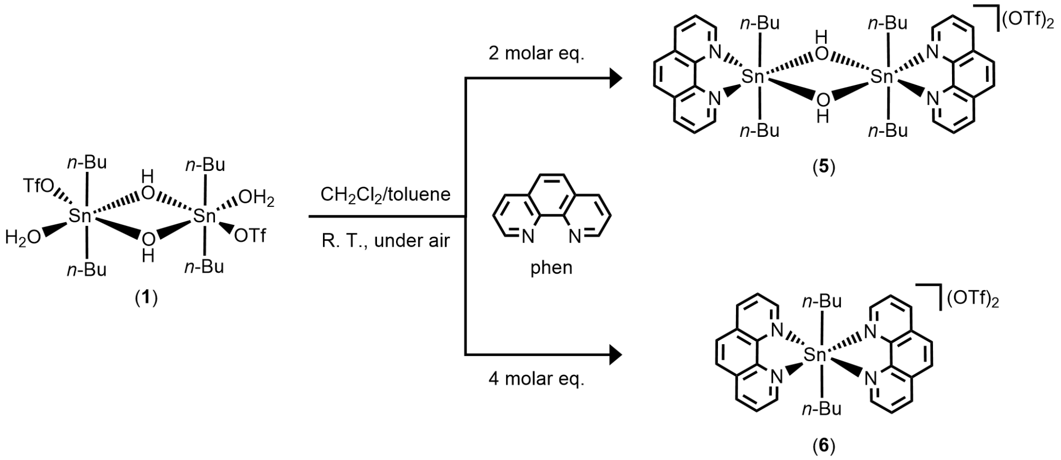

Scheme 2. Synthetic pathway leading to **5** and **6**.

$[CF_3SO_3]_2$ (**5**) and $[n\text{-}Bu_2Sn(phen)_2][CF_3SO_3]_2$ (**6**) were obtained at room temperature, under air atmosphere, from a mixture of dichloromethane/toluene by reacting dimeric trifluoromethanesulfonato hydroxo organotin(IV) $[n\text{-}Bu_2Sn(OH)(H_2O)(CF_3SO_3)]_2$ (**1**) with two molar equivalents of 1,10-phenenthroline ($C_{12}H_8N_2$, phen) (Scheme 2). A pinkish precipitate is first formed, leading, after recrystallization in dichloromethane/toluene, to the formation of single crystals later characterized as **6**. Colorless single crystals of **5** were obtained from the filtrate of the mother liquor by slow evaporation at room temperature.

The two new organotin compounds which are ionic were characterized by elemental analysis, ESI-MS, IR and NMR spectroscopy, and single-crystal X-ray diffraction analysis. Compound **5** exhibits good solubility in organic solvents such as dichloromethane, acetone, and acetonitrile. In CD_3CN, the $^{119}Sn\{^1H\}$ NMR spectrum of **5** exhibits one single resonance at $\delta\,-226$ ppm (Figure S1). Such a chemical shift is in agreement with a six-coordinate tin atom substituted by two n-butyl moieties. It is interesting to note that in acetone-d_6, the signal moves significantly, shifting to −150 ppm, suggesting that the tin center is pentacoordinated in this solvent environment. For comparison, the tin atoms of $[n\text{-}Bu_2Sn_2(OH)(CF_3SO_3)]_2O$ (**4**), which is characterized as a distannoxane, exhibit two resonances in acetone-d_6 at −146 and −151 ppm [9,12]. The ^1H and $^{13}C\{^1H\}$ NMR spectra of **5** depicted in Figures S2 and S3, respectively, corroborate the structure depicted in Scheme 2, showing two sets of signals characteristic of phenanthroline ligands and n-butyl substituents. The CF_3 moieties of the $CF_3SO_3^-$ anions are also clearly identified in the $^{13}C\{^1H\}$ NMR spectrum, giving a typical quartet at $\delta 119.9$ ppm, with a distinctive $^1J_{C\text{–}F}$ coupling constant of 318 Hz. The ^{19}F NMR spectrum exhibits one singlet at $\delta\,-78.2$ ppm (Figure S4). The infrared spectrum of **5** highlights a distinctive broad absorption centered at 3321 cm^{-1} (Figure 1b), which is quite different from the fingerprint of **1** (Figure 1a), but can be assigned to the presence of OH groups (Figure 1b). Characteristic vibration bands of trifluoromethasulfonate lig-

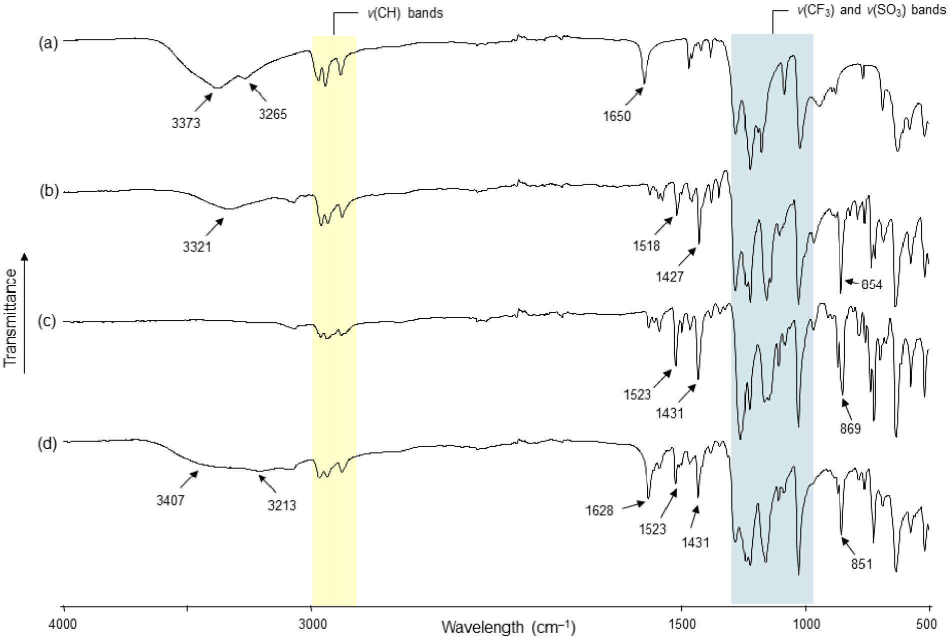

Figure 1. FT-IR (ATR) spectra of (a) [n-Bu$_2$Sn(OH)(H$_2$O)(CF$_3$SO$_3$)]$_2$ (**1**), (b) [n-Bu$_2$Sn(μ-OH)(phen)]$_2$ [CF$_3$SO$_3$]$_2$ (**5**), (c) [n-Bu$_2$Sn(phen)$_2$][CF$_3$SO$_3$]$_2$ (**6**), and (d) [n-Bu$_2$Sn(phen)(OH)(H$_2$O)][CF$_3$SO$_3$] (**7**).

ands, in particular ν(CF$_3$) and ν(SO$_3$), are also observed for **3** in the stretching region between 1000 and 1300 cm^{-1} (outlined by a blue banner in Figure 1) [19–21]. The additional intense bands at 1518, 1427 and 854 cm^{-1} arise from the ν(C=C), ν(C=N) and γ(C–H aromatic rings) absorptions of the phen ligands, respectively. The coordination of these ligands to tin is supported by the shift of the two bands at 1518 cm^{-1}, and 1427 cm^{-1} relative to the free ligand (1503 cm^{-1} and 1420 cm^{-1}) [22,23]. An electrospray mass spectrum (positive mode) of **5** in a mixture of dichloromethane/methanol displays major mass clusters centered at m/z = 431.11333 Da (100%), which fits closely with the [n-Bu$_2$Sn(OH)(phen)]$^+$ fragment (C$_{20}$H$_{27}$N$_2$OSn, calc.: 431.11453 Da) (Figure S5). Finally, the micro-analytical (C, H, N, S) data also support the composition of **5** (see Section 4).

Compound **6** was collected as a precipitate from the starting reaction. However, it was found to be well soluble in acetone and dichloromethane. Suitable single-crystals for X-ray diffraction analysis were grown from a dichloromethane/toluene mixture. Compared with **1** and **5**, the infrared spectrum of **6** shows no absorption bands above 3100 cm^{-1} excluding the presence of OH or H$_2$O ligands. Otherwise, the characteristic absorption bands of n-butyl chain [ν(C–H)], CF$_3$SO$_3$, and phen are present and support the coordination of the phen ligand to the tin center (Figure 1c). In the aceton-d_6 solution, the ^{119}Sn{^{1}H} NMR of **6** reveals a broad resonance at δ −231 ppm (Figure S6) [for comparison, in the same deuterated solvent, **5** exhibits a weak resonance at δ −150 ppm (Figure S7)], and the ^{1}H NMR spectrum shows a 1:1 integration ratio between the protons of the n-butyl chains and the phen ligands (Figure S8). The ^{13}C{^{1}H} NMR spectrum exclusively reveals phen and n-butyl resonances and highlights the presence of CF$_3$SO$_3^-$ anions by giving a quartet centered at δ121.9 ppm, which is attributable to CF$_3$ moieties ($^1J_{\text{C–F}}$ = 321 Hz) (Figure S9). A single resonance at δ −78.8 ppm is also observed in the ^{19}F NMR spectrum (Figure S10). The electrospray mass spectrum (positive mode) of **6** in a mixture of dichloromethane/methanol displays two predominant mass clusters centred at m/z = 445.13055 Da (100%) and 431.11559 Da (80%), which can be assigned to [n-Bu$_2$Sn(phen)(OCH$_3$)]$^+$ (C$_{21}$H$_{29}$N$_2$OSn, calc.: 445.13019 Da) and [n-Bu$_2$ Sn(phen)(OH)]$^+$ (C$_{20}$H$_{27}$N$_2$OSn, calc.: 431.11454 Da) fragments, respectively (Figure S11).

2.2. *Single-crystal X-ray diffraction analysis of* **5**

The solid-state structure of **5** consists of a [*n*-$Bu_2Sn(OH)(phen)]_2^{2+}$ dication surrounded by two non-coordinated $CF_3SO_3^-$ anions. An ORTEP view of **5** is shown in Figure 2 together with the selected bond distances and angles. The inorganic core of the cation is based on a planar four-membered distannoxane $[Sn_2(\mu\text{-}OH)_2]$ unit, where the tin atoms are bridged by two hydroxide ligands. The two tin atoms are bound to two *n*-butyl ligands [Sn–C13 = 2.131(2), Sn–C17 = 2.128(2) Å], to two oxygen atoms of bridging hydroxide ligands [Sn–O1 = 2.0828(13), Sn–O1^i = 2.2334(14) Å], and are chelated by a bidentate 1,10-phenanthroline molecule forming five-membered rings. However, the Sn–N distances show significant differences [Sn–N1 = 2.4171(17), Sn–N2 = 2.6330(18) Å]. Thus, the tin centers can be considered to be hexacoordinated, adopting a markedly distorted octahedral geometry [C17–Sn–C13 = 156.93(9)°, N1–Sn–O1^i = 156.85(5)°, N2–Sn–O1 = 150.33(6)°]. Furthermore, the phen ligands are parallel to each other and exhibit a twist angle of 25.55(4)° to the plane containing the Sn_2O_2 ring. Two trifluoromethanesulfonate anions complete the structure of **5**. For both $CF_3SO_3^-$, one of their oxygen atoms is involved in hydrogen interaction with a hydroxide group of the cation [$O_3\cdots HO$ = 2.791(2) Å]. Moreover, we can also suspect for each $CF_3SO_3^-$ a possible weak interaction involving another oxygen atom of sulfonate functions and one tin atom of the cation [O4$\cdots$Sn = 3.342(2) Å], which could explain the different Sn–N distances. The existence of such long-distance Sn$\cdots$O interactions in the solid state has already been underlined for previous diorganotin compounds [10,24]. In the past, *Blaschette* and *Jones* reported the isolation of $[Me_2\{(MeSO_2)_2N\}(phen)Sn(\mu\text{-}OH)]_2$, a compound structurally analogous to **5** and prepared from $Me_2Sn[N(SO_2Me)_2]_2$ and 1,10-phenanthroline by adventitious hydrolysis [25]. Interestingly, in this compound, the $(MeSO_2)_2N^-$ anions operate in the same manner as the triflate anions of **5**. They are non-coordinated and are involved in hydrogen bonding and long Sn$\cdots$O interactions. The authors then described the tin atoms as being heptacoordinated in a pentagonal bipyramidal arrangement. With regard to compound **5** and based on the $^{119}Sn\{^1H\}$ NMR chemical shift value (δ −226 ppm in CD_3CN), we argue in this case for the hexacoordination of the tin atoms.

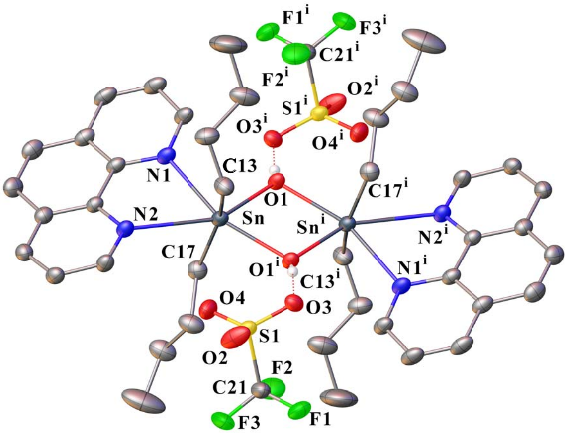

Figure 2. ORTEP drawing of **5** using a partial atom labeling scheme (30% probability thermal ellipsoids). Hydrogen atoms of phenanthroline ligands and *n*-butyl chains are omitted for clarity. Hydrogen bonds involving CF_3SO_3– and μ–OH groups are represented by red dotted lines. Selected bond lengths (Å) and angles (°): Sn–C17 2.128(2), Sn–C13 2.131(2), Sn–O1 2.0820(13), Sn–O1^i 2.2343(14), Sn–N1 2.4171(17), C21–F3 1.315(3), C21–F1 1.329(3), C21–F2 1.334(3), C21–S1 1.816(3), S1–O2 1.4239(19), S1–O4 1.4331(18), S1–O3 1.4406(15); O1–Sn–C17 100.02(7), O1–Sn–C13 102.51(8), C17–Sn–C13 156.93(9), O1–Sn–O1^i 72.08(6), C17–Sn–O1^i 90.38(8), C13–Sn–O1^i 91.85(8), O1–Sn–N1 84.98(6), C17–Sn–N1 90.58(8), C13–Sn–N1 96.24(8), O1^i–Sn–N1 156.85(5), Sn–O1–Sn^i 107.92(6), F3–C21–F1 107.0(2), F3–C21–F2 108.8(3), F1–C21–F2 106.7(2), F3–C21–S1 112.27(19), F1–C21–S1 110.9(2), F2–C21–S1 110.95(18), O2–S1–O4 116.03(13), O2–S1–O3 114.98(13), O4–S1–O3 113.25(10), O2–S1–C21 103.25(13), O4–S1–C21 104.76(13), O3–S1–C21 102.36(10) (symmetry transformations used to generate equivalent atoms: (^{i}) : $3/2-x, 1/2-y, -z$).

2.3. *Single-crystal X-ray structural analysis of* **6**

The structure of salt 6 in the solid state consists of a [*n*-$Bu_2Sn(Phen)_2]^{2+}$ dication surrounded by

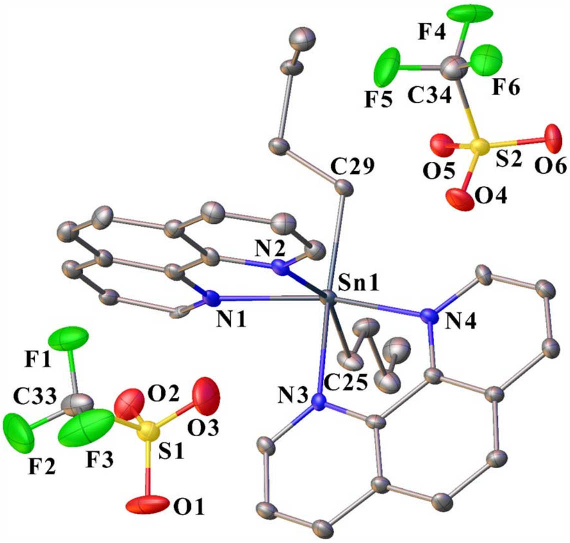

Figure 3. Ortep drawing of **6** using a partial atom labeling scheme (30% probability thermal ellipsoids). Hydrogen atoms and one molecule of toluene (solvent) are omitted for clarity. Selected bond lengths (Å) and angles (°): Sn1–C29 2.162(9), Sn1–C25 2.158(9), Sn–N1 2.273(8), Sn–N2 2.369(8), Sn–N3 2.309(7), Sn–N4 2.275(8), S1–O2 1.415(8), S1–O1 1.427(8), S1–O3 1.431(9), S1–C33 1.823(11), C33–F1 1.299(12), C33–F2 1.328(14), C33–F3 1.312(13), C25–Sn1–C29 116.9(4), N1–Sn1–N2 71.9(3), N1–Sn1–N3 87.7(3), N1–Sn1–N4 154.5(3), C29–Sn1–N1 98.0(3), C25–Sn1–N1 97.0(4), N3–Sn1–N2 76.3(3), N4–Sn1–N2 87.5(3), C29–Sn1–N2 84.12(3), C25–Sn1–N2 157.9(3), N4–Sn1–N3 72.6(3), C29–Sn1–N3 156.9(3), C25–Sn1–N3 84.3(3), C29–Sn1–N4 94.6(3), C25–Sn1–N4 96.9(4).

two non-coordinating CF$_3$SO$_3^-$ anions. One toluene molecule (crystallization solvent) co-crystallizes with **6**. Figure 3 shows an Ortep view of **6** with the atom numbering scheme, and Figure 4 shows a perspective view of the crystal packing in the unit cell. The molecular structure of the title compound consists of a central six-coordinated tin atom that exhibits an octahedral coordination environment comprising four nitrogen atoms from two distinct chelating phen ligands and two carbon atoms of the two *n*-butyl chains. The ligands are positioned in a *cis*-arrangement. The N1–Sn–N4, N2–Sn–C25, N3–Sn–C29 bond angles measure 154.5(3), 157.9(3), and 156.9(3)°, respectively, indicating a distortion from an ideal octahedral geometry. The two phen ligands are bidentate to tin, forming five-membered chelate rings that are nearly planar. The Sn–N distances are in the range of 2.273(8) and 2.368 Å. They are comparable to that found in [MeSn(phen)2]$^{2+}$ [26], which is, to the best of our knowledge, the only example reported to date for a diorganotin complex bis-*N*,*N*-chelated by two 1,10-phenanthroline ligands.

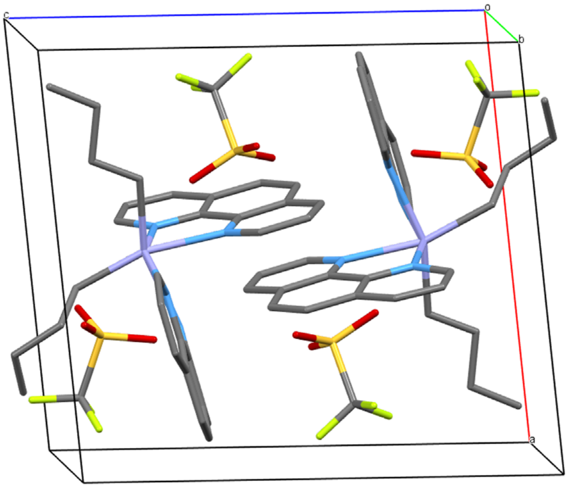

Figure 4. Projection of the crystal structure approximately along the *b* axis, showing the orientation of the phen ligands between two neighboring cations of **6**. The solvent toluene molecules co-crystallizing with **6** and hydrogen protons are omitted (Mercury representation [27], color code: Sn = violet, N = blue, C = gray, O = red, S = yellow, F = green).

From a supramolecular point of view, the molecules of **6** are organized in pairs *via* offset π–π interactions involving the aromatic rings of each phen ligand (Figure 4). The interplanar and centroid-to-centroid distances between the two parallel phen molecules are 3.393 and 4.732 Å, respectively. In general, for such interactions, the interplanar distance is assumed to be in the range of 3.3–3.8 Å [28]. In the arrangement of **6**, the rings are severely offset with a slippage angle (angle between the normal to the planes and the centroid vector centroid vector) of 44.19°, which corresponds to a slip distance of 3.298 Å.

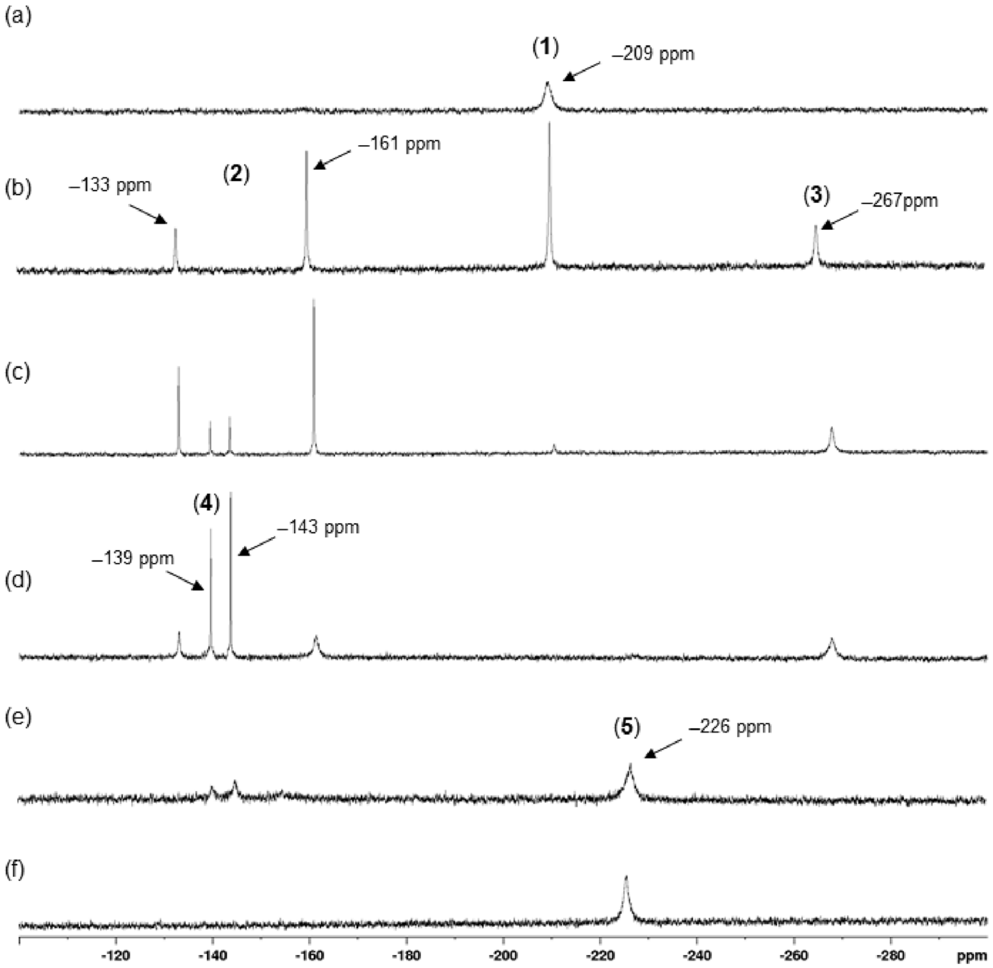

Figure 5. ^{119}Sn{^{1}H} NMR monitoring of the evolution of a solution of **1** in CD_3CN ([0.08 M], 298 K) as a function of successive additions of 1,10-phenanthroline (phen): (a) starting solution of **1**, (b) after addition of 0.5 molar equivalent, (c) of 0.75 molar equivalent, (d) of 1 molar equivalent, (e) of 2 molar equivalent, and (f) of 3 molar equivalent.

2.4. *Solution ^{119}Sn{^{1}H} NMR monitoring*

The reactivity of **1** toward successive additions of 1,10-phenanthroline was followed by ^{119}Sn{^{1}H} spectroscopy in CD_3CN directly in an NMR tube, as shown in Figure 5. In CD_3CN, compound **1** shows a broad signal at δ −209 ppm in agreement with the value reported previously in the literature [8] (Figure 5a). The addition of 0.5 molar equivalents of phen leads to the appearance of three new signals at δ −133, −161, and −267 ppm in addition to the signal of **1**, which is still present at δ −209 ppm (Figure 5b). The two de-shielded chemical shifts exhibiting a 1:2 intensity ratio correspond to the signature of the ionic complex **2**, already known and characterized by us as the unusual trinuclear complex $\{[n\text{-}Bu_2Sn(H_2O)]_2O\cdot n\text{-}Bu_2Sn(OH)_2\}$ $[CF_3SO_3]_2$ (**2**) (Scheme 3a) [16], while the signal at δ −267 ppm can be attributed to a new species **3** whose composition and structure will be discussed later. Further addition of phen (up to 1 molar equivalent) lead to a progressive disappearance of the previously described resonances in favor of the emergence, and then the predominance, of a new pair of signals located at

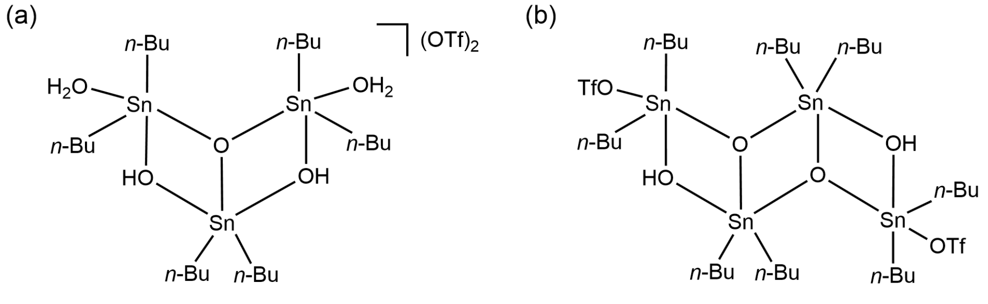

(**2**) (**4**)

Scheme 3. Molecular representations of **2** (a) and **4** (b).

Table 1. $^{119}\{^1H\}$ NMR chemical shift data of di-n-butyltin(IV) trifluoromethanesulfonates

Compounds	δ (ppm)^a		
	In CD_2Cl_2	In acetone-d_6	in CD_3CN
1	−145		−209
2	−127, −149 [18]		−133, −161
3	−288		−267
4	−135, −144 [18]	−146, −151 [12]	−139, −143
5	Not visible	−150	−226
6	Not visible	−231	Insoluble
7			−260

^{a} At $T = 298$ K.

−139 and −143 ppm (Figure 5b and c). They reflect the formation of 3-hydroxy-1-(triflato)tetra-n-butyldistannoxane, $[n\text{-}Bu_2Sn_2(OH)(CF_3SO_3)]_2O$ (**4**), whose solid-state structure was initially established by Otera *et al.* (Scheme 3b) [9]. For our part, we had previously shown the possible transformation of **2** to **4** in the presence of phenazine [16]. It is likely that a similar reaction can occur in the presence of 1,10-phenanthroline. When the addition of phen reaches two molar equivalents, the residual signals of **4** are still visible, but a broad resonance, prevailing, appears at δ −226 ppm (Figure 5e). This corresponds to the formation of complex **5**. In the presence of three molar equivalents, this compound is the only species detected in solution (Figure 5f). However, a white precipitate is also observed at the bottom of the NMR tube, which corresponds to complex **6** insoluble in CD_3CN. The values of the $^{119}Sn\{^1H\}$ NMR chemical shifts of the different organotin species implicated in this study are summarized in Table 1.

2.5. *Isolation and characterization of species* **3**

During the monitoring of the reaction by $^{119}Sn\{^1H\}$ NMR, all signals were attributed to identified organotin species, except for the single broad resonance at δ −267 ppm in CD_3CN (Figure S12), which was assigned to compound **3**. We did not find any bibliographic data associated with this species; therefore, it appeared to be new and its composition remains to be clarified. We first sought to isolate it by reproducing the experimental conditions of the NMR measurement depicted in Figure 5d in glassware conditions, i.e., by adding 1 molar equivalent of phen to a solution of **1** in a mixture of acetonitrile/toluene (15 mL/10 mL). After three successive separations by crystallization at 4 °C (**2** and **4** were collected as crystalline products) in a CH_3CN/toluene mixture, it was possible to isolate only **3**. After complete evaporation of the solvents, **3** consists of a colorless pasty solid. Infrared analysis, shown in Figure S13, reveals several characteristic bands: (i) ν(C–H) absorption bands between 2800 and 3000 cm^{-1}, (ii) ν(C=C), ν(C=N) and δ(C–H) fingerprints of the phen ligand [22,23], and (iii) stretching vibration bands of trifluoromethasulfonate ligands [$\nu(CF_3)$ and $\nu(SO_3)$] between 1000 and 1300 cm^{-1} [19–21]. A $^{119}Sn\{^1H\}$ NMR spectrum of a solution of **3** in CD_2Cl_2 shows a singlet resonance at δ −288 ppm. The $^{13}C\{^1H\}$ NMR spectrum of **3** in CD_2Cl_2 (Figure S14) highlights two sets of signals attributed to the presence of n-butyl and phenanthroline ligands. A quartet at δ 121.2 ppm ($^1J_{C–F}$ = 320 Hz) reveals the presence of CF_3 moieties, which is corroborated by the ^{19}F NMR spectrum, which exhibits one singlet at δ −78.4 ppm (Figure S15). The ^1H spectrum establishes a phen/n-butyl ligand ratio of 1:2 (Figure S16). The electrospray mass spectrum (positive mode) of **3** in dichloromethane/acetonitrile solution displays three intense mass clusters (Figure S17). The first one centered at m/z = 563.0613 Da (z = 1, 67%) matches with high accuracy to a mononuclear di-n-butyltin fragment bearing a positive charge that can be assigned to $[n\text{-}Bu_2Sn(phen)(CF_3SO_3)]^+$ ($C_{21}H_{26}O_3N_2F_3SSn$, calc. = 563.0628 Da), whereas the cluster centered at m/z = 1275.07507 Da (z = 1, 100%) is consistent with the monocationic dinuclear framework of the empirical formula $C_{43}H_{52}O_9N_4F_9S_3Sn_2$ (calc. = 1275.07912 Da). The intermediate cluster at m/z = 893.0887 Da (67%) is compatible with $[M+H–phen–n\text{-}Bu_2Sn]^+$ ($C_{34}H_{35}O_6N_4F_6S_2Sn$, calc. = 893.0819 Da). Simulations of these ESI-MS mass clusters are depicted in Figures S18–S20. On the basis of these data, we suggest that for species **3**, the structure reproduced on Figure 6 could correspond to two $[n\text{-}Bu_2Sn(phen)(CF_3SO_3)]$ entities bounded by a bridging trifluoromethanesulfonate ligand, $[\{n\text{-}Bu_2Sn(phen)(CF_3SO_3)\}_2(\mu\text{-}CF_3SO_3)][CF_3SO_3]$. The overall positive charge of **3** is compensated by an $CF_3SO_3^-$ anion. To the best of our knowledge, such a structure has not yet been described in the literature. However, there are some reports confirming in the solid-state the existence of $–CF_3SO_3$ groups bridging di-n-butyltin derivatives. In general, this results in the propagation of polymeric networks: $[Sn_2(CF_3O_3S)_2(C_4H_9)_4(OH)_2]_n$ [10], $^2_\infty\{[n\text{-}Bu_2(\mu\text{-}OH)SnOSn(\mu\text{–}\eta^2\text{–}OSO_2CF_3)n\text{-}Bu_2]\}$ [9], $^2_\infty\{[n\text{-}Bu_2(\mu\text{-}OH)SnOSn(\mu\text{–}\eta^2\text{–}O_3SCF_3)n\text{-}Bu_2]_2[n\text{-}Bu_2(\eta^1\text{-}O_3SCF_3)SnOSn(\mu\text{-}OH)n\text{-}Bu_2]_2\}$ [12]. In **3**, the presence of phen ligands occupying two coordination sites on each tin atom probably prevents polymerization. In the context of the related chemistry of organotin(IV) alkanesulphonates, Shankar *et al.* recently reported the solid-state structures of di-n-butyltin complexes with bridging and terminal $–OSO_2R$ ligands (R = Me, Et), quite comparable to the structure suspected for **3** [29].

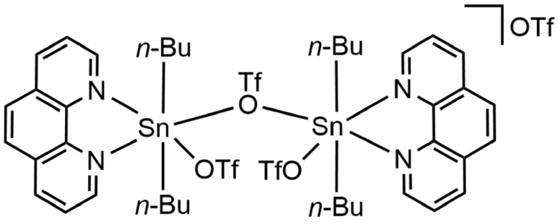

Figure 6. Possible molecular representation of **3** (OTf = CF_3SO_3).

The elemental analysis calculated for $[\{n\text{-}Bu_2Sn(phen)(CF_3SO_3)\}_2(\mu\text{-}CF_3SO_3)][CF_3SO_3]$ ($C_{44}H_{52}F_{12}N_4O_{12}S_4Sn_2$, 1422.57 g·$mol^{-1}$) is also in accordance with the formula suggested for **3**: Calculated: C, 37.17; H, 3.68; N, 3.94; S, 9.02 Found: C, 36.43; H, 3.74; N, 4.13; S, 8.16%. Furthermore, as highlighted by the NMR measurements reported in Figures 5d and 5e, we verified that the addition of phen to a solution of **3** in CDCN does indeed result in the appearance of the characteristic signal of **5** at δ −227 ppm. However, to date, it was not possible to confirm the proposed structure by single crystal X-ray diffraction analysis because the compound does not crystallize properly in acetonitrile.

2.6. *Reactivity in dichloromethane*

In contrast, when the reaction between **1** and phen (in 1:1 molar ratio) is conducted in dichloromethane instead of acetonitrile, colourless single crystals are grown at −20 °C from the filtrate of the reaction. They are unstable and melt very quickly as the temperature increases. This is recurrent and was observed in several batches. The crystallographic analysis could be performed despite the poor quality of crystals. However, several difficulties were encountered during the treatment of the crystallographic data: (i) the determination of the space group was delicate and

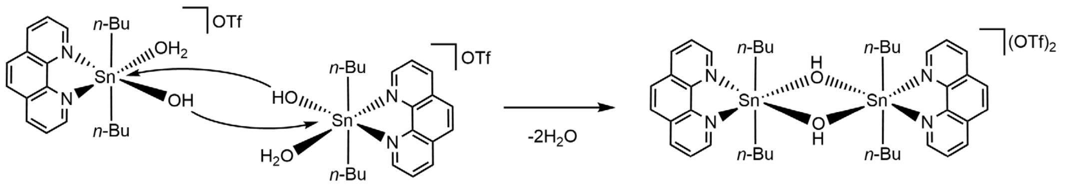

(**7**) (**7**) (**5**)

Scheme 4. Plausible mechanism leading to the formation of **5** from **7**.

finally defined as C2/c, (ii) several ligands were affected by disorders, (iii) a solvent-accessible voids remained. The resolution of the structure remains imperfect, but we believe that the structural data provided are informative in relation to the intermediate species leading to **5** and **6**. Thus, the structure of compound **7** (Figure 7) established the presence of a cationic mononuclear compound based on a tin atom carrying two *n*-butyl chains [Sn–C13 = 2.136(7), Sn–C17 = 2.123(7) Å] in *trans*-position with respect to each other and chelated by a bidentate phenanthroline ligand [Sn–N1 = 2.208(11), Sn–N2 = 2.342(8) Å]. The Sn–N bond lengths are comparable with those measured for **6**. Two oxygen atoms, O1 and O2, complete the coordination sphere of the tin atom, which describes a distorted octahedral geometry [N1–Sn–O1 = 157.1(3), N2–Sn–O2 = 162.2(3), C17–Sn–C13 = 156.89(9)]. The O1 and O2 atoms are assigned to OH_2 and OH ligands, respectively, but unfortunately, their hydrogen atoms could not be located. Their assignments were nevertheless possible based on the Sn–O interatomic distances, which are significantly different: Sn1–O1 = 2.512(8), as opposed to Sn–O2 = 2.142(5) Å. Distances greater than 2.3 Å have already been observed for several di-*n*-butyltin derivatives with Sn–OH_2 bonds: 2.365 Å in [n-$Bu_2Sn(H_2O)(\mu\text{-}OH)]_2[CF_3SO_3]$ [5], 2.409 Å in [n-$Bu_2Sn(\mu\text{-}OH)(H_2O)(CF_3SO_3)]_2$ [4], 2.511 Å in $\{[n\text{-}Bu_2Sn(H_2O)]_2O\cdot n\text{-}Bu_2Sn(OH)_2\}[CF_3SO_3]_2$ [16]. Sn–OH bonds are generally shorter: between 2.062 and 2.150 Å in [n-$Bu_2Sn(H_2O)(\mu\text{-}OH)]_2[CF_3SO_3]$ [5], 2.120 Å in $\{[n\text{-}Bu_2Sn(H_2O)]_2O\cdot n\text{–}Bu_2Sn(OH)_2\}[CF_3SO_3]_2$ [16]. These examples support the attribution of O1 and O2. The positive charge of $[n\text{-}Bu_2Sn(phen)(OH)(H_2O)]^+$ is compensated by one non-coordinated $CF_3SO_3^-$ anion. To the best of our knowledge, such a structure describing a monomeric complex is unprecedented. Diorganotin hydroxides are difficult to purify and characterize [30]. In the solid state, they are mainly described as dimers, hydroxyl groups acting as bridging ligands between two tin atoms, and also as polymers. Thus, the number of complexes with an OH group singly coordinated to tin is very limited [31–33]. In the case of **7**, although the resolution of its structure is not optimal, we assume that the coordination of the phen ligand favours the existence of a monomeric form. To the best of our knowledge, another example of tin-hydroxide stabilized by a phen ligand was previously reported by Aghabozorg *et al.*, characterized by X-ray crystallographic structure as being $[Sn(pydc)(phen)(OH)_2]\cdot 3H_2O$ (pydc = pyridine-2,6-dicarboxyate) [34]. The two terminal OH groups occupy the apical positions of a pentagonal bipyramid. The IR spectrum recorded from the crystals of **7** corroborates the presence of H_2O and OH ligands by showing two shoulders centered at 3407 and 3213 cm^{-1} and a sharp band at 1628 cm^{-1} assigned to $\delta(H_2O)$ elongation. The characteristic absorption bands of CF_3SO_3 and phen are also well visible (Figure 1d). Globally, the IR fingerprint of **7** shows strong similarities to that of **5**.

Compound **7** can be viewed as a reaction intermediate resulting from the reactivity of **1** toward 1,10-phenanthroline under sub-stoichiometric phen conditions (Equation (1)). This can then lead to the formation of **5** by dimerization, driven by the nucleophilicity of the OH group, resulting in the expulsion of aqua ligands (Scheme 4). This mechanism is similar to that proposed earlier by Chandrasekhar *et al.* for the dimerization of $\{[n\text{-}Bu_2Sn(OH_2)_4]^{2+}[2,5\text{-}Me_2C_6H_3SO_3^-]_2$ into $\{[n\text{-}Bu_2Sn(\mu\text{-}OH)(O_3SC_6H_3\text{-}2,5\text{-}Me_2)]_2\}_n$ [35].

$$\begin{aligned} &\underset{(\mathbf{1})}{1/2[n-\mathrm{Bu_2Sn}(\mu-\mathrm{OH})(\mathrm{H_2O})(\mathrm{CF_3SO_3})]_2} + \mathrm{phen} \\ &\longrightarrow \underset{(\mathbf{7})}{[n-\mathrm{Bu_2Sn(phen)(OH)(H_2O)}][\mathrm{CF_3SO_3}]} \end{aligned} \tag{1}$$

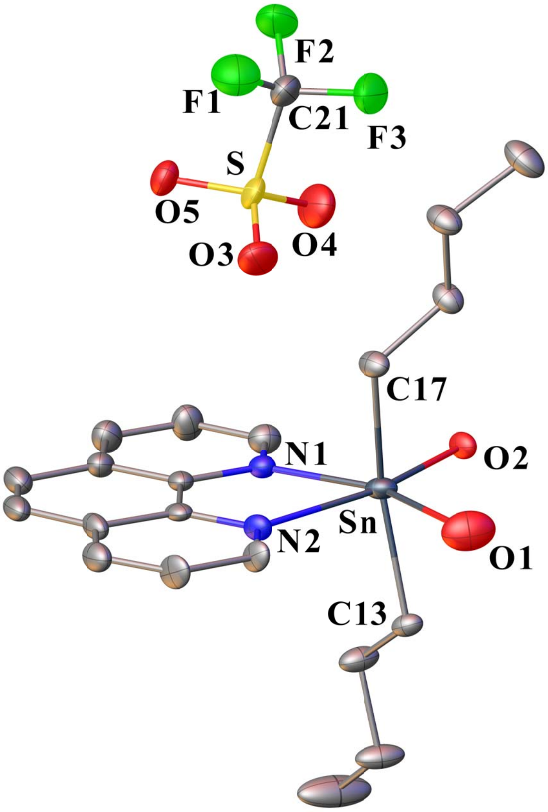

Figure 7. ORTEP drawing of **7** using the atom labeling scheme (30% probability thermal ellipsoids). The hydrogen atoms of O1 and O2 could not be precisely located. Selected bond lengths (Å) and angles (°): Sn–N1 2.208(11), Sn–N2 2.342(8), Sn–O1 2.512(8), Sn–O2 2.142(5), Sn–C13 2.136(17), Sn–C17 2.123(7), S–O3 1.466(7), S–O4 1.403(8), S–O5 1.408(6), C21–F1 1.311(13), C21–F2 1.309(12), C21–F3 1.330(11), C21–S 1.794(11); O1–Sn–O2 113.8(3), O2–Sn–O1 89.1(3), O2–Sn–N2 162.2(3), N1–Sn–O1 157.1(3), N1–Sn–N2 73.1(4), N2–Sn–O1 84.1(3), C13–Sn–C17 161.9(3), C13–Sn–O1 79.9(3), C13–Sn–O2 91.9(2), C13–Sn–N1 100.1(4), C13–Sn–N2 90.7(3), C17–Sn–O1 82.2(3), C17–Sn–O2 97.4(2), C17–Sn–N1 95.6(4), C17–Sn–N2 85.2(3), O3–S–C21 103.7(5), O4–S–C21 104.5(5), O4–S–O3 113.9(5), O4–S–O5 117.0(5), O5–S–C21 104.2(4), O5–S–O3 111.7(4). F1–C21–F3 109.1(11), F1–C21–S 110.5(7), F2–C21–F1 106.5(9), F2–C21–F3 106.6(9), F2–C21–S 113.1(9), F3–C21–S 110.8(7).

From a structural point of view, **7** can be related to the salt {[n-Bu$_2$Sn(OH$_2$)(phen)(O$_3$SC$_6$H$_3$-2,5-Me$_2$)]+[2,5-Me$_2$C$_6$H$_3$SO$_3$]$^-$} also described by Chandrasekhar *et al.*, and isolated by reacting {[n-Bu$_2$Sn(OH$_2$)$_4$]$^{2+}$[2,5-Me$_2$C$_6$H$_3$SO$_3^-$]$_2$ with 1,10-phen [35]. The two compounds exhibit strong similarities. They consist of mononuclear hydrated diorganotin cations chelated by a phen ligand. In the *Chandrasekhar* cation, the coordination of the tin atom is completed by a sulfonate ligand, whereas for **7**, we claim the presence of a terminal OH group. It is interesting to note that in solution in CD$_3$CN, the ^{119}Sn{^{1}H} NMR spectroscopic analysis of the crystals of **7** shows the presence of a mixture of four species (Figure S21), which highlights the instability of the mononuclear cation **7** also in solution. It is nevertheless possible to identify the characteristic resonances of compounds **2** (−133, −161 ppm), **4** (−139, −143 ppm), and **5** (−226 ppm). The most shielded signal at −260 ppm is thus attributed to **7**. Based on the relative integration, the two main species are **5** and **7**, which is consistent with the dimerization reaction suggested in Scheme 4. However, the presence of species **2** and **4**, which are in the minority according to a ^{119}Sn{^{1}H} NMR spectrum and do not bear phen ligands, from **7**, is still unexplained.

Thus, the solid-state structure of **7** resulting from the reaction in dichloromethane differs markedly from the results obtained in acetonitrile, leading to the hypothesis of compound **3**. This implies a determining role of the solvent used on the nature of the trifluoromethanesulfonate intermediate species formed. This has already been demonstrated experimentally in the past by Otera *et al.*, who showed that when n-Bu$_2$SnO reacts with triflic acid in CH$_2$Cl$_2$ conditions, the compound **1**, characterized as a dimeric cation is preferentially formed [8], whereas in acetonitrile, a polymeric structure prevails, alternating anhydrous and hydrated moieties of [n-Bu$_2$Sn(OH)(OTf)]$_2$ and [n-Bu$_2$Sn(OH)(OTf)(H$_2$O)]$_2$, respectively [5]. In the future, we plan to use this modularity to explore the performance of the compounds described in this study for tin-assisted organic reactions, especially since 1,10-phenanthroline derivatives are known to be efficient and stable ligands in homogeneous catalysis [36].

2.7. *Isolation and solid-state structure of $[C_{12}H_9N_2][CF_3SO_3]$ (**phenHOTf**)*

In addition to **7**, single crystals of 1,10-phenanthrolinium trifluoromethanesulfonate, $[C_{12}H_9N_2][CF_3SO_3]$ (**phenHOTf**), were obtained after a few days from the filtrate of the mother-liquor. The **phenHOTf** salt consists of a monoprotonated 1,10-phenanthrolinium cation interacting with a surrounding trifluoromethanesulfonate anion through N–H···O hydrogen bonding [N1···O3 = 2.804(2) Å, N1–H···O3 = 147.61(11)°]. An ORTEP representation is shown in Figure 8. To date, a large number of structures of 1,10-phenanthrolinium salts $[C_{12}H_9N_2][X]$ have been resolved by X-ray crystallography, such as X = Cl^- [37], BPh_4^- [38], I_3^- [39], PF_6^- [40]. The structure of **phenHOTf** is a new example. The crystal stacking of **phenHOTf** (Figure 9) shows that the phenanthrolinium cations are grouped in pairs *via* offset π–π interactions characterized by an interplanar distance of 3.398 Å, a centroid–centroid distance of 4.878 Å, and a slippage distance of 3.50 Å (slippage angle = 45.85°).

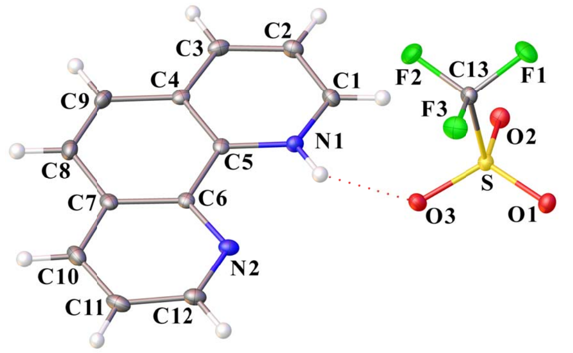

Figure 8. ORTEP drawing of **phenHOTf** using the atom labeling scheme (30% probability thermal ellipsoids). The N–H···O interaction is indicated by a red dotted line. Selected bond lengths (Å) and angles (°): C1–N1 1.333(2), C5–N1 1.358(2), C5–C6 1.438(3), C6–N2 1.359(2), C12–N2 1.326(3), O1–S 1.4367(14), O2–S 1.4417(14), O3–S 1.4505(14), C13–S 1.825(2), C13–F1 1.336(2), C13–F2 1.335(2), C13–F3 1.335(2); C1–N1–C5 123.04(17), C12–N2–C6 116.54(18), O1–S–C13 103.50(9), O1–S–O2 115.68(8), O1–S–O3 114.80(8), O2–S–C13 103.31(9), O2–S–O3 114.88(8), O3–S–C13 102.07(9), F1–C13–F3 107.57(16), F1–C13–S 111.34(13), F2–C13–F1 107.49(16), F2–C13–F3 107.62(15), F2–C13–S 111.31(14), F3 C13 S 111.31(14).

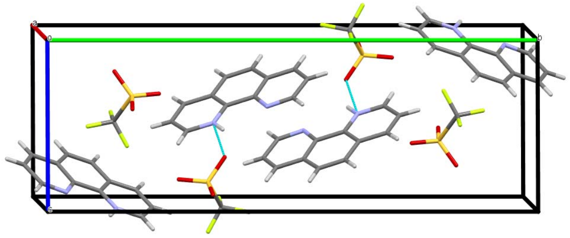

Figure 9. Crystal packing of **phenHOTf** along the *a*-axis. (MERCURY representation [27], color code: N = blue, C = gray, H = white, O = red, S = yellow, F = green.)

2.8. *Reactivity of 1 to 2,9-dimethyl-1,10-phenanthroline*

Subsequently, the reactivity of **1** was extended to the disubstituted 1,10-phenanthrolines. Under the reaction conditions (room temperature, dichloromethane/toluene mixture), we found that 4,7-diphenyl-1,10-phenanthroline (bathophenanthroline) did not react, fully recovering the starting compounds. However, in the presence of 2,9-dimethyl-1,10-phenanthroline (**dmphen**), two types of colorless crystals were successively obtained from the mother liquor. Monitoring of the reaction by $^{119}Sn\{^1H\}$ NMR in CD_2Cl_2 revealed the transformation of **1** into distannoxanes **2** and **4**. However, we did not detect the formation of organotin species coordinated by dmphen ligands, as in the case of compounds **5**, **6** and **7**. This is probably due to steric hindrance caused by the presence of methyl substituents. The first type of crystals collected as long needles was characterized by X-ray diffraction analysis as being the organic salt $[C_{14}H_{13}N_2][CF_3SO_3]$ (**dmphenHOTf**). An ORTEP representation is shown in Figure 10. The monoprotonation of dmphen led to the formation of the cation $[C_{14}H_{13}N_2]^+$. The positive charge is balanced by a triflate anion, which is also involved in hydrogen bonding to the cation *via* an N–H···O interaction [N1···O1 = 2.910 Å, N1–H1···O1 = 157.63(14)°]. The crystal packing view of **dmphenHOTf** shows a folded sheet organization

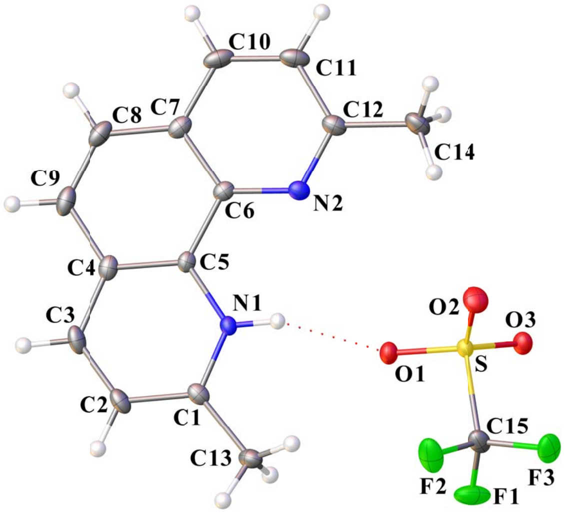

Figure 10. Ortep drawing of **dmphenHOTf** using the atom labeling scheme (30% probability thermal ellipsoids). The N–H···O interaction is indicated by a red dotted line. Selected bond lengths (Å) and angles (°): N1–C5 1.371(3), N1–C1 1.336(3), N2–C6 1.355(3), N2–C12 1.327(3), S–O1 1.4472(17), S–O2 1.4306(19), S–O3 1.4359(17), S–C15 1.832(3), F1–C15 1.329(3), F2–C15 1.334(3), F3–C15 1.336(3); O1–S–C15 102.31(11), O3–S–O1 115.26(11), O3–S–C15 103.14(12), O2–S–O1 115.68(12), O2–S–O3 114.96(11), O2–S–C15 102.71(14), F2–C15–S 111.2(2), F2–C15–F3 107.5(2), F3–C15–S 111.46(18), F1–C15–S 111.25(18), F1–C15–F2 108.1(2), F1–C15–F3 107.2(2).

(Figure 11), stacked along the *a*-axis via π–π interactions between the aryl rings of $[C_{14}H_{13}N_2]^+$ with an interplanar distance of 3.449 Å, a centroid–centroid distance of 3.626 Å, and a slippage distance of 1.119 Å (slip angle of 17.98°). Recently, *Assefa* and *Gore* unintentionally obtained the same compound by adding 2,9-dimethyl-1,10-phenanthroline drop wise to a $Eu(CF_3O_3S)_3$ solution [41]. In addition, several structures of 2,9-dimethyl-1,10-phenanthrolinium salts $[C_{14}H_{13}N_2][X]$ have already been solved. This is the case for $X = ClO_4^-$ [42], Cl^- [43], NO_3^- [44], PF_6^- [45].

A second type of colorless crystals, exhibiting a different shape (prism), was collected from the filtrate of the solution from which **dmphenHOTf** crystals were initially obtained. Their composition consists of a monoprotonated dmphen molecule (**dmphenH**) co-crystallizing with a free dmphen molecule to form **dmphenHOTf·dmphen**. The two components interact through an N–H···N hydrogen bond [N1···N3 = 2.927(3) Å]. In fact, the hydrogen atom is split between the two nitrogen atoms [N1–H···N3 = 152.78(14)°, N3–H···N1 = 159.92(14)°]. Interestingly, the steric hindrance of the methyl substituents leads to a positioning close to orthogonality between the two heterocycles. Their arrangement can be described as a head–tail assembly. A dihedral angle of 77.74(3)° was determined between the two planes containing dmphenH and dmphe. The overall positive charge is compensated by the presence of a triflate anion. An Ortep view of **dmphenHOTf·dmphen** is shown in Figure 12. The crystal packing view, depicted in Figure 13, also shows that the dmphen rings are in π–π aromatic interaction and are organized in pairs. However, two distinctive stacking patterns can be observed for **dmphen** and **dmphenH**, respectively, characterized by interplanar distances of 3.631 and 3.353 Å, centroid–centroid distances of 3.762 Å and 4.445 Å, and slip distances of 0.984 Å (slip angle of 15.16°) and 2.918 Å (slip angle of 41.03°), respectively.

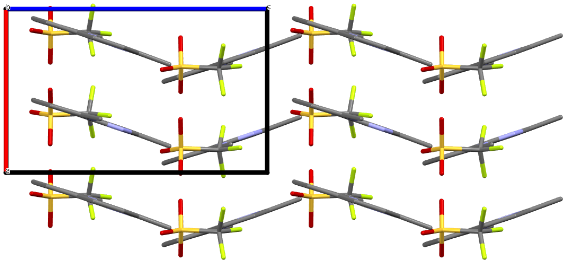

Figure 11. Organization of **dmphenHOTf** in the crystal lattice along the *a*-axis. Hydrogen atoms are omitted for clarity (Mercury representation [27], color code: N = blue, C = gray, O = red, S = yellow, F = green).

In the past, we have shown the possibility of accessing phenazinium and acridinium trifluoromethanesulfonate salts by reacting compound **1**, at room temperature, in the presence of phenazine (phz) [12] and acridine (acr) [46], respectively. The isolation of original architectures based on molecular stacks driven by hydrogen and π–π interactions, has underlined the predisposition of *N*-heterocyclic molecules as suitable building-blocks. In our opinion, this approach, *via* the assistance of an organotin

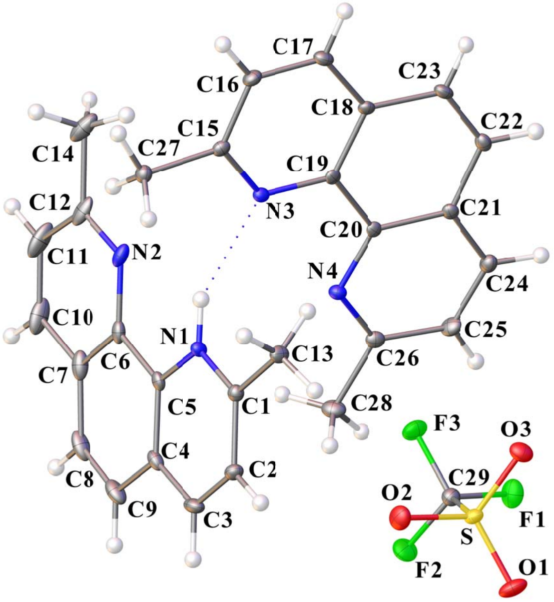

Figure 12. ORTEP drawing of **dmphenHOTf·dmphen** using the atom labeling scheme (30% probability thermal ellipsoids). The N–H···N interaction is indicated by a blue dotted line. Selected bond lengths (Å) and angles (°): C1–N1 1.336(3), C5–N1 1.366(3), C6–N2 1.366(3), C12–N2 1.324(3), C15–N3 1.335(3), C19–N3 1.367(3), C20–N4 1.357(3), C26–N4 1.330(3), C29–F1 1.334(3), C29–F2 1.333(3), C29–F3 1.340(3), C29–S 1.832(3), O1–S 1.4364(18), O2–S 1.4423(19), O3–S 1.4426(18); F2–C29–F3 107.3(2), F2–C29–F1 107.4(2), F2–C29–S 111.80(18), F3–C29–S 110.85(17), F1–C29–F3 107.1(2), F1–C29–S 112.11(17), O2–S–C29 102.19(12), O2–S–O3 114.84(11), O3–S–C29 103.17(11), O1–S–C29 103.78(11), O1–S–O2 115.20(12), O1–S–O3 115.13(12).

compound, could be seen as an innovative method of crystal engineering. It is successfully applied here to 1,10-phenanthroline and 2,9-dimethyl-1,10-phenanthroline, leading to new phenanthrolinium trifluoromethanesulfonate salts.

3. Conclusion and perspectives

In conclusion, the study of the reactivity between 1,10-phenanthroline (phen) and the complex [n-$Bu_2Sn(\mu\text{-}OH)(H_2O)(CF_3SO_3)]_2$ (**1**) led to the complete characterization of two new di-n-butyltin(IV) trifluoromethanesulfonates, **5** and **6**, N,N-bis-chelated with phen ligands. Furthermore, using $^{119}Sn(^1H)$ NMR spectroscopy as an investigation probe under deuterated acetonitrile conditions, we were also able to highlight the formation of additional tin trifluoromethanesulfonate intermediates. Two, **2** and **4**, exhibiting distannoxane-like frameworks but without phen-coordinated ligands, were clearly identified by comparison with previous work while investigations were conducted to clarify the unknown $^{119}Sn(^1H)$ NMR fingerprint attributed to **3**. Crystallization attempts are underway to corroborate the suggested dinuclear structure. We also observed that the identity of the solvent used for the reaction had a notable impact on the intermediates formed. In the presence of dichloromethane, the solid-state structure of a mononuclear hydrated di-n-butyltin hydroxide, stabilized by a phen ligand and assigned to **7**, was revealed. To the best of our knowledge, there are few comparable examples to date. Thus, new structural and spectroscopic insights into organotin(IV) trifluoromethanesulfonates have been obtained, thereby opening the way for further investigations. In the future, we plan to explore the catalytic properties of these compounds.

4. Experimental section

4.1. *Materials and instrumentation*

Organic solvents, dichloromethane (Carlo Erba, 99.5% purity), toluene (Acros, 99.99%), acetonitrile (99.9% purity), were refluxed over appropriate dessicants, distilled, and saturated with argon prior to use. Chemicals were purchased from Aldrich, Acros Organics, and Fluka and used without further purification. The starting compound [n-$Bu_2Sn(OH)(H_2O)(CF_3SO_3)]_2$ (**1**) was synthesized from n-Bu_2SnO (Acros, 98% purity) and trifluoromethanesulfonic acid (Fluka, 98% purity) in acetonitrile, according to a published method [8]. The ^1H, ^{19}F, $^{119}Sn\{^1H\}$, and $^{13}C\{^1H\}$ NMR experiments were recorded on Bruker Avance 300 and 500 MHz spectrometers and calibrated with Me_4Si, trifluoromethylbenzene, or Me_4Sn as an internal standard. Chemical shift δ values are given in ppm. FT-IR spectra were recorded on a Bruker Alfa spectrometer equipped with a Specac Golden Gate™ ATR device.

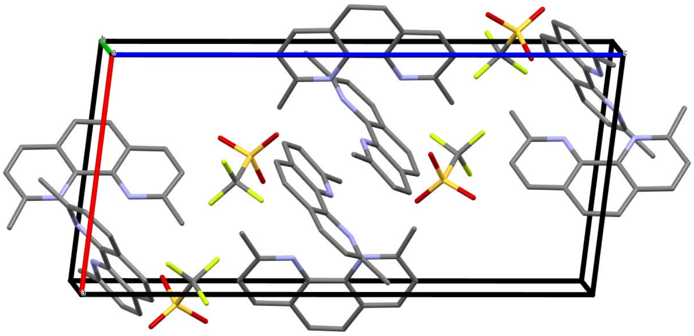

Figure 13. Crystal packing of **dmphenHOTf·dmphen** along the *b*-axis. Hydrogen atoms are omitted for clarity (Mercury representation [27], color code: N = blue, C = gray, O = red, S = yellow, F = green).

ESI-MS spectra were obtained on a Bruker micro Q-TOF instrument using acetonitrile, dichloromethane and methanol mobile phases. Elemental analyses (C, H, N, S) were performed at the Institut de Chimie Moléculaire de l'Université de Bourgogne, Dijon.

4.2. *Preparation of [n-Bu$_2$Sn(OH)(phen)]$_2$[CF$_3$SO$_3$]$_2$ (**5**) and [n-Bu$_2$Sn(Phen)$_2$][CF$_3$SO$_3$] (**6**) from [n-Bu$_2$Sn(OH)(H$_2$O)(CF$_3$SO$_3$)]$_2$ (**1**) and 1,10-phenanthroline*

Two molar equivalents of 1,10-phenanthroline ($C_8H_8N_2$, Sigma-Aldrich, 99% purity) (0.130 g, 0.72 mmol) were added to a colourless solution of [n-Bu$_2$Sn(OH)(H$_2$O)(CF$_3$SO$_3$)]$_2$ (**1**) (0.300 g, 0.360 mmol) in a mixture of dichloromethane/toluene (15 mL/10 mL). The reaction medium is stirred for 3 h at room temperature leading to a clear pinkish solution. A precipitate (0.160 g) was collected after one week of evaporation at room temperature. This corresponds to the formation of compound **6**, which was then recrystallized as fine needles in dichloromethane/toluene. Compound **5** was obtained a few days later from the reaction filtrate as colorless, parallelepipedal crystals (0.050 g). The use of four equivalents of 1,10-phenanthroline gave exclusive access to compound **6**.

5: ^{1}H NMR (300 MHz, CD$_2$Cl$_2$, 301 K): δ0.5–2.1 (m, 36H, Ant), 3.78 (br, 2H), 8.02 (m, 4H), 8.11 (s, 4H), 8.66 (m, 4H), 9.37 (m, 4H); ^{13}C{^{1}H} NMR (75 MHz, CD$_2$Cl$_2$, 300 K): δ13.4, 26.5, 27.6, 120.8 (q, $^1J_{CF}$ = 320 Hz), 125.7, 127.8, 130.1, 139.9, 141.7, 149.9; ^{19}F NMR (282 MHz, CD$_2$C1$_2$, 301 K): δ −78.5 (s, CF$_3$SO$_3^-$); ^{119}Sn{^{1}H} (186 MHz, CD$_3$CN, 298 K): δ −226; ^{119}Sn{^{1}H} (186 MHz, acetone-d_6, 298 K): δ −150; ESI-HRMS (+): m/z 431.1133 Da (100%) [M–OH–phen–n-Bu$_2$Sn]$^+$ ($C_{20}H_{27}N_2OSn$, calc.: 431.1145 Da); FT-IR (ATR, cm^{-1}): 3321, 3081, 3066, 2956, 2929, 2871, 1626, 1575, 1589, 1543, 1518, 1427, 1379, 1282, 1237, 1223, 1155, 1027, 854, 731, 717, 683, 633, 573, 515. Anal. Calc. For $C_{42}H_{54}F_6N_4O_8S_2Sn_2$ (1158.44): C, 43.55; H, 4.70; N, 4.84; S, 5.54. Found: C, 43.42; H, 5.45; N, 4.90; S, 4.32%.

6: ^{1}H NMR (500 MHz, acetone-d_6, 298 K): 0.65 (t, J = 7.3 Hz, 6H), 1.20 (m, 4H), 1.34 (m, 4H), 2.10 (m, 4H), 8.26 (m, 4H), 8.50 (s, 4H), 9.18 (m, 8H); ^{13}C{^{1}H} NMR (125 MHz, acetone-d_6, 298 K): δ13.1, 26.5, 27.8, 27.81, 121.9 (q, $^1J_{CF}$ = 321 Hz), 127.20, 128.7, 131.0, 138.5, 142.9, 149.0; ^{19}F NMR (470 MHz, acetone-d_6, 298 K): δ −78.8 (s, CF$_3$SO$_3^-$); ^{119}Sn{^{1}H} (186 MHz, acetone-d_6, 298 K): δ −231; ESI-HRMS (+): m/z 445.1305 Da (100%) [M–phen+OCH$_3$]$^+$ ($C_{21}H_{29}N_2OSn$, calc.: 445.1301 Da), m/z 431.11559 Da (80%) [M–phen+OH]$^+$ ($C_{20}H_{27}N_2OSn$, calc.: 431.11454 Da); FT-IR (ATR, cm^{-1}): 3104, 3070, 2960, 2925, 2870, 2860, 1630, 1589, 1543, 1523, 1431, 1259, 1223, 1153, 1027, 868, 720, 633, 573, 516. Anal. Calc. For $C_{34}H_{34}F_6N_4O_6S_2Sn$ (891.49): C, 45.81; H, 3.84; N, 6.28; S, 7.19 Found: C, 45.56; H, 3.38; N, 6.30; S, 7.29%.

4.3. *Isolation and characterization of **3***

The protocol used the same conditions as those used in the ^{119}Sn{^{1}H} NMR experiment shown in Figure 5d. One molar equivalent of 1,10-phenanthroline (0.065 g, 0.360 mmol) was added to a colourless solution of [n-Bu$_2$Sn(OH)(H$_2$O)(CF$_3$SO$_3$)]$_2$ (**1**) (0.300 g, 0.360 mmol) in a mixture of acetonitrile/toluene

(15 mL/10 mL). The solution was progressively enriched in compound **3** by eliminating species **2**, **3**, and **4** by successive crystallizations, and the filtrate was stored each time at −20 °C. **3** was finally obtained after three cycles (^{119}Sn{^{1}H} NMR monitoring) and after the total evaporation of the solvents leading to a colorless pasty solid.

3: ^{1}H NMR (499 MHz, CD_3CN, 298 K): 0.61 (t, J = 7.0 Hz, 6H), 1.09 (m, 4H), 1.17 (m, 4H), 2.08 (m, 4H), 8.36 (m, 2H), 8.41 (s, 2H), 9.13 (m, 2H), 9.53 (m, 2H); ^{13}C{^{1}H} NMR (125 MHz, CD_3Cl_2, 298 K): 13.1, 25.9, 27.3, 33.9, 120.55 ($^{1}J_{CF}$ = 319 Hz), 127.2, 128.6, 130.9, 139.4, 143.0, 150.3; ^{19}F NMR (470 MHz, CH_2Cl_2, 298 K): δ −78.4 (s, $CFSO_3$); ^{119}Sn{^{1}H} (149 MHz, CD_3CN, 298 K): δ −266, ^{119}Sn{^{1}H} (186 MHz, CD_2Cl_2, 298 K): δ −288; ESI MS (+): m/z 1275.07507 Da (100%) $[M]^+$ ($C_{43}H_{52}O_9N_4F_9S_3Sn_2$, calc.: 1275.07912 Da), m/z 893.0887 Da (67%) $[M+H\text{–phen–}n\text{-}Bu_2Sn]^+$ ($C_{34}H_{35}O_6N_4F_6S_2Sn$, calc.: 893.09201 Da), m/z 563.06134 Da (z = 1, 67%) $[n\text{-}Bu_2Sn(phen)(CF_3SO_3)]^+$ ($C_{21}H_{26}O_3N_2F_3SSn$, calc.: 563.06328 Da); FT-IR (ATR, cm^{-1}): 3091, 3071, 2960, 2931, 2871, 1631, 1607, 1586, 1525, 1264, 1200, 1162, 1016, 866, 723, 691, 631, 573, 513, 426. Anal. Calc. For $C_{44}H_{52}F_{12}N_4O_{12}S_4Sn_2$ (1422.57): C, 37.15; H, 3.68; N, 3.94; S, 9.02 Found: C, 36.43; H, 3.74; N, 4.13; S, 8.16%.

4.4. *Isolation and characterization of* ***phenHOTf***

Small crystals of **phenHOTf** were obtained from the filtrate of the mother-liquor from which compound **7** had been isolated.

phenHOTf: ^{1}H NMR (500 MHz, CD_2Cl_2, 298 K): δ8.03 (dd, 1H, J = 8.17, 5.02 Hz), 8.08 (s, 1H), 8.16 (brs, 2H), 8.71 (d, 1H, J = 8.12 Hz), 8.79 (d, 1H, J = 7.30 Hz), 9.36 (d, 1H, J = 4.35 Hz), 9.64 (brs, 1H); ^{19}F NMR (470 MHz, CD_2Cl_2, 298 K): δ −78.57 (s, $CFSO_3$); ^{13}C{^{1}H} NMR (125 MHz, CD_2Cl_2, 298 K): 120.4 ($^{1}J_{CF}$ = 320 Hz), 125.6, 126.6, 127.5, 129.8, 130.3, 137.8, 141.4, 147.8, 150.5; FT-IR (ATR, cm^{-1}): 3100, 3070, 3043, 2960, 2930, 2872, 1598, 1542, 1525, 1497, 1471, 1438, 1283, 1223, 1152, 10256, 847, 719, 632, 571, 514, 463.

4.5. *Isolation and characterization of* ***dmphenHOTf*** *and* ***dmphenHOTf·dmphen***

Four molar equivalents of 2,9-dimethyl-1,10-phenanthroline ($C_{10}H_{12}N_2$, Sigma-Aldrich, 99% purity) (0.200 g, 0.96 mmol) were added to a colourless solution of $[n\text{-}Bu_2Sn(OH)(H_2O)(CF_3SO_3)]_2$ (**1**) (0.200 g, 0.24 mmol) in a dichloromethane/toluene mixture (10 mL/5 mL). The reaction medium is stirred for 3 h at room temperature in ambient air. In the following days, ***dmphenHOTf*** crystals first grew and then, after filtration of the mother-liquor, new crystals characterized as ***dmphenHOTf·dmphen*** were collected.

dmphenHOTf: ^{1}H NMR (300 MHz, CD_2Cl_2, 299 K): δ8.65 (d, 2H, J = 8.4 Hz), 8.08 (s, 2H), 7.90 (d, 2H, J = 8.4 Hz), 7.66 (br, 1H), 3.18 (s, 6H, CH_3); ^{19}F NMR (470 MHz, CD_2Cl_2, 298 K): δ −78.93 (s, $CFSO_3$); ^{13}C{^{1}H} NMR (125 MHz, CD_2Cl_2, 298 K): 23.3, 121.2 ($^{1}J_{CF}$ = 320 Hz), 126.8, 126.9, 128.2, 137.4, 141.5, 159.9; FT-IR (ATR, cm^{-1}): 3174, 3111, 3046, 3016, 2980, 1635, 1604, 1533, 1503, 1463, 1278, 1253, 1246, 1222, 1142, 1032, 813, 719, 691, 677, 631, 573, 542, 513; Anal. Calc. For $C_{15}H_{13}F_3N_2O_3S$ (358.34): C, 50.28; H, 3.66; N, 7.829; S, 8.95. Found: C, 49.96; H, 4.05; N, 7.82; S, 6.29%.

dmphenHOTf·dmphen: ^{1}H NMR (500 MHz, CD_2Cl_2, 298 K): δ8.33 (d, 4H, J = 8.30 Hz), 7.84 (s, 4H), 7.57 (d, 4H, J = 8.38 Hz), 7.41 (br, 1H), 2.59 (s, 12H, CH_3); ^{19}F NMR (470 MHz, CD_2Cl_2, 298 K): δ–78.92 (s, $CFSO_3$); ^{13}C{^{1}H} NMR (125 MHz, CD_2Cl_2, 298 K): 23.6, 121.3 ($^{1}J_{CF}$ = 321 Hz), 125.4, 126.4, 127.96, 139.08, 141.7, 159.1; FT-IR (ATR, cm^{-1}): 2958, 2929, 2858, 1636, 1626, 1605, 1595, 1541, 1499, 1466, 1353, 1257, 1221, 1152, 1027, 853, 754, 735, 724, 634, 570, 546, 515, 441; Anal. Calc. For $C_{29}H_{25}F_3N_4O_3S$ (566.59): C, 61.47; H, 4.45; N, 9.89; S, 5.66. Found: C, 60.93; H, 4.80; N, 10.08; S, 5.09%.

4.6. *X-ray diffraction analysis and refinement*

Crystallographic data and structure refinement details for **5**, **6**, **7**, **phenHOTf**, **dmphenHOTf·** and **dmphenHOTf·dmphen** are reported and detailled in *Supporting information – Crystallographic Data.*

Declaration of interests

The authors do not work for, advise, own shares in, or receive funds from any organization that could benefit from this article, and have declared no affiliations other than their research organizations.

Funding

The authors are grateful to the University of Burgundy-Dijon and the CNRS for their constant financial support.

Acknowledgements

The authors would particularly like to thank Dr. Q. Bonin, Ms M.-J. Penouilh (ESI-HRMS) and Ms T. Régnier (elemental analysis), as well as the Professor Klaus Jurkschat and the second anonymous reviewer for their corrections and suggestions, which significantly improved the initial manuscript.

Supplementary data

Supporting information for this article is available on the journal's website under https://doi.org/10.5802/crchim.260 or from the author.

Additional spectroscopic data (^{1}H, ^{19}F, ^{13}C{^{1}H}, ^{119}Sn{^{1}H}, FT-IR, and ESI-MS spectra; Figures S1–S21) related to complexes **5**, **6**, **7** are given in *Supporting Information—Spectroscopic Data*. Crystallographic data regarding the X-ray structures reported in this study (compounds **5**, **6**, **7**, **phenHOTf**, **dmphenHOTf**, and **dmphenHOTf·dmphen**) are available in *Supporting Information—Crystallographic Data*.

CCDC 2254272 (**5**), 2254273 (**6**), 2254274 (**7**), 2254275 (**phenHOTf**), 2254276 (**dmphenHOTf**), and 2254277 (**dmphenHOTf·dmphen**) contain the supplementary crystallographic data for this paper. These data can be obtained free of charge from the Cambridge Crystallographic Data Centre via www.ccdc.cam.ac.uk/data_request/cif.

References

[1] M. Schmeisser, P. Sartori, B. Lippsmeier, *Chem. Ber.*, 1970, **103**, 868-879.

[2] T. Sato, Y. Wakahara, J. Otera, H. Nozaki, *Tetrahedron*, 1991, **47**, 9773-9782.

[3] T. Sato, Y. Wakahara, J. Otera, H. Nozaki, *Tetrahedron Lett.*, 1990, **31**, 1581-1584.

[4] K. Sakamoto, Y. Hamada, H. Akashi, A. Orita, J. Otera, *Organometallics*, 1999, **18**, 3555-3557.

[5] H. Lee, J. Y. Bae, O. S. Kwon, S. J. Kim, S. D. Lee, H. S. Kim, *J. Organomet. Chem.*, 2004, **689**, 1816-1820.

[6] J.-C. Choi, K. Kohno, Y. Ohshima, H. Yasuda, T. Sakakura, *Catal. Commun.*, 2008, **9**, 1630-1633.

[7] P. Švec, R. Olejník, Z. Padělková, A. Růžička, L. Plasseraud, *J. Organomet. Chem.*, 2012, **708–709**, 82-87.

[8] K. Sakamoto, H. Ikeda, H. Akashi, T. Fukuyama, A. Orita, J. Otera, *Organometallics*, 2000, **19**, 3242-3248.

[9] A. Orita, J. Xiang, K. Sakamoto, J. Otera, *J. Organomet. Chem.*, 2001, **624**, 287-293.

[10] D. Ballivet-Tkatchenko, H. Cattey, L. Plasseraud, P. Richard, *Acta Crystallogr.*, 2006, **E62**, m2820-m2822.

[11] P. B. Hitchcock, M. F. Lappert, G. A. Lawless, G. M. de Lima, L. J.-M. Pierssens, *J. Organomet. Chem.*, 2000, **601**, 142-146.

[12] L. Plasseraud, H. Cattey, P. Richard, D. Ballivet-Tkatchenko, *J. Organomet. Chem.*, 2009, **694**, 2386-2394.

[13] J. Beckmann, *Appl. Organomet. Chem.*, 2005, **19**, 494-499.

[14] L. Plasseraud, H. Cattey, P. Richard, *Z. Naturforsch.*, 2010, **65b**, 1293-1300.

[15] L. Plasseraud, H. Cattey, P. Richard, *Z. Naturforsch.*, 2011, **66b**, 262-268.

[16] A. Orita, K. Sakamoto, H. Ikeda, J. Xiang, J. Otera, *Chem. Lett.*, 2001, **30**, 40-41.

[17] A. Orita, J. Xiang, K. Sakamoto, J. Otera, *J. Organomet. Chem.*, 2001, **624**, 287-293.

[18] L. Plasseraud, B. Therrien, A. Růžička, H. Cattey, *Inorg. Chim. Acta*, 2012, **380**, 50-56.

[19] G. A. Lawrance, *Chem. Rev.*, 1986, **86**, 17-33.

[20] D. H. Johnston, D. F. Shriver, *Inorg. Chem.*, 1993, **32**, 1045-1047.

[21] S. J. Angus-Dunne, L. E. P. Lee Chin, R. C. Burns, G. A. Lawrance, *Transit. Met. Chem.*, 2006, **31**, 268-275.

[22] E. König, K. Madeja, *Spectrochim. Acta*, 1964, **43**, 45-54.

[23] F. F. Jian, H. L. Xiao, H. X. Wang, K. Jiao, *J. Korean Chem. Soc.*, 2003, **47**, 26-30.

[24] D. Ballivet-Tkatchenko, H. Chermette, L. Plasseraud, O. Walter, *Dalton Trans.*, 2006, 5167-5175.

[25] I. Lange, O. Moers, A. Blaschette, P. G. Jones, *Z. Anorg. Allg. Chem.*, 1997, **623**, 1665-1671.

[26] A. Wirth, O. Moers, A. Blaschette, P. G. Jones, *Z. Anorg. Allg. Chem.*, 2000, **626**, 529-535.

[27] C. F. Macrae, I. J. Bruno, J. A. Chisholm, P. R. Edgington, P. McCabe, E. Pidcock, L. Rodriguez-Monge, R. Taylor, J. Van de Streek, P. A. Wood, *Appl. Crystallogr.*, 2008, **41**, 466-470.

[28] C. Janiak, *J. Chem. Soc. Dalton Trans.*, 2000, 3885-3896.

[29] R. Shankar, P. Chauhan, E. Jakhar, A. Dubey, G. Kociok-Köhn, *Inorg. Chem.*, 2023, **62**, 2181-2187.

[30] A. G. Davis, *Organotin Chemistry*, Wiley-VCH, Weinheim, 2004, 179 pages.

[31] H. Reuter, H. Puff, *J. Organomet. Chem.*, 1989, **379**, 223-234.

[32] H. K. Sharma, F. Cervantes-Lee, J. S. Mahmoud, K. H. Pannell, *Organometallics*, 1999, **18**, 399-403.

[33] A. Růžička, Z. Padělková, P. Švec, V. Pejchal, L. Česlová, J. Holeček, *J. Organomet. Chem.*, 2013, **732**, 47-57.

[34] H. Aghabozorg, F. Ramezanipour, B. Nakhjavan, J. Soleimannejad, J. Attar Gharamaleki, M. A. Sharif, *Cryst. Res. Technol.*, 2007, **42**, 1137-1144.

[35] V. Chandrasekhar, P. Singh, K. Gopal, *Organometallics*, 2007, **26**, 2833-2839.

[36] K. Hensen, B. Spangenberga, M. Bolteb, *Acta Crystallogr.*, 2000, **C56**, 208-210.

[37] M.-Y. Hu, Q. He, S.-J. Fan, Z.-C. Wang, L.-Y. Liu, Y.-J. Mu, Q. Peng, S.-F. Zhu, *Nature Commun.*, 2018, **9**, article no. 221.

[38] P. K. Bakshi, T. S. Cameron, O. Knop, *Can. J. Chem.*, 1996, **74**, 201-220.

[39] M. Bujak, W. Frank, *Z. Kristallogr. New Cryst. Struct.*, 2014, **229**, 379-380.

[40] B. Milani, A. Anzilutti, L. Vicentini, A. Sessanta, O. Santi, E. Zangrando, S. Geremia, G. Mestroni, *Organometallics*, 1997, **16**, 5064-5075.

[41] Z. Assefa, S. B. Gore, *Bull. Chem. Soc. Ethiop.*, 2016, **30**, 231-239.

[42] A. Morsali, *Anal. Sci.: X-Ray Struct. Anal.*, 2005, **21**, x21-x22 (Online).

[43] D. E. Braun, K. Raabe, A. Schneeberger, V. Kahlenberg, U. J. Griesser, *Molecules*, 2017, **22**, article no. 2238.

[44] Y.-Q. Yu, C.-F. Ding, M.-L. Zhang, X.-M. Li, S.-S. Zhang, *Acta Crystallogr.*, 2006, **E62**, o2187-o2189.

[45] J. H. Buttery, P. C. J. Effendy, S. Mutrofin, B. W. Skelton, C. R. Whitaker, A. H. White, *Z. Anorg. Allg. Chem.*, 2006, **632**, 1326-1339.

[46] L. Plasseraud, H. Cattey, *C. R. Chim.*, 2013, **16**, 613-620.

ACADÉMIE
DES SCIENCES
INSTITUT DE FRANCE

Comptes Rendus. Chimie
2024, Vol. 27, Special issue S1, p. 35-44
`https://doi.org/10.5802/crchim.266`

Research article

French/Nordic Special Issue on Materials and Coordination Chemistry

Parallel-mode EPR spectra of the hexaaqua manganese(II) Ion in tetrahedral symmetry

Margrete Juel Henrichsen [*, a], **Jesper Bendix** [a] and **Høgni Weihe** [a]

[a] Department of Chemistry, University of Copenhagen, Universitetsparken 5,
DK-2100 Copenhagen, Denmark
E-mail: mnr410@alumni.ku.dk (M. Juel Henrichsen)

Abstract. Parallel-mode X-band EPR spectra of the manganese(II) hexaaqua ion as substitutional impurity in $Cs[Mg(H_2O)_6]AsO_4$ are presented and interpreted. In this lattice the aqua ion, considering also the disposition of the hydrogen atoms, occupies a crystallographic site with tetrahedral symmetry. This rare situation enables that the line positions as well as the intensities in the parallel-mode EPR spectra can be modelled with a simple three-parameter cubic-symmetry spin Hamiltonian, including the isotropic Zeeman interaction (g) pertinent to the $S = 5/2$ electronic spin, the isotropic hyperfine interaction (A), between the electronic spin and the $I = 5/2$ nuclear spin, and the cubic splitting (a) of the $S = 5/2$ manifold. A simple formalism, based on perturbation theory to grossly account for the observed intensities, is presented. We observe all parallel-mode-allowed hyperfine transitions associated with all fine-structure transitions.

Keywords. Parallel-mode EPR, Manganese(II), Hyperfine interaction, Cubic symmetry, Flip-flop transitions.

Manuscript received 31 May 2023, revised 28 July 2023, accepted 12 October 2023.

1. Introduction

Parallel-mode EPR (Electron Paramagnetic Resonance) spectra are recorded with the magnetic component of the microwave radiation oscillating parallel to the applied magnetic field, in contrast to the normal perpendicular-mode setting where the magnetic component of the microwave radiation is perpendicular to the applied magnetic field. Different selection rules are associated with these two instrumental settings, and therefore the parallel-mode setting may induce transitions inaccessible by perpendicular mode. The intensity and overall appearance of the parallel-mode spectrum of a given spin system is strongly dependent on the composition of the spin system, and the magnitude of (as well as the ratio between) various parameters in the effective Hamiltonian describing the spin system. These parameters encompass the quantification of Zeeman terms, various anisotropy parameters, exchange coupling constants, and hyperfine coupling constants. Hence, the simple appearance of a parallel-mode spectrum, i.e., the number of lines, may reveal the intensity-giving mechanism.

Parallel-mode EPR spectra have been successfully recorded for a wide variety of both simple and composite spin systems. In the following, not exhaustive list, we group the systems into two classes, namely those exhibiting no resolved hyperfine splittings, and those exhibiting clear hyperfine splittings.

The former class is exemplified by the following works: the parallel-mode setting was used to elucidate the electronic spin-quintet ($S = 2$) ground state

---

[*] Corresponding author

of the iron(II) ion in myoglobin [1]; the ground state $S = 4$ spin multiplet of the all-ferrous state of the [4Fe–4S] cluster in nitrogenase was characterized by parallel-mode EPR [2]; and several parallel-mode resonances were detected in the ground $S = 6$ state of a dodecanuclear chromium(III) spin cluster [3].

For the latter class exhibiting clear hyperfine splittings, parallel-mode EPR was applied: to determine the sign and magnitude of the pseudo-axial anisotropy splitting in manganese(III) ions, $S = 2, I = 5/2$ (with I being the nuclear-spin quantum number), in superoxide dismutase [4]; to study small splittings arising from the Jahn–Teller distortion in the manganese(III) hexaaqua ion [5]; to observe and resolve the Mn–F superhyperfine interaction in two fluorido complexes of manganese(III), namely MnF_6^{3-} and $Mn(salen)F_2^-$ [6]; and to characterize several cobalt(II) complexes with $(S, I) = (3/2, 7/2)$ [7]. Recently, parallel-mode spectra of Bi as an impurity in silicon were presented and the complementary information obtained from parallel-mode was used to aid the interpretation of the perpendicular-mode spectra of two molecular bismuth radicals with $(S, I) = (1/2, 9/2)$ [8]. Also recently, a detailed exposition of the parallel-mode EPR spectrum of hydrogen atoms with $(S, I) = (1/2, 1/2)$ and deuterium atoms with $(S, I) = (1/2, 1)$ trapped in silsesquioxanes was given [9]. We note in passing that understanding this very simple spin system is important for radio astronomy, as the splitting of the 21 cm, 1420.4 MHz, line originating from hydrogen atoms in galaxies might give information about interstellar magnetic fields [10].

For an isolated isotropic spin multiplet with spin quantum number S, the parallel-mode spectrum has no intensity simply because the $2S + 1$ projections $|S, M\rangle$ are exact eigenfunctions to the $\hat{S}_z$ operator (cf. Equation (5) below). Therefore, the parallel-mode intensity observed in the nuclear spin–free spin systems, as, e.g., in refs [1–3], is induced by the anisotropic terms in the Hamiltonian. Parallel-mode intensities in these spin systems are rather high and can be comparable to the usual perpendicular-mode intensities.

However, for an electronic spin interacting with a nuclear spin, the situation is slightly different as here the hyperfine interaction constitutes an additional intensity-giving mechanism. All the parallel-mode lines in the class of systems exhibiting resolved hyperfine splittings, quoted above, are hyperfine transitions between the two components of an effective non-Kramers [4–6] or a genuine [7,8] $S = 1/2$ spin system. The parallel-mode spectra of the manganese(III) systems all exhibit $2I + 1 = 6$ hyperfine lines connected to only a single fine-structure transition, with $I = 5/2$ appropriate for the ^{55}Mn nucleus. In these systems, the intensity is induced by a small splitting of a non-Kramers doublet. However, the parallel-mode spectrum of Bi in silicon [8] exhibits $2I = 9$ lines, with $I = 9/2$ for ^{209}Bi. Likewise, spectrum of hydrogen and deuterium exhibit $2I_H = 1$ and $2I_D = 2$ lines, respectively, where $I_H = 1/2$ and $I_D = 1$, respectively. In the bismuth, hydrogen, and deuterium spectra, the intensity is induced solely by the hyperfine interaction.

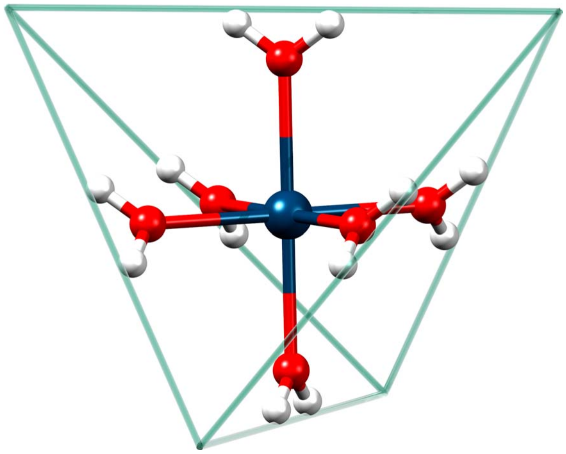

Figure 1. Illustration of the hexaaqua manganese(II) ion in strict tetrahedral symmetry. Blue: Manganese, Red: Oxygen, White: Hydrogen. The circumscribed tetrahedron whose sides straddle the hydrogen atoms has been drawn to emphasize the T_d lattice-point symmetry of the hexaaqua ion.

We are not aware of any reports on parallel-mode spectra of an $S > 1/2$ spin system exhibiting all the possible allowed fine-structure transitions. Therefore, in this contribution we present parallel- as well as perpendicular-mode spectra of Mn^{2+} in strict tetrahedral symmetry (Figure 1) where all metal centers are magnetically and crystallographically equivalent.

This paper is organized as follows. In Section 2 we summarize the experimental details; in Section 3 we present a first-order perturbational treatment of the parallel-mode intensities for a spin system where an electronic spin S is interacting with a nuclear spin I via an isotropic hyperfine interaction. Although the treatment is fairly general, it is aimed at the present spin system, namely Mn^{2+} with $S = 5/2$ and $I = 5/2$; and in Section 4 we present and discuss single-crystal perpendicular-mode and parallel-mode EPR spectra of manganese(II) hexaaqua ions in perfect tetrahedral symmetry.

2. Experimental

2.1. *Synthesis*

The synthesis of single crystals of $Cs[Mg(H_2O)_6]AsO_4$ was performed largely as described in refs. [11,12], but with some modifications in order to produce large single crystals.

Initially, two solutions were prepared. Solution 1: to 90 ml of water were added 3.92 g of 75% arsenic acid (20.7 mmol) and 2.77 g (20.4 mmol) of sodium acetate trihydrate. Solution 2: to 43 ml of water were added 2.0 ml (30 mmol) of glacial acetic acid, 3.34 g (10.0 mmol) cesium carbonate, and 4.20 g (20.0 mmol) of magnesium acetate tetrahydrate. To solution 2 were finally added 5 mg (0.02 mmol) or 50 mg (0.20 mmol) of manganese(II) acetate tetrahydrate to achieve a doping level of 0.1% or 1%, respectively.

Solution 1 (2 ml) and solution 2 (1 ml) were mixed in a small test tube resulting in a clear solution. The small test tube was placed in a larger test tube containing 4 ml pyridine. The large test tube was stoppered and left for five days. Large octahedrally shaped crystals were separated from a viscous gel by filtration and washed with water. Crystals with edge length up to 1.5 mm could be obtained by this slow vapor diffusion of pyridine into the solution. A microcrystalline powder could be produced by slow addition of ammonia (1 M).

2.2. *X-ray crystallography*

The identity of the single crystals as well as the microcrystalline powder was verified with single-crystal X-ray diffraction as well as X-ray powder diffraction (see supporting information). The single-crystal X-ray diffraction studies were performed at 100 K on a Bruker D8 VENTURE diffractometer equipped with a Mo Kα high-brilliance IμS radiation source (λ = 0.71073 Å), a multilayer X-ray mirror and a PHOTON 100 CMOS detector, and an Oxford Cryosystems low-temperature device. The instrument was controlled with the APEX3 software package using SAINT [13]. Final cell constants were obtained from least squares fits of several thousand strong reflections. Intensity data were corrected for absorption using intensities of redundant reflections with the program SADABS [14]. Powder X-ray diffraction studies were performed at room temperature on a Bruker D8 advanced equipped with a Cu Kα source (λ = 1.5406 Å).

2.3. *EPR spectroscopy*

Room-temperature EPR spectra were recorded on a Bruker Elexsys spectrometer equipped with an ER4116DM dual-mode cavity. The crystal was rotated around ⟨110⟩ axis, and hence the magnetic field vector sweeps a plane containing one four-fold (S_4), one two-fold (C_2), and two three-fold (C_3) axes. The power used for perpendicular-mode measurements was 6.325 mW, and for parallel mode 200 mW. Modulation amplitude was in perpendicular-mode 1 G, and for parallel-mode a larger modulation amplitude of 4 G was used due to the low intensity. At room temperature we observed no saturation effects nor multiple quantum transitions [15,16].

3. Theory

Eigenvalues and eigenvectors pertinent to the EPR spectra of the tetrahedral symmetric manganese(II) hexaaqua ion are obtained by numerical diagonalization of the matrix representation of the spin Hamiltonian [17]

$$\hat{H} = g\mu_B \boldsymbol{B}\cdot\hat{\boldsymbol{S}} + A\hat{\boldsymbol{S}}\cdot\hat{\boldsymbol{I}} + \frac{a}{6}\left(\hat{S}_x^4 + \hat{S}_y^4 + \hat{S}_z^4 - \frac{707}{16}\right), \quad (1)$$

which is applicable to our spin system with $S = 5/2$ and $I = 5/2$. In Equation (1) $\boldsymbol{B}$, $\hat{\boldsymbol{S}} = (\hat{S}_x, \hat{S}_y, \hat{S}_z)$, and $\hat{\boldsymbol{I}} = (\hat{I}_x, \hat{I}_y, \hat{I}_z)$ are the magnetic field vector, the electron spin operator, and the nuclear spin operator, respectively. g is the electron spin g factor, A is the hyperfine coupling constant, and a quantifies the cubic splitting of the $S = 5/2$ manifold into a quartet and a doublet. This splitting is $3a$ with the quartet higher in energy for $a > 0$. The linewidths of the spectra presented below did not warrant the inclusion of terms accounting for the nuclear Zeeman effect and nuclear quadrupole splittings.

Fitting of spectral traces of both perpendicular-mode and parallel-mode spectra was performed with a locally developed software as described earlier [18,19].

To grossly account for the main features, i.e., the number of lines and their intensities in the parallel-mode X-band EPR spectra, we wrote down the first-order corrected wave functions for this system. To do so we chose the z-axis in the direction of the magnetic field and approximated the Hamiltonian as

$$\hat{H} \approx \hat{H}^{(0)} + \hat{H}^{(1)}, \tag{2}$$

where $\hat{H}^{(0)} = g\mu_{\mathrm{B}}B\hat{S}_z + A\hat{S}_z\hat{I}_z$ and $\hat{H}^{(1)} = (A/2)(\hat{S}_+\hat{I}_- + \hat{S}_-\hat{I}_+)$. In this discussion of the parallel-mode intensities we are ignoring the last term of Equation (1). In the present case with cubic manganese(II), this is fully justified, as the energetic consequence of the a term is very much smaller compared to the hyperfine interaction and the Zeeman term at field values corresponding to resonances at X-band. However, in Section 4 we use the full Hamiltonian Equation (1) to reproduce the experimental spectra. The direct-product functions $|M,m\rangle$ with M and m being electron spin and nuclear spin components, respectively, are eigenfunctions to $\hat{H}^{(0)}$. With $\hat{H}^{(1)}$ as a perturbation we obtain the following expression for the non-normalized first-order corrected wavefunctions

$$\begin{aligned}|M,m\rangle_{\mathrm{c}} &= |M,m\rangle\\ &-\left(\frac{A}{2}\right)\frac{\langle M+1,m-1|\hat{S}_+\hat{I}_-|M,m\rangle}{E(M+1,m-1)-E(M,m)}|M+1,m-1\rangle\\ &-\left(\frac{A}{2}\right)\frac{\langle M-1,m+1|\hat{S}_-\hat{I}_+|M,m\rangle}{E(M-1,m+1)-E(M,m)}|M-1,m+1\rangle.\end{aligned} \tag{3}$$

At field values corresponding to resonances at X-band, the denominators have absolute values roughly equal to $h\nu$. Therefore, we approximate

$$\begin{aligned}|M,m\rangle_{\mathrm{c}} &= |M,m\rangle\\ &-\left(\frac{A}{2h\nu}\right)\langle M+1,m-1|\hat{S}_+\hat{I}_-|M,m\rangle|M+1,m-1\rangle\\ &+\left(\frac{A}{2h\nu}\right)\langle M-1,m+1|\hat{S}_-\hat{I}_+|M,m\rangle|M-1,m+1\rangle.\end{aligned} \tag{4}$$

The intensity of the transitions in parallel mode is now computed as the squared expectation value of $g\hat{S}_z$, as

$$I(|M,m\rangle_{\mathrm{c}} \to |M',m'\rangle_{\mathrm{c}}) = |(\langle M',m'|_{\mathrm{c}})g\hat{S}_z(|M,m\rangle_{\mathrm{c}})|^2. \tag{5}$$

Inspection of the $(2S+1)(2I+1)$ first-order corrected wavefunctions reveals that only $(2S)(2I)$ transitions have non-vanishing parallel-mode intensity in the $g \approx 2$ field region. These are those for which $M' = M \pm 1$ concerted with $m' \mp 1$. Hence,

$$\begin{aligned}&I(|M,m\rangle_{\mathrm{c}} \to |M+1,m-1\rangle_{\mathrm{c}})\\ &\quad= \left(\frac{gA}{2h\nu}\right)^2[(S-M)(S+M+1)][(I+m)(I-m+1)].\end{aligned} \tag{6}$$

Hence, each $\Delta M = +1$ transition consists of $2I$ hyperfine lines with relative intensity given by the last factor of Equation (6) and a common scaling factor given by the first two factors of Equation (6).

For $S > 1/2$ the factor containing S influences the relative intensities of all the possible resonances. The smallest and largest value of this factor is $2S$ and $S(S+1)+x$, respectively, with $x = 0$ and $x = 1/4$ for S being integer and half-integer, respectively. Similarly, the smallest and largest value of the factor containing I is $2I$ and $I(I+1)+y$, respectively, with $y = 0$ and $y = 1/4$ for I being integer and half-integer, respectively. Hence, the ratio of the largest to smallest intensity is

$$\frac{I(\text{largest})}{I(\text{smallest})} = \frac{[S(S+1)+x][I(I+1)+y]}{(2S)(2I)}. \tag{7}$$

In the present case with Mn^{2+}, $(S,I) = (5/2,5/2)$ we have the intensity ratio $I(\text{largest})/I(\text{smallest}) = 81/25$.

The intensities for the allowed perpendicular-mode transitions are in stark contrast to those for parallel mode. For perpendicular mode, the intensities are obtained by computing the squared expectation values of $g\hat{S}_x$, and the result is

$$I(|M,m\rangle \to |M+1,m\rangle) = \left(\frac{g}{2}\right)^2[(S-M)(S+M+1)]. \tag{8}$$

These theoretical perpendicular-mode intensities do not contain the factor $(A/h\nu)^2$, and unless A is comparable to $h\nu$, intensities of parallel-mode spectra are significantly less than those of perpendicular-mode spectra. In the present case with the parameters determined below (see Section 4), this factor is less than 0.001.

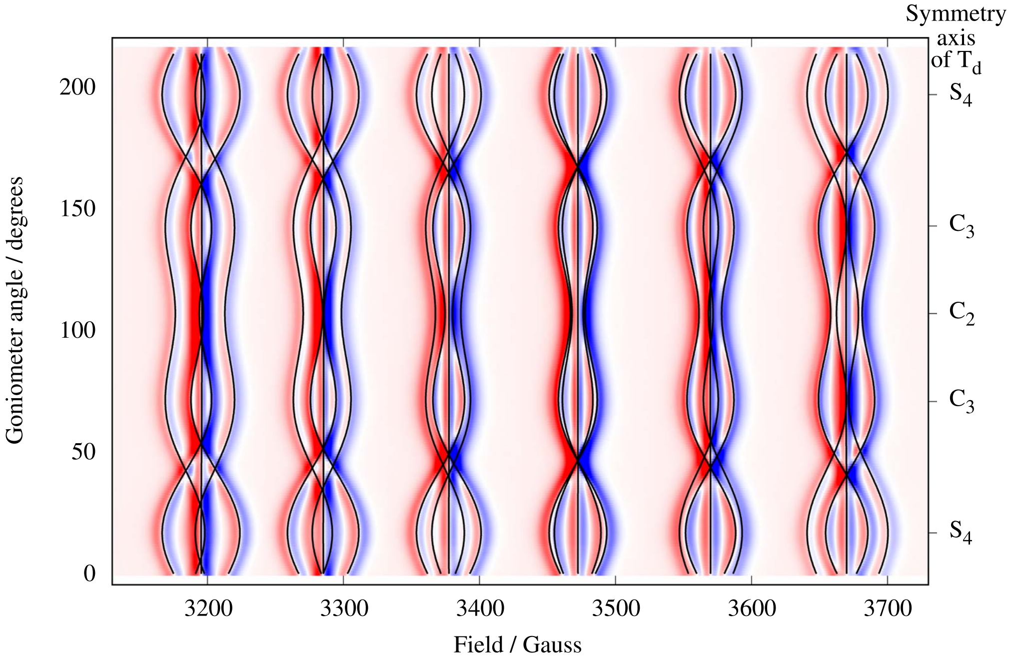

Figure 2. Perpendicular-mode (9.6 GHz) density plot of the angular dependence of the 30 allowed transitions of Mn^{2+} (0.1%) in $Cs[Mg(H_2O)_6]AsO_4$. Red and blue colors represent positive and negative derivative intensities, respectively. The crystal was rotated around a C_2 axis with the magnetic field vector sweeping a plane containing molecular S_4, C_3, and C_2 axes. These special orientations are labelled on the right ordinate axis. The solid black lines are computed resonance magnetic fields based on Equation (1) and the parameters in Table 1.

4. Results and discussion

In order to identify the crystal orientation, perpendicular-mode spectra were recorded prior to the parallel-mode spectra.

4.1. *Perpendicular-mode EPR*

Single-crystal perpendicular-mode spectra of $Cs[Mg_{0.999}Mn_{0.001}(H_2O)_6]AsO_4$ are presented in Figure 2 as a density plot. The spectrum extent on the field axis is roughly 535 G. Forbidden lines of the type $|\Delta M| = 1$, $\Delta m = \pm 1$ observed in other studies [21,23] of cubic Mn(II) systems were not visible here. The peak-to-peak linewidths of 7–10 G are significantly broader compared to linewidths in spectra of other cubic manganese(II) systems [21]. A source of the broad lines is the direct dipole–dipole interaction between the electron spin and the 12 protons of the coordinated water molecules. The magnitude of this dipole–dipole interaction can be estimated by using the classical expression for the interaction energy between two magnetic dipoles separated by the distance R. This interaction energy amounts to 1.5×10^{-4} cm^{-1} for each proton at a distance $R = 2.611$ Å from the metal center. For each proton, this interaction energy translates into approximately 1.5 G, and hence is likely the explanation for the rather broad lines. The angular variation of the resonance magnetic field for each line does not exceed 36 G, i.e., about 6% of the full extent of the spectrum. Spectra for three selected orientations of the magnetic field are shown in Figure 3. To determine the parameters of Equation (1), the three spectral traces were simultaneously fitted to theoretical spectra based on Equation (1) [18,19]. The values obtained for parameters g, a, and A are collected in Table 1. The calculated spectra are virtually identical to the experimental spectra. The energy level diagram in $g \approx 2$ field region pertinent to the magnetic field parallel to an S_4 axis is shown in Figure 4. The 30 allowed transitions are indicated with vertical arrows.

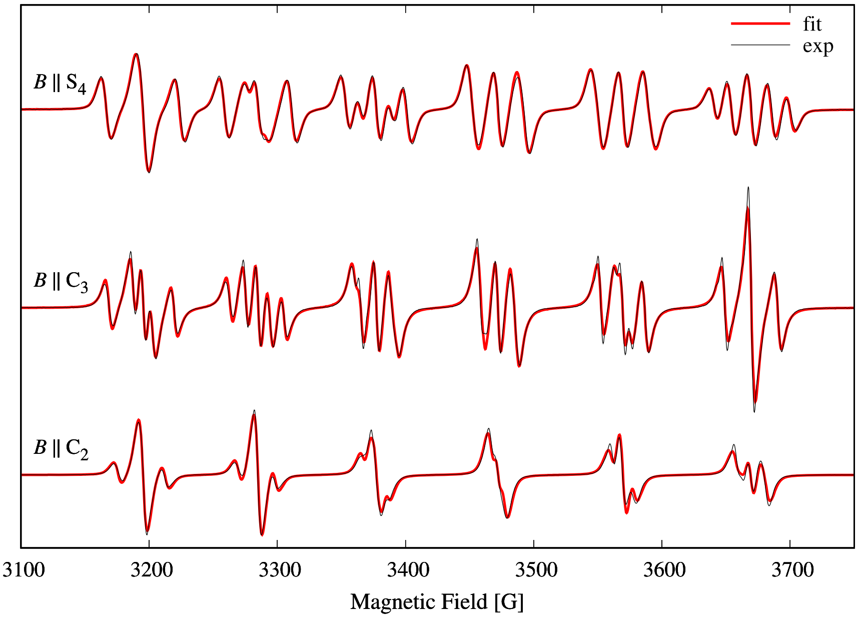

Figure 3. Experimental (solid black traces) perpendicular-mode (9.6 GHz) spectra for three selected magnetic field orientations from Figure 1: ***B*** ∥ S_4, ***B*** ∥ C_3, and ***B*** ∥ C_2. Linewidths of the resonances are in the range 7–10 G. The result of a simultaneous fit of the three perpendicular-mode spectra to Equation (1) is shown with red solid lines.

Table 1. Room temperature spin-Hamiltonian parameters (second, third, and fourth columns) for Mn^{2+} as a six-coordinate substitutional impurity in five different cubic lattices (first column). The fifth column lists the metal-ligand bond length of the host lattice. Data for perpendicular- and parallel-mode are indicated with an "⊥" and "∥" superscript, respectively

Host	g	a (10^{-4} cm^{-1})	A (10^{-4} cm^{-1})	M–L distance (Å)	Reference
$KMgF_3{}^a$	2.000	8.0	−91.2	1.994	[20]
$Cs[Mg(H_2O)_6]AsO_4{}^{\perp}$	1.998	8.2	−88.7	2.064	This work
$Cs[Mg(H_2O)_6]AsO_4{}^{\parallel}$	1.997	8.2	−88.5	2.064	This work
MgO^a	2.000	18.3	−81.4	2.107	[21,22]
CaO^a	2.001	5.6	−80.8	2.405	[21]
SrO^a	2.001	3.0	−78.2	2.562	[21]

By comparing Figure 4 with Figure 2 we see that the 5 transitions at approximately 3200 G correspond to $\Delta M = 1$ and $m = 5/2$, whereas the 5 transitions just below 3700 G correspond to $\Delta M = 1$ and $m = -5/2$.

4.2. *Parallel-mode EPR*

In order to increase the signal-to-noise ratio we recorded the parallel-mode spectra of a crystal containing 1% Mn^{2+}. Single-crystal parallel-mode spectra of $Cs[Mg_{0.99}Mn_{0.01}(H_2O)_6]AsO_4$ are presented in Figure 5 as a density plot. The spectrum extent on the field axis is 790 G, i.e., significantly larger compared to Figure 2. The broader lines, 17–26 G, are a result of the higher doping level [24]. The spectra exhibit 9 features centered at roughly 2960, 3044, 3126, 3215, 3303, 3403, 3503, 3608, and 3722 G, and the features are composed of 1, 2, 3, 4, 5, 4, 3, 2,

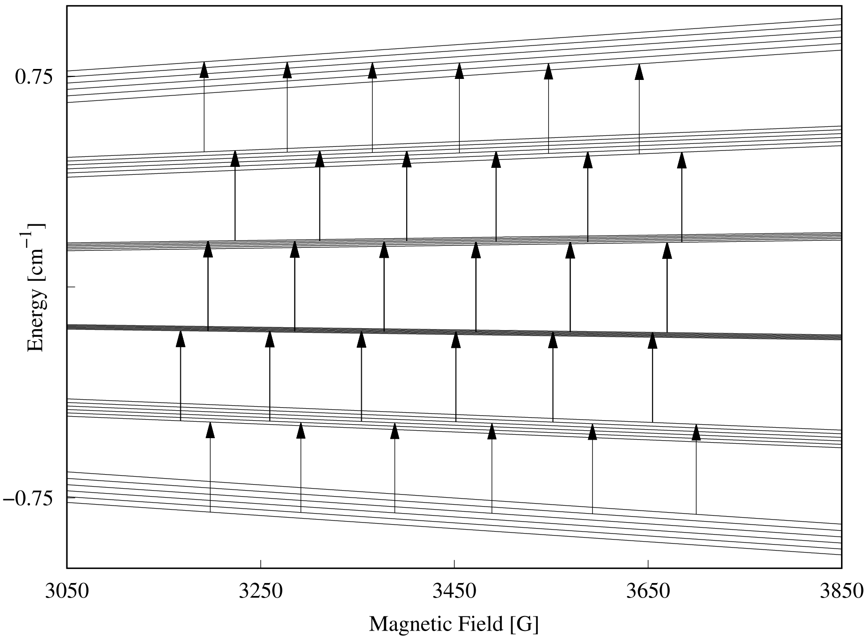

Figure 4. Energy level diagram for $\boldsymbol{B} \parallel S_4$ in the $g \approx 2$ field region obtained by numerical diagonalization of the matrix representation of Equation (1) with the parameters from Table 1. The arrows indicate the allowed perpendicular-mode (9.6 GHz) transitions with $\Delta M = 1$ and $\Delta m = 0$.

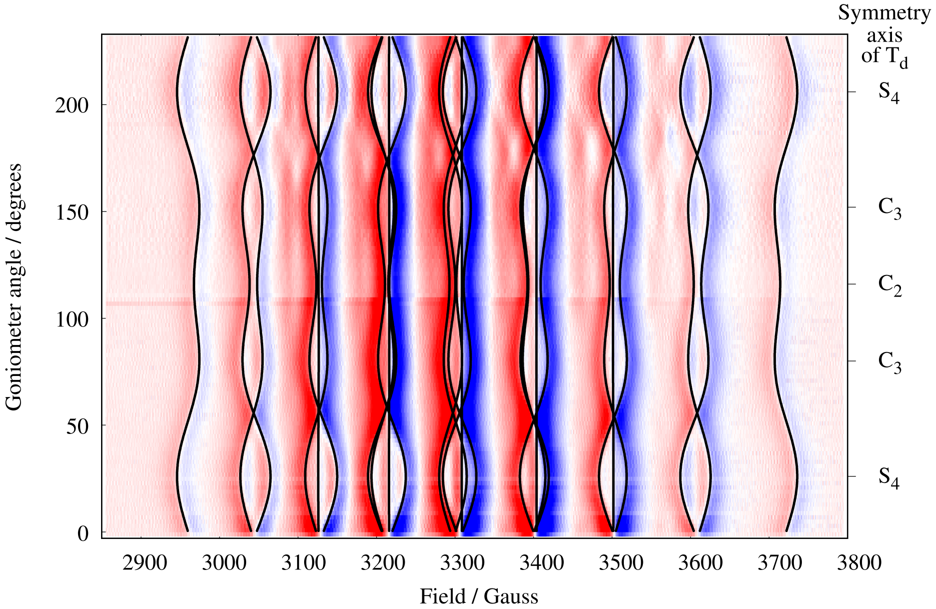

Figure 5. Parallel-mode (9.3 GHz) density plot of the angular dependence of the 25 allowed transitions of Mn^{2+} (1.0%) in $Cs[Mg(H_2O)_6]AsO_4$. For each spectra 10 scans were made, due to the low intensity. Color code and crystal orientations as described in caption to Figure 2. The solid black lines are computed resonance magnetic fields based on Equation (1) and the parameters in Table 1.

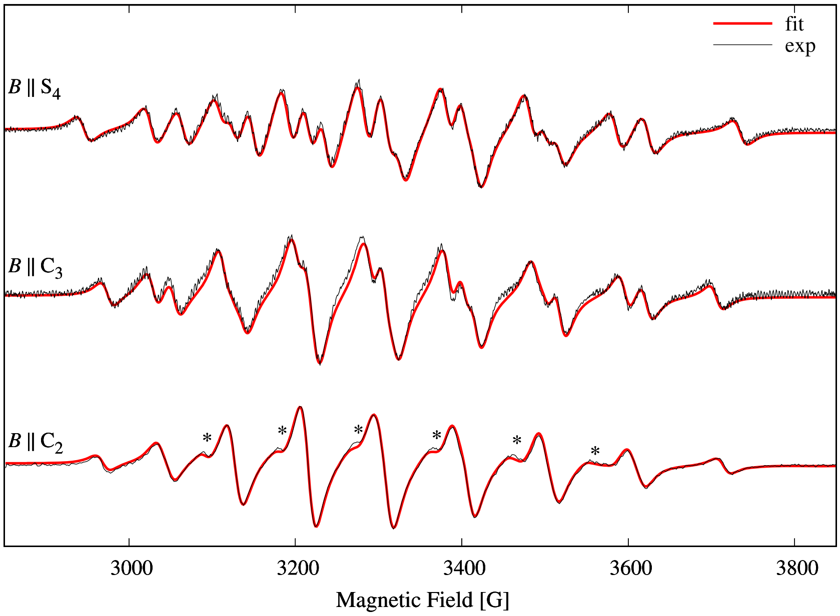

Figure 6. Experimental (solid black traces) parallel-mode (9.3 GHz) spectra for three selected magnetic field orientations from Figure 5: $\boldsymbol{B} \parallel S_4$, $\boldsymbol{B} \parallel C_3$, and $\boldsymbol{B} \parallel C_2$. Linewidths of the resonances are in the range 17–26 G. The result of a simultaneous fit of the three parallel-mode spectra to Equation (1) is shown with red solid lines. The presences of a small amount, 0.7‰, of perpendicular-mode in the microwave field is the source of the shoulders marked with a star (*). Relative intensities of the 9 observed lines for $\boldsymbol{B} \parallel C_2$: 19, 64, 152, 207, 259, 263, 182, 80, 20.

and 1, respectively, separate, partly overlapping or fully overlapping transitions (see also Figure 7). Experimental spectra for three selected orientations of the magnetic field relative to the molecular axes are shown as black traces in Figure 6. Due to the rather large bandwidths combined with the small splittings, only 20 of the 25 possible transitions could be resolved for this high doping level (see the spectrum with $B \parallel S_4$ in Figure 6). The spectrum with $B \parallel C_2$, lowest trace in Figure 6, exhibits only 9 lines as a result of overlapping transitions (see also Figure 7). The relative intensity of each line can be estimated as $h_{pp} \times w_{pp}^2$, where h_{pp} and w_{pp} are the peak-to-peak height and width, respectively. The result is given in the caption of Figure 6. The corresponding theoretical intensities are obtained by vertical additions of the relative intensities in Figure 7. The result is 25, 80, 154, 224, 259, 224, 154, 80, 25. The agreement is fair considering that most of the lines in the lowest trace of Figure 6 are composite and not perfectly overlapping lines.

The three spectral traces were again simultaneously fitted to theoretical spectra based on Equation (1) in order to determine the parameters of Equation (1). The obtained parameters are collected in Table 1. The theoretical spectra are shown with red lines in Figure 6, and the agreement is good. The most noticeable discrepancies are indicated with a “*” in the lowest trace of Figure 6. These weak shoulders result from the presence of 0.7‰ of perpendicular-mode microwave field.

The energy level diagram in the $g \approx 2$ field region calculated with the magnetic field parallel to a C_2 axis is shown in Figure 7. The 25 parallel-mode allowed transitions are indicated with vertical arrows.

5. Discussion

The parameter values determined in the two independent fits of the spectra in Figures 3 and 6 are consistent and are collected in Table 1. In the table we have also collected EPR data of manganese(II)

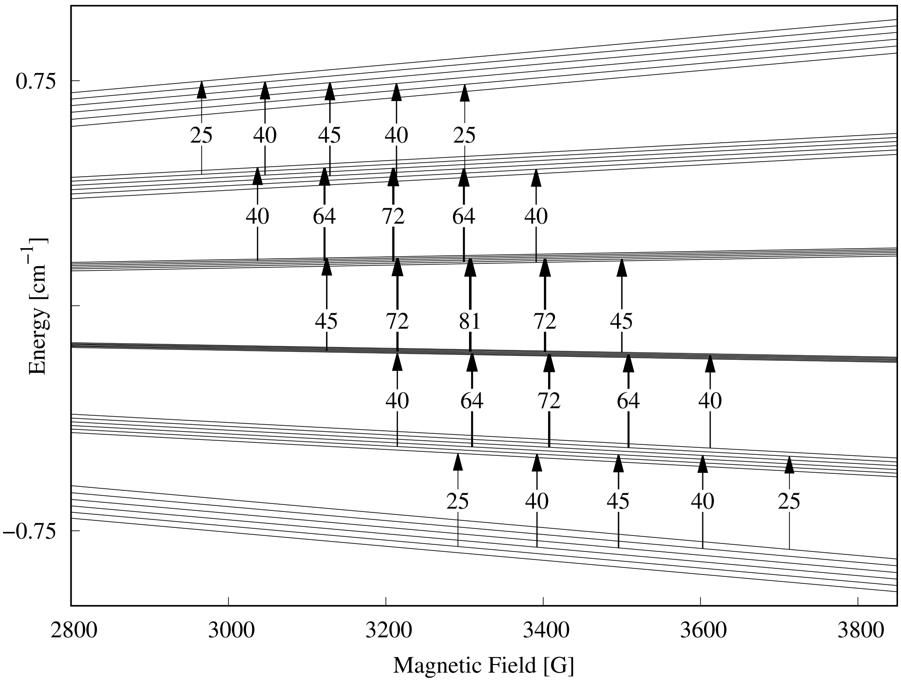

Figure 7. Energy level diagram for $\boldsymbol{B} \parallel C_2$ in the $g \approx 2$ field region obtained as described in the caption to Figure 3. The arrows indicate the allowed parallel-mode (9.3 GHz) transitions with $\Delta M = +1$ and $\Delta m = -1$. The number attached to each arrow represent the relative intensity obtained from the product of the last two factors of Equation (6).

ions as a substitutional impurity in other cubic hosts wherein the metal ion is six-coordinated?

The cubic parameter a of the hexaaqua ion is found to be positive in agreement with all results found for eight-, six-, and tetra-coordinated Mn^{2+} in cubic lattices [25].

The isotropic hyperfine coupling constant A for the hexaaqua ion is slightly smaller but comparable in magnitude with the hyperfine coupling constant found for the hexafluorido ion in $KMgF_3$ (see Table 1). This is in agreement with water and fluoride having similar ligand-to-metal donor properties [26]. The slightly smaller value of A for the aqua ion is also in agreement with the Mn–OH_2 bond being more covalent compared to the Mn–F bond [25]. By the same token, the magnitude of the A parameters for Mn^{2+} in the oxide lattices (see Table 1) are significantly smaller than that for the aqua ion. This indicates that the Mn–O bond is more covalent than the Mn–OH_2 bond despite the fact that the Mn–O bond length is significantly longer than the Mn–OH_2 bond length. Finally we notice that slightly larger and anisotropic hyperfine coupling constants were found for $Mn(H_2O)_6^{2+}$ as an impurity in hexaaqua zinc hexafluorosilicate and in the ammonium zinc Tutton salt [27].

In summary, we have presented and interpreted parallel-mode EPR spectra of the manganese(II) aqua ion as a substitutional impurity in $Cs[Mg(H_2O)_6]AsO_4$, wherein the aqua ion occupies a crystallographic site with perfect tetrahedral symmetry. The interpretation agrees with the crystal symmetry by the fact that only a three-parameter cubic model excellently reproduces the experimental spectra. To the best of our knowledge, this is the first report of parallel-mode EPR spectrum of an $S > 1/2$ spin system wherein all the allowed fine-structure transitions with associated hyperfine transitions are observed. Expressions based on perturbation theory were derived to account for the relative intensities of the allowed transitions. All the allowed parallel-mode resonances are of the flip-flop type, being zero-quantum coherences [28], i.e., energy but no angular momentum is transferred from the microwave field to the spin system.

Declaration of interests

The authors do not work for, advise, own shares in, or receive funds from any organization that could benefit from this article, and have declared no affiliations other than their research organizations.

Supplementary data

Supporting information for this article is available on the journal's website under https://doi.org/10.5802/crchim.266 or from the author.

References

[1] M. P. Hendrich, P. G. Debrunner, *J. Magn. Reson.*, 1988, **78**, 133-141.

[2] S. J. Yoo, H. C. Angove, B. K. Burgess, M. P. Hendrich, E. Münck, *J. Am. Chem. Soc.*, 1999, **121**, 2534-2545.

[3] S. Piligkos, D. Collison, V. S. Oganesyan, G. Rajaraman, G. A. Timco, A. J. Thomson, R. E. P. Winpenny, E. J. L. McInnes, *Phys. Rev. B*, 2004, **69**, 134424-134428.

[4] K. A. Campbell, E. Yikilmas, C. V. Grant, W. Gregor, A. F. Miller, R. D. Britt, *J. Am. Chem Soc.*, 1999, **121**, 4714-4715.

[5] I. Krivokapic, C. Noble, S. Klitgaard, P. Tregenna-Piggott, H. Weihe, A. L. Barra, *Angew. Chem. Int. Ed.*, 2005, **44**, 3613-3616.

[6] Q. Scheifele, T. Birk, J. Bendix, P. L. W. Tregenna-Piggott, H. Weihe, *Angew. Chem. Int. Ed.*, 2008, **47**, 154-156.

[7] A. R. Marts, S. M. Greer, D. R. Whitehead, T. M. Woodruff, R. M. Breece, S. W. Shim, S. N. Oseback, E. T. Papish, F. E. Jacobsen, S. M. Cohen, D. L. Tierney, *Appl. Magn. Reson.*, 2011, **40**, 501-511.

[8] J. Haak, J. Krüger, N. V. Abrosimov, C. Helling, S. Schultz, G. E. Cutsail, *Inorg. Chem.*, 2022, **61**, 11173-11181.

[9] G. Mitrikas, Y. Sanakis, N. Ioannidis, *Appl. Magn. Reson.*, 2020, **51**, 1451-1466.

[10] J. A. Weil, *Concepts Magn. Reson. Part A Bridg. Educ. Res.*, 2006, **28A**, 331-336.

[11] M. Weil, *Acta Crystallogr. E*, 2009, **65**, i2.

[12] A. Ferrari, L. Cavalca, M. Nardelli, *Gazz. Chim. Ital.*, 1955, **85**, 1232-1238.

[13] Bruker; Bruker AXS, Inc, *SAINT, Version 7.68A*, Bruker AXS, Madison, WI, 2009.

[14] G. Sheldrick, *Version 2008/2*, University of Göttingen, Germany, 2003.

[15] S. Bertaina, N. Groll, L. Chen, I. Chiorescu, *Phys. Rev. B*, 2011, **84**, article no. 134433.

[16] P. Sorokin, I. Gelles, W. Smith, *Phys. Rev.*, 1958, **112**, 1513-1515.

[17] J. S. Griffith, *The Theory of Transition Metal Ions*, Cambridge University Press, Cambridge, 1961.

[18] H. H. Husein, H. Weihe, J. Bendix, *J. Magn. Res.*, 2010, **207**, 283-286.

[19] S. Piligkos, I. Laursen, A. Morgenstjerne, H. Weihe, *Mol. Phys.*, 2007, **105**, 2025-2030.

[20] S. Ogawa, *Jpn. J. Appl. Phys.*, 1960, **15**, 1475-1481.

[21] O. Rubio, P. E. Muñoz, O. J. Boldú, Y. Chen, M. M. Abraham, *J. Chem. Phys.*, 1979, **70**, 633-638.

[22] W. Low, *Phys. Rev.*, 1957, **105**, 793-800.

[23] S. Smith, P. Auzins, J. Wertz, *Phys. Rev.*, 1968, **166**, 222-225.

[24] J. Thorp, A. Skinner, *J. Magn. Magn. Mater.*, 1987, **69**, 34-42.

[25] A. Abragam, B. Bleaney, *Electron Paramagnetic Resonance of Transition Ions*, Oxford University Press, England, 1970, 420-440 pages.

[26] J. Glerup, O. Mønsted, C. E. Schäffer, *Inorg. Chem.*, 1976, **15**, 1399-1407.

[27] B. Bleaney, D. J. E. Ingram, *Proc. Roy. Soc. A*, 1951, **205**, 336-356.

[28] J. A. Weil, J. R. Bolton, *Electron Paramagnetic Resonance: Elementary Theory and Practical Applications*, 2nd ed., John Wiley and Sons, Inc., Hoboken, New Jersey, 2007.

ACADÉMIE
DES SCIENCES
INSTITUT DE FRANCE

Comptes Rendus. Chimie
2024, Vol. 27, Special issue S1, p. 45-67
https://doi.org/10.5802/crchim.301

Review article

French/Nordic Special Issue on Materials and Coordination Chemistry

Polymeric nanoreactors for catalytic applications

Chantal Joseph Abou-Fayssal [a, b], **Rinaldo Poli** [*, b, c], **Karine Philippot** [*, b], **Anders Riisager** [*, a] and **Eric Manoury** [*, b]

[a] Centre for Catalysis and Sustainable Chemistry, Department of Chemistry, Technical University of Denmark, Kemitorvet, Building 207, 2800 Kgs. Lyngby, Denmark

[b] CNRS, Laboratoire de Chimie de Coordination (LCC), Université de Toulouse, UPS, INPT, 205 route de Narbonne, BP 44099, F-31077 Toulouse Cedex 4, France

[c] Institut Universitaire de France, 1, rue Descartes, 75231 Paris Cedex 05, France

E-mails: rinaldo.poli@lcc-toulouse.fr (R. Poli), karine.philippot@lcc-toulouse.fr (K. Philippot), ar@kemi.dtu.dk (A. Riisager), eric.manoury@lcc-toulouse.fr (E. Manoury)

Abstract. Mimicking Nature is one drive for chemists to design efficient architectures matching the activity and selectivity of natural catalytic systems, such as enzymes. To this extent, the developed architectures need to have a selective and active site for the transformation of a given substrate to a target product. In addition, the catalyst must be recoverable and recyclable in order to improve the efficiency and be sustainable. Nature achieves these goals by embedding the catalytically active site in an adapted organic matrix that allows controlling the confinement of the catalytic site and its access by the substrate. Organic polymers allow confining diverse catalysts inside organic nanodomains, following the concept of catalytic nanoreactors. Anchoring the catalyst inside the polymer core protects it from the surrounding environment. This strategy also provides an efficient way to separate the catalyst from the products, thus permitting its recovery and recycling. This review provides an overview of unimolecular nanoreactor systems designed from macromolecular building blocks and their application in biphasic catalysis.

Keywords. Catalytic nanoreactors, Biphasic catalysis, Macromolecular building blocks, Polymers.

Funding. European Research Council (grant agreement No. 860322).

Manuscript received 11 September 2023, revised 21 December 2023 and 7 February 2024, accepted 12 February 2024.

1. Introduction

Catalysis is a key technology for our society with extensive contributions in diverse areas such as energy, chemicals and food production, cosmetics, health, etc. [1,2]. Heterogeneous catalysis, where the catalyst and the substrate are in two different phases, provides easy catalyst separation and reuse, which often results in extended catalyst lifetime and use of lower amounts of solvents. These features have made heterogeneous catalysts predominant in industry (about 80% of processes). However, heterogeneous catalytic systems typically require harsher reaction conditions than homogeneous analogs and this may lead to lower selectivities. Heterogeneous catalytic systems may also suffer from mass transport limitations, which may decrease the activity. In addition, the exploration of reaction kinetics and mechanistic understanding are often more problematic for heterogeneous catalysts. Conversely, homogeneous catalysts

---

[*] Corresponding authors

usually provide high activities and selectivities under milder reaction conditions. They also allow easier mechanistic investigations. However, since the catalyst and the substrate coexist in the same physical phase (typically a liquid phase), these systems inherently suffer from difficult catalyst separation and reuse. Hence, down-stream separation procedures such as precipitation, extraction or ultrafiltration are typically required to recover the catalyst. These operations need additional equipment and undesirable large amount of solvent and entail extra costs.

To circumvent these issues, several strategies have been implemented for the recycling of homogeneous catalysts in large-scale processes. These strategies include: (1) employing specially designed membranes capable of selectively percolating catalyst-supporting molecules (such as dendrimers or colloids) through micro-/ultra-/nanofiltration or reverse osmosis processes [3,4], tailored to the size and geometry of the catalyst; (2) utilizing biphasic catalysis, where the catalyst is immobilized in a separate, immiscible liquid phase from that of the reaction products [3] (for instance, the Rhône-Poulenc/Ruhrchemie hydroformylation of propene and butene involving water as the immiscible phase [5]); and (3) employing catalyst confinement techniques [6], where the catalyst support can be a solid phase with the molecular catalyst either grafted onto the surface or enclosed within the pores of insoluble polymers (such as resins), inorganic oxides (like silica and alumina), metal-organic frameworks (MOFs) or carbon materials (including carbon black, carbon nanotubes, and graphene), known as heterogenized homogeneous catalysis, or a separate liquid phase, referred to as liquid/liquid biphasic catalysis. The latter strategy is an effective and low-cost solution to preserve the catalytic performance and facilitate catalyst recovery. Whatever the catalyst support, solid or liquid, catalyst confinement approaches combine the benefits of homogeneous and heterogeneous catalysis. This is also possible via microheterogenization using colloidal assemblies [3], also referred to as nanoreactors.

Polymeric nanoreactors that contain covalently linked ligands in their core architecture offer an interesting approach for anchoring and protecting the catalyst from the surrounding environment, while facilitating its recovery and recycling [4]. One of the prominent techniques for catalyst recovery and recycling is liquid/liquid biphasic catalysis using two immiscible liquid phases, one containing the catalyst and the other one containing the reaction products and any unreacted substrate [5,7,8]. In this approach, the two phases can be separated by a simple decantation, thus facilitating the reuse of the catalyst phase without the introduction of any thermal or chemical stress. Four distinct operational modes may be associated to the liquid/liquid biphasic approach, as listed for the biphasic aqueous catalysis [5]: (i) homogeneous in the aqueous catalyst phase, if the substrate is sufficiently water-soluble; (ii) homogeneous in the substrate/product phase, if the catalyst is sufficiently soluble in the substrate phase or can be transported there by a temperature stimulus (thermomorphic approach) [9–11] or by a phase-transfer agent; (iii) interfacial when neither component is sufficiently soluble in the other component phase and the transformation occurs exclusively at the interface; (iv) homogeneous within the nanoreactors, which form a stable dispersion in a phase different from that of the substrates/products [12,13]. The latter approach, with the catalyst confinement within a small container, can allow precise control over its interaction with the substrate. This can lead to different reaction pathways compared to the free catalyst, resulting in significantly improved selectivities compared to the non-confined analogs [14,15]. The catalyst host can either be molecular or macromolecular. This review deals with macromolecular nanoreactors.

Nanostructured materials can be produced for use as nanoreactors [16–19]. They have a higher surface area relative to their volume compared to complex and bulk materials. This property allows for enhanced interactions with the surrounding environment, leading to increased reactivity and improved performance in various applications. Also, nanostructured materials often exhibit, despite their small size, excellent mechanical properties like high strength and hardness compared to their bulk counterparts [20]. This is mainly due to their unique structural features, including the presence of grain boundaries and interfaces, which can hinder dislocation movement and improve overall material strength. In addition, nanostructured materials can exhibit enhanced electrical conductivity and optical properties [21–23], making them suitable for various electronic and optoelectronic applications as well as favorable

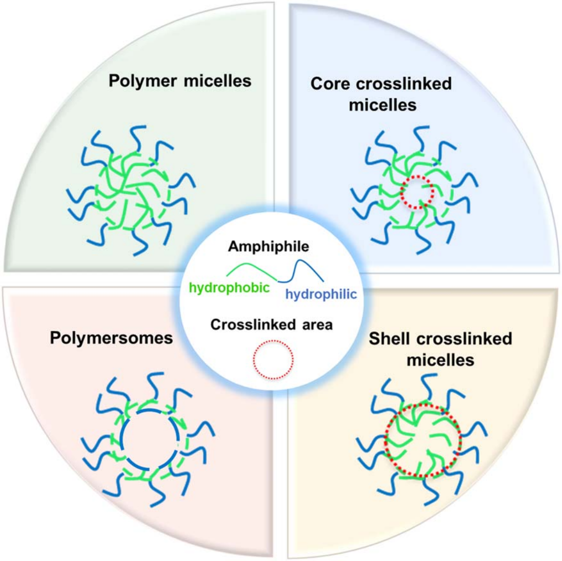

Figure 1. Different polymeric nanoreactors for catalytic applications.

for energy storage and conversion applications. For example, a high surface area improves electrode–electrolyte interactions in batteries and supercapacitors, resulting in enhanced energy storage capabilities [24,25]. Most importantly, metal nanomaterials with high specific surface area are often used as catalysts [4,26,27] due to their ability to provide a large number of active sites for chemical reactions. The increased surface area allows for more efficient adsorption and reaction processes, leading to enhanced catalytic activity and often also selectivity.

A powerful toolbox is available to access a wide array of polymeric nanoreactors [8,9] through controlled and living polymerization techniques [28] such as reversible addition-fragmentation chain transfer (RAFT) polymerization, ring-opening anionic, -cationic and -metathesis polymerization (AROP, CROP and ROMP), and atom transfer radical polymerization (ATRP). These polymerization methods have successfully been used to synthesize various nanoreactor architectures for application in catalysis, including self-assembled micelles, multifunctional micelles [29], polymersomes [30–35] and star polymers [36] (Figure 1). In all cases, a common aim is to embed and protect the catalyst while allowing the substrate to easily reach the reactive sites and the products to migrate back toward the bulk phase. This review provides an overview of the currently known polymer-based nanoreactor systems used in biphasic catalysis, designed from macromolecular building blocks. Special attention is given to core-crosslinked micelles (CCMs) obtained by RAFT polymerization. The progress made on the synthesis of this particular type of unimolecular nanoreactors and on their use in micellar-type aqueous biphasic catalysis will be highlighted.

2. Catalysis within confined spaces

One of the captivating approaches in homogeneous biphasic catalysis is micellar catalysis. Each micelle is an independent reaction locus and can thus be described as a catalytic “nanoreactor” [4,14–16,29, 31,37–41]. Two fundamentally different implementations of micelles in catalysis can be distinguished [42]. In the initially developed one, the catalyst is dissolved in the aqueous phase, or held close to the micellar surface by coulombic forces (if the catalyst has an opposite charge to that of the micelle surface) or by covalent grafting. The catalytic reaction occurs at the interface between the bulk aqueous phase and the nanoreactor core where the hydrophobic substrate is located. The beneficial effect of the micelles is thus merely the increase of the water/organic interface, thus improving mass transport kinetics in an interfacial catalysis approach. This is what the “micellar catalysis” terminology has typically been referring to, but a more appropriate description should be “micelle-aided catalysis”. This topic has been extensively reviewed and will not be considered here [1,43–48]. The second type of micellar catalysis, developed more recently, deals with systems where the catalyst is embedded, by interaction with core-anchored ligands, in the hydrophobic core of the micelles. The catalytic reaction occurs in the homogeneous environment of the hydrophobic micellar core, benefitting from a high local concentration of both substrate and catalyst [14,42]. The kinetics of the overall transformation can thus favorably compare with that of the analogous homogeneous process.

The first reports on micellar catalysis, based on micelles that are self-assembled from a simple surfactant (e.g. potassium dodecanoate, hexadecyltrimethylammonium bromide (CTAB), sodium dodecyl sulfate, etc.), date back to 1970 [49]. Many additional investigations into the preparation,

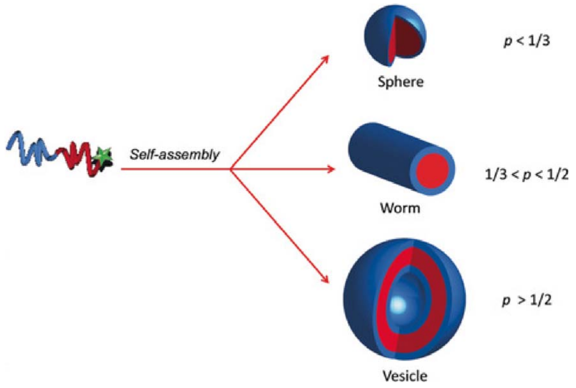

Figure 2. Dependence of the morphology of the self-assembled objects on the packing parameter p. Reprinted with permission of Wiley-VCH Verlag GmbH & Co. KGaA, Weinheim from [59]. Copyright 2019.

characterization and catalytical applications have followed [43,44,49–57].

3. Macromolecular nanoreactors

For micelles generated by amphiphilic macromolecules, typically named "polymer micelles", different morphologies exist depending on the packing parameter p that was defined by Israelachvili [58] through Equation (1), where v is the volume, a_0 is the optimal area of the head group and l_c is the length of the hydrophobic tail.

$$p = v/a_0 \cdot l_c \tag{1}$$

Spherical micelles are obtained when $p \leq 1/3$ whereas worm-like micelles are formed when $1/3 \leq p \leq 1/2$. If $p \geq 1/2$, vesicles result from the self-assembled micelles. Within each morphology group, a smaller size leads to a higher interface area and thus improves the kinetics of mass transport between the hydrophobic bulk phase and the nanoobject core (Figure 2).

Another factor that also plays a major role is the hydrophobicity of the local pocket [59]. Self-assembled nanoreactors are non-covalent macromolecular entities assembled from their initial building blocks [31,33–35,60]. They form good compartmentalization of catalytic systems, providing advantages on the kinetics (faster reaction rate) and on thermodynamics (lowering the energy of the transitional state). In an aqueous medium, the formation of amphiphilic micelles (Figure 3) that tend to assemble above the so-called "critical aggregation concentration" leads to complex supramolecular architectures depending on the structure of the molecular amphiphiles [61].

As a function of the packing parameter p defined above, three different morphologies can be observed, combining the following terms of Gibbs free energy [37]:

(i) a favorable entropic contribution resulting from the assembly of the hydrophobic parts of the molecule,

(ii) a tendency of amphiphiles to minimize unfavorable lipophilic–water interaction by closely packing and to spread apart as the result of electrostatic repulsion between the hydrophilic head groups, defined as surface term,

(iii) a limitation to the possible geometry of aggregation, requiring that the hydrophobic cores only assemble in water or polar solvent, defined as the packing parameter explained above.

These aggregates have dimensions in the nanometer regime. The inclusion of catalytic sites in these aggregates, whether by the polymerization or by the coordination of the pre-catalyst, results in the formation of nanoreactors. In such nanoreactors, the reaction selectivity can be modified by tuning the nature of the monomers in the core block.

3.1. *Polymer micelles*

Polymer micelles [62–65] (PMs) are described as aggregates resulting from the self-association of amphiphilic polymers owing to hydrophobic interactions between polymer molecules. However, interactions may also be electrostatic or via hydrogen bonds or coordination bonds. The morphology of these block copolymer micelles resembles that of molecular surfactant micelles. They can be spherical or cylindrical micelles, as well as vesicles, where the hydrophobic polymer chains form the core and the hydrophilic polymer chains form the shell when dispersed in aqueous media. The morphology of the PMs depends on the ratio between the hydrophobic and hydrophilic chains, capable of accommodating

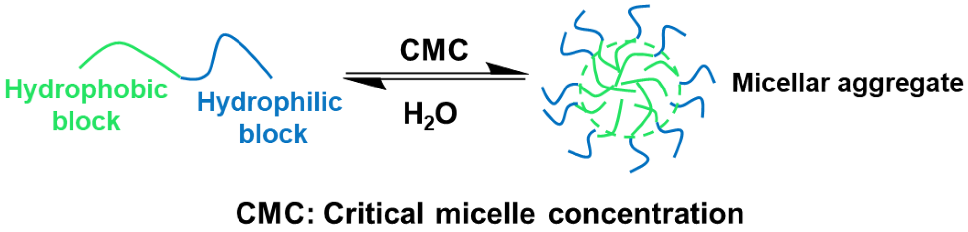

Figure 3. Self-assembly of amphiphilic micelles in water.

the catalyst [62]. PMs are efficient systems for the encapsulation of hydrophobic compounds due to the hydrophobic nature of their core and the hydrophilic corona, and these nanoreactors have many applications besides catalysis, especially in the medical field for, e.g. drug delivery [66,67] and magnetic resonance imaging (MRI) [68].

Chen and coworkers [69] have described the synthesis and application of thermo-responsive polymer micelle-based nanoreactors containing polyoxometalates (POMs) and poly(*N*-isopropylacrylamide)-*b*-poly(L-lysine) (PNIPAM-*b*-PLys-POM) electrostatically linked via the POM and amino groups of poly(L-lysine) for catalytic wet hydrogen peroxide oxidation (CWPO) of phenol. Similarly, Suzuki et al. [70] performed Pd-catalyzed Mizoroki–Heck coupling of iodobenzene and *n*-butyl acrylate in aqueous solution using thermo-responsive PMs based on poly(*N*-isopropyl-acrylamide) (PNIPAAm), which is known as an efficient thermo-responsive polymer due to its lower critical solution temperature (LCST) of 32 °C in water [71] (Figure 4).

The block copolymer **2** with a thermo responsive NIPAAm block and a neutral poly(ethylene glycol) (PEG) chain was prepared from **1** via ATRP (Scheme 1). The resulting block copolymer had a narrow size distribution (15–20 nm at 25 °C) and was water-soluble at room temperature but when heated up to 60 °C the polymer was insoluble, and the solution became opaque. Characterization by dynamic light scattering (DLS) demonstrated that the formation of the PMs by **2** was thermo-induced and the switchable nature improved product extraction. The PMs also limited the use of organic solvent for product separation from the aqueous reaction mixture, but 2 mol% of Pd was required to obtain good product yield in the Pd-catalyzed Mizoroki–Heck cross-coupling [70].

NaCl was also introduced to the block polymer containing proline to lower the solubility of the organic solute in the aqueous phase and help directing it to the core of the PMs [70]. This “salting-out” protocol led to the design of a new thermo-responsive block copolymer with an anionic sodium sulfate segment, PNIPAAm-*b*-PSSNa **9**, also prepared using RAFT polymerization. In the synthesis protocol, *N*-isopropylacrylamide and sodium *p*-styrenesulfonate were polymerized in the presence of the RAFT agent **6** forming **7**, followed by depolymerization of *p*-styrenesulfonate by a radical desulfurization process that led to the removal of trithiocarbonate moiety at the end of the polymer-chain to yield the anionic-type copolymer (Scheme 2). A larger particle size was obtained with the anionic PMs compared to the neutral one, likely due to electrostatic repulsion among the anionic polymer chains. Further analysis also showed that the anionic copolymer exhibited its LCST behavior at 40–55 °C. When the aqueous Pd-catalyzed Mirozoki–Heck coupling of iodobenzene and *n*-butyl acrylate was performed with **9** using 0.5 mol% Pd, a better yield (though moderate) was obtained compared to the previous reaction with the neutral copolymer and 2 mol% Pd (Scheme 2), thus demonstrating how rational PM design can improve catalytic performance. To recover the catalyst, the authors investigated various solvents for product extraction. In general, using diethyl ether proved less effective than using ethyl acetate. Interestingly, polymer **9** demonstrated higher efficiency than polymer **2**, despite the fact that the recovered amount of **5a** was only half that obtained with pure water. These findings suggested that thermoresponsive block copolymers PNIPAAm-*b*-PEG **2** and PNIPAAm-*b*-PSSNa **9** are not only effective in the Pd-catalyzed Mirozoki–Heck reaction in water, but also in extracting the product from the aqueous reaction mixture.

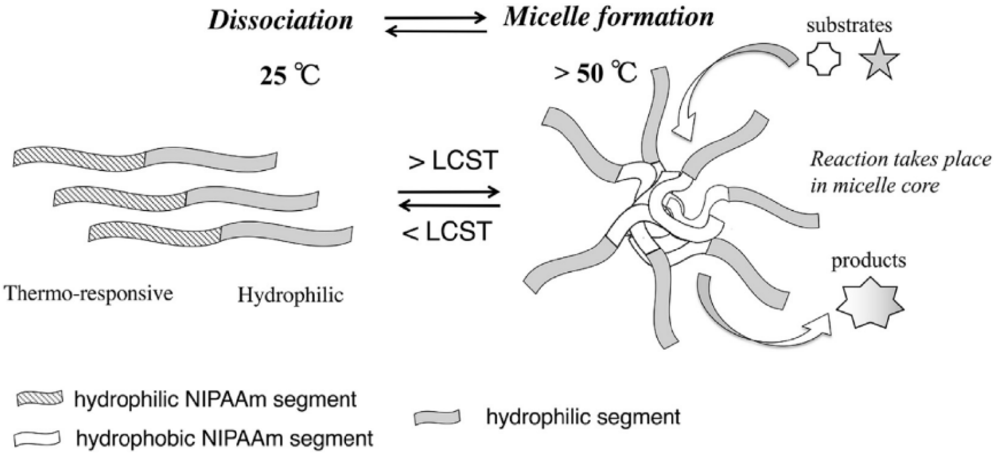

Figure 4. Thermo-responsive micelles switched on/off by temperature. Reprinted with permission of Elsevier from [70]. Copyright 2019.

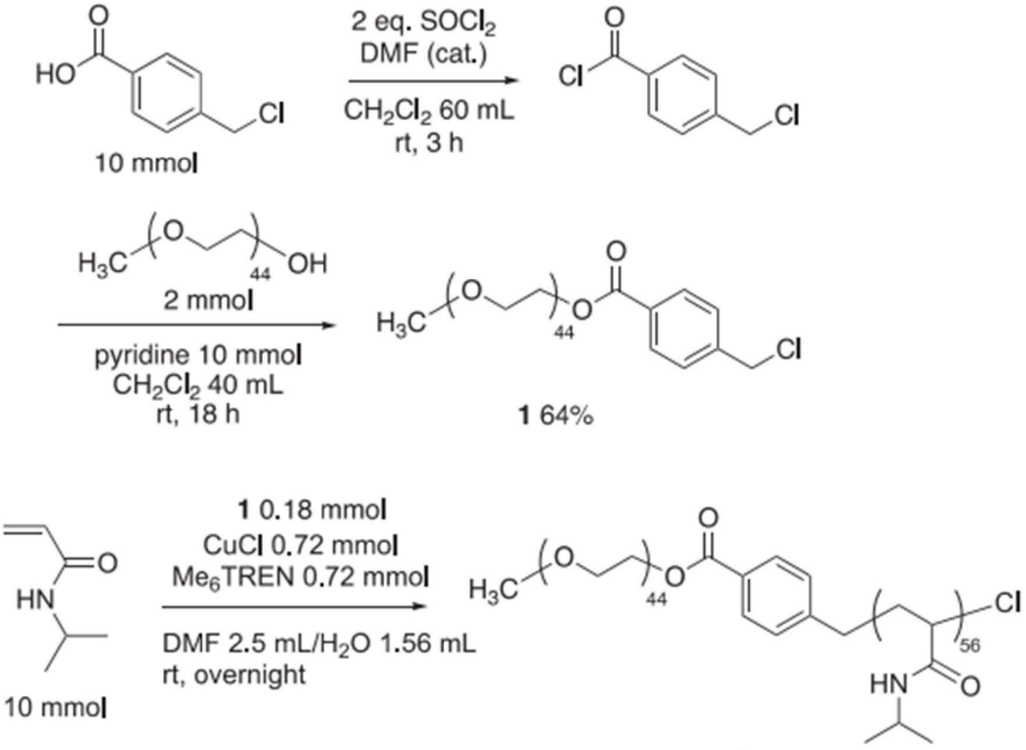

2

Scheme 1. Preparation of NIPAAm-*b*-PEG **2** with PEGylated ATRP agent. Reprinted with permission of Elsevier from [70]. Copyright 2019.

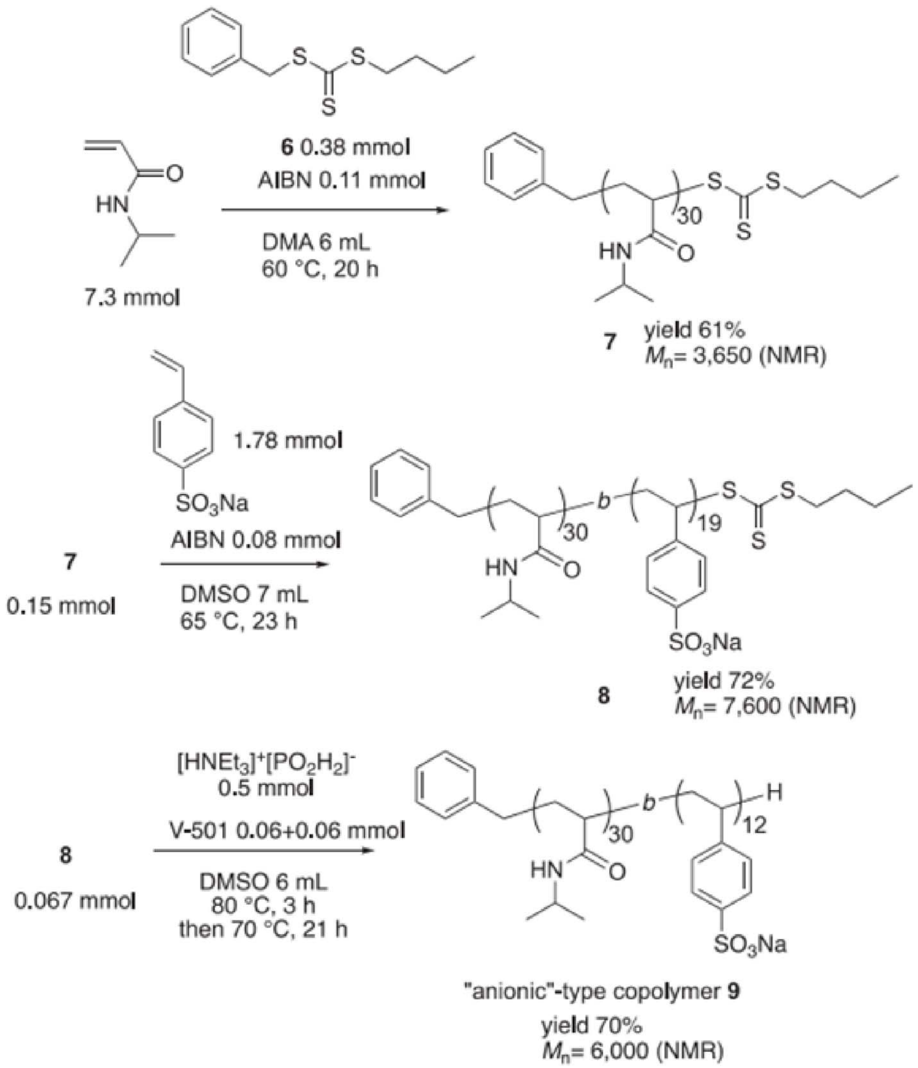

Scheme 2. Preparation of PNIPAAm-*b*-PSSNa **9** by RAFT polymerization. Reprinted with permission of Elsevier from [70]. Copyright 2019; permission conveyed through Copyright Clearance Center, Inc.

The introduction of the catalyst in the core of the micellar nanoreactors can be realized in different ways, either by polymerizing a pre-catalyst-functionalized monomer into the hydrophobic compartment, followed by self-assembly, or by ligand exchange between a molecular pre-catalyst, introduced by mass transport inside the already assembled micelles, to a core-anchored ligand. An example of the former method [72] is the copolymerization of styrene and a functionalized styrene containing a 4-(dimethylamino)pyridine (DMAP) organocatalyst, using the RAFT technique, to yield a hydrophobic macroRAFT agent **2**, which was then chain-extended with a hydrophilic poly(*N*-isopropylacrylamide) (PNIPAM) block (Scheme 3). The catalytic activity of the compartmentalized organocatalyst in the core was found to be high, improving the DMAP-catalyzed acylation reaction of alcohols with anhydrides, with rates up to 100 times compared to those for unsupported DMAP in organic solvents (Table 1). The authors explored catalyst recycling by leveraging the system stimulus-responsive property. Following the extraction of the synthesized product with diethyl ether, the aqueous phase containing the micellar catalyst underwent heating to a temperature over 50 °C. Hereby the polymer transformed into a fine powder, which was subsequently gathered through centrifugation. These catalytic nanoreactors were recycled up to six times without losing catalytic activity.

Despite successful applications, these and other micellar catalysts have one major drawback: the equilibrium between micelles and free surfactant macromolecules. This equilibrium can lead to undesired formation of stable emulsions, slow micelle/product separation caused by excessive swelling, and catalyst loss through the formation of Langmuir–Blodgett films at the liquid/liquid interface and/or inverse micelles in the bulk organic phase [73]. Another major drawback related to the thermo-responsive PMs is their dynamic nature that renders them sensitive to their environment. To circumvent these issues, the micelles can be turned into unimolecular persistent objects by crosslinking, which can be accomplished by various strategies as described below. These cross-linked PMs constitute an attractive alternative with improved characteristic and catalytical behavior.

3.2. *Polymersomes*

The stability of micelle- and vesicle-based systems depends on the environment, such as the temperature of the solution and the concentration of the surfactant. To obtain better defined and more stable systems, macromolecular polymers have been considered as alternative nanoreactors, with a higher kinetic stability compared to the self-assembled molecular surfactant (*vide supra*). When vesicles are self-assembled from macromolecular amphiphiles (or block copolymers), they are referred to as polymersomes. Polymersomes [74–78] have increased rigidity and stability compared to micelles and vesicles, and their structure can vary from simple coil-like diblock copolymers to rod-like, rod-coil diblock or multiblock polymers with or without additional cross-linker groups [79]. The variation in structuring can be tuned by varying the relative block lengths, which results in modified size, structure, polarity, and permeability of the polymersomes.

Eisenberg and coworkers [80] were the first to generate a block copolymer system with six different morphologies of "crew-cut" aggregates of polystyrene-*b*-poly(acrylic acid) block copolymers. Shortly after, Meijer and coworkers [81] reported the synthesis of polystyrene-poly(propylene)imine, thus starting a new research line based on the relation between amphiphilic properties and molecular structure towards the preparation of many other polymersomes by various approaches [82–84] and with different application scope. For enzymatic ring-opening polymerization, Nolte and coworkers [85] developed polystyrene-polyisocyanopeptide (PS-PIAT) based polymersomes, while van Hest and coworkers [86] reported a polymersome-stabilized Pickering emulsion at the water/oil interface that was later applied in biphasic enzymatic catalysis. Also, Lecommandoux, van Hest and coworkers [87] reported a cascade reaction in which small polymersomes were loaded into larger ones, resulting in a multicompartmentalized polymersome-in-polymersome system (Figure 5).

To demonstrate the functional and structural control of the system, they investigated a model reaction with isolated enzymes in the different compartments. The first step of the reaction was a Baeyer-Villiger oxidation of a substituted hydroxyphenoxazinone ketone **1**. The resulting ester **2** was then hydrolyzed with a lipase (enzyme) to form the corresponding primary alcohol **3**, which was subsequently oxidized by alcohol dehydrogenase and a cofactor nicotinamide adenine dinucleotide (NAD) to yield the corresponding aldehyde product **4**. The final step of the catalytic transformation was a spontaneous β-elimination leading to 7-hydroxy-3H-phenoxazin-3-one-10-oxide **5** (Scheme 4). The concept of enzyme compartmentalization in the cascade reaction spatially separated incompatible enzymes to retain their functionality, thus resembling the intracellular organization of eukaryotic cells. This concept allows to separate and conduct incompatible reactions simultaneously in a confined environment with increased efficiency, and is a very powerful tool in material chemistry. For the catalyst recovery, the sample was promptly subjected to centrifugation (25 °C, 500 g force, 4 min). Subsequently, the suspension of polymersomes-in-polymersomes in the aqueous phase was retrieved from the lower layer.

Using the micellar or vesicular approaches, the formation of stable emulsions may occur due to the excessive swelling of the micellar core [88]. Parameters such as temperature, dilution, and the composition of the mixed solvent [89–92] determine

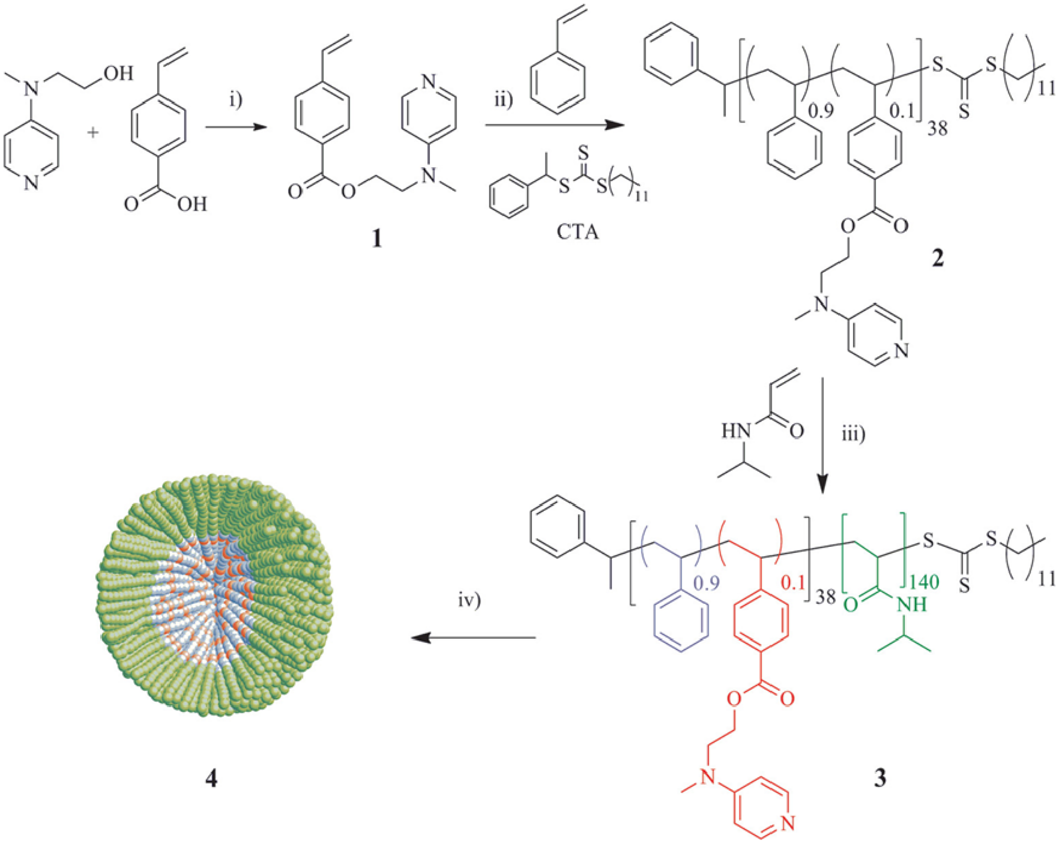

Scheme 3. Four-step synthesis of micelles **4** containing the DMAP functionality covalently attached to the hydrophobic core. Reprinted with permission of American Chemical Society from [72]. Copyright 2012.

Table 1. Acylation reactions in the micelles **4** (adapted from [72])[a]

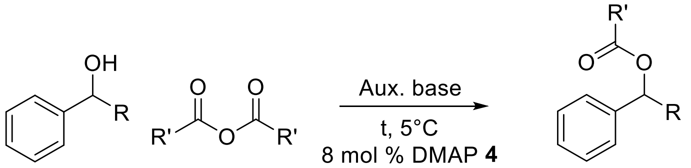

Entry	R	R′	Conversion (%) (15 min)	Conversion (%) (24 h)
1	CH_3	CH_3	26	32
2	CH_2CH_3	CH_3	28	29
3	CH_3	$CH_2CH_2CH_3$	47	53
4[b]	CH_3	$CH_2CH_2CH_3$	65	66
5[b]	CH_2CH_3	$CH_2CH_2CH_3$	94	98

[a] All reactions contained 8 mol% DMAP, [OH] = 0.02 M, 1.5 equiv of auxiliary base (TEA), 1 equiv of alcohol, and 3 equiv of anhydride. Conversions determined by HPLC measurements with mesitylene as the internal standard. [b] *N*,*N*-Diisopropylethylamine (DIPEA) was used as auxiliary base instead of TEA.

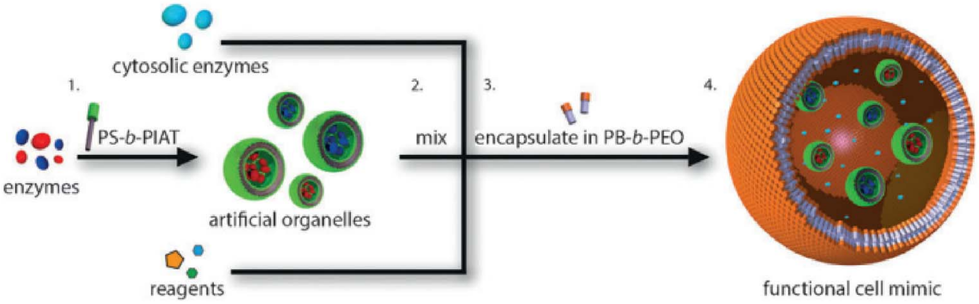

Figure 5. Multi-compartmentalized polymersome-in-polymersome system. Reprinted with permission of Wiley-VCH Verlag GmbH & Co. KGaA, Weinheim from [87]. Copyright 2014.

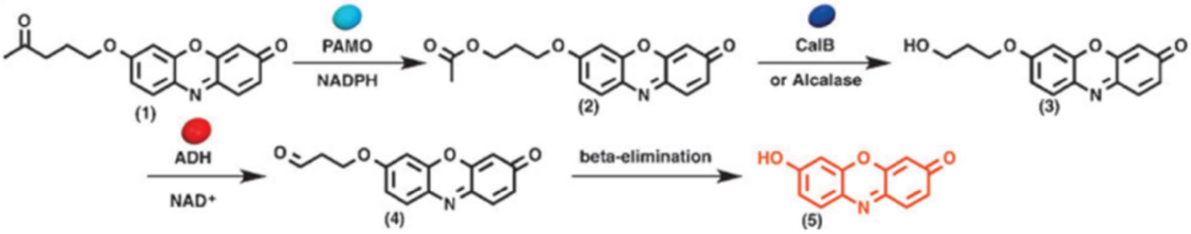

Scheme 4. Enzymatic cascade reactions in multi-compartmentalized polymersomes. Reprinted with permission of Wiley-VCH Verlag GmbH & Co. KGaA, Weinheim from [87]. Copyright 2014.

the equilibrium between micelles/vesicles and single amphiphilic chains. An alternative and promising method to overcome these disadvantages is to cross-link all amphiphilic polymer chains to form unimolecular nanoobjects, thus removing the dynamic micelle/single chain equilibrium [42,60,93].

3.3. *Unimolecular nanoreactors*

3.3.1. *Shell cross-linked micelles*

Wooley and coworkers [94] developed a method to prepare functionalized micelles from low polydispersity macromolecules with a defined structure and an immobilized permeable cross-linked shell and labile core. Unlike dendrimers [95] these shell-cross-linked knedel-like (SCK) particles have greater peripheral functions and nanometer-size diameters, and are therefore more considered as hybrids between dendrimers, hollow spheres, latex particles, and block copolymer micelles (Figure 6). The SCKs were prepared by a two-step synthesis procedure using a block copolymer of polystyrene and poly(4-vinyl pyridine), PSt-*b*-PVP, obtained by anionic polymerization. The PSt served as the hydrophobic block and the quaternized PVP generated the hydrophilic block and introduced the cross-linkable group. Besides micellar catalysis [94], the SCKs find many applications in other fields such as, e.g. recording materials, hydraulic fluids, delivery processes, phase transfer reactions, solvation, coatings and fillers.

O'Reilly and coworkers [96] reported the copolymerization of an amphiphilic copolymer in which the hydrophobic domain was selectively functionalized with terpyridine groups using nitroxide mediated polymerization (NMP) techniques, that has been extensively studied and optimized by Schubert and coworkers [97,98] (Scheme 5). The resulting shell cross-linked micelles (SCMs) (Figure 7) were then modified by metal ion complexation, notably Cu^+, and used as catalysts for 1,3-dipolar cycloaddition reactions ("click reactions") of azido- and alkynyl-functionalized small molecules [96].

Weck and coworkers [99] also reported the synthesis of various SCMs and their catalytic applications [100]. Initially, they reported the synthesis

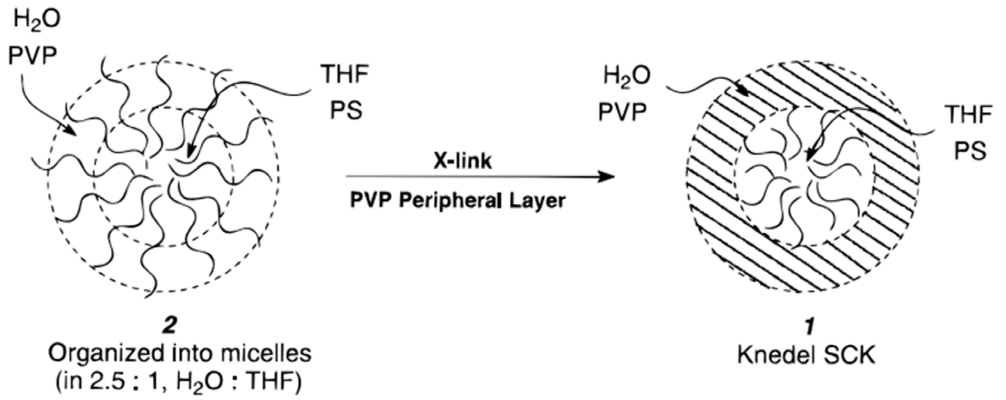

Figure 6. Schematic representation of the basic approach for the formation of SCK's. Micellization of amphiphilic **2** is followed by cross-linking through the styrene side chains located in the peripheral water to yield **1**. Reprinted with permission of American Chemical Society from [94]. Copyright 1996.

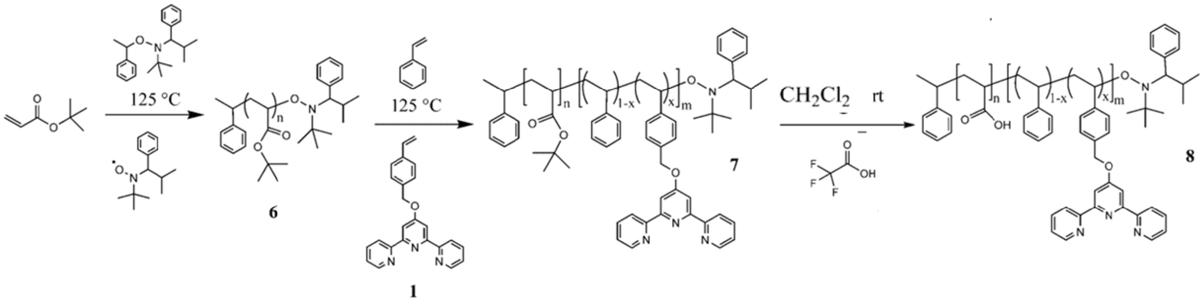

Scheme 5. Synthesis of a *tert*-butyl acrylate block **6** using NMP, followed by chain extension to block copolymer **7** that incorporates terpyridine functionality, and then formation of an amphiphilic diblock copolymer **8** with terpyridine functionality embedded within the hydrophobic segment. Reprinted with permission of American Chemical Society from [96]. Copyright 2008.

of poly(norbornene) block copolymer-based amphiphilic ABC triblock copolymers via ROMP [99]. The middle block (B block) was functionalized with a photochemically active cinnamate group for crosslinking, and the terminal hydrophobic block (C block) contained a Co-salen ligand. The Co-salen functionalized SCMs catalysts were then used for hydrolytic kinetic resolution (HKR) of epichlorohydrin. They showed that the structure of the SCM catalysts was stabilized by the cross-linked shell, which assisted recyclability of the catalysts. Then they also prepared SCMs containing Co(III)-salen cores from amphiphilic poly(2-oxazoline) triblock copolymers [100] and studied substrate selectivity in HKR with various terminal epoxides. More recently, they also developed trifunctional SCMs for enantioselective three-step tandem catalysis [101], which were based on poly(2-oxazoline) synthesized through living CROP [102,103] that permitted compartmentalization of three incompatible catalysts. The SCM consisted of carboxylic acids in the hydrophilic outer shell, Rh-based *N*-tosylated 1,2-diphenyl-1,2-ethylenediamine (Rh-TsDPEN) in the intermediate cross-linked shell, and 4-dimethylaminopyridine (DMAP) in the hydrophobic core. The spatial architecture of each catalyst was designed to selectively exploit the path of the substrate during each step of the reaction; the first step involved ketal hydrolysis to the corresponding prochiral ketone, the second step asymmetric transfer hydrogenation (ATH) to yield an enantio-enriched secondary alcohol, and the final step selective acylation to the desired

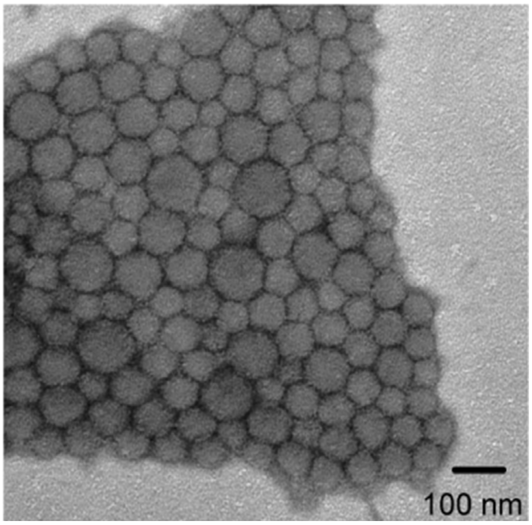

Figure 7. Representative transmission electron microscopy (TEM) images of SCM. Reprinted with permission of American Chemical Society from [96]. Copyright 2008.

ester product (Scheme 6). Higher conversions were observed with more hydrophobic ketals and anhydrides, and the role of the intermediate shell cross-linked layer in preventing deactivation of the DMAP catalyst supported inside the micellar core was also shown. The conversion was determined from aliquots taken at certain time intervals, extracted with ethyl acetate. No recyclability tests were reported.

Optimally, SCMs act as nano-incubators for loaded catalysts and protect the catalyst from passivation or deactivation. However, the cross-linked shell also introduces a physical barrier between the hydrophobic core and the hydrophilic shell, which can lower the mass transport of certain chemicals and limit SCMs applicability for certain catalytical transformations.

3.3.2. *Core cross-linked micelles*

To circumvent the mass transport restrictions of SCMs, other polymeric structures have been developed. The first structure, called core-crosslinked micelle (CCM), consists of ligand-functionalized amphiphilic diblock copolymers that are cross-linked at the end of the hydrophobic chain. This provides star-block unimolecular nano-objects where the ligands are located on flexible arms outside of the cross-linked area. The second structure, known as nanogel (NG), features a fully cross-linked core, with the catalyst binding sites being situated within the cross-linked core [88]. Various strategies have been reported in the literature for the synthesis of CCMs, including ATRP [104], as used by Sawamoto and Terashima. They were the first to use NG-type nanoreactors in catalysis and the Ru-containing NG polymers made by ATRP [42,105–108], and RAFT-mediated polymerization-induced self-assembly (PISA) [109]. The latter strategy is a particularly attractive approach as it allows to produce block copolymer nano-objects with a full synthesis protocol in one-pot. A survey of the different synthetic approaches is beyond the scope of this review and the reader is referred to the literature [110–115] for further details.

Rieger and coworkers [116] reported the synthesis of a core–shell NG using a previously established method involving RAFT radical polymerization in an aqueous dispersion that provided nanometer-sized, uniform core–shell particles with a cross-linkable core. Poly(*N*,*N*-dimethylacrylamide) served as the stabilizing shell, and (*N*,*N*-diethylacrylamide) (PDEAAm) was used for the core matrix through aqueous heterogeneous polymerization at a moderate temperature. The NG was formed in water at 70 °C through RAFT dispersion polymerization of *N*,*N*-diethylacrylamide (DEAAm; 85 mol%), DMAEA (10 mol%), and *N*,*N*-methylenebis(acrylamide) (MBA; 5 mol%), with a stabilizing macromolecular RAFT agent based on poly(*N*,*N*-dimethylacrylamide) (PDMAAmmacro-RAFT). The resulting nanostructured core–shell NG demonstrated the ability to stabilize Pd^0 nanoparticles (NPs) in its core. Pd NPs were incorporated into the NG by adding a Pd^{II} salt, expected to coordinate with the nitrogen functions of DMAEA units, followed by metal reduction with ethanol. The hybrid PdNP@NG exhibited stability in both solid and solution states, making it an effective catalyst for the Mizoroki–Heck reaction between *n*-butylacrylate and activated bromo- and iodoarenes. After catalysis, the hybrid NG could be recovered, dried, and reused for three consecutive runs without significant loss of the catalytic activity. However, after the fourth reuse, a decline in catalytic activity was observed. Analysis of the recovered hybrid

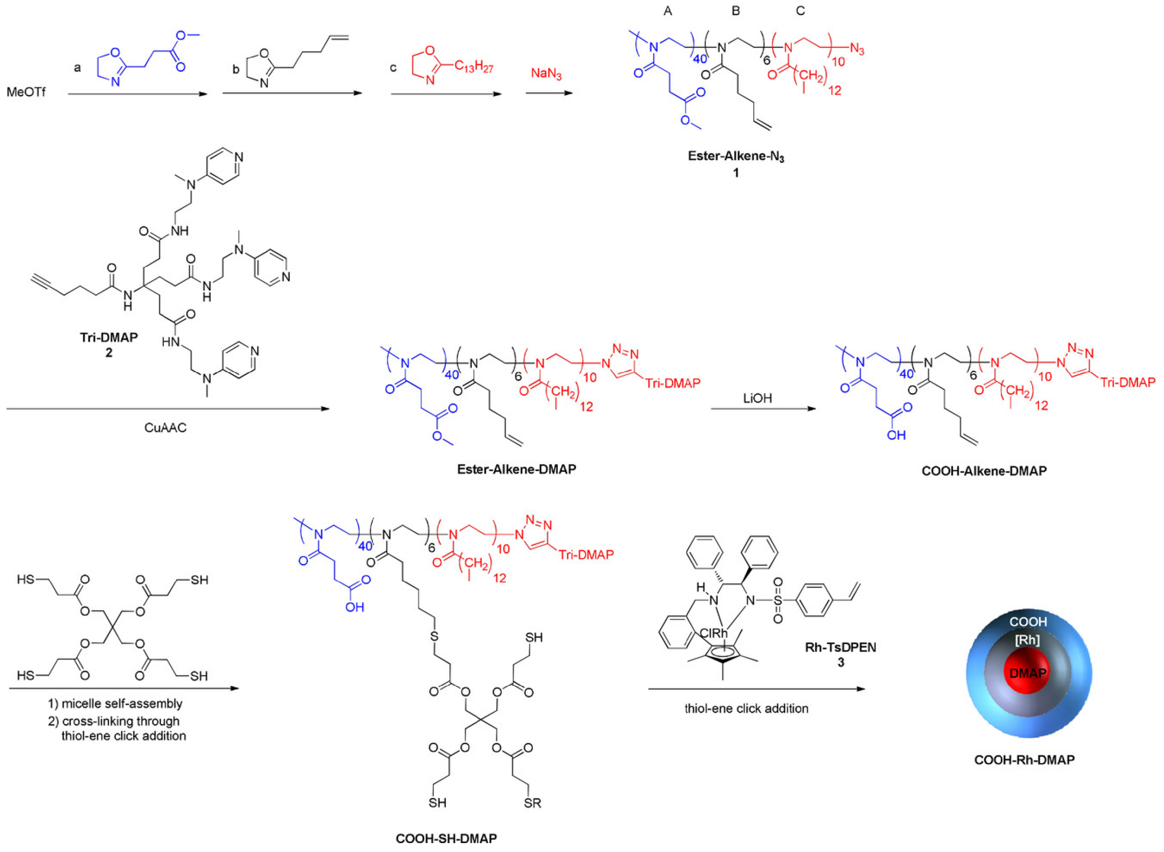

Scheme 6. Synthesis of the trifunctional SCM nanoreactor COOH-Rh-DMAP. Reprinted with permission of Wiley-VCH Verlag GmbH & Co. KGaA, Weinheim from [101]. Copyright 2018.

PdNP@NG revealed the presence of large Pd aggregates and significant oxidation of Pd^0 to Pd^{II} (Figure 8). Additionally, analysis by inductively coupled plasma mass spectrometry (ICP-MS) showed a substantial loss of Pd from the polymeric NG support. This suggested that part of the catalysis occurred outside the NG, explaining the observed limited recyclability.

Stenzel and coworkers [117] used RAFT polymerization technique to synthesize poly(2-hydroxyethyl acrylate)-poly(*n*-butyl acrylate) block copolymers using either poly(2-hydroxyethylacrylate) or poly(*n*-butyl acrylate) macromolecular RAFT (macroRAFT) agents with narrow molecular weight distributions. These macroRAFT agents were further extended by polymerization of a diacrylate monomer, yielding CCMs. No catalytic application was described for these CCMs.

Furthermore, three generations of CCMs with amphiphilic unimolecular polymer-based nanoreactors [88] having neutral (CCM-N), cationic (CCM-C) and anionic (CCM-A) shells, respectively, have been prepared by RAFT PISA and used for aqueous biphasic catalysis (Figure 9) [118]. In all cases, special attention was devoted to the catalyst recovery using an optimized procedure. Briefly, after phase separation, the latex was extracted with diethyl ether or toluene, and the combined organic phases subjected to analysis by gas chromatography (GC). For the recycling experiments, a fresh substrate solution (same amount as in the initial run) was added to the same vial, followed by reaction and product separation according to the same protocol.

The first generation CCM-N [119] was designed with an uncharged water-soluble shell by copolymerization of methacrylic acid (MAA) and

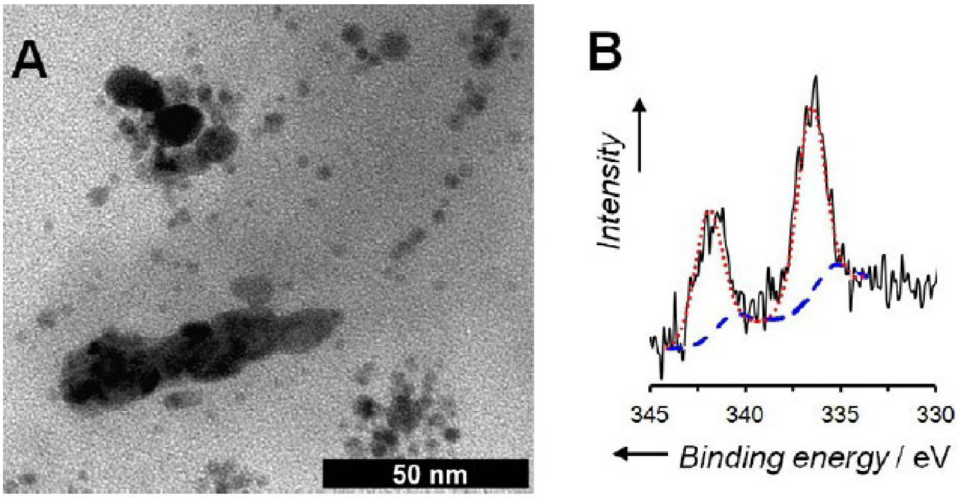

Figure 8. (A) TEM image and (B) Pd 3d X-ray photoelectron spectrum (XPS) of the hybrid PdNP@NG after four catalytic cycles (solid black line) and its deconvolution into Pd^0 (dashed blue line) and Pd^{II} (dotted red line). Reprinted with permission of Wiley-VCH Verlag GmbH & Co. KGaA, Weinheim from [116]. Copyright 2017.

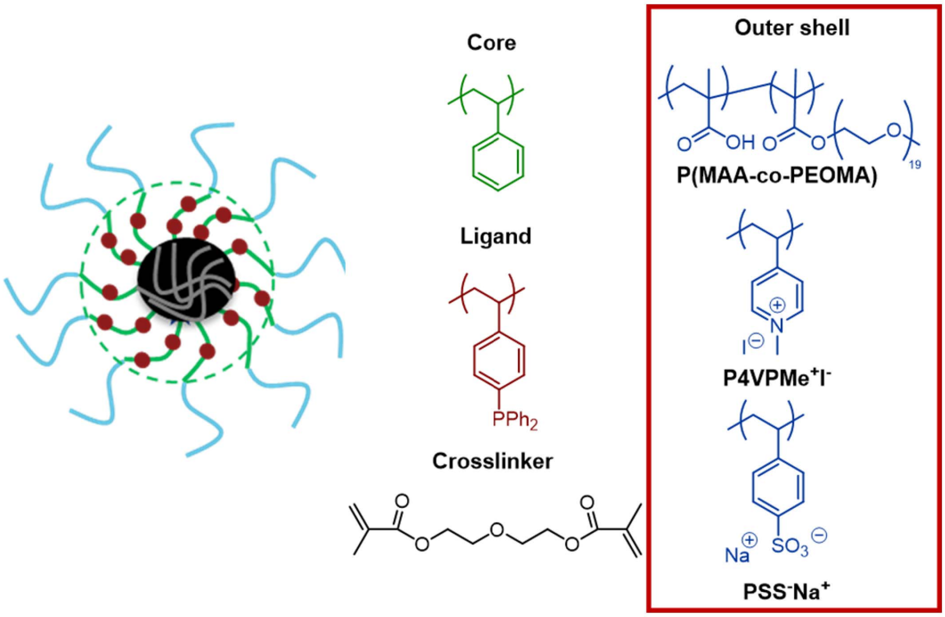

Figure 9. Three generations of CCMs with triphenylphosphine (TPP) core and different outer shell.

poly(ethylene oxide) methyl ether methacrylate (PEOMA) to generate a P(MAA-*co*-PEOMA) macro-RAFT agent (Scheme 7). Addition of styrene (St) and DPPS (diphenylphosphinostyrene) as core ligand generated P(MAA-*co*-PEOMA)-b-P(St-*co*-DPPS) amphiphilic block copolymers that self-assembled into well-defined micellar particles (d = 72 nm), which was crosslinked using diethylene glycol dimethacrylate (DEGDMA) forming CCM-N (d = 79 nm). The average formula of the single polymer chains is R_0-$(MAA_{0.5}$-co-$PEOMA_{0.5})_{30}b$-$(St_{1-n}$-co-$DPPS_n)_{300}$-b-$(St_{0.9}$-co-$DEGDMA_{0.1})_{100}$-SC(S)SPr, with

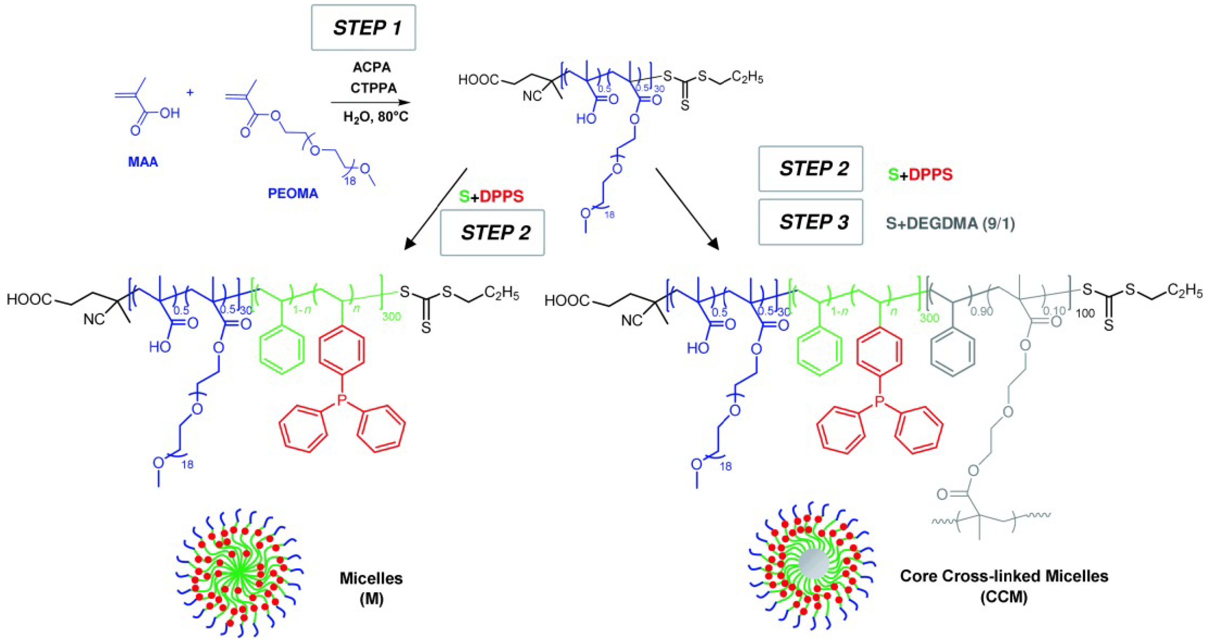

Scheme 7. General strategy of RAFT-mediated emulsion polymerization for the synthesis of various types of core-shell nanoreactors. Reprinted with permission of Wiley-VCH Verlag GmbH & Co. KGaA, Weinheim from [119]. Copyright 2014.

the chain ends ($R_0 = C(CH_3)(CN)CH_2CH_2COOH$ and SC(S)SPr) provided by the RAFT chain transfer agent (CTA). The uniformity of the CCM-Ns was demonstrated by size exclusion chromatography (SEC), TEM and DLS analyses, which also evidenced the latex stability. Moreover, nuclear magnetic resonance (NMR) spectroscopy and DLS confirmed the transport of hydrophobic molecules across the hydrophilic shell into the polymer core to be fast and leading to increased particle size owing to the particle swelling ($d = 117$ nm).

As a proof-of-principle application, the CCM-Ns were loaded with $[Rh(acac)(CO)_2]$ (acac = acetylacetonate) and evaluated for aqueous biphasic hydroformylation of 1-octene [120]. High activity, low isomerization as well as good stability and recyclability (Rh leaching of a few ppm) were found, but the system was moderately mass-transfer limited at high Rh concentrations and non-negligeable leaching appeared to result from particle aggregation. Subsequent follow-up studies addressed the metal leaching mechanism [121], metal migration and cross-exchange in amphiphilic core-shell polymer latexes [122] and mass-transport limitations [123]. Later, Poli, Manoury and coworkers [124] extended the family of ligand-functionalized CCMs using the same synthesis protocol to include the bidentate Nixantphos ligand in the CCM-N. After loading with $[Rh(acac)(CO)_2]$ the system was also applied to the aqueous biphasic hydroformylation of 1-octene, where only moderate activity (mass-transfer limitation) but excellent regioselectivity was found for the formation of n-nonanal.

A convergent synthesis of polymeric nanoreactors containing polymerizable Rh^I-NHC^R complexes [53] was then developed (Scheme 8). TEM images of the resulting Rh-NHC^R@CCM nanoreactors with R = Me (**5a**) and R = Mes (**5b**) (Figure 10) revealed formation of particles with a broad size distribution (diameter of 123.3 ± 19.2 nm). Under optimized reaction conditions, the **5b** nanoreactors yielded good activity and excellent recyclability for styrene hydrogenation with Rh-leaching <0.6 ppm per reaction cycle (measured by ICP-MS) after some initial decomposition of the Rh-complex by cleavage of the Rh-NHC bond in the initial two runs (Table 2, entries 1 and 2). Despite the

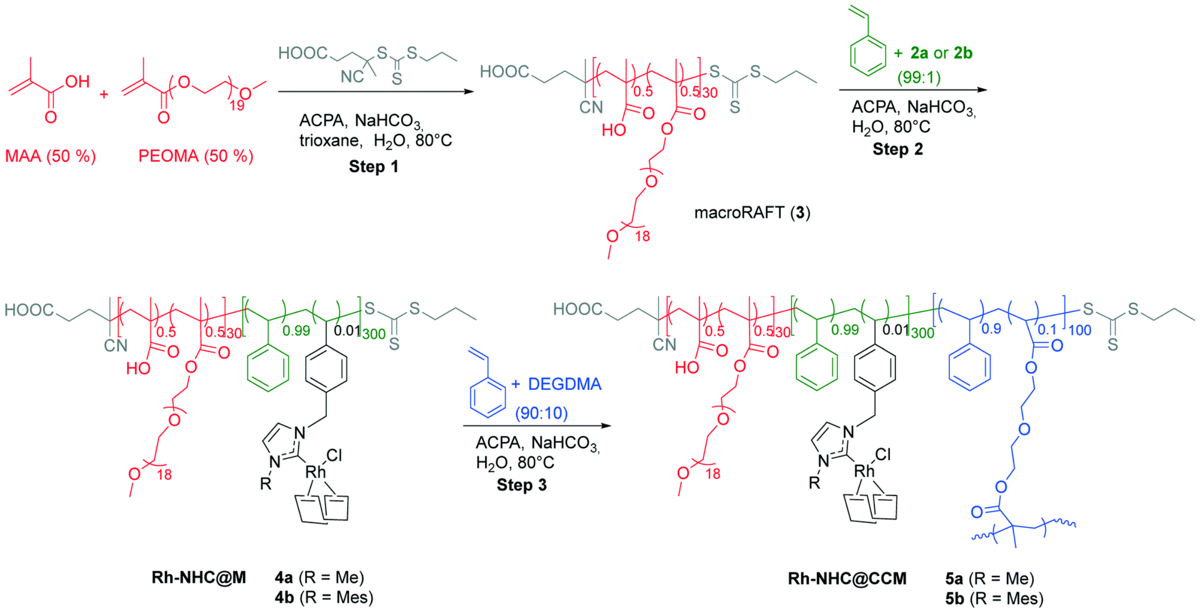

Scheme 8. Synthesis of Rh-NHC^R@CCMs **5a** (R = *N*-methylimidazole (Me)) and **5b** (R = *N*-mesitylimidazole (Mes)) by RAFT-PISA polymerization. Reprinted with permission of The Royal Society of Chemistry from [53]. Copyright 2021.

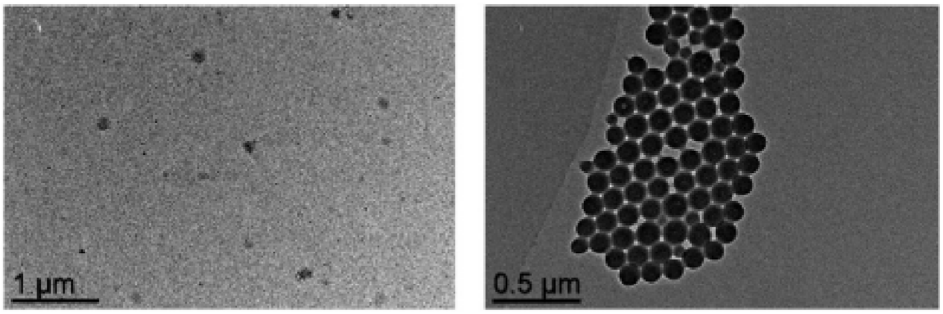

Figure 10. TEM images of Rh-NHC^R@CCMs **5a** (left) and **5b** (right) (numbers as in Scheme 8). Reprinted with permission of The Royal Society of Chemistry from [53]. Copyright 2021.

encouraging recyclability results, mass-transfer limitations and impractical slow separation of the catalyst and reaction mixture remained for this catalyst, like for the other CCM-N catalysts.

To circumvent the mass-transfer and separation issues with CCM-N, a second generation of CCM nanoreactors with an outer polycationic shell (CCM-C) based on poly(1-methyl-4-vinylpyridinium) (CCM-Cs) was developed via RAFT polymerization [125]. The macroRAFT agent was synthesized by RAFT polymerization of 4-vinylpyridine (4VP) in aqueous ethanol, followed by a chain extension with a PSt block and quaternization of the P4VP block. A core-anchored triphenylphosphine (TPP) ligand functionality, diluted in styrene was introduced by chain extension in a fourth synthetic step and the CCM-C was finally formed in a fifth step by core cross-linking by a DEGDMA:St (10:90) mixture [126] (Scheme 9). DLS and TEM analyses showed that all obtained polymers ($x = 5$, 10 or 20%) have spherical morphology, a narrow size distribution (d = 130–150 nm) and a positive zeta potential.

Table 2. Recycling study of Rh-NHC$^{\text{Mes}}$@CCM **5b** (number as in Scheme 8) catalyst in styrene hydrogenation (adapted from [53])

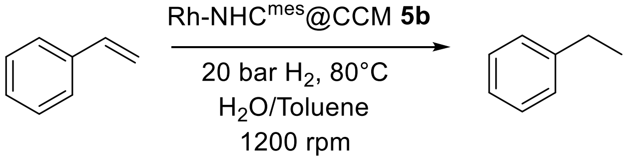

Entry	Run	St/Rh	St Conversion^{a} (%)	EB Selectivity^{a} (%)	Rh leaching^{b} (ppm)
1	1st	1000/1	>99.5	>99.5	0.87
2	2nd		>99.5	>99.5	1.47
3	3rd		>99.5	>99.5	0.24
4	4th		>99.5	>99.5	0.34
5	5th		>99.5	>99.5	0.21
6	1st	10,000/1	73	>99.5	0.39
7	2nd		77	>99.5	0.61
8	3rd		>99.5	>99.5	0.54
9	4th		>99.5	>99.5	0.31
10	5th		98	>99.5	0.13

Conditions: styrene (79.3 mg, 0.75 mmol), CCM **5b** (85 mg, 7.9×10^{-7} mol of Rh for St/Rh = 1000/1 or 8.5 mg, 7.9×10^{-8} mol of Rh for St/Rh = 10,000/1), decane (31.5 mg, 0.225 mmol), toluene (1 mL)/water (0.5 mL). [a] Measured by GC. [b] Measured by ICP-MS.

After loading with $[RhCl(COD)]_2$ (COD = 1,5-cyclooctadiene), the aqueous biphasic hydrogenation of 1-octene and styrene revealed improved mass transport properties and superior performance of the CCM-Cs, in terms of both catalytic activity, stability, and recovery, relative to the neutral-shell analogues [126]. Importantly, also less catalyst leaching occurred due to an enhanced ability of the polycationic shell to confine the nanoreactors in the aqueous phase. Moreover, in substrate scope investigations where the catalytic hydrogenation of acetophenone was attempted, the [RhCl(COD)(TPP@CCM-C)] latex turned black, suggesting reduction of the molecular Rh^{I} complex to Rh^{0} metal. Actually, this turned out to be an excellent approach to generate Rh NPs directly inside the core of CCMs (Figure 11), triggering further investigations of biphasic hydrogenation with Rh NPs [127].

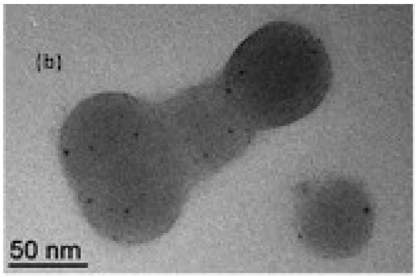

Figure 11. TEM image of Rh NPs generated in the core of CCM-C. Reprinted with permission of The Royal Society of Chemistry from [127]. Copyright 2021.

The RhNP@CCM-C system was initially tested for aqueous biphasic hydrogenation of acetophenone, but only low conversions were obtained, unless high temperature (90 °C) was used. The slow reaction rate was attributed to a poor mass transport of the acetophenone into the CCM-C core, resulting from a possible electrostatic interaction between its carbonyl group and the cationic pyridinium functions present in the shell [127]. Conversely, the catalytic performances were excellent when the catalyst system was applied to the hydrogenation of

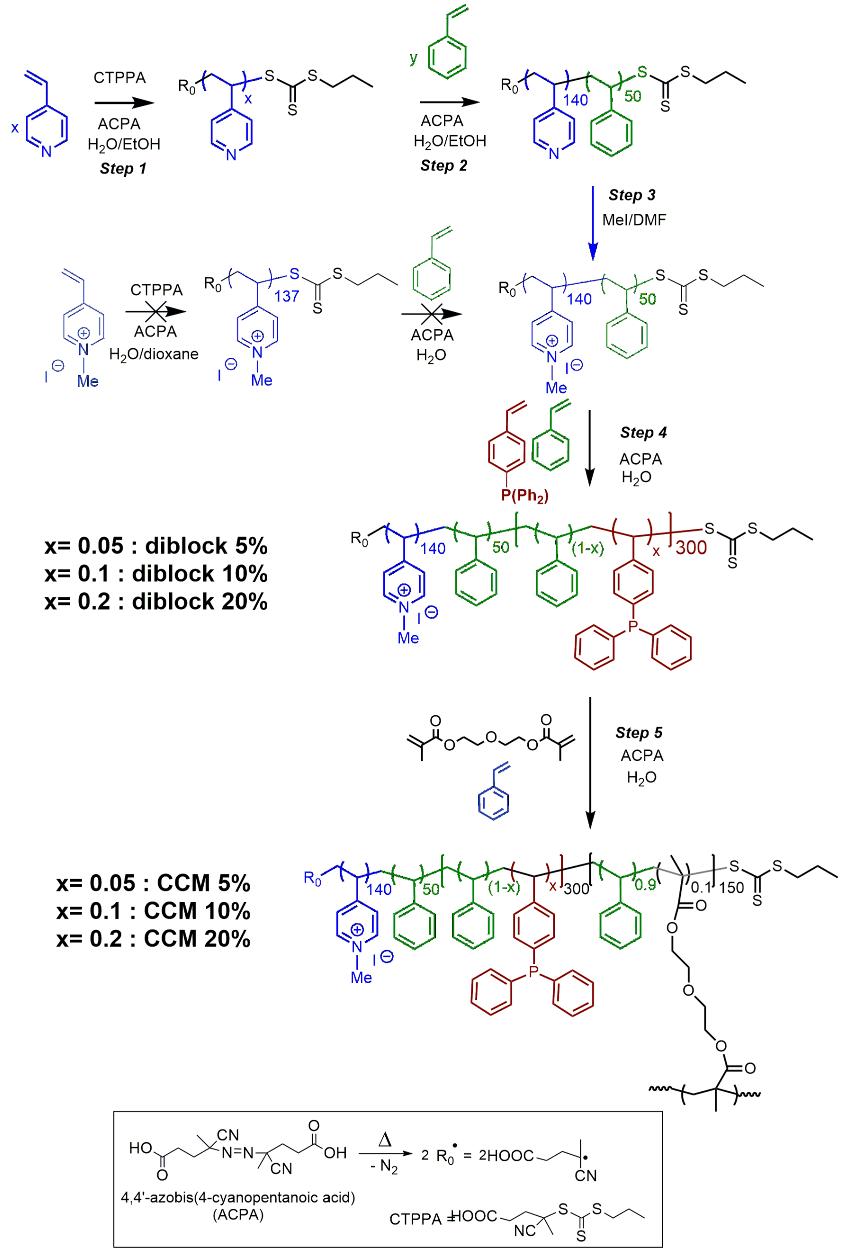

Scheme 9. Synthesis of CCM-C. Adapted with permission of Wiley-VCH Verlag GmbH & Co. KGaA, Weinheim from [126]. Copyright 2019.

1-octene and styrene, with full conversion and full selectivity towards the hydrogenation of the olefinic group. Notably, the catalytic activity was superior to that of molecular Rh^I systems. The RhNP@CCM-C system proved also recyclable for styrene hydrogenation up to four runs without loss of activity and with the Rh NPs remaining well-dispersed when toluene was used for product recovery/catalyst recycling. However, when using diethyl ether as extraction solvent a dramatic loss of activity was observed.

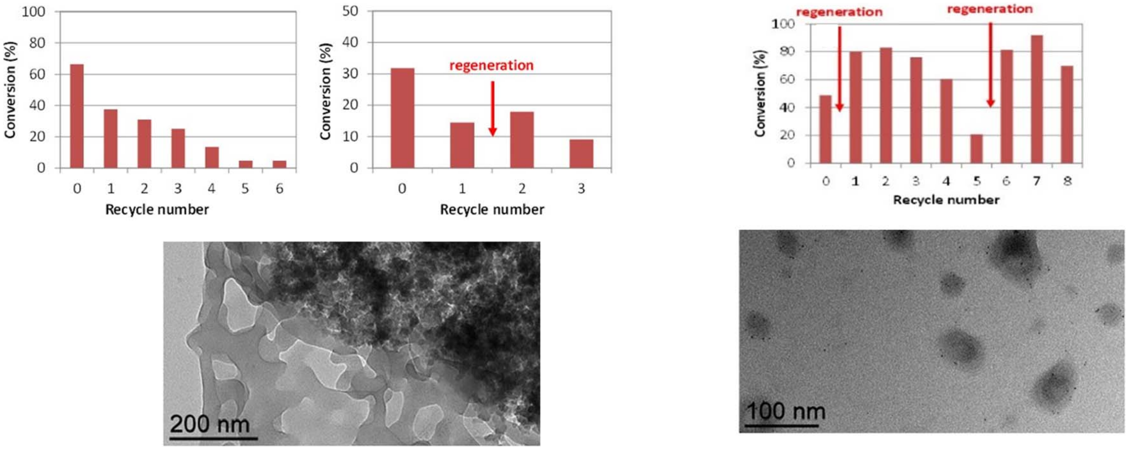

Figure 12. Recycling tests in the hydrogenation of styrene with RhNP@CCM-C using diethyl ether (left) and toluene (right) as extraction solvent (25 °C, 0.5 h, styrene/Rh = 2000/1) (top). TEM images of the recovered catalyst latexes after the final run (bottom). Reprinted with permission of The Royal Society of Chemistry from [127]. Copyright 2021.

This phenomenon was attributed to facilitated extraction of the Rh NPs from the CCM-C core by the oxygen-based solvent (Figure 12).

To address the substrate scope limitation of the CCM-C nanoreactors, a third generation of phosphine-functionalized CCM nanoreactors was developed with a polyanionic poly(styrene sulfonate)-based shell (CCM-A) [12,118]. The synthesis route was identical to those used for the syntheses of CCM-N and CCM-C described above, except for using the water-soluble sodium styrene sulfonate monomer in the first step (Scheme 10, Figure 13).

For application in aqueous biphasic styrene hydrogenation, the CCM-A nanoreactors were loaded with $[RhCl(COD)]_2$, as previously done for the CCM-N and CCM-C counterparts (*vide supra*). However, interaction between the Rh dimer complex and the outer shell of the CCM-A limited the transfer of the metal complex to the core, presumably via chelating Rh^I-sulfonate complex formation. This bottleneck was circumvented by “dilution” of the shell with a neutral monomer (PEOMA), forming a mixed polyanionic-neutral CCM, which allowed Rh^I complexation in the core. Nevertheless, the mixed polyanionic-neutral CCM nanoreactors had inferior performance compared to equivalent nanoreactors with neutral and polycationic shells, which seemed to stem from catalyst alterations induced by migration of the Rh centers towards the shell sulfonate groups [12,118]. Thus, despite significant progress in the development of CCMs, further improvements are still needed to obtain efficient and durable nanoreactor systems for aqueous biphasic hydrogenation catalysis.

4. Conclusion

Nanostructured materials with high specific surface area offer many advantages, attributed to their unique properties, paving the way for advances in various fields such as nanotechnology, materials science, electronics, energy storage, and catalysis. This review has highlighted major developments in the synthesis and catalytic applications of self-assembled nanoreactors made from amphiphilic macromolecules such as polymer micelles, polymersomes and unimolecular nanoreactors. The approaches using macromolecular nanoreactors as potential catalyst supports, hold many unique advantages owing to the diverse synthesis strategies for the generation and tuning of the nanoreactors, which could lead to unique industrial applications.

In particular, unimolecular nanoreactors have been the topic of extensive recent research. The perspectives of these systems are numerous, owing to their modularity and simple syntheses, notably by

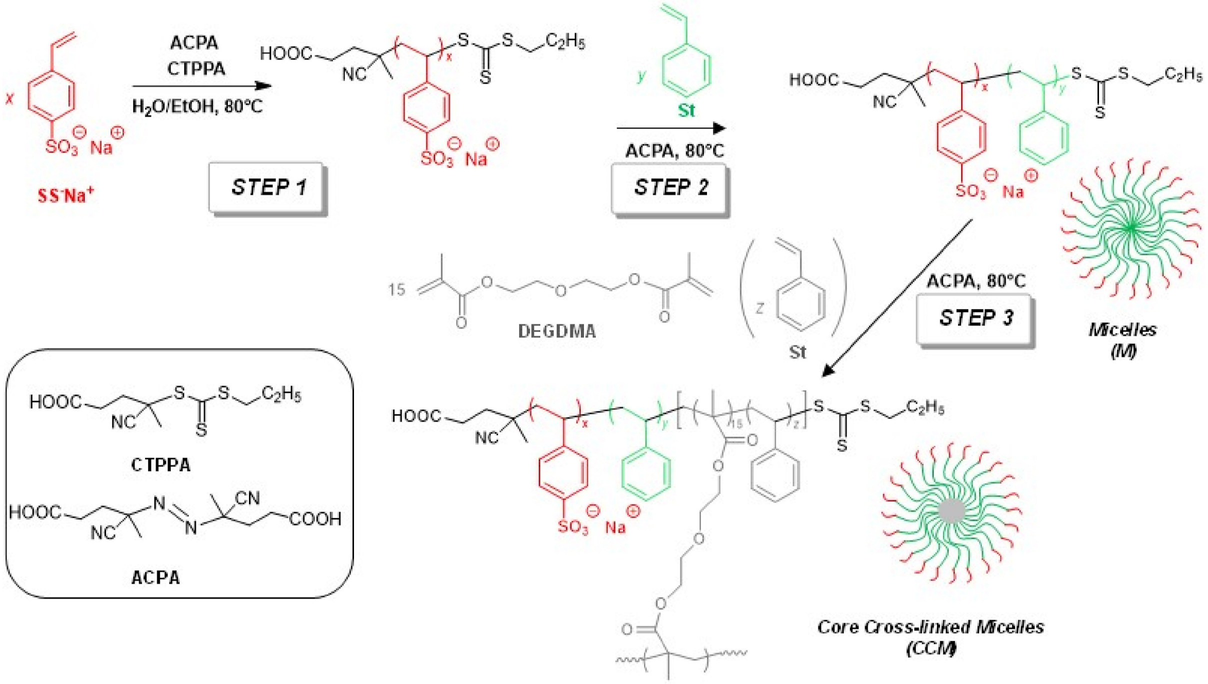

Scheme 10. Synthesis route to CCM-A. Reprinted with permission of Elsevier Ltd [12]. Copyright 2022.

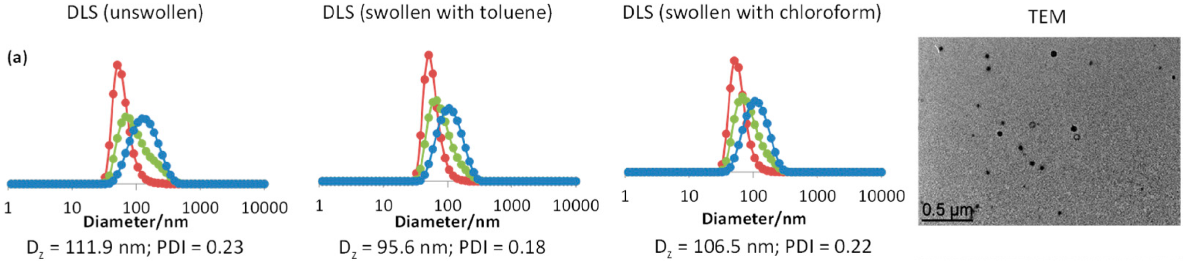

Figure 13. DLS (before and after swelling with toluene or chloroform) and TEM image of the CCM-A. Color coding for the DLS size distributions: number (red), volume (green) and intensity (blue). Reprinted with permission of [118]. MDPI (https://creativecommons.org/licenses/by/4.0/).

the PISA RAFT protocol, which provides access to ligand-functionalized CCM nanoreactors. In such nanoreactors, the chemical nature and the degree of polymerization of the core and the shell, the type and density of the core-anchored ligands, as well as the nature of the coordinated metal pre-catalyst can all be readily varied. This makes the unimolecular nanoreactors highly adaptable and applicable to aqueous biphasic catalysis, thus providing new avenues of research with several potential applications.

Declaration of interest

The authors do not work for, advise, own shares in, or receive funds from any organization that could benefit from this article, and have declared no affiliations other than their research organizations.

Funding

This work has been supported by the European Research Council, as part of the Horizon 2020 research and innovation program under the Marie Skodowska-Curie grant agreement No. 860322.

References

[1] M. Niyaz Khan, *Micellar Catalysis*, CRC Press, Boca Raton, 2006, ISBN: 9780429133749.

[2] R. A. Sheldon, I. Arends, U. Hanefeld, *Green Chemistry and Catalysis*, vol. 295, John Wiley & Sons, New York, 2007.

[3] O. Nuyken, P. Persigehl, R. Weberskirch, *Macromol. Symp.*, 2002, **177**, 163-173.

[4] M. T. De Martino, L. K. E. A. Abdelmohsen, F. P. J. T. Rutjes, J. C. M. van Hest, *Beilstein J. Org. Chem.*, 2018, **14**, 716-733.

[5] E. Wiebus, B. Cornils, *Biphasic Systems: Water — Organic, Catalyst Separation, Recovery and Recycling, Catalysis by Metal Complexes*, vol. 30, Springer, Dordrecht, 2006.

[6] M. Benaglia, A. Puglisi, *Catalyst Immobilization: Methods and Applications*, Wiley-VCH Verlag GmbH & Co. KgaA, Weinheim, 2020, ISBN: 9783527817290.

[7] R. V. Chaudhari, B. M. Bhanage, R. M. Deshpande, H. Delmas, *Nature*, 1995, **373**, 501-503.

[8] M. Pera-Titus, L. Leclercq, J. M. Clacens, F. De Campo, V. Nardello-Rataj, *Angew. Chem. Int. Ed.*, 2015, **54**, 2006-2021.

[9] Y. Zhou, Z. Guo, W. Hou, Q. Wang, J. Wang, *Catal. Sci. Technol.*, 2015, **5**, 4324-4335.

[10] M. Mkosza, M. Fedoryski, *Russ. Chem. Bull.*, 2011, **60**, 2141-2146.

[11] T. Ooi, K. Maruoka, *Angew. Chem. Int. Ed.*, 2007, **46**, 4222-4266.

[12] H. Wang, C. Fliedel, E. Manoury, R. Poli, *Polymer*, 2022, **243**, article no. 124640.

[13] H. Wang, L. Vendrame, C. Fliedel, S. Chen, F. Gayet, F. D'Agosto, M. Lansalot, E. Manoury, R. Poli, *Chem. Eur. J.*, 2021, **27**, 5205-5214.

[14] S. H. A. M. Leenders, R. Gramage-Doria, B. De Bruin, J. N. H. Reek, *Chem. Soc. Rev.*, 2015, **44**, 433-448.

[15] C. Gaeta, P. La Manna, M. De Rosa, A. Soriente, C. Talotta, P. Neri, *ChemCatChem*, 2021, **13**, 1638-1658.

[16] R. Syah, M. Zahar, E. Kianfar, *Int. J. Chem. React.*, 2021, **19**, 981-1007.

[17] R. J. Varghese, E. H. M. Sakho, S. Parani, S. Thomas, O. S. Oluwafemi, J. Wu, in *Nanomaterials for Solar Cell Applications* (S. Thomas, E. H. M. Sakho, N. Kalarikkal, S. O. Oluwafemi, J. Wu, eds.), Elsevier, 2019, Chapter 3, p. 75–95. ISBN 9780128133378.

[18] E. Roduner, *Chem. Soc. Rev.*, 2006, **35**, 583-592.

[19] N. Baig, I. Kammakakam, W. Falath, I. Kammakakam, *Mater. Adv.*, 2021, **2**, 1821-1871.

[20] Q. Wu, W. S. Miao, Y. Du Zhang, H. J. Gao, D. Hui, *Nanotechnol. Rev.*, 2020, **9**, 259-273.

[21] R. Tomar, A. A. Abdala, R. G. Chaudhary, N. B. Singh, *Mater. Today Proc.*, 2020, **4**, 967-973.

[22] A. P. Alivisatos, *Science*, 1996, **271**, 933-937.

[23] S. K. Krishnan, E. Singh, P. Singh, M. Meyyappan, H. S. Nalwa, *RSC Adv.*, 2019, **9**, 8778-8781.

[24] E. Pomerantseva, F. Bonaccorso, X. Feng, Y. Cui, Y. Gogotsi, *Science*, 2019, **366**, article no. 969.

[25] H. Das, B. Pathak, S. Khanam, P. K. Kalita, P. Datta, *MRS Commun.*, 2022, **12**, 285-294.

[26] P. Serp, K. Philippot (eds.), *Nanomaterials in Catalysis*, Wiley-VCH, Weinheim, 2012, Online ISBN: 9783527656875.

[27] D. Astruc (ed.), *Nanoparticles and Catalysis*, Wiley-VCH, Weinheim, 2007, Online ISBN: 978352762132.3.

[28] A. Kilbinger, *Angew. Chem. Int. Ed.*, 2010, **49**, 1191-1192.

[29] A. H. Gröschel, A. H. E. Müller, *Nanoscale*, 2015, **7**, 11841-11876.

[30] C. Bouilhac, E. Cloutet, D. Taton, A. Deffieux, R. Borsali, H. Cramail, *J. Polym. Sci. A Polym. Chem.*, 2009, **47**, 197-209.

[31] J. I. van der Vlugt, T. S. Koblenz, J. Wassenaar, J. N. H. Reek, in *Molecular Encapsulation: Organic Reactions in Constrained Systems* (U. H. Brinker, J.-L. Mieusset, eds.), John Wiley & Sons, Inc., Hoboken, New Jersey, 2010, p. 145–174.

[32] M. Wang, Y. Min, J. Huang, Y. Shi, X. Dong, X. Zhou, X. Yu, D. Qi, Z. Hua, T. Chen, *ACS Appl. Polym. Mater.*, 2022, **4**, 1411-1421.

[33] W. Demos, C. R. Bittencourt, L. Nardino, F. Nome, A. P. Gerola, *ACS Appl. Nano Mater.*, 2021, **4**, 644-651.

[34] M. Kuepfert, E. Ahmed, M. Weck, *Macromolecules*, 2021, **54**, 3845-3853.

[35] B. M. Rossbach, K. Leopold, R. Weberskirch, *Angew. Chem. Int. Ed.*, 2006, **45**, 1309-1312.

[36] J. M. Ren, T. G. McKenzie, Q. Fu, E. H. H. Wong, J. Xu, Z. An, S. Shanmugam, T. P. Davis, C. Boyer, G. G. Qiao, *Chem. Rev.*, 2016, **116**, 6743-6836.

[37] D. M. Vriezema, M. C. Aragonès, J. A. A. W. Elemans, J. J. L. M. Cornelissen, A. E. Rowan, R. J. M. Nolte, *Chem. Rev.*, 2005, **105**, 1445-1489.

[38] P. Cotanda, N. Petzetakis, R. K. O'reilly, *MRS Commun.*, 2012, **2**, 119-126.

[39] C. Deraedt, D. Astruc, *Coord. Chem. Rev.*, 2016, **324**, 106-122.

[40] V. Mouarrawis, R. Plessius, J. I. van der Vlugt, J. N. H. Reek, *Front. Chem.*, 2018, **6**, article no. 623.

[41] M. R. Buchmeiser, *ChemCatChem*, 2021, **13**, 785-786.

[42] R. Poli (ed.), *Effects of Nanoconfinement on Catalysis*, Springer International Publishing, Cham, 2017, ISBN: 978-3-319-50205-2.

[43] G. La Sorella, G. Strukul, A. Scarso, *Green Chem.*, 2015, **17**, 644-683.

[44] T. Dwars, E. Paetzold, G. Oehme, *Angew. Chem. Int. Ed.*, 2005, **44**, 7174-7199.

[45] B. Cornils, W. A. Herrmann, M. Beller, R. Paciello (eds.), *Applied Homogeneous Catalysis with Organometallic Compounds: A Comprehensive Handbook in Four Volumes*, Wiley-VCH, Weinheim, 2017, ISBN: 9783527651733.

[46] A. G. Volkov (ed.), *Interfacial Catalysis*, Marcel Dekker, Inc., New York, Basel, 2003, ISBN: 0-8247-0839-3.

[47] O. Nuyken, R. Weberskirch, T. Kotre, D. Schönfelder, A. Wörndle, *Polymeric Materials in Organic Synthesis and Catalysis*, Wiley-VCH, Weinheim, 2005, p. 277–304.

[48] D. J. Cole-Hamilton, *Science*, 2003, **299**, 1702-1706.

[49] E. J. Fendler, J. H. Fendler, *Adv. Phys. Org. Chem.*, 1970, **8**, 271-406.

[50] D. Christophe, S. Lionel, E. Laetitia, R. Jaime, A. Didier, *Chem. Commun.*, 2013, **49**, 8169-8171.

[51] J. Lu, J. Dimroth, M. Weck, *J. Am. Chem. Soc.*, 2015, **137**, 12984-12989.

[52] L. Onel, N. J. Buurma, *Annu. Rep. Prog. Chem. B*, 2010, **106**, 344-375.

[53] S. S. Sambou, R. Hromov, I. Ruzhylo, H. Wang, A. Allandrieu, C. Sabatier, Y. Coppel, J. C. Daran, F. Gayet, A. Labande, E. Manoury, R. Poli, *Catal. Sci. Technol.*, 2021, **11**, 6811-6824.

[54] G. Delaittre, C. Dire, J. Rieger, J. L. Putaux, B. Charleux, *Chem. Commun.*, 2009, **20**, 2887-2889.

[55] M. Steinbeck, G. D. Frey, W. W. Schoeller, W. A. Herrmann, *J. Organomet. Chem.*, 2011, **696**, 3945-3954.

[56] M. R. Nabid, Y. Bide, *Appl. Catal. A Gen.*, 2014, **469**, 183-190.

[57] M. Galetti, S. Rossi, C. Caffarra, A. G. Gerboles, M. Miragoli, in *Micro and Nano Technologies, Exposure to Engineered Nanomaterials in the Environment* (N. Marmiroli, J. C. White, J. Song, eds.), Elsevier, 2019, Chapter 9, p. 235–262. ISBN: 9780128148358.

[58] J. N. Israelachvili, D. J. Mitchell, B. W. Ninham, *Biochim. Biophys. Acta*, 1977, **470**, 185-201.

[59] F. D'Agosto, J. Rieger, M. Lansalot, *Angew. Chem. Int. Ed.*, 2020, **59**, 8368-8392.

[60] Y. Wang, X. Zhu, *Nanoscale*, 2020, **12**, 12698-12711.

[61] W. Blokzijl, J. B. F. N. Engberts, *Angew. Chem. Int. Ed.*, 1993, **32**, 1545-1579.

[62] S. Yusa, P. Bahadur, H. Matsuoka, T. Sato (eds.), *Polymer Micelles, Polymers*, MDPI, Basel, 2018, ISBN: 978-3-03842-808-4.

[63] A. O. Moughton, M. A. Hillmyer, T. P. Lodge, *Macromolecules*, 2012, **45**, 2-19.

[64] R. K. O'Reilly, *Philos. Trans. R. Soc. Lond. A*, 2007, **365**, 2863-2878.

[65] S. E. Webber, *J. Phys. Chem. B*, 1998, **102**, 2618-2626.

[66] P. Zhang, X. Zhang, C. Li, S. Zhou, W. Wu, X. Jiang, *ACS Appl. Mater. Interfaces*, 2019, **11**, 32697-32705.

[67] G. Yang, L. Xiao, L. Lamboni, *Bioinspired Materials Science and Engineering*, John Wiley & Sons, Inc., Hoboken, New Jersey, 2018, Online ISBN: 9781119390350.

[68] C. M. Ellis, D. Yuan, F. E. Mózes, J. J. Miller, J. J. Davis, *Chem. Commun.*, 2023, **59**, 1605-1608.

[69] X. Wu, Y. Hu, X. Wang, L. Chen, *Catal. Commun.*, 2015, **58**, 164-168.

[70] N. Suzuki, T. Takabe, Y. Yamauchi, S. Koyama, R. Koike, M. Rikukawa, W. T. Liao, W. S. Peng, F. Y. Tsai, *Tetrahedron*, 2019, **75**, 1351-1358.

[71] N. Suzuki, R. Akebi, T. Inoue, M. Rikukawa, Y. Masuyama, *Curr. Organocatal.*, 2016, **3**, 306-314.

[72] P. Cotanda, A. Lu, J. P. Patterson, N. Petzetakis, R. K. O'Reilly, *Macromolecules*, 2012, **45**, 2377-2384.

[73] J. C. Ravey, M. Buzier, *Macro- and Microemulsions: Theory and Applications: Based on a Symposium Sponsored by the Division of Industrial and Engineering Chemistry at the 186th Meeting of the American Chemical Society, Washington, DC*, ACS Symposium Series, vol. 272, American Chemical Society, Washington, DC, 1985, p. 253–263.

[74] R. Bleul, R. Thiermann, M. Maskos, *Macromolecules*, 2015, **48**, 7396-7409.

[75] L. K. E. A. Abdelmohsen, R. S. M. Rikken, P. C. M. Christianen, J. C. M. van Hest, D. A. Wilson, *Polymer*, 2016, **107**, 445-449.

[76] E. Lorenceau, A. S. Utada, D. R. Link, G. Cristobal, M. Joanicot, D. A. Weitz, *Langmuir*, 2005, **21**, 9183-9186.

[77] H. K. Cho, I. W. Cheong, J. M. Lee, J. H. Kim, *Korean J. Chem. Eng.*, 2010, **27**, 731-740.

[78] J. Lefley, C. Waldron, C. R. Becer, *Polym. Chem.*, 2020, **11**, 7124-7136.

[79] D. E. Discher, A. Eisenberg, *Science*, 2002, **297**, 967-973.

[80] L. Zang, A. Eisenberg, *Science*, 1995, **268**, 1728-1731.

[81] J. C. M. van Hest, D. A. P. Delnoye, M. W. P. L. Baars, M. H. P. van Genderen, E. W. Meijer, *Science*, 1995, **268**, 1592-1595.

[82] H. C. Shum, D. A. Weitz, *Soft Matt.*, 2011, **7**, 8762-8765.

[83] N. P. Kamat, J. S. Katz, D. A. Hammer, *J. Phys. Chem. Lett.*, 2011, **2**, 1612-1623.

[84] H. Che, J. C. M. van Hest, *ChemNanoMat*, 2019, **5**, 1092-1109.

[85] M. Nallani, H. P. M. de Hoog, J. J. L. M. Cornelissen, A. R. A. Palmans, J. C. M. van Hest, R. J. M. Nolte, *Biomacromolecules*, 2007, **8**, 3723-3728.

[86] Z. Wang, M. C. M. van Oers, F. P. J. T. Rutjes, J. C. M. van Hest, *Angew. Chem.*, 2012, **124**, 10904-10908.

[87] R. J. R. W. Peters, M. Marguet, S. Marais, M. W. Fraaije, J. C. M. van Hest, S. Lecommandoux, *Angew. Chem.*, 2014, **126**, 150-154.

[88] E. Manoury, F. Gayet, F. D'Agosto, M. Lansalot, H. Delmas, C. Julcour, J.-F. Blanco, L. Barthe, R. Poli, *Effects of Nanoconfinement on Catalysis. Fundamental and Applied Catalysis*, Springer, Berlin, 2017, p. 147–172.

[89] Y. Chevalier, T. Zemb, *Rep. Prog. Phys.*, 1990, **53**, 279-371.

[90] D. J. Mitchell, B. W. Ninham, *J. Chem. Soc. Faraday Trans.*, 1981, **2**, 601-629.

[91] J. F. Gohy, *Adv. Polym. Sci.*, 2005, **190**, 65-136.

[92] M. J. Blandamer, P. M. Cullis, L. G. Soldi, J. B. F. N. Engberts, A. Kacperska, N. M. Van Os, M. C. S. Subha, *Adv. Colloid Interface Sci.*, 1995, **58**, 171-209.

[93] P. Qu, M. Kuepfert, E. Ahmed, F. Liu, M. Weck, *Eur. J. Inorg. Chem.*, 2021, **15**, 1420-1427.

[94] K. I. Bruce Thurmond, T. Kowalewski, K. L. Wooley, *J. Am. Chem. Soc.*, 1996, **118**, 7239-7240.

[95] M. Petriccone, R. Laurent, C.-O. Turrin, R. M. Sebastián, A.-M. Caminade, *Organics*, 2022, **3**, 240-261.

[96] A. D. Levins, X. Wang, A. O. Moughton, J. Skey, R. K. O'Reilly, *Macromolecules*, 2008, **41**, 2998-3006.

[97] H. Hofmeier, U. S. Schubert, *Chem. Soc. Rev.*, 2004, **33**, 373-399.

[98] U. S. Schubert, C. Eschbaumer, O. Hien, P. R. Andres, *Tetrahedron Lett.*, 2001, **42**, 4705-4707.

[99] Y. Liu, V. Piñón, M. Weck, *Polym. Chem.*, 2011, **2**, 1964-1975.

[100] Y. Liu, Y. Wang, Y. Wang, J. Lu, V. Piñón, M. Weck, *J. Am. Chem. Soc.*, 2011, **133**, 14260-14263.

[101] M. Kuepfert, A. E. Cohen, O. Cullen, M. Weck, *Chem. Eur. J.*, 2018, **24**, 18648-18652.

[102] M. Glassner, M. Vergaelen, R. Hoogenboom, *Polym. Int.*, 2018, **67**, 32-45.

[103] B. Verbraeken, B. D. Monnery, K. Lava, R. Hoogenboom, *Eur. Polym. J.*, 2017, **88**, 451-469.

[104] A. F. Cardozo, E. Manoury, C. Julcour, J. F. Blanco, H. Delmas, F. Gayet, R. Poli, *ChemCatChem*, 2013, **5**, 1161-1169.

[105] T. Terashima, M. Ouchi, T. Ando, M. Sawamoto, *J. Polym. Sci. A Polym. Chem.*, 2011, **49**, 1061-1069.

[106] T. Terashima, M. Ouchi, T. Ando, M. Sawamoto, *J. Polym. Sci. A Polym. Chem.*, 2010, **48**, 373-379.

[107] M. Ouchi, T. Terashima, M. Sawamoto, *Chem. Rev.*, 2009, **109**, 4963-5050.

[108] T. Terashima, M. Kamigaito, K. Y. Baek, T. Ando, M. Sawamoto, *J. Am. Chem. Soc.*, 2003, **125**, 5288-5289.

[109] S. L. Canning, G. N. Smith, S. P. Armes, *Macromolecules*, 2016, **49**, 1985-2001.

[110] Y. Niu, Y. Lu, *J. Appl. Polym. Sci.*, 2022, **139**, article no. e52753.

[111] K. Shiraishi, S. I. Yusa, M. Ito, K. Nakai, M. Yokoyama, *Polymers*, 2017, **9**, article no. 710.

[112] S. Kramer, K. O. Kim, R. Zentel, *Macromol. Chem. Phys.*, 2017, **218**, article no. 1700113.

[113] X. Zhang, H. Dong, S. Fu, Z. Zhong, R. Zhuo, *Macromol. Rapid Commun.*, 2016, **37**, 993-997.

[114] J. He, Y. Xia, Y. Niu, D. Hu, X. Xia, Y. Lu, W. Xu, *J. Appl. Polym. Sci.*, 2017, **134**, article no. 44421.

[115] L. Tian, L. Yam, J. Wang, H. Tat, K. E. Uhrich, *J. Mater. Chem.*, 2004, **14**, 2317-2324.

[116] A. Pontes da Costa, D. R. Nunes, M. Tharaud, J. Oble, G. Poli, J. Rieger, *ChemCatChem*, 2017, **9**, 2167-2175.

[117] L. Zhang, K. Katapodi, T. P. Davis, C. Barner-Kowollik, M. H. Stenzel, *J. Polym. Sci. A Polym. Chem.*, 2006, **44**, 2177-2194.

[118] H. Wang, C. J. Abou-Fayssal, C. Fliedel, E. Manoury, R. Poli, *Polymers*, 2022, **14**, article no. 4937.

[119] X. Zhang, A. F. Cardozo, S. Chen, W. Zhang, C. Julcour, M. Lansalot, J. F. Blanco, F. Gayet, H. Delmas, B. Charleux, E. Manoury, F. D'Agosto, R. Poli, *Chem. Eur. J.*, 2014, **20**, 15505-15517.

[120] A. F. Cardozo, C. Julcour, L. Barthe, J. F. Blanco, S. Chen, F. Gayet, E. Manoury, X. Zhang, M. Lansalot, B. Charleux, F. D'Agosto, R. Poli, H. Delmas, *J. Catal.*, 2015, **324**, 1-8.

[121] S. Chen, F. Gayet, E. Manoury, A. Joumaa, M. Lansalot, F. D'Agosto, R. Poli, *Chem. Eur. J.*, 2016, **22**, 6302-6313.

[122] S. Chen, E. Manoury, F. Gayet, R. Poli, *Polymers*, 2016, **8**, article no. 26.

[123] A. Joumaa, S. Chen, S. Vincendeau, F. Gayet, R. Poli, E. Manoury, *Mol. Catal.*, 2017, **438**, 267-271.

[124] A. Joumaa, F. Gayet, E. J. Garcia-Suarez, J. Himmelstrup, A. Riisager, R. Poli, E. Manoury, *Polymers*, 2020, **12**, article no. 1107.

[125] H. Wang, L. Vendrame, C. Fliedel, S. Chen, F. Gayet, E. Manoury, X. Zhang, F. D'Agosto, M. Lansalot, R. Poli, *Macromolecules*, 2020, **53**, 2198-2208.

[126] H. Wang, L. Vendrame, C. Fliedel, S. Chen, F. Gayet, F. D'Agosto, M. Lansalot, E. Manoury, R. Poli, *Chem. Eur. J.*, 2021, **27**, 5205-5214.

[127] H. Wang, A. M. Fiore, C. Fliedel, E. Manoury, K. Philippot, M. M. Dell'Anna, P. Mastrorilli, R. Poli, *Nanoscale Adv.*, 2021, **3**, 2554-2566.

ACADÉMIE
DES SCIENCES
INSTITUT DE FRANCE

Comptes Rendus. Chimie
2024, Vol. 27, Special issue S1, p. 69-75
`https://doi.org/10.5802/crchim.292`

Research article

French/Nordic Special Issue on Materials and Coordination Chemistry

1,2,4-Triamino-5-nitrobenzene as air-stable aromatic polyamines for coordination chemistry

Simon Pascal[*, a, b], **Elena Zaborova**[a] and **Olivier Siri**[*, a]

[a] Aix-Marseille Univ, Centre Interdisciplinaire de Nanoscience de Marseille (CINaM), CNRS UMR 7325, Campus de Luminy, case 913, Marseille cedex 09 13288, France

[b] Nantes Université, CNRS, CEISAM, UMR 6230, Nantes, F-44000, France

E-mails: simon.pascal@cnrs.fr (S. Pascal), olivier.siri@univ-amu.fr (O. Siri)

Abstract. We report the synthesis and characterization of two nickel complexes **7** and **8** based on 1,2,4-triamino-5-nitrobenzene **6**. The formation of these compounds is observed from the same precursor, their stoichiometry depending on the nature of the solvent used for the crystallization. The key role of the nitro group in **6** is discussed, demonstrating its major impact on the stability and reactivity of the ligand. Each nickel complex could be characterized by single crystal X-ray analysis, highlighting the importance of the intramolecular H-bonding interactions on the stability of the complexes incorporating a monodentate aromatic amine-type ligand.

Keywords. Aromatic amines, Acac ligand, Metal coordination, X-ray structure, Nickel complexes.

Funding. CNRS, French "Ministère de la Recherche et de l'Enseignement Supérieur".

Manuscript received 31 August 2023, revised 9 November 2023, accepted 24 January 2024.

1. Introduction

Phenylenediamine derivatives **1–3** (Figure 1) are an important class of organic compounds with rich chemical and physical properties [1–3] and remarkable applications as precursors in color chemistry [4, 5]. Their coordinating ability has been less investigated because phenylenediamines do not form very stable complexes with bivalent metal ions [6]. This poor stability can be explained by the low basicity of the aromatic amines due to the delocalization of the lone pair of the nitrogen atom toward the p orbitals of the aromatic ring, decreasing the electron density on the nitrogen atom available for the bond formation with a metal center. The coordinating ability of aromatic diamines is also conditioned by the position of the nitrogen atoms on the aromatic ring (*ortho*, *meta* or *para*). *o*-Phenylenediamine ligand **1** coordinates either in a monodentate, chelating bidentate and bridging bidentate fashion in different dinuclear complexes, with possible oxidation of **1** depending on the metal center [7]. Studies of coordination compounds of **2** and **3** in solution and solid state are rare, possibly because these ligands can only coordinate one nitrogen atom to a metal center by means of a weak linkage [7], but also because of oxidation processes forming *p*-benzoquinonediimine ligands [8]. Falthouse and Hendrickson have reported a series of binuclear Cu(II) complexes in which **2** acts as a bridging bidentate ligand but the instability inherent to the phenylenediamines made it difficult to fully characterize the complexes [9].

---

[*] Corresponding authors

ISSN (electronic): 1878-1543

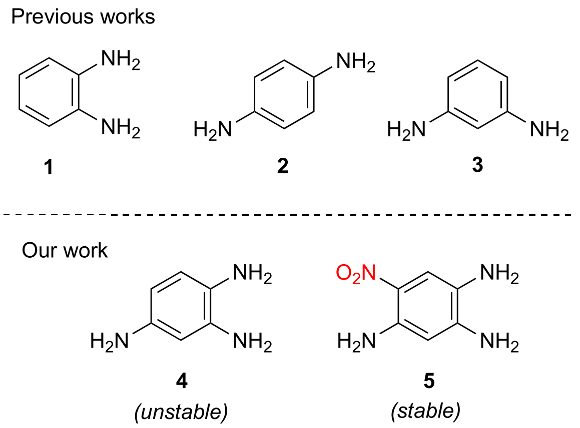

Figure 1. Molecules studies in previous works and our work.

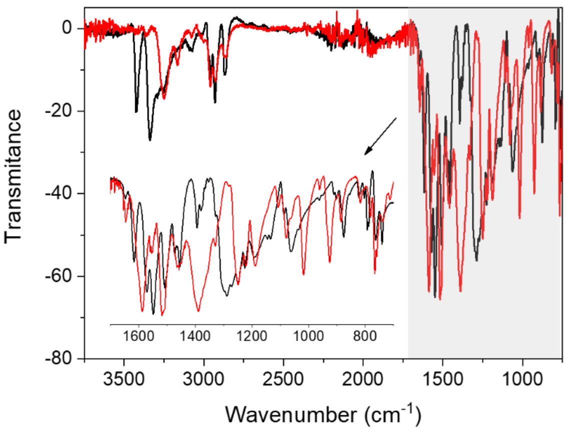

Figure 2. IR spectra of precursor **6** (black) and **BP** (red).

As an extension of these studies, it appeared very attractive to investigate 1,2,4-triaminobenzene **4**, which combines the structural elements of **1**, **2** and **3**, as ligand in coordination chemistry. However, bearing three amino functions, molecule **4** is highly unstable in air and can be easily oxidized, sacrificing its aromatic character in favor of a quinoidal form. To overcome this limitation, we envisaged the use of analogs of type **5** because the incorporation of an electron-withdrawing nitro group should strongly reduce the electron density and consequently prevent air oxidation of the molecule.

Herein, we wish to describe the synthesis and X-ray diffraction analysis of two new complexes (**7** and **8**), based on the air-stable 1,2,4-triamino-5-nitrobenzene derivative **6**. Importantly, the key role of the nitro group on the stability and the reactivity of the ligand is clearly emphasized, illustrating a further aspect to be considered in the coordination chemistry of aromatic amines.

2. Results and discussion

Precursor **6** was first prepared as recently reported in the literature [10]. Its metalation with Ni(acac)$_2$ in toluene at room temperature led to the formation of a beige precipitate (**BP**) that could be isolated by filtration (Scheme 1). IR analysis of this powder compared to the precursor **6** (Figure 2) revealed the appearance of strong bands around 1380, 1020 and 925 cm^{-1}, which could be attributed to carbon–oxygen and carbon–carbon bonds. In addition, the N–H vibrations above 3250 cm^{-1} for **6** are shifted for **BP** whereas the C–H vibrations (2900 cm^{-1}) are not affected. These observations are consistent with the coordination of one or several NH$_2$ group(s) to the nickel center and the presence of acetylacetonate (acac) moieties as ancillary ligand.

Next, we characterized **BP** in solution. Its ^{1}H NMR spectra in acetone-*d*$_6$ and methanol-*d*$_4$ are reported in Figure 3, showing signals of aliphatic chains of ligand **6** and peaks of the acac moiety in the 1–5 ppm region, together with the presence of square planar low-spin complexes (i.e., diamagnetic character). Unfortunately, further investigations by mass spectrometry could not afford usable data due to the presence of numerous peaks in both methanol and acetone solutions.

Interestingly, the UV–Vis spectroscopic data recorded in methanol and acetone revealed the same absorption profile for **BP** and **6** (Figure 4). This observation proved the instability of the complex **BP** in solution by means of a weak linkage, suggesting that **6** probably coordinates only one nitrogen atom to a metal center (unlike **1**) [7]. Crystallization attempts of **BP** in different solvents were then performed to gain insights into the nature of the coordination mode of **6**.

Single crystals suitable for structural determination could be obtained by slow evaporation of a

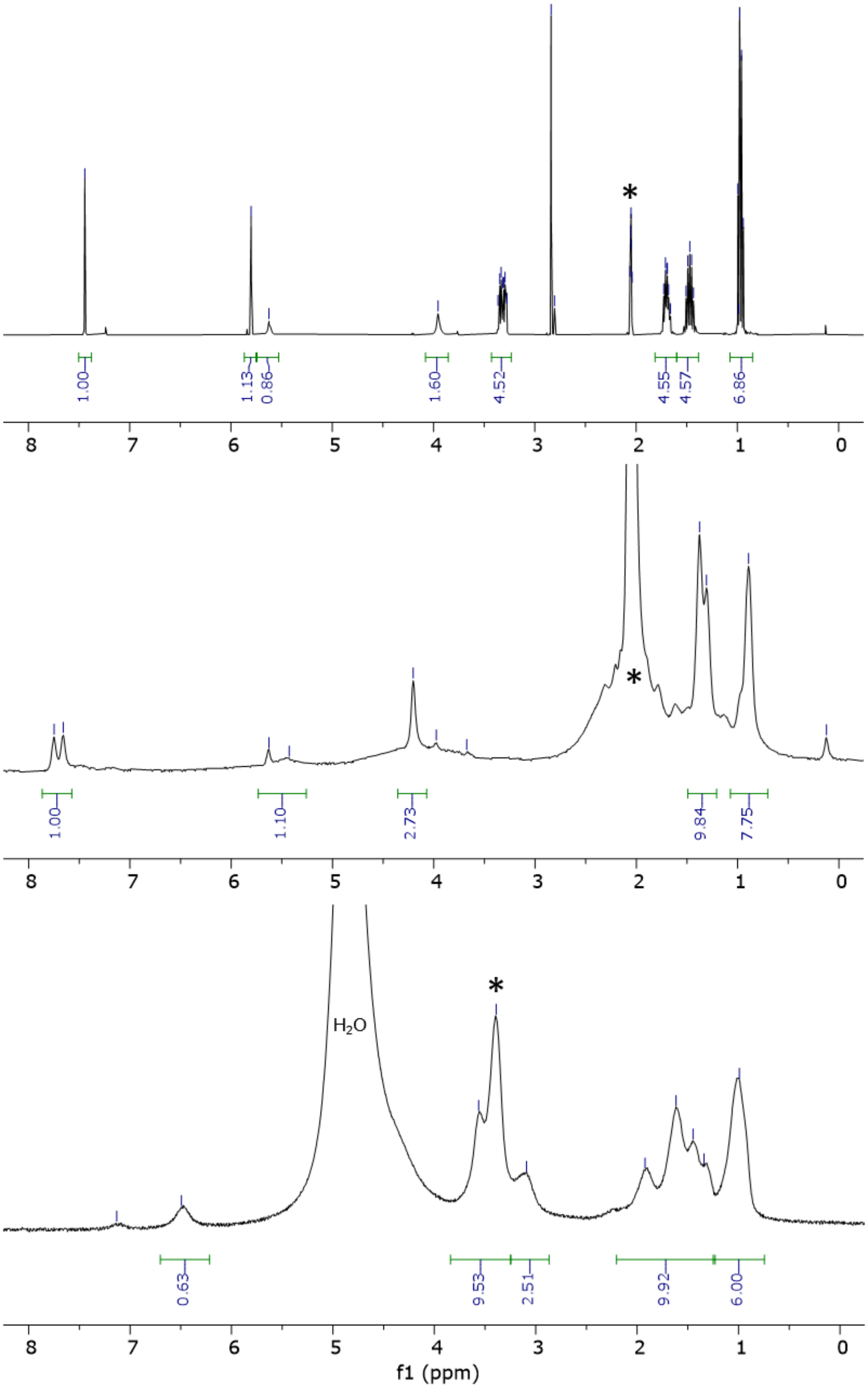

Figure 3. ^{1}H NMR (400 MHz) spectrum of **6** in acetone-d_6 (top) and **BP** in acetone-d_6 (middle) or methanol-d_4 (bottom). The solvent's residual peak is indicated with an asterisk.

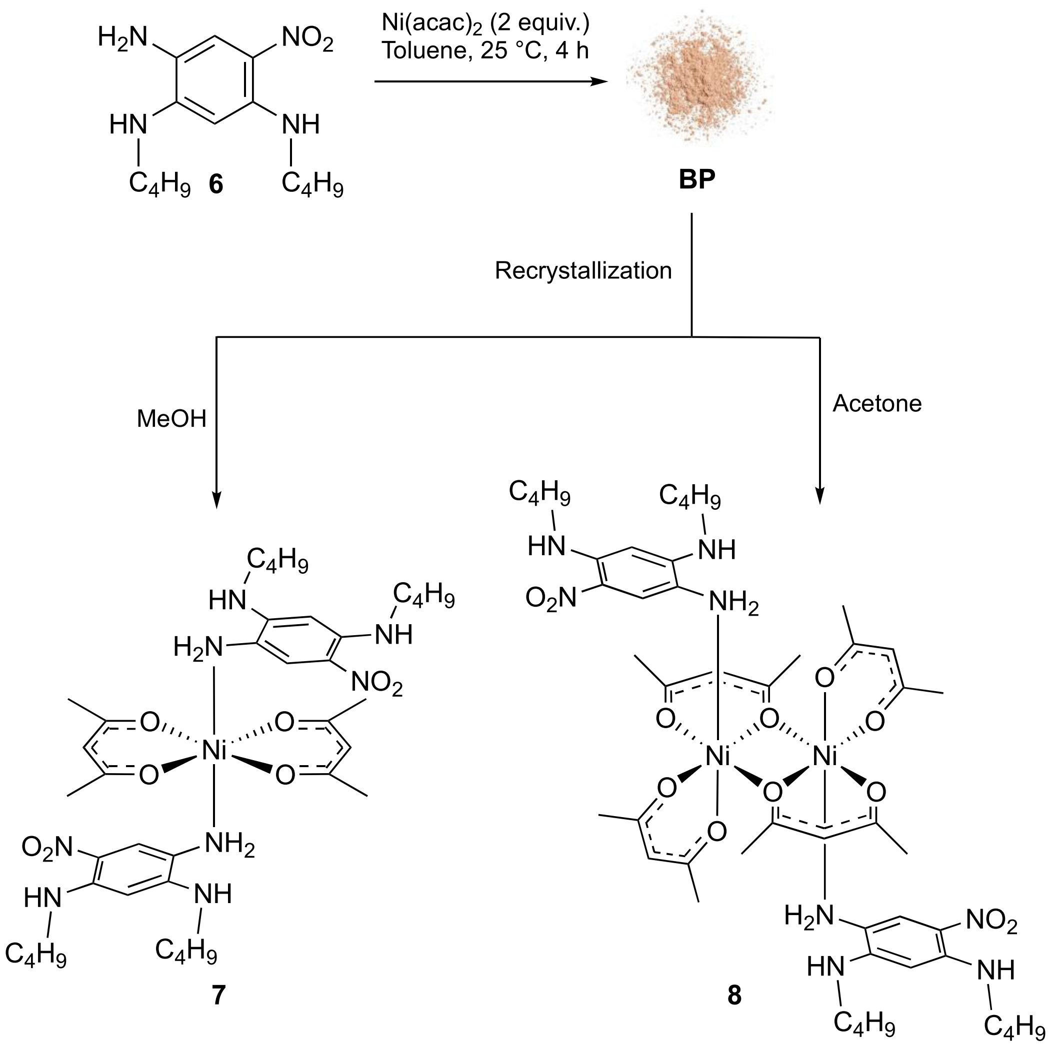

Scheme 1. Synthesis of complexes **7** and **8** (acac = acetylacetonate).

solution of **BP** in methanol. The X-ray diffraction analysis revealed the formation of a 1:2 (metal (Ni)/ligand (**6**)) complex **7** in which the nickel ion is found in an octahedral geometry and surrounded by two acac moieties coordinated in a planar fashion with respect to the metal center (Figure 5).

The Ni coordination sphere is completed by two additional ligands **6** in which a single amino group N(1) (and N′(1)) is coordinated. The monodentate coordination mode of **6** can be explained by a closer look at its molecular structure. Since only the amine function N(1) in *meta* position is not conjugated with the nitro group, it coordinates specifically with a metal center due to the availability of its lone pair, in contrast to the two other amine functions in *para* and *ortho* positions, which are highly conjugated with the nitro group. This hypothesis is confirmed experimentally by examination of the bond lengths between the nitrogen atoms of the amines and their corresponding aromatic carbons. The distance N(1)···C(Ar) of 1.437 Å clearly indicates a lack of conjugation and availability of

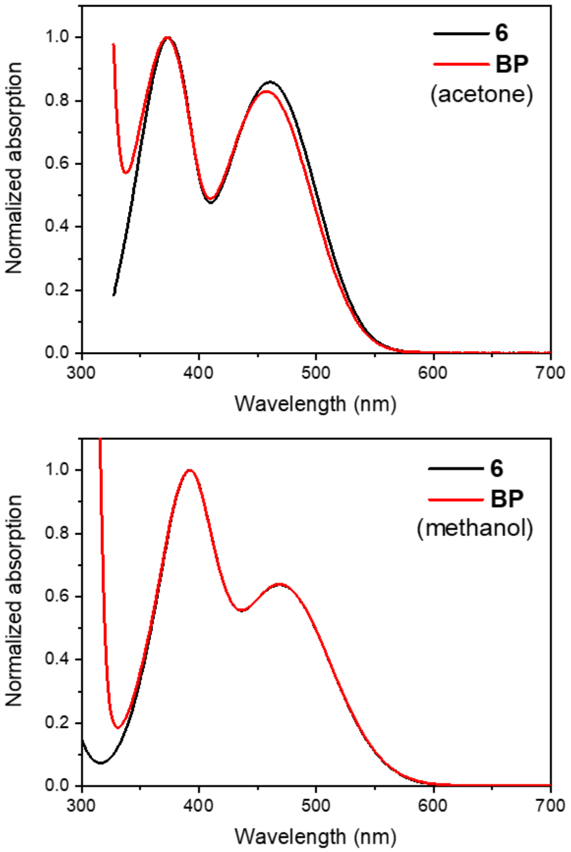

Figure 4. UV–visible absorption spectra of **6** and **BP** dissolved in acetone (top) or methanol (bottom).

the lone pair whereas the distances N(4)···C(Ar) and N(3)···C(Ar) are much shorter due to the conjugation with NO_2 (1.355 and 1.350 Å, respectively). A close examination of the hydrogen-bonding interactions in **7** revealed H-bonds involving N(1), N(2) and N(3) (as H-donor or H-acceptor) that clearly stabilize the molecular architecture in the solid state (Figure 5).

Remarkably, we observed that recrystallisation of **BP** in acetone instead of methanol led to the formation of complex **8** having the same octahedral geometry but a different stoichiometry (2:2 versus 1:2) (Figure 6). By analogy with **7**, ligand **6** is monodentate since only the amine function N(1), in *meta* position with respect to the nitro group, is coordinated to the Ni center owing to the availability of its lone pair. Numerous N–H···O bonding interactions involving N(1), N(2) and N(3), ranging from 1.976 to 2.251 Å, contribute to the stabilization of the complex.

The most striking feature of **8** is the coordination mode adopted by two of the six acac ligands, one of whose oxygen atoms coordinates to two metal centers, acting as a bridging ligand (Figure 6). As a result, the two Ni centers are in proximity (d(Ni···Ni) = 3.215 Å). To the best of our knowledge, this arrangement was only observed for modified acac in which electron-donating substituents in the 3-position of the pentane-2,4-dionato group were added [11].

3. Experimental section

3.1. *General*

Solvents (HPLC grade) and reagents were purchased from Sigma Aldrich and were used as received. Compound **6** was prepared according to published procedures [10]. NMR spectra were recorded on a JEOL ECS400 NMR spectrometer at room temperature. IR spectra were recorded on an Agilent Cary 630 FTIR equipped with an attenuated total reflectance (ATR) sampling. Suitable crystals were mounted on a Rigaku Oxford Diffraction SuperNova diffractometer and measured at 293 K at the Cu radiation (λ = 1.54184 Å). Data collection, reduction and multiscan ABSPACK correction were performed with CrysAlisPro (Rigaku Oxford Diffraction). Using Olex2, the structures were solved with the ShelXT structure solution program using Intrinsic Phasing and refined with ShelXL using least-square minimization.

3.2. *Synthesis of **BP***

$Ni(acac)_2$ (m = 204 g, 0.792 mmol, 2 equiv) was added to an orange–red solution of **6** (100 mg, 0.396 mmol, 1 equiv) in 20 ml of toluene under vigorous stirring. The reaction mixture was stirred at room temperature for 4 h. The precipitate obtained was then isolated by filtration on a sintered glass funnel and dried in vacuo to afford **BP** as a beige solid (m = 184 mg).

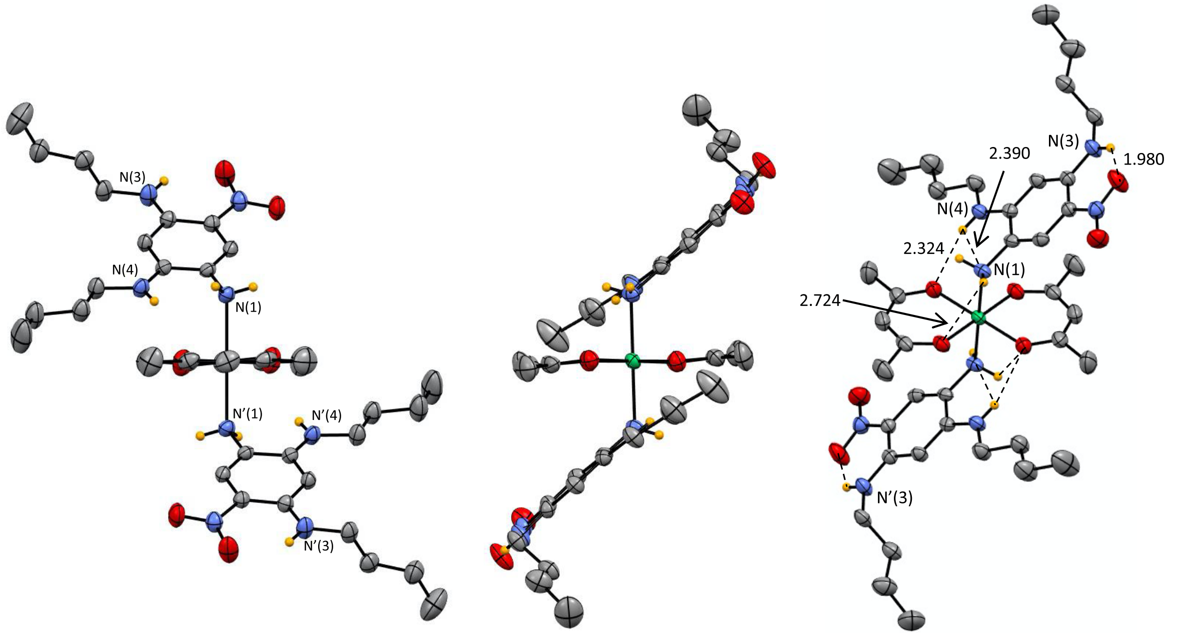

Figure 5. Single-crystal X-ray structure of **7** (recrystallization of **BP** in methanol). Selected bond lengths are indicated in Å.

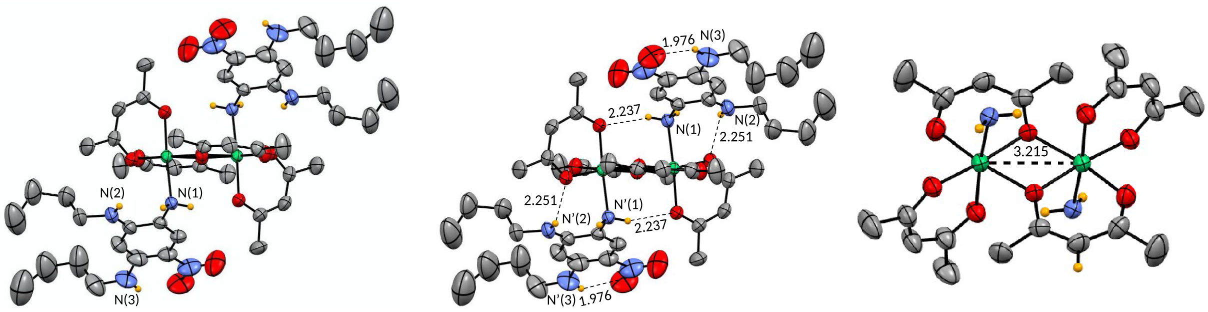

Figure 6. Single-crystal X-ray structure of **8** (recrystallization of **BP** in acetone). For the ortep view on the right, the aromatic amino ligand **6** is omitted for clarity except for the amino function coordinated to the Ni center. Selected bond lengths are indicated in Å.

4. Conclusion

We have prepared and crystallized novel nickel complexes **7** and **8** incorporating a new aromatic triamino ligand **6**. This ligand behaves in a monodentate fashion in coordination chemistry because of the presence of the electron-withdrawing group NO_2 that "deactivates" the two amine functions in *ortho* and *para* position. Although scarce in the literature due to a weak linkage inherent to the monodentate aromatic amines, complexes **7** and **8** could be fully characterized by X-ray diffraction, probably because of the presence of numerous intramolecular H-bonding interactions. The structure determination clearly established two different metal (Ni)/ligand (**6**) stoichiometry depending on the solvent used for crystallization, and the formation of a 1:2 complex (**7**) or a 2:2 adduct (**8**) could be observed in methanol and acetone, respectively. This work might open new perspectives in coordination chemistry of aromatic polyamines by exploiting the NH_2/NO_2 balance to tune the reactivity of the ligand and/or the stability of the metal complexes.

Declaration of interests

The authors do not work for, advise, own shares in, or receive funds from any organization that could benefit from this article, and have declared no affiliations other than their research organizations.

Funding

This work was supported by the CNRS and the French "Ministère de la Recherche et de l'Enseignement Supérieur."

Acknowledgements

The authors thank M. Giorgi (Spectropole, Marseille) for the X-ray diffraction studies.

Supplementary data

Supporting information for this article is available on the journal's website under https://doi.org/10.5802/crchim.292 or from the author.

References

[1] G. Cohen, A. Parola, G. H. Parsons, *Chem. Rev.*, 1973, **73**, 141-161.

[2] H. Masuhara, N. Mataga, *Acc. Chem. Res.*, 1981, **14**, 312-318.

[3] G. J. Kavarnos, N. J. Turro, *Chem. Rev.*, 1986, **86**, 401-449.

[4] N. M. Aljamali, M. A. Abdulzahra, M. S. Mohamad, W. Hashim, Y. Almuhana, M. A. Hadi, *Int. J. Innov. Sci. Eng.*, 2019, **9**, 9-23, https://ijise.in/abstract.php?id=70.

[5] M. J. Shah, W. S. Tolgyesi, A. D. Britt, *J. Soc. Cosmet. Chem.*, 1972, **23**, 853-861, https://citeseerx.ist.psu.edu/document?repid=rep1&type=pdf&doi=a8ef1f7735353d1ed60015f4b54ffca974385f12.

[6] F. J. Andres-Ordax, J. M. Merino, *Bull. Soc. Chim. France*, 1980, 1-61.

[7] A. Mederos, S. Domínguez, R. Hernández-Molina, J. N. Sanchiz, F. Brito, *Coord. Chem. Rev.*, 1999, **193–195**, 913-939.

[8] S. Pascal, O. Siri, *Coord. Chem. Rev.*, 2017, **350**, 178-195.

[9] T. R. Felthouse, D. N. Hendrickon, *Inorg. Chem.*, 1978, **17**, 2636-2648.

[10] T. Munteanu, V. Mazan, M. Elhabiri, C. Benbouziyane, G. Canard, D. Jacquemin, O. Siri, S. Pascal, *Org. Lett.*, 2023, **25**, 3886-3891.

[11] A. Döhring, R. Goddard, P. W. Jolly, C. Krüger, V. R. Polyakov, *Inorg. Chem.*, 1997, **36**, 177-183.

ACADÉMIE
DES SCIENCES
INSTITUT DE FRANCE

Comptes Rendus. Chimie
2024, Vol. 27, Special issue S1, p. 77-89
`https://doi.org/10.5802/crchim.307`

Research article

French/Nordic Special Issue on Materials and Coordination Chemistry

(Pyridin-2-ylmethyl)porphyrins: synthesis, characterization and C–N oxidative fusion attempts

Mathieu Berthelot [a], Julie Echaubard [a], Asmae Bousfiha [a] and Charles H. Devillers *, [a]

[a] Institut de Chimie Moléculaire de l'Université de Bourgogne, UMR CNRS 6302, Université de Bourgogne, Faculté des Sciences Mirande, Aile B-Chimie, 9 avenue Alain Savary - BP 47870, 21078 DIJON Cedex, France

E-mail: charles.devillers@u-bourgogne.fr (C. H. Devillers)

Abstract. A new route for the synthesis of *meso*-(pyridin-2-ylmethyl)porphyrins was developed, based on the nucleophilic attack of (pyridin-2-ylmethyl)lithium reagent on a porphyrin bearing one free *meso* position. The latter is then metalated with Zn(II) and Ni(II). These products were characterized by NMR spectroscopy, UV–visible absorption spectroscopy, mass spectrometry and electrochemistry. Attempts to generate the C–N-fused compound by oxidation (new bond between the nitrogen of the pyridinyl substituent and the β-pyrrolic position of the porphyrin) are also described.

Keywords. Pyridinylporphyrin, Pyridine, Oxidative C–N fusion, π-extension, Cyclic voltammetry, NMR spectroscopy.

Funding. Université de Bourgogne, Université de Bourgogne Franche-Comté, CNRS (Centre National de la Recherche Scientifique), Conseil Régional de Bourgogne, Fonds Européen de Développement Régional (FEDER), Agence Nationale de la Recherche (ANR-15-CE28-0018-01), Conseil Régional de Bourgogne Franche-Comté and French "Investissement d'Avenir" program (ANR-15-IDEX-03).

Manuscript received 14 October 2023, revised 11 January 2024, accepted 15 March 2024.

1. Introduction

Pyridinyl-based porphyrins are quite rare in the literature since their synthesis is cumbersome. Possible applications for these derivatives have already been reported such as photo-electrochemistry [1], light-harvesting charge separation systems [2,3], supramolecular chemistry [4–13], catalysis [9,14], fast energy transfer [12,15], molecular assembly on Au(III) [16] and dendrimer formation [17]. The full development of these pyridinylporphyrin derivatives may be restricted due to these synthetic limitations. The main issue stems from the first condensation steps with pyridinyl-based aldehyde and pyrrole, pyridinyl-based dipyrromethane with aldehydes or dipyrromethane with pyridinyl-based aldehydes, which results in low yields. Indeed, the pyridinyl fragment is able to trap protons from the Brønsted acid catalyst or deactivate the Lewis Acid catalyst in the common Adler and Longo or Lindsey condensation reactions. In our group, we have been interested in the exploitation of these pyridinyl-based porphyrins for molecular recognition of phenol derivatives [18] but also as precursors of C–N-fused cationic compounds obtained by oxidative pathway [19,20]. For this latter purpose, mercaptopyridinylporphyrins have been successfully fused and the original physicochemical properties of the C–N-fused porphyrins have been explored in details (Previous work, Scheme 1). To extend the scope of this

---

*Corresponding author

C–N oxidative fusion reaction, we wanted to replace the sulfur atom by a carbon atom and investigate if this reaction could work (This work, Scheme 1).

This manuscript describes the synthesis and characterization of (pyridin-2-ylmethyl)porphyrin **H_2-7** (Scheme 3) as well as the synthesis of its respective Zn(II) and Ni(II) complexes **Zn-7** and **Ni-7**. Preliminary C–N oxidative fusion attempts are also described.

2. Results and discussion

2.1. *Synthesis of (pyridin-2-ylmethyl)porphyrins* **2**, **Zn-2** *and* **Ni-2**

Our initial objective was to synthesize 5,10,15,20-tetrakis(pyridin-2-ylmethyl)porphyrin **H_2-1** by condensation of pyrrole with aldehyde **2** produced by oxidation of commercially available 2-(2-hydroxyethyl)pyridine (**3**, Scheme 2).

Two experimental conditions were tested for the aldehyde **2** synthesis: Swern conditions, using oxalyl chloride in DMSO and oxidation by a cerium(IV)-based oxidant [21,22]. Despite several attempts with these two oxidants, the oxidation step of the alcohol function systematically failed. The targeted aldehyde **2** may be in equilibrium with its enol form [23], which could explain the difficulties in isolating/forming this aldehyde. Given these disappointing results, an alternative route was developed. The latter was based on the synthesis of a porphyrin monofunctionalized at the *meso* position with 2-methylpyridine (Scheme 3).

The first step consisted in the preparation of the (pyridin-2-ylmethyl)lithium (**5**) reagent by addition of *n*-butyllithium on 2-picoline (**6**). This orange solution was then added in excess to the tri-*meso*-arylporphyrin **H_2-4** following a protocol similar to the one previously described by Senge and colleagues for the phenylation of porphyrins [24]. Under these conditions, the original (pyridin-2-ylmethyl)porphyrin **H_2-7** was isolated in 63% yield (Scheme 3). The corresponding Zn(II) and Ni(II) complexes (**Zn-7** and **Ni-7**, respectively) were also synthesized in good yields by standard metalation procedure (see experimental part) using the respective acetate salts [25]. It should be noted that another report from Barbe and coworkers describes the synthesis of a pyridin-2-ylmethylporphyrin (**Zn-14**, Scheme 4) [26]. This synthesis was based on the Suzuki cross-coupling of 5-bromo-2-chloromethylpyridine (**13**) (synthesized in two steps from bromopicolinaldehyde (**11**), Scheme 4) with zinc(II) *meso*-substituted dioxoborolaneporphyrin **Zn-10** (synthesized in three steps from the 5,10,15-trimesitylporphyrin). According to these authors and contrary to their expectations, only the chlorinated carbon atom of **13** was coupled with the porphyrin and not the brominated one.

Thus our proposed synthesis is more straightforward since it involves only two steps for the synthesis of **H_2-7** starting from the tri-*meso*-arylporphyrin **H_2-4**.

2.2. *Characterization of (pyridin-2-ylmethyl)porphyrins* **H_2-7**, **Zn-7** *and* **Ni-7**

2.2.1. *NMR characterization of (pyridin-2-ylmethyl)porphyrins* **H_2-7**, **Zn-7** *and* **Ni-7**

A focus on the aromatic part of the ^{1}H NMR spectra of compounds **6**, **H_2-7**, **Zn-7** and **Ni-7** is presented in Figure 1. Noteworthy, for **Zn-7**, $CDCl_3$ had to be replaced by $(CD_3)_2CO$ due to solubility problems. In addition, one drop of pyridine-d_5 was used to prevent the formation of coordination polymers upon coordination of the pyridinyl nitrogen atom onto the metallic center of another **Zn-7** porphyrin. 2-Picoline **6** is characterized by a singlet at 2.33 ppm for the methyl group and four multiplets between 6.84 ppm and 8.28 ppm. The ^{1}H NMR spectra of **H_2-7**, **Zn-7** and **Ni-7** show similar chemical shifts for the pyridinyl moiety ($6.73 < \delta < 7.32$ ppm) except for the α proton doublet which appears between 8.59 and 8.75 ppm. For comparison purpose, the α proton doublet of **6** appears at a slightly lower chemical shift (8.28 ppm). Thus the porphyrin ring has little influence on the chemical shifts of the pyridinyl moiety contrary to what is observed for the $-CH_2-$ spacer for which the methylene singlets of **H_2-7**, **Zn-7** and **Ni-7** are observed between 6.21 and 6.70 ppm, a much higher value as compared to 2.33 ppm for **6**. The same range of chemical shift was observed by Barbe and coworkers with the free-base analogue of **Zn-14** [26], where the methylene bridge appeared at 6.59 ppm. This behavior is typically observed for protons that are lying outside the shielding cone of the porphyrin. The β-pyrrolic protons of **H_2-7**, **Zn-7** and **Ni-7** are located between

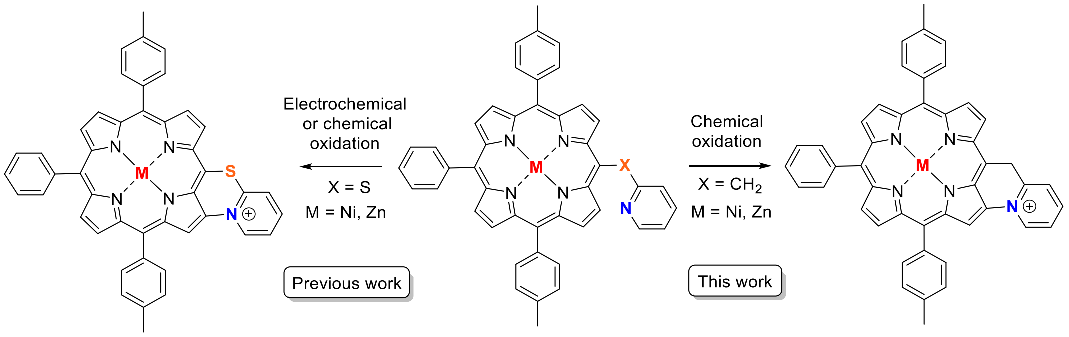

Scheme 1. Previous work: C–N oxidative fusion with a mercaptopyridinylporphyrin; This work: planned target obtained after C–N oxidative fusion of a pyridinylmethylporphyrin precursor.

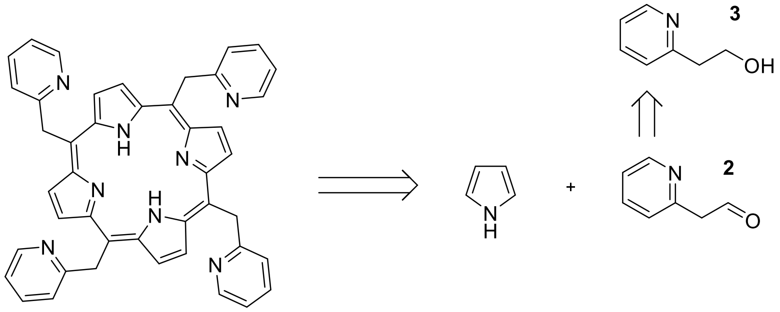

H$_2$-1

Scheme 2. Attempted synthesis of 5,10,15,20-tetrakis(pyridin-2-ylmethyl)porphyrin **H$_2$-1**.

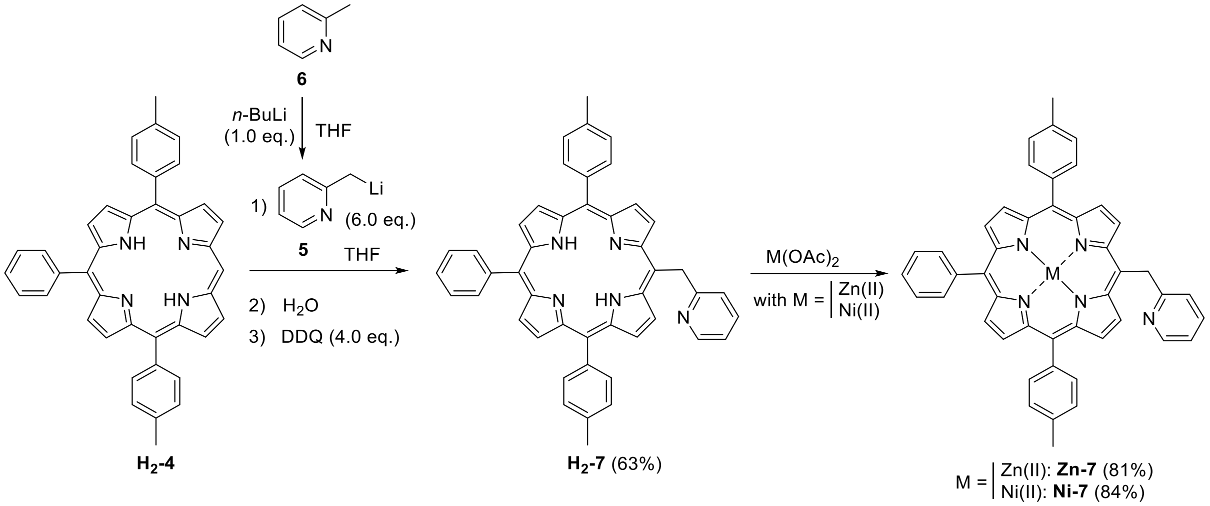

Scheme 3. Synthesis of (pyridin-2-ylmethyl)porphyrin **H$_2$-7** and the corresponding Zn(II) and Ni(II) complexes **Zn-7** and **Ni-7**.

8.70 and 9.74 ppm. The more deshielded β-pyrrolic doublet appears between 9.32 and 9.74 ppm and is attributed to the protons that are closest to the methylpyridinyl substituent.

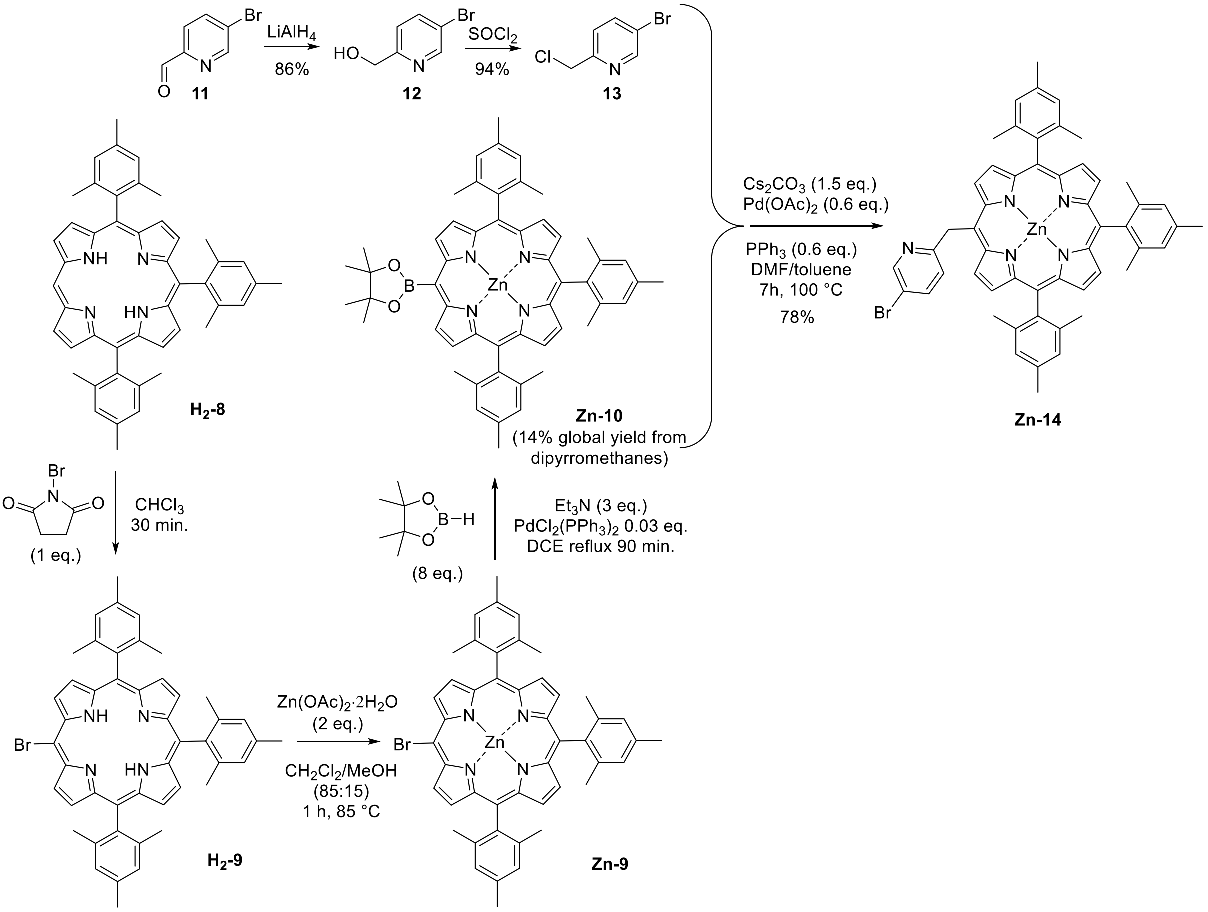

Scheme 4. Synthesis of pyridin-2-ylporphyrin **Zn-14** as described by Barbe and coworkers [26].

2.2.2. *UV–visible absorption spectroscopy of* $\mathbf{H_2}$**-7**, **Zn-7** *and* **Ni-7**

UV–visible absorption spectra of $\mathbf{H_2}$**-7**, **Zn-7** and **Ni-7** are presented in Figure 2. Porphyrin $\mathbf{H_2}$**-7** exhibits a Soret band at 419 nm and four less intense Q bands at 516, 552, 592 and 648 nm, as expected for a free base porphyrin. The corresponding nickel(II) complex **Ni-7** shows a 3-nm hypsochromic shift of the Soret band as compared to $\mathbf{H_2}$**-7**. Indeed, while the metallic cation accepts the lone-pair electrons of the nitrogen atoms of the porphyrin ring, its electrons are donated to the macrocycle. The resulting flow of electrons of the delocalized π-system increases the energy available for electron transition, leading to the blueshift observed for the Soret band of **Ni-7** [27]. The number of Q bands for this derivative is reduced to one as shown by comparison with the UV–visible absorption spectrum of $\mathbf{H_2}$**-7**, in agreement with the enhanced symmetry of the porphyrin induced by the metalation.

In the specific case of **Zn-7**, the CH_2Cl_2 solvent had to be replaced by DMF to improve the solubility of the porphyrin by preventing the formation of the coordination polymers. The Soret band is observed at 427 nm and only two Q bands are seen at 561 and 601 nm, for symmetry reasons.

2.2.3. *Electrochemical characterization of* $\mathbf{H_2}$**-7**, **Zn-7** *and* **Ni-7**

All potential values reported in this manuscript are vs. the saturated KCl calomel electrode (SCE), unless otherwise mentioned. The cyclic voltammogram of **Ni-7** is presented in Figure 3 (top black curve). The first fully irreversible oxidation takes place at $E_{\mathrm{pa}}(\mathrm{O1}) = 0.85$ V which is less positive than the first

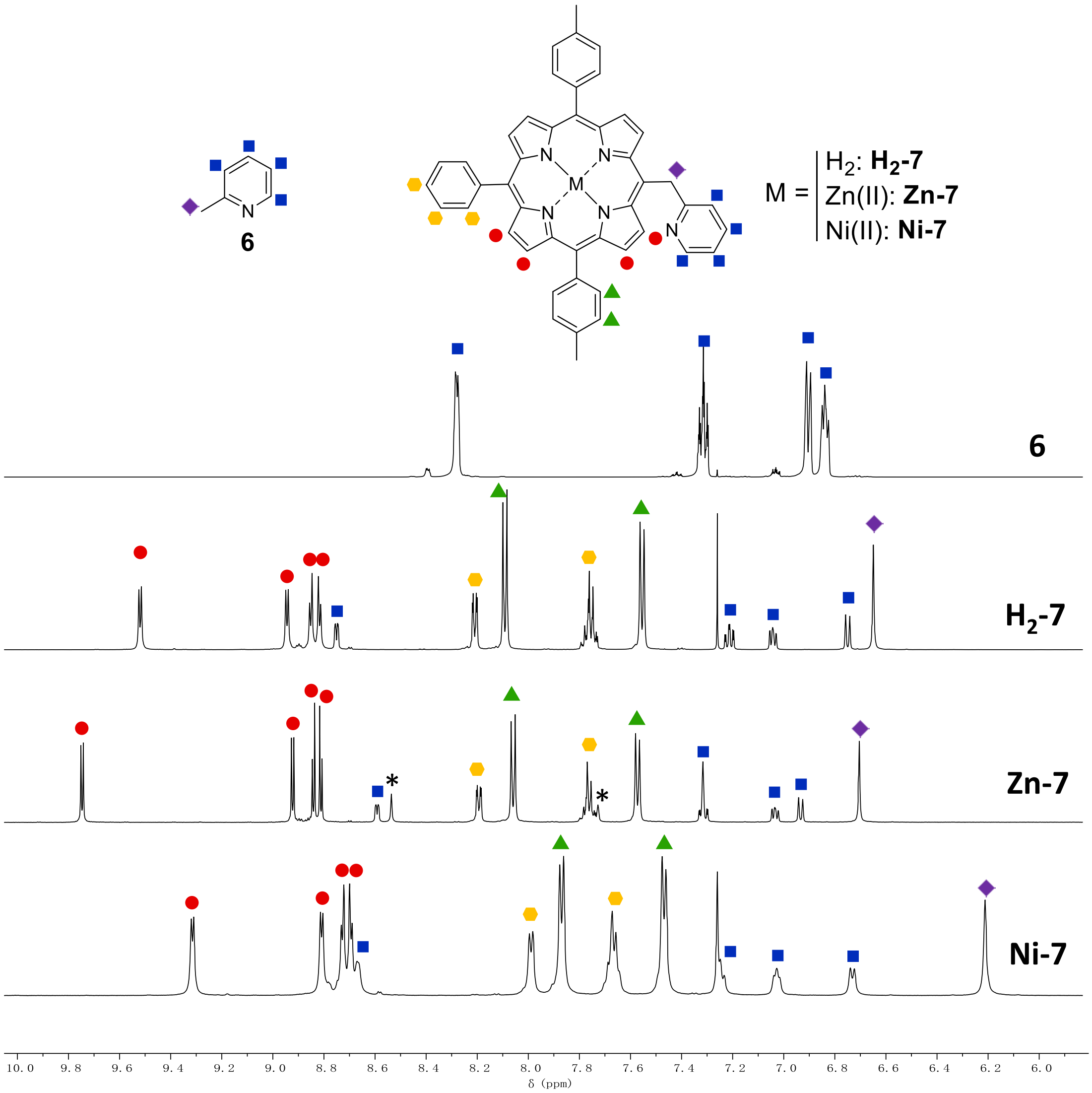

Figure 1. Partial ^{1}H NMR spectra of **6**, **H_2-7**, **Zn-7** and **Ni-7** ($CDCl_3$ ($(CD_3)_2CO$ + one drop of pyridine-d_5 for **Zn-7**), 500 MHz, 298 K). The asterisk $*$ indicates not fully deuterated pyridine signals in the ^{1}NMR spectrum of **Zn-7**. Small signals observed on the ^{1}NMR spectrum of **6** correspond to unknown impurities that are present in the commercial reagent.

oxidation potentials of Ni(II) porphyrins functionalized with 2-mercaptopyridine ($E_{pa} \approx 1.10$ V) [19]. This behavior agrees with the donor inductive effect of the –CH_2– group, compared to the sulfur atom involved in a thioether function. This irreversibility which follows the porphyrin cation radical formation might also be a good indication that the C–N fusion reaction takes place. Two other reversible oxidation peaks are observed at $E_{pa}(O2) = 0.98$ V and $E_{pa}(O3) = 1.29$ V. Only one poorly reversible reduction peak is seen at $E_{pc}(R1) = -1.56$ V.

The zinc(II) complex **Zn-7** exhibits very low solubility in CH_2Cl_2. The latter probably arises from coordination polymers that may be formed by coordination of the pyridinyl moiety onto the zinc(II) atom of another porphyrin [3,10,11,17]. This behavior has been already experienced by us with the zinc(II) complexes substituted by one or two

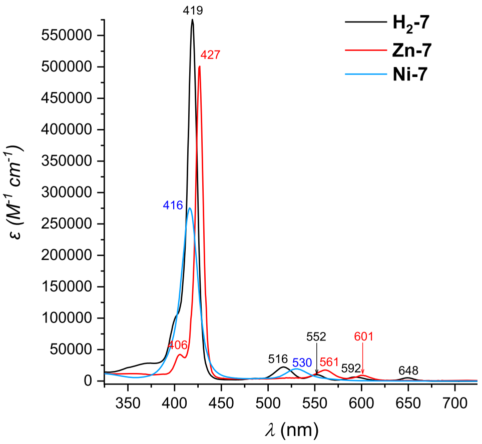

Figure 2. UV–visible absorption spectra of $\mathbf{H_2}$**-7** (black curve), **Zn-7** (red-curve) and **Ni-7** (blue curve) in CH_2Cl_2 or for **Zn-7** in DMF.

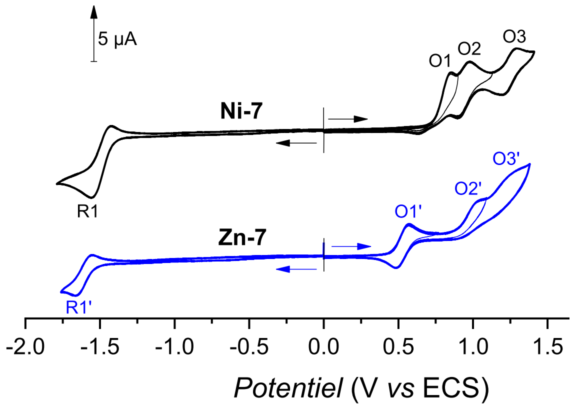

Figure 3. Cyclic voltammograms of **Ni-7** (top, black curve) and **Zn-7** (bottom, blue curve). Conditions: $C = 10^{-3}$ M, CH_2Cl_2 0.1 M $TBAPF_6$, WE = Pt Ø = 2 mm, $v = 100$ mV·s^{-1}. For solubility reason, 1.0 equiv of pyridine has been added to the solution containing **Zn-7**.

mercaptopyridinyl fragment(s) [20]. The addition of 1.0 equiv of pyridine to a solution of **Zn-7** in CH_2Cl_2 was supposed to break the coordination polymers. Indeed, all the porphyrin became soluble which supported our initial hypothesis. The first oxidation wave is much more reversible than for **Ni-7** ($E_{pa}(O1') = 0.57$ V, $E_{1/2} = 0.53$ V, $\Delta E_p = 80$ mV). Two other irreversible oxidation peaks are observed at ca. $E_{pa}(O2') = 1.05$ V and ($E_{pa}(O3') = 1.27$ V. The reduction peak R1′ is almost reversible and is observed at $E_{pc}(R1') = -1.66$ V.

2.3. *Oxidative C–N fusion attempts*

Following our previous work on the oxidative C–N fusion of pyri(mi)dine-based porphyrins (see Scheme 1 and Refs. [19,20,28]), fusion tests have been performed in CH_2Cl_2 on **Ni-7** and **Zn-7** with PIFA ((bis(trifluoroacetoxy)iodo)benzene), a two-electron acceptor. In principle, if the C–N oxidative fusion reaction of 2-picoline on the porphyrin nucleus occurs, the use of a base to neutralize the protons released by the C–N coupling reaction is necessary. Indeed, unlike 2-mercaptopyridine whose pK_a is very low (−1.07) [29,30], 2-picoline has a pK_a of 5.96 [31] which is higher than that of trifluoroacetate ions ($pK_a = 0.23$). Thus, the trifluoroacetate anions released during the reduction of PIFA are no longer sufficiently basic to capture the protons released during the formation of the C–N bond. A first reaction test between **Ni-7** and PIFA was carried out in CH_2Cl_2 in the presence of potassium carbonate as a base. After reacting for 1 h with 1.0 equiv of PIFA, a brown product, more polar than compound **Ni-7**, was observed on a TLC plate (SiO_2, CH_2Cl_2). Then 0.2 and 0.8 equiv of PIFA were added at one-hour intervals. One hour after the last addition of oxidant, the stirring was stopped because no further development was observed. 2,6-Lutidine, whose pK_a is 6.72 [31], is perfectly miscible under our experimental conditions, unlike potassium carbonate which mainly remains as a precipitate. This organic base was therefore chosen for a new C–N fusion test of 2-picoline on the porphyrin core. Thus, the reaction between **Ni-7** and PIFA, in the presence of 2.0 equiv of 2,6-lutidine, in dichloromethane, was monitored by TLC (SiO_2, CH_2Cl_2), in order to determine the amount of oxidant necessary for the consumption of the starting product. After 23 h of reaction at room temperature and addition of 2.0 equiv of PIFA, the crude reaction no longer seemed to evolve. The latter contained **Ni-7** and a more polar brown product which did not migrate onto the TLC plate. MALDI-TOF mass spectrometry analysis of the crude reaction shows a peak at $m/z = 712.1$, attributed to the C–N fusion product ($m/z = 712.2026$), a peak at $m/z = 713.1$ corresponding to **Ni-7** and a more intense peak at $m/z = 726.1$ corresponding to the exact mass of compound **Ni-7** to which 13 mass units are added. This mass may be related to the fusion of 2-picoline with porphyrin and formation of a carbonyl on the CH_2 bridge (Figure 4).

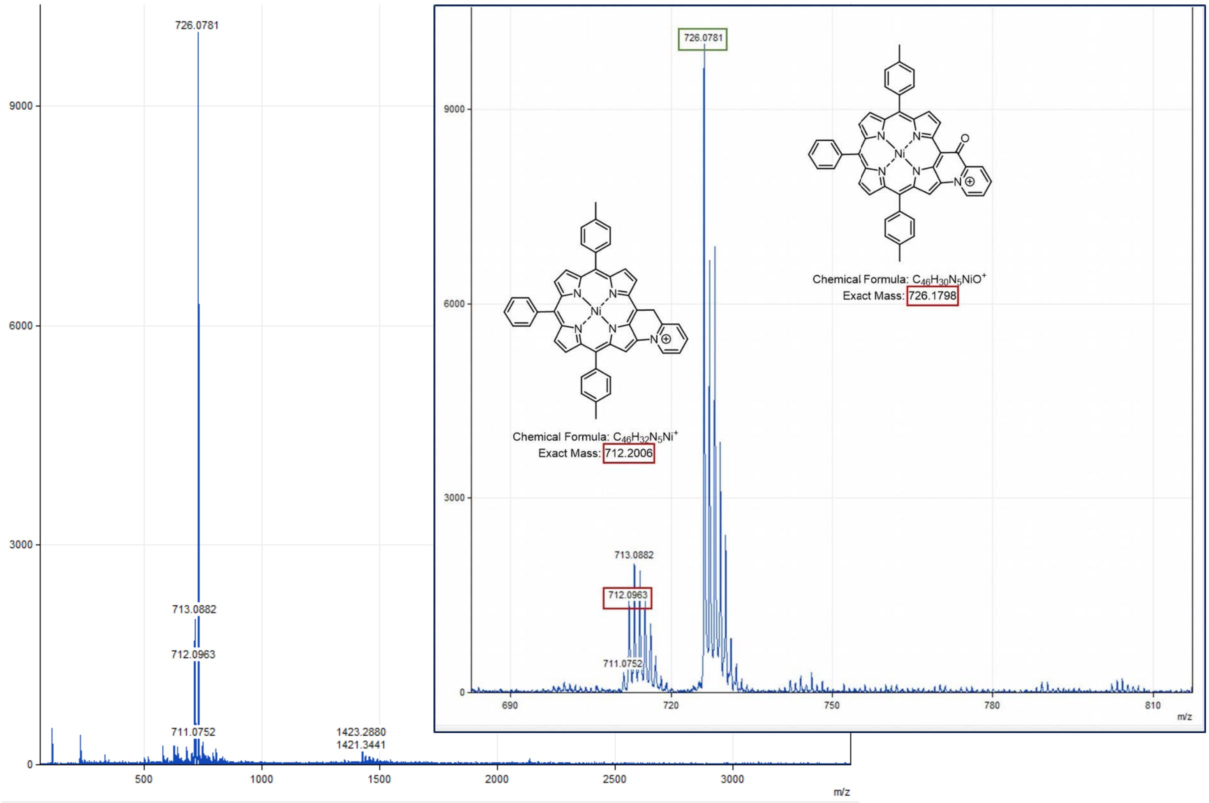

Figure 4. MALDI-TOF spectrum (global and zoom views) obtained from the crude solution resulting from the addition of 2.0 equiv of 2,6-dimethylpyridine and 2.0 equiv of PIFA on **Ni-7**, after stirring for 23 h in CH_2Cl_2.

Two chemical fusion tests were also carried out on **Zn-7** with PIFA at room temperature in dichloromethane, one in the presence of 2.0 equiv of potassium carbonate, the other in the presence of 2.0 equiv of 2,6-lutidine. When the reaction is carried out in the presence of potassium carbonate as base, 1.8 equiv (first 1.0 equiv, then 1.5 h of stirring, then 0.8 additional equiv added in 4 times at one-hour intervals) of PIFA are necessary to consume all the precursor. Under these conditions, two products are formed, one being more polar (purple/pink) and the other less polar (dark purple) than the product **Zn-7** (purple). The ^{1}H NMR analysis of the raw reaction product carried out in acetone-d_6 in the presence of a drop of pyridine-d_5 did not give any information (poorly resolved signals). An ESI mass analysis was performed to obtain more information, but none of the observed peaks could be assigned. The oxidation of compound **Zn-7** in the presence of 2,6-lutidine only leads to the formation of a single dark purple product, more polar than the precursor to be fused. In this case, the use of a total of 2.2 equiv of PIFA did not allow all the starting material to be consumed, even after 23 h of reaction. MALDI-TOF analysis of the crude reaction (Figure 5) shows a peak at an m/z value of 719.1 corresponding to the initial product (m/z theoretical = 719.2027) but also at m/z = 718.1 (C–N coupling product, theoretical m/z = 718.1944) and 717.1 (loss of an additional proton), all three minor in terms of intensity compared to a peak at 732.1, whose m/z ratio corresponds to the mass of **Zn-7** to which 13 units of mass are added. The latter may, as in the case of the oxidation of derivative **Ni-7**, correspond to the fusion product with the formation of a carbonyl function on the bridging carbon atom. Finally, an isotopic cluster between m/z = 1435 and m/z = 1445 is also observed. It could be assigned to the formation of a dimer of unknown structure.

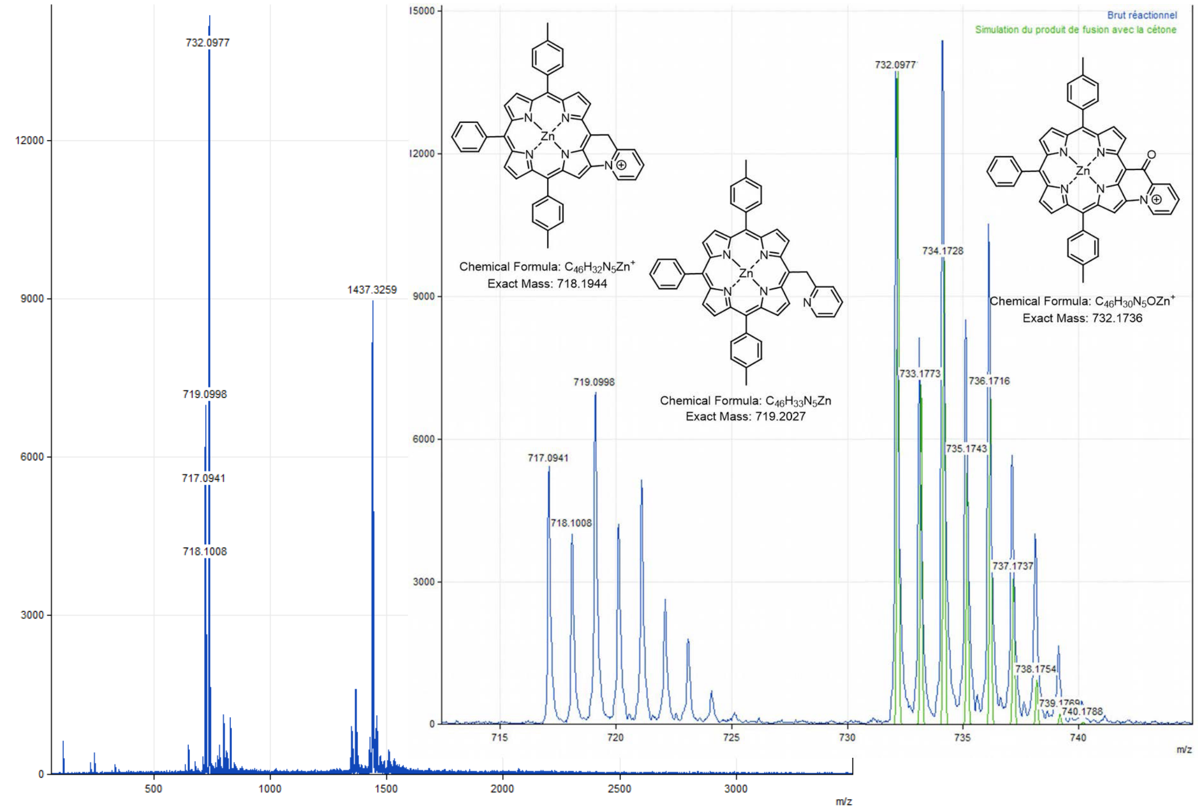

Figure 5. MALDI-TOF spectrum (global and zoom views) obtained from the crude solution resulting from the addition of 2.0 equiv of 2,6-dimethylpyridine and 2.0 equiv of PIFA on **Zn-7**, after stirring for 23 h in CH_2Cl_2.

3. Experimental section

3.1. *Reagents and instrumentation*

Unless otherwise noted, all reactions were carried out without protection from air. CH_2Cl_2, MeCN, THF were dried over alumina cartridges using a solvent purification system PureSolv PS-MD-5 model from Innovative Technology and kept under argon. The following reagents were used: *n*-BuLi (1.6 M in hexane, Acros Organics), 2-picoline (98%, Acros Organics), 2,3-dichloro-5,6-dicyano-p-benzoquinone (DDQ, 98%, Sigma-Aldrich), [bis(trifluoroacetoxy)iodo]benzene ((PIFA), 98%, Acros Organics), 2,6-lutidine (99%, Sigma-Aldrich), pyridine (99%, Acros Organics), K_2CO_3 (99%, anhydrous, Alfa Aesar), $Zn(OAc)_2{\cdot}2H_2O$ (99.5%, Acros Organics), $Ni(OAc)_2{\cdot}4H_2O$ (99%, Alfa Aesar), 10-phenyl-5,15-di-p-tolylporphyrin **H_2-4** was synthesized as reported in [32]. Our data (^1H NMR, ^{13}C NMR, UV–Visible absorption, and MALDI-TOF mass spectrum) were consistent with those described in Ref. [32]. Tetra-*n*-butylammonium hexafluorophosphate was synthesized by mixing stoichiometric amounts of HPF_6 (60% in water, Acros Organics) and tetra-*n*-butylammonium hydroxide (40% in water, Alfa Aesar). The resulting solution was filtrated on a Büchner filter under vacuum and the white crystals were collected. These crystals were recrystallized twice in EtOH and then dried in a stove at 110 °C for 48 h.

^1H, ^{13}C NMR spectra were recorded either on a Bruker Avance 400, on a Bruker Avance 500 or on a Bruker Avance 600 III HD spectrometer. Chemical shifts are expressed in parts per million (ppm) from the residual non-deuterated solvent signal [33]. J values are expressed in Hz.

High-resolution mass spectra (HRMS) were recorded either on a Thermo LTQ Orbitrap XL apparatus equipped with an ESI source or on a Bruker UltraflexII LRF 2000 MALDI-TOF mass spectrometer (matrix: dithranol).

UV–visible absorption spectra were recorded on a VARIAN Cary 50 UV–Visible spectrophotometer using quartz cells.

All electrochemical manipulations were performed using Schlenk techniques in an atmosphere of dry oxygen-free argon at room temperature ($T = 20$ °C ± 3 °C). The supporting electrolyte was degassed under vacuum before use and then dissolved to a concentration of 0.1 mol·L^{-1}. Voltammetric analyses were carried out in a standard three-electrode cell, with an Autolab PGSTAT 302 N potentiostat, connected to an interfaced computer that employed Electrochemistry Nova software or on a Biologic SP-300 potentiostat, connected to an interfaced computer that employed EC-Lab (v. 11.25) software. The reference electrode was a saturated KCl calomel electrode (SCE) separated from the analysed solution by a sintered glass disk filled with the background solution. The auxiliary electrode was a platinum wire separated from the analysed solution by a sintered glass disk filled with the background solution. For all voltammetric measurements, the working electrode was a platinum disk electrode (Ø = 1.6 mm). In these conditions, when operating in CH_2Cl_2 (0.1 M $TBAPF_6$), the formal potential for the ferrocene (+/0) couple was +0.46 V.

3.2. *Synthesis of 5-(Pyridin-2-methyl)-10,20-bis(p-tolyl)-15-phenylporphyrin (**H_2-7**)*

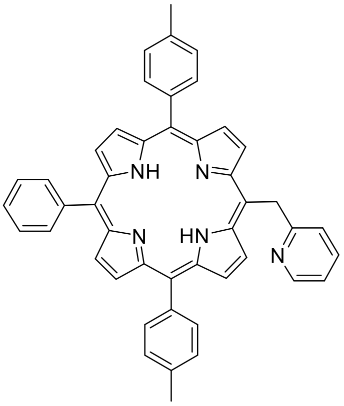

7

Chemical Formula: $C_{46}H_{35}N_5$
Exact Mass: 657.2892
Molecular Weight: 657.8210

This protocol was inspired by the one described by Senge and coworkers for aryl and alkyl functionalization of porphyrins [24]. A 20 mL Schlenk flask was evacuated and flushed with argon three times. 2-Picoline (197.5 µL, 2.0 mmol, 1.0 equiv) was then added to the Schlenk flask followed by dry THF (0.88 mL). The solution was cooled to −10 °C then a commercial solution of *n*-BuLi (1.6 M in *n*-hexane) was added dropwise (1.25 mL, 2.0 mmol, 1.0 equiv). The resulting orange solution was stirred at room temperature for 1 h. **H_2-4** (100.00 mg, 1.76×10^{-1} mmol, 1.0 equiv) was kept under vacuum for 2 h in a second Schlenk flask and then flushed with argon. Dry THF (45 mL) was then introduced into the Schlenk flask containing the porphyrin and the solution was cooled to −30 °C. 1.2 mL (1.032 mmol, 6.0 equiv) of the orange solution obtained in the first Schlenk flask were added dropwise to the solution of porphyrin. The resulting solution was stirred at room temperature for 20 min, then a solution of H_2O (0.84 mL) and dry THF (8.4 mL) previously degassed by bubbling argon was added dropwise to the reaction mixture. The green solution was stirred for a further 10 min at room temperature and DDQ (163.72 mg, 7.07×10^{-1} mmol, 4.0 equiv) was added to the Schlenk flask. The resulting red solution was stirred at room temperature for 1 h and then filtered on a pad of alumina, eluting with CH_2Cl_2. The crude product was purified by column chromatography (SiO_2, CH_2Cl_2/CH_3OH (99.5:0.5, v/v)). Three fractions were collected containing an unknown impurity (Fraction 1), **H_2-7** (Fraction 2) and traces of a product which could be unreacted **H_2-4** (Fraction 3). Fraction 2 was recrystallized in a CH_2Cl_2/CH_3OH mixture. The obtained precipitate was filtered under vacuum, washed with CH_3OH and dried at 110 °C overnight to give **H_2-7** in 63% yield (74.28 mg, 1.13×10^{-1} mmol). ^1H NMR ($CDCl_3$, 500 MHz, 298 K): δ (ppm) 9.52 (d, $^3J_{H\text{–}H} = 4.8$ Hz, 2H), 8.94 (d, $^3J_{H\text{–}H} = 4.8$ Hz, 2H), 8.85 (d, $^3J_{H\text{–}H} = 4.8$ Hz, 2H), 8.82 (d, $^3J_{H\text{–}H} = 4.7$ Hz, 2H), 8.75 (ddd, $^3J_{H\text{–}H} = 5.0$ Hz, $^4J_{H\text{–}H} = 1.9$ Hz, $^4J_{H\text{–}H} = 0.9$ Hz, 1H), 8.21, (dd, $^3J_{H\text{–}H} = 7.7$ Hz, $^4J_{H\text{–}H} = 1.6$ Hz, 2H), 8.09 (d, $^3J_{H\text{–}H} = 7.9$ Hz, 4H), 7.82 − 7.70 (m, 3H), 7.55 (d, $^3J_{H\text{–}H} = 7.6$ Hz, 4H), 7.21 (td, $^3J_{H\text{–}H} = 7.7$ Hz, $^4J_{H\text{–}H} = 1.9$ Hz, 1H), 7.04 (ddd, $^3J_{H\text{–}H} = 7.3$ Hz, $^4J_{H\text{–}H} = 5.0$ Hz, $^4J_{H\text{–}H} = 1.2$ Hz, 1H), 6.75 (d, $^3J_{H\text{–}H} = 8.1$ Hz, 1H), 6.65 (s, 2H), 2.72 (s, 6H), −2.64 (s, 2H); $^{13}C\{^1H\}$ NMR ($CDCl_3$, 126 MHz, 298 K): δ (ppm) 164.1, 149.1, 142.2, 139.4, 137.5, 136.6, 134.6, 134.6, 127.8, 127.5, 126.8, 124.5, 121.1, 120.2, 120.1, 114.7, 43.7, 21.7; R_f 0.07 (SiO_2, CH_2Cl_2); λ_{max} (CH_2Cl_2)/nm (log ε): 419 (5.76), 516 (4.35), 552 (4.10), 592 (3.81), 648 (3.71); HRMS (ESI+): m/z cald for $C_{46}H_{35}N_5$ $[M + H]^+$ 658.29652, found 658.29638.

3.3. *Synthesis of [5-(Pyridin-2-methyl)-10,20-bis(p-tolyl)-15-phenylporphyrinato]zinc(II) (***Zn-7***)*

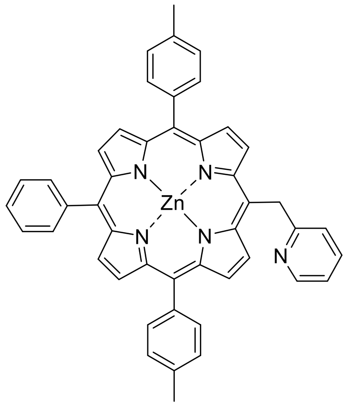

Zn-7

Chemical Formula: $C_{46}H_{33}N_5Zn$
Exact Mass: 719.2027
Molecular Weight: 721.1850

A solution of $\mathbf{H_2}$**-7** (30.05 mg, 4.57×10^{-2} mmol, 1.0 equiv) and $Zn(OAc)_2{\cdot}2H_2O$ (10.20 mg, 9.16×10^{-2} mmol, 2.0 equiv) in a mixture of $CHCl_3$ (2.7 mL) and CH_3OH (1.0 mL) was stirred at 60 °C for 1.5 h, monitoring the progress of the reaction by TLC (SiO_2, CH_2Cl_2). The solvent was then removed by rotary evaporation and the crude product was recrystallized in a CH_2Cl_2/CH_3OH mixture. The precipitate was filtered under vacuum, washed with a small amount of CH_3OH and dried at 110 °C overnight to give **Zn-7** in 81% yield (26.72 mg, 3.71×10^{-2} mmol). ^1H NMR ($(CD_3)_2CO$ + one drop pyridine-d_5, 500 MHz, 298 K): δ (ppm) 9.75 (d, $^3J_{H\text{–}H}$ = 4.7 Hz, 2H), 8.92, (d, $^3J_{H\text{–}H}$ = 4.7 Hz, 2H), 8.84 (d, $^3J_{H\text{–}H}$ = 4.6 Hz, 2H), 8.81 (d, $^3J_{H\text{–}H}$ = 4.6 Hz, 2H), 8.59 (ddd, $^3J_{H\text{–}H}$ = 5.0 Hz, $^4J_{H\text{–}H}$ = 1.9 Hz, $^4J_{H\text{–}H}$ = 0.9 Hz, 1H), 8.19 (dd, $^3J_{H\text{–}H}$ = 7.6 Hz, $^4J_{H\text{–}H}$ = 1.7 Hz, 2H), 8.06 (d, $^3J_{H\text{–}H}$ = 7.8 Hz, 4H), 7.80–7.70 (m, 3H), 7.57 (d, $^3J_{H\text{–}H}$ = 7.5 Hz, 4H), 7.34–7.29 (m, 1H), 7.03 (ddd, $^3J_{H\text{–}H}$ = 7.3 Hz, $^4J_{H\text{–}H}$ = 4.9 Hz, $^4J_{H\text{–}H}$ = 1.2 Hz, 1H), 6.93 (d, $^3J_{H\text{–}H}$ = 8.1 Hz, 1H), 6.70 (s, 2H), 2.68 (s, 3H); $^{13}C\{^1H\}$ NMR ($(CD_3)_2CO$ + one drop Pyridine-d_5, 126 MHz, 298 K): δ (ppm) 151.8, 150.9, 150.7, 150.4, 150.2, 150.0, 149.7, 141.4, 137.7, 137.7, 136.8, 136.8, 136.3, 136.1, 135.9, 135.2, 135.2, 133.0, 132.4, 132.2, 130.7, 128.1, 127.9, 127.3, 124.6, 124.2, 124.0, 123.8, 121.5, 121.2, 117.0, 21.5; R_f 0.47 (SiO_2, CH_2Cl_2); λ_{max} (DMF)/nm (log ε): 406 (4.55), 427 (5.70), 561 (4.05), 600 (3.44); HRMS (ESI+): m/z cald for $C_{46}H_{33}N_5Zn$ $[M + H]^+$ 720.21002, found 720.21151.

3.4. *Synthesis of [5-(Pyridin-2-methyl)-10,20-bis(p-tolyl)-15-phenylporphyrinato]nickel(II) (***Ni-7***)*

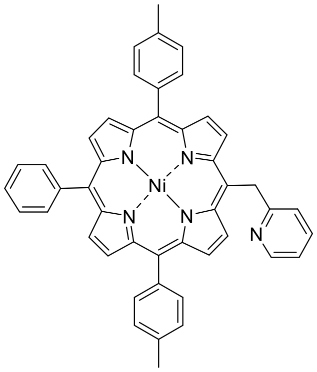

Ni-7

Chemical Formula: $C_{46}H_{33}N_5Ni$
Exact Mass: 713.2089
Molecular Weight: 714.4984

A Schlenk flask containing $\mathbf{H_2}$**-7** (40.02 mg, 6.08×10^{-2} mmol, 1.0 equiv) and $Ni(OAc)_2{\cdot}4H_2O$ (30.31 mg, 1.22×10^{-1} mmol, 2.0 equiv) was evacuated and flushed with argon three times. Dry DMF (3 mL) was then added and the solution was stirred at 160 °C under argon for 1.5 h, monitoring the progress of the reaction by TLC (SiO_2, CH_2Cl_2). The red solution obtained was allowed to cool to room temperature, then water was added (10 mL) to precipitate the product. The precipitate obtained was filtered under vacuum, washed with water and dried at 150 °C under vacuum for 4.5 h to give **Ni-7** in 84% yield (36.61 mg, 5.12×10^{-2} mmol). ^1H NMR ($CDCl_3$, 500 MHz, 298 K): δ (ppm) 9.31 (d, $^3J_{H\text{–}H}$ = 5.0 Hz, 2H), 8.81 (d, $^3J_{H\text{–}H}$ = 4.9 Hz, 2H), 8.73 (d, $^3J_{H\text{–}H}$ = 4.9 Hz, 2H), 8.69 (d, $^3J_{H\text{–}H}$ = 4.9 Hz, 2H), 8.67 (d, $^3J_{H\text{–}H}$ = 5.0 Hz, 1H), 7.99 (d, $^3J_{\text{H–H}}$ = 6.4 Hz, 2H), 7.87 (d, $^3J_{\text{H–H}}$ = 7.5 Hz, 4H), 7.74 – 7.61 (m, 3H), 7.47 (d, $^3J_{\text{H–H}}$ = 7.6 Hz, 4H), 7.24 (d, $^3J_{\text{H–H}}$ = 9.5 Hz, 1H), 7.03 (t, $^3J_{\text{H–H}}$ = 6.2 Hz, 1H), 6.73 (d, $^3J_{\text{H–H}}$ = 8.1 Hz, 1H), 6.21 (s, 2H), 2.64 (s, 2H); ^{13}C{^{1}H} NMR ($CDCl_3$, 126 MHz, 298 K): δ (ppm) 149.1, 143.2, 142.7, 142.5, 141.0, 138.0, 137.6, 136.6, 133.8, 133.7, 133.2, 132.4, 132.2, 130.2, 127.8, 127.7, 127.0, 124.1, 121.1, 118.9, 113.3, 21.6; R$_f$ 0.17 (SiO_2, CH_2Cl_2); $\lambda_{\max}$ (CH_2Cl_2)/nm (log ε): 416 (5.44), 530 (4.29); HRMS (ESI+): m/z cald for $C_{46}H_{33}N_5Ni$ [M + H]$^+$ 714.21622, found 714.21738.

3.5. *Attempted synthesis of fused [5-(Pyridin-2-methyl)-10,20-bis(p-tolyl)-15-phenylporphyrinato] nickel(II) (***Ni-7***$^+$,***PF$_6$***$^-$)*

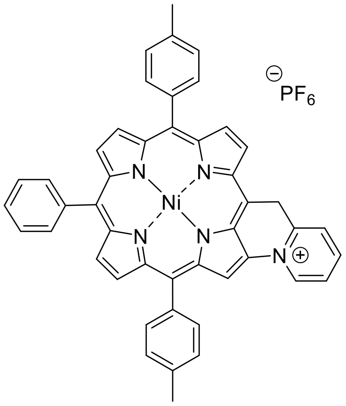

Ni-7$^+$,PF$_6^-$

Chemical Formula: $C_{46}H_{32}F_6N_5NiP$
Molecular Weight: 858,4546

Nickel(II) porphyrin **Ni-7** (1.0 equiv), 2,6-lutidine (2.0 equiv) and PIFA (1.0 equiv) were dissolved in dry CH_2Cl_2 (0.05 M). The reaction mixture was then stirred at room temperature for 1 h, monitoring the progress of the reaction by TLC (SiO_2, CH_2Cl_2). At that time, an additional amount of PIFA (0.2 equiv) was added. The mixture was stirred for 1.5 h and a further amount of PIFA was again added (1.0 equiv). After a total of 23 h of reaction, the solvent was evaporated. MALDI-TOF: m/z cald for $C_{46}H_{32}N_5Ni^+$ [M-PF$_6$-] 712.2026, found 712.2006 (assigned to the fused compound); 713.0963 (assigned to **Ni-7**) and 726.1798 ([M-2H$^+$-PF$_6$-+O] assigned to the fused compound with a carbonyl function on the bridging carbon atom).

3.6. *Attempted synthesis of fused [5-(Pyridin-2-methyl)-10,20-bis(p-tolyl)-15-phenylporphyrinato] zinc(II) (***Zn-7***$^+$,***PF$_6$***$^-$)*

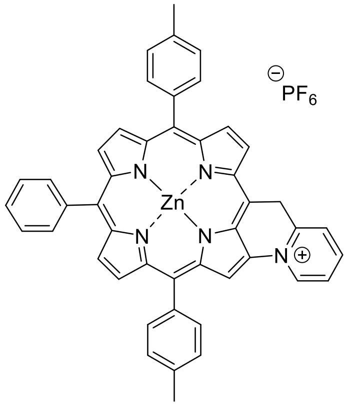

Zn-7$^+$,PF$_6^-$

Chemical Formula: $C_{46}H_{32}F_6N_5PZn$
Molecular Weight: 865,1412

Zinc(II) porphyrin **Zn-7** (1.0 equiv), 2,6-lutidine (2.0 equiv) and PIFA (1.0 equiv) were dissolved in dry CH_2Cl_2 (0.05 M). The reaction mixture was then stirred at room temperature for 1 h, monitoring the progress of the reaction by TLC (SiO_2, CH_2Cl_2). At that time, an additional amount of PIFA (0.2 equiv) was added. The mixture was stirred for 1.5 h and a further amount of PIFA was again added (1.0 equiv). After a total of 23 h of reaction, the solvent was evaporated. MALDI-TOF: m/z cald for $C_{46}H_{32}N_5Zn^+$ [M-PF$_6$-] 718.1944, found 717.0941 (assigned to the fused compound with the loss of one proton), 718.1008 (assigned to the fused compound); 719.0998 (assigned to **Zn-7**) and 732.0977 ([M-2H$^+$-PF6$^-$+O] assigned to the fused compound with a carbonyl function on the bridging carbon atom).

4. Conclusion

In summary, a new straightforward route for the synthesis of *meso*-(pyridin-2-ylmethyl)porphyrins was developed. This original pathway involves the nucleophilic attack of (pyridin-2-ylmethyl)lithium reagent on 10-phenyl-5,15-di-p-tolylporphyrin bearing one free *meso* position. The obtained free base porphyrin was then metalated providing the zinc(II) and nickel(II) complexes. These products were characterized by common analytical techniques (NMR, UV–vis., mass spectrometry and electrochemistry). Preliminary attempts to chemically generate the corresponding C–N-fused compounds (new bond between the nitrogen of the pyridinyl substituent and the β-pyrrolic position of the porphyrin) by oxidation with PIFA have been explored. Unfortunately, none of these attempts have lead to the formation and isolation of the desired fused porphyrins. Although the analyses performed on the crude mixtures suggest the formation of the fused porphyrins with formation of a carbonyl on the CH_2 bridge, the isolation of these compounds to confirm their structure was not successful.

Declaration of interests

The authors do not work for, advise, own shares in, or receive funds from any organization that could benefit from this article, and have declared no affiliations other than their research organizations.

Funding

This work was supported by the Université de Bourgogne, Université de Bourgogne Franche-Comté, CNRS (Centre National de la Recherche Scientifique), Conseil Régional de Bourgogne through the "Plan d'Actions Régional pour l'Innovation (PARI)" and the "Fonds Européen de Développement Régional (FEDER)" programs). MB and CHD thank the Agence Nationale de la Recherche for funding (ANR-15-CE28-0018-01). CHD acknowledges the Conseil Régional de Bourgogne Franche-Comté for a PhD grant (PORFELEC project) and the French "Investissement d'Avenir" program, project ISITE-BFC (contract ANR-15-IDEX-03) for funding.

Acknowledgments

The authors are thankful to Sophie Fournier for technical support, to the "Plateforme d'Analyse Chimique et de Synthèse Moléculaire de l'Université de Bourgogne" (PACSMUB, http://www.wpcm.fr) for ESI-HRMS analyses.

Supplementary data

Supporting information for this article is available on the journal's website under https://doi.org/10.5802/crchim.307 or from the author.

References

[1] K. Takahashi, T. Komura, H. Imanaga, *Bull. Chem. Soc. Japan*, 1989, **62**, 386-391.

[2] Y. Shinozaki, K. Ohkubo, S. Fukuzumi, K. Sugawa, J. Otsuki, *Chem. Eur. J.*, 2016, **22**, 1165-1176.

[3] J. Otsuki, T. Okumura, K. Sugawa, S. Kawano, K. Tanaka, T. Hirao, T. Haino, Y. J. Lee, S. Kang, D. Kim, *Chem. Eur. J.*, 2021, **27**, 4053-4063.

[4] A. M. Shachter, E. B. Fleischer, R. C. Haltiwanger, *J. Chem. Soc. Chem. Commun.*, 1988, 960-961.

[5] R. T. Stibrany, J. Vasudevan, S. Knapp, J. A. Potenza, T. Emge, H. J. Schugar, *J. Am. Chem. Soc.*, 1996, **118**, 3980-3981.

[6] K. Funatsu, T. Imamura, A. Ichimura, Y. Sasaki, *Inorg. Chem.*, 1998, **37**, 1798-1804.

[7] G. Ercolani, M. Ioele, D. Monti, *New J. Chem.*, 2001, **25**, 783-789.

[8] A. Tsuda, T. Nakamura, S. Sakamoto, K. Yamaguchi, A. Osuka, *Angew. Chem. Int. Ed.*, 2002, **41**, 2817-2821.

[9] J. S. Rebouças, M. E. M. D. de Carvalho, Y. M. Idemori, *J. Porphyr. Phthalocyanines*, 2002, **06**, 50-57.

[10] A. Tsuda, S. Sakamoto, K. Yamaguchi, T. Aida, *J. Am. Chem. Soc.*, 2003, **125**, 15722-15723.

[11] T. Kamada, N. Aratani, T. Ikeda, N. Shibata, Y. Higuchi, A. Wakamiya, S. Yamaguchi, K. S. Kim, Z. S. Yoon, D. Kim, A. Osuka, *J. Am. Chem. Soc.*, 2006, **128**, 7670-7678.

[12] R. F. Kelley, R. H. Goldsmith, M. R. Wasielewski, *J. Am. Chem. Soc.*, 2007, **129**, 6384-6385.

[13] Y. Shinozaki, G. Richards, K. Ogawa, A. Yamano, K. Ohara, K. Yamaguchi, S. Kawano, K. Tanaka, Y. Araki, T. Wada, J. Otsuki, *J. Am. Chem. Soc.*, 2013, **135**, 5262-5265.

[14] N. W. J. Kamp, J. R. Lindsay Smith, *J. Mol. Catal. A: Chem.*, 1996, **113**, 131-145.

[15] R. A. Jensen, R. F. Kelley, S. Joong Lee, M. R. Wasielewski, J. T. Hupp, D. M. Tiede, *Chem. Commun.*, 2008, 1886-1888.

[16] S. Yoshimoto, *Chem. Commun.*, 2012, **48**, 4612-4614.

[17] Y. Shinozaki, T. Tsubomura, K. Sugawa, J. Otsuki, *Tetrahedron Lett.*, 2016, **57**, 48-52.

[18] J. Echaubard, A. Bousfiha, M. Berthelot, J. Roger, P. Fleurat-Lessard, H. Cattey, S. Fournier, C. H. Devillers, D. Lucas, *Eur. J. Inorg. Chem.*, 2020, **2020**, 551-560.

[19] M. Berthelot, G. Hoffmann, A. Bousfiha, J. Echaubard, J. Roger, H. Cattey, A. Romieu, D. Lucas, P. Fleurat-Lessard, C. H. Devillers, *Chem. Commun.*, 2018, **54**, 5414-5417.

[20] M. Berthelot, F. Akhssas, A. K. D. Dimé, A. Bousfiha, J. Echaubard, G. Souissi, H. Cattey, D. Lucas, P. Fleurat-Lessard, C. H. Devillers, *Inorg. Chem.*, 2022, **61**, 7387-7405.

[21] F. Shirini, H. Tajik, A. Aliakbar, A. Akbar, *Synth. Commun.*, 2001, **31**, 767-770.

[22] F. Shirini, M. Esm-Hosseini, Z. Hejazi, *Synth. Commun.*, 2005, **35**, 2913-2919.

[23] V. Corcé, S. Renaud, I. Cannie, K. Julienne, S. G. Gouin, O. Loréal, F. Gaboriau, D. Deniaud, *Bioconjugate Chem.*, 2014, **25**, 320-334.

[24] M. O. Senge, X. Feng, *J. Chem. Soc. Perkin Trans. 1*, 2000, 3615-3621.

[25] A. D. Adler, F. R. Longo, F. Kampas, J. Kim, *J. Inorg. Nucl. Chem.*, 1970, **32**, 2443-2445.

[26] M. E. Ojaimi, B. Habermeyer, C. P. Gros, J.-M. Barbe, *J. Porphyr. Phthalocyanines*, 2010, **14**, 469-480.

[27] W. Zheng, N. Shan, L. Yu, X. Wang, *Dyes Pigments*, 2008, **77**, 153-157.

[28] A. Bousfiha, N. Amiri, F. Akhssas, M. Berthelot, J. Echaubard, M. Pirrotta, H. Cattey, P. Fleurat-Lessard, J. Roger, C. H. Devillers, *Org. Lett.*, 2023, **25**, 7979-7983.

[29] A. Albert, G. B. Barlin, *J. Chem. Soc.*, 1959, 2384-2396.

[30] E. F. V. Scriven, R. Murugan, *Kirk-Othmer Encyclopedia of Chemical Technology*, John Wiley & Sons, Ltd, 2005.

[31] R. J. L. Andon, J. D. Cox, E. F. G. Herington, *Trans. Faraday Soc.*, 1954, **50**, 918-927.

[32] C. H. Devillers, S. Hebié, D. Lucas, H. Cattey, S. Clément, S. Richeter, *J. Org. Chem.*, 2014, **79**, 6424-6434.

[33] G. R. Fulmer, A. J. M. Miller, N. H. Sherden, H. E. Gottlieb, A. Nudelman, B. M. Stoltz, J. E. Bercaw, K. I. Goldberg, *Organometallics*, 2010, **29**, 2176-2179.

ACADÉMIE
DES SCIENCES
INSTITUT DE FRANCE

Comptes Rendus. Chimie
2024, Vol. 27, Special issue S1, p. 91-103
`https://doi.org/10.5802/crchim.335`

Research article

French/Nordic Special Issue on Materials and Coordination Chemistry

Cherenkov radiation energy transfer from [^{18}F]-fluorodeoxyglucose to subphthalocyanine fluorophores

Vivian Lioret [a] **and Richard A. Decréau** [*, a]

[a] Université de Bourgogne, Institut de Chimie Moléculaire ICMUB, Sciences Mirande, 21000 Dijon, France

E-mail: Richard.Decreau@u-bourgogne.fr (R. A. Decréau)

Abstract. Cherenkov radiation (CR) is an optical light that is emitted during the decay of beta-particle-emitting radionuclides, such as ^{18}F, which is present in [^{18}F]-fluorodeoxyglucose, a well-known tracer used in positron emission tomography. The CR emission occurs from relaxation of molecules of the dielectric medium surrounding the emitted beta-particle. The Cherenkov radiation energy transfer (CRET) to a CR acceptor, such as subphthalocyanine, was analyzed. Subphthalocyanine is a unique concave-shaped 14π-electron fluorophore with optical properties. The relevance of such a CR emitter/acceptor couple to performing CRET is discussed.

Keywords. Cherenkov radiation energy transfer (CRET), Subphthalocyanine, Cherenkov luminescence imaging (CLI).

Funding. CNRS “Chaire d’Excellence”, Burgundy/Burgundy Franche-Comté (BFC) Regional Councils (FABER, 3MIM, PARI, respectively), French Ministry of Higher Education, Research and Innovation for a scholarship, ANR-EQPX-IMAPPI, PO-FEDER-FSE Bourgogne, Canceropôle Est (CLI Emergence Project), SATT-SAYENS (CLI-PDT).

Note. This proof-of-concept study was performed within the framework of a PhD thesis [1].

Manuscript received 17 May 2024, revised 26 August 2024, accepted 4 September 2024.

1. Introduction

Cherenkov radiation (CR) is emitted during radionuclide decay when a beta particle is released at a speed that causes the surrounding molecules from the dielectric medium (along the track of the particle) to attain an excited/polarization state. Subsequent relaxation of the surrounding molecules proceeds with light emission, which is called Cherenkov radiation. Overall, such a CR emission occurs when the energy of the beta particle is so high that it can travel even faster than light in a given dielectric medium [2–14] (which is a medium that could be polarized by an electric field). Hence an analogy can be drawn: the noise emitted when airplanes break the sound barrier may somehow compare with CR, which is emitted when beta particles break the light barrier in a dielectric medium.

The history of CR [2–14] began from its prediction by Oliver Heaviside in 1888, then Arnold Sommerfeld in 1904, and followed by its first observation by Marie Curie who detected its emission from radium samples in the 1910s. Later in the 1920s, Lucien Mallet demonstrated that it was emitted from transparent bodies and could record its spectrum. Then Pavel Cherenkov, a graduate student of Sergei Vavilov at the Lebedev Institute (FIAN), demonstrated its origin

---

[*] Corresponding author

ISSN (electronic): 1878-1543

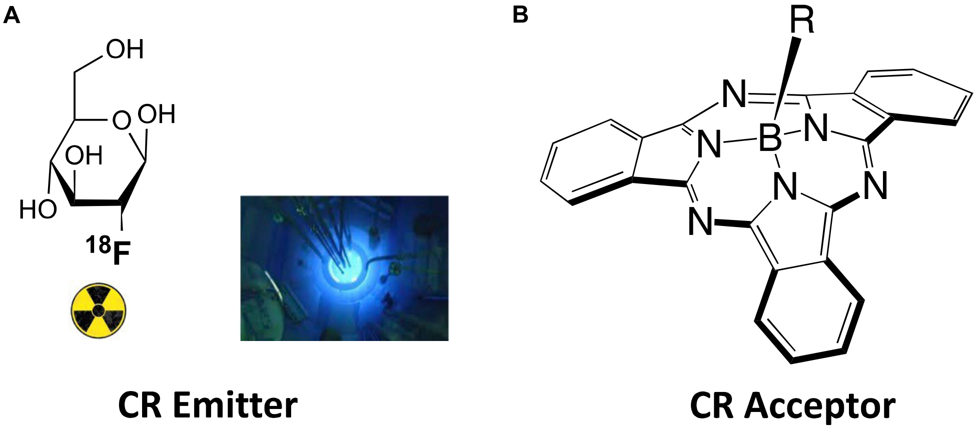

Figure 1. (A) CR emitter: [^{18}F]-fluorodeoxyglucose ([^{18}F]-FDG). Inset (left): CR as seen in pools that cool nuclear rods. (B) CR acceptor: subphthalocyanine (**SUB**).

and properties and that it consists of a continuous spectrum. Ilya Frank and Igor Tamm subsequently performed the theoretical interpretation of this emission, and they were awarded the Nobel Prize in 1958 together with Pavel Cherenkov. About 100 years after the first observation of CR, the development of a sensitive camera allowed the use of CR in a variant of optical imaging named Cherenkov luminescence imaging (CLI), first in 2009 in preclinical settings [15–18] and later in 2013 in clinical settings [19,20].

Cherenkov radiation is an alternative light source to perform fluorophore photoactivation, which originates from atomic decay (radionuclides) and surrounding molecules relaxation. Cherenkov radiation energy transfer (CRET) to fluorophores is expected to be efficient as long as there is a good match/overlap between the CR emission spectrum and the fluorophore absorption spectrum [21–27], which roughly falls in the 300–600 nm window of the electromagnetic spectrum. It is required that the optical properties of both the CR emitter and the CR acceptor are acceptable. This means a high CR quantum yield for the former and high brightness B for the latter (with high values of either one or both of its components: fluorescence quantum yield Φ_F and molar coefficient absorption ε). These matters related to CRET will be addressed on choosing two partners of interest for future biomedical applications, such as **^{18}F** as the CR emitter and subphthalocyanine (**SUB**) as the CR acceptor (Figure 1).

2. Results and discussion

2.1. *Synthesis and radiosynthesis of CR emitter and CR acceptor*

2.1.1. *CR emitter: fluorine-18 (^{18}F) in [^{18}F]-fluorodeoxyglucose [^{18}F]-FDG*

Fluorine-18 (^{18}F) is the most widely used radionuclide for positron emission tomography (PET) imaging in clinical settings [28–31]. Fluorine-18 emits a positron (β^+) that annihilates on reaction with an electron to produce two gamma rays that are detected and used for PET imaging purposes. The actual study focuses on the ability of the positron to trigger the emission of CR with the surrounding dielectric medium. [^{18}F]-fluorodeoxyglucose ([^{18}F]-FDG) is synthesized by electrophilic *or* nucleophilic fluorination [28–31] (Figure 2). In electrophilic fluorination, tri-O-acetyl-D-glucal reacted with [^{18}F]-F_2 or [^{18}F]-CH_3CO_2F to produce a mixture of fluorinated molecules. From among these molecules, the difluoroglucose derivative was isolated and subsequently hydrolyzed to form [^{18}F]-FDG (in 8% yield in 2 h). In nucleophilic fluorination, the [^{18}F]-F^- ion is in the presence of Kryptofix 222™, a cyclic crown ether that binds the potassium ion, which prevents the formation of poorly reactive [^{18}F]-KF and makes [^{18}F]-F^- more reactive in the nucleophilic substitution. The radioactive anion will displace the triflate leaving group in tetra-O-acetyl-triflate mannose to form [^{18}F]-FDG.

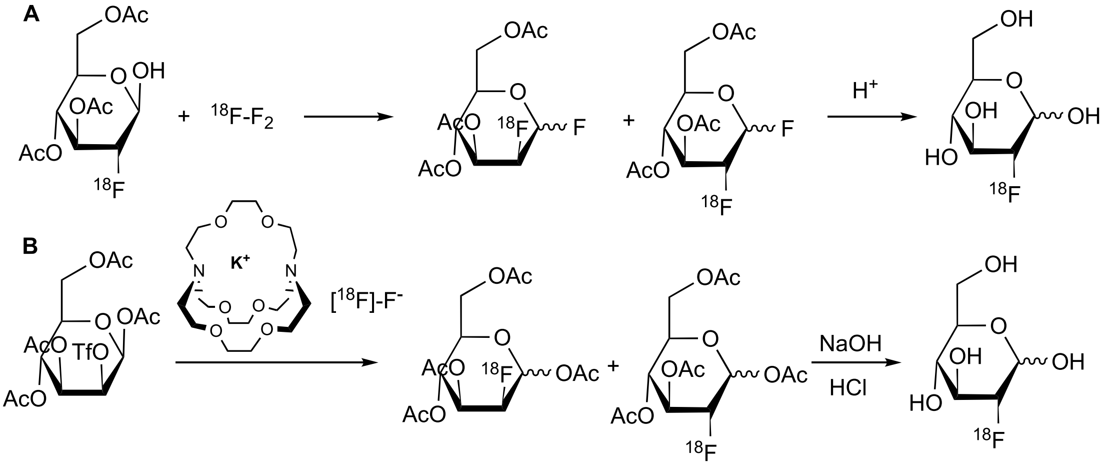

Figure 2. [^{18}F]-fluorodeoxyglucose ([^{18}F]-FDG) synthesis, following the electrophilic (A) and nucleophilic (B) fluorination reactions [28–31].

2.1.2. *CR acceptor: subphthalocyanine*

Subphthalocyanines (**SUB**, also reported with the acronym SubPc in the literature) are 14-π electron macrocycles that are reported as fluorophores of interest for fluorescence imaging [32,33]. Their shape is unique; they have a domed concave structure, which is an appealing feature in biomedical applications because it does not favor aggregation, a deactivation phenomenon in fluorescence imaging.

The first step in **SUB** platform synthesis (Figure 3) is the dicyanobenzene cyclotrimerization reaction that is typically achieved in 1,2-dichlorobenzene as a solvent under inert atmosphere in the presence of boron trichloride to form golden sparkling chlorosubphthalocyanine dye (SUB-Cl, **1**) of approximately 58% yield. Subsequent reaction of **1** with phenol/hydroxyaryl-containing reagents leads to the replacement of the axial chlorine atom with the corresponding aryloxy substituent of interest, also of 60–64% yield (which corresponds to 35–37% overall yield in **2** and **3**). The first rationale of such an addition was to further address the three-dimensional feature of the dye, that is, subsequently preventing aggregation. The second rationale was to conveniently afford a chemical functionality for further derivatization of **SUB** platforms as with nitrophenoxy substituent in SUB-PH **2** (which could be reduced into an amine for further conjugation). The third rationale was to append a UV/blue absorbing fluorophore to produce a SUB-COUM **3** dyad, which could undergo more CR absorption and contribute to its transfer toward a less energetic wavelength potentially less absorbed by biological tissues.

2.2. *Luminescence studies: CR emitter, CR acceptor, and their combination to achieve CRET*

2.2.1. *CR emitter:* ^{18}F

Theory [31]

- Fluorine-18 ($^{18}_{9}$F) is a “neutron-deficient” or “proton-rich” radionuclide that decays by emitting a positron (β^+) particle, a neutrino (ν), and its daughter radionuclide $^{18}_{8}$O (the atomic number of which is one unit less than that of its starting $^{18}_{9}$F parent):

$$^{18}_{9}\mathrm{F} \rightarrow {}^{18}_{8}\mathrm{O} + \beta^+ + \nu$$

- ^{18}F decay follows the *radioactivity decay law* (Equation (1)):

$$A_t = A_0 e^{-\lambda t} \qquad (1)$$

Parameters of the equation: A_t, activity at time t; A_0, activity at $t = 0$; λ, decay constant—it is the probability of disintegration per unit time and it is related to the half-life ($0.693/t_{1/2}$); $t_{1/2}$, half-life of the

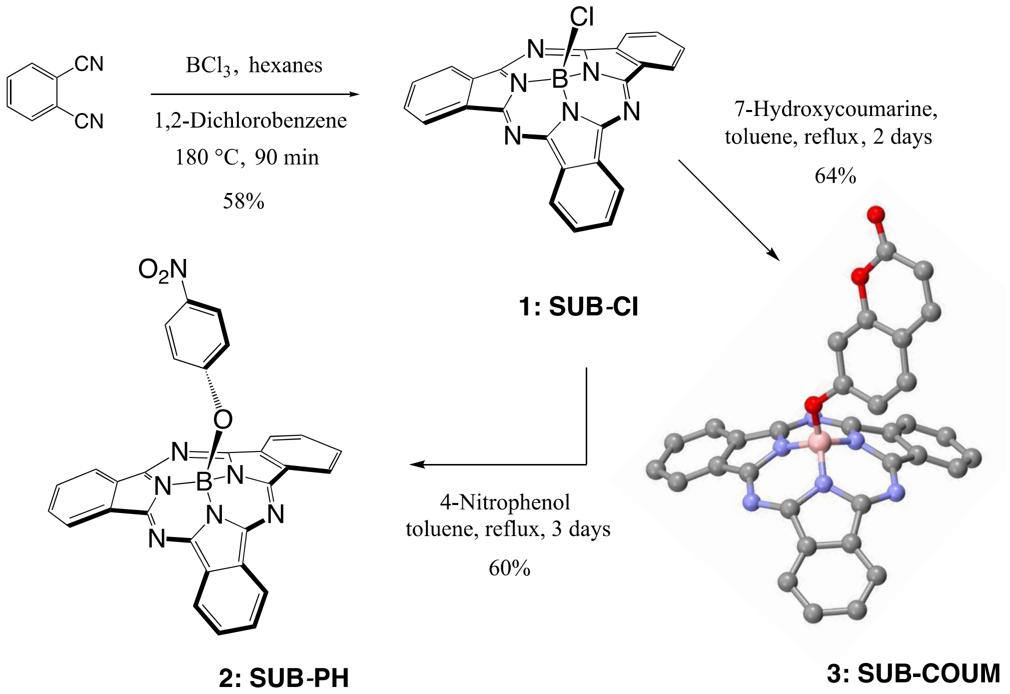

Figure 3. Syntheses of subphthalocyanine (**SUB**) targets bearing three distinct axial features: a chlorine atom (**SUB-Cl**, **1**), a nitrophenoxy group (**SUB-PH**, **2**), and a coumarin (**SUB-COUM**, **3**) [32,33].

Figure 4. Emission of the Cherenkov Radiation (CR) from radionuclides, and as it is seen in pools that cool nuclear rods.

radionuclide, the time the starting activity drops to one half—it is related to activity A and the number of radioactive atoms N; activity of a radionuclide, or radioactivity, is the disintegration rate: $A = \lambda N = -\mathrm{d}N/\mathrm{d}t$.

Equation (1): radioactivity decay law.

- To achieve CR emission (Figure 4), the energy of the beta particle emitted by a radionuclide during the decay process has to be beyond the Cherenkov threshold. Cherenkov emission occurs above this threshold, which is a function of the nature of the medium. When the medium is water, the Cherenkov threshold is 264 keV. The energy of the beta particle emitted by a radionuclide such as fluorine-18 (^{18}F) is 634 keV, which makes it a good candidate for CLI because it is about 2.5-fold beyond the Cherenkov threshold [2–14].
- The number of Cherenkov photons emitted follows the equation reported by Ilya Frank and Igor Tamm (Equation (2)) [2–14]:

$$\frac{\mathrm{d}N}{\mathrm{d}x} = 2\pi\alpha\left(\frac{1}{\lambda_1} - \frac{1}{\lambda_2}\right)\left(1 - \frac{1}{\beta^2\eta^2}\right) \qquad (2)$$

Parameters of the equation: dN/dx, number of photons per unit of path length whose wavelength is between the λ_1 and λ_2 intervals; α, fine structure constant (1/137); β, velocity of the particle (in the medium) divided by that in vacuum (c); η, refractive index (RI).

Equation (2): determination of the number of Cherenkov photons generated during radionuclide decay.

- The number of optical photons (400–800 nm) per nuclear decay is reported to be 0.8–1.4 photons per decay of ^{18}F atom on a 50 µm step path [15–18]. A Monte Carlo simulation showed that CR emitted from ^{18}F is confined within 0.3 mm [15–18].
- **CR yield is a function of three parameters:**
  * A—energy of the beta particle
  * B—activity loaded
  * C—RI of the medium

Experiment

Three parameters governing radiance/CR yield were examined throughout the studies. The emission of CR was recorded both on a spectrofluorometer and on an optical imager.

* **A—energy of the beta particle.** Experiments were conducted on the spectrofluorometer. The fluorescence cell was filled with a solution of a [^{18}F]-FDG (34.5 MBq) and recording was achieved on a bioluminescence mode (no laser irradiation) with maximum open slits and maximum scans. Under the experimental conditions, a spectrum develops, which is UV/blue weighted (Figure 5). The CR profile is the same from one radionuclide to another. When the energy of the beta particle is raised, such as ^{90}Y (E_β = 2.2 MeV), the luminescence intensity is raised compared to ^{18}F (E_β = 0.63 MeV). Hence, ^{90}Y appears as a more appealing CR emitter than ^{18}F. However, the latter was chosen because of its ready availability and for cost reasons.

* **B—activity loaded.** 96-well plates were filled with 5–25 MBq (0.135–0.676 mCi) [^{18}F]-FDG solution and the remainder of the medium with water. CLI luminescence studies were performed on the *optical imager*, with images recorded just a few minutes after sample deposition, using an open filter mode. Photon emission is a function of activity: a rise in activity (with no change in medium composition) subsequently leads to a corresponding rise in radiance. The radiance of several activities has been measured by detecting all emitted photons (no filter used) for 1 s (Figure 6).

* **C—RI of the medium.** The value of the measured radiance varied depending on the nature of the co-solvent. The co-solvent with the highest RI led to the highest radiance as expected from Equation (1) (Figure 7). Hence, when DMSO with RI = 1.477 was used as the co-solvent, a radiance was measured that was 1.2–1.5 times as much as that of other co-solvents, the RIs of which were lower, that is, in the 1.3 range. Conversely a striking observation could be made: although the methanol RI value was slightly lower (1.328) than that of serum (1.34), its radiance evolved the other way around. This may possibly be explained because the RI value is the average of values recorded on the whole UV–vis window. Although the RI value of methanol measured at 400 nm is noticeably higher (1.374) (Figure S1) than that measured at 700 nm (1.320), the reported value (1.331) [34] corresponds to the average value of all other measured RIs at various wavelengths. Hence, at 400 nm, which corresponds to a region of the spectrum where CR emission is more intense, the RI value for methanol (1.374) is higher than that of water (1.34).

2.2.2. *CR acceptor:* **SUB** *(fluorescence studies)*

The optical properties of subphthalocyanine measured in toluene indicate a maximal absorption at 562 nm and emission at 572 nm (i.e. 10 nm Stokes shift). It was noted that the fluorescence quantum yield Φ_F measured in toluene of the subphthalocyanine dropped when the axial chlorine atom was substituted (0.32 for **1**, 0.17 and 0.19 for **2** and **3**, respectively).

2.2.3. *CRET studies*

Rationale. Hence, studies reported in Sections 2.2.1 (Figure 5) and 2.2.2 (Figure 8) indicate that the spectral overlap between the CR acceptor and the CR emitter is optimum (Figure 9A). Hence, subsequent CRET studies on the optical imager could be performed, the concept of which is depicted in Figure 9B,C, and CLI images displayed in Figure 10.

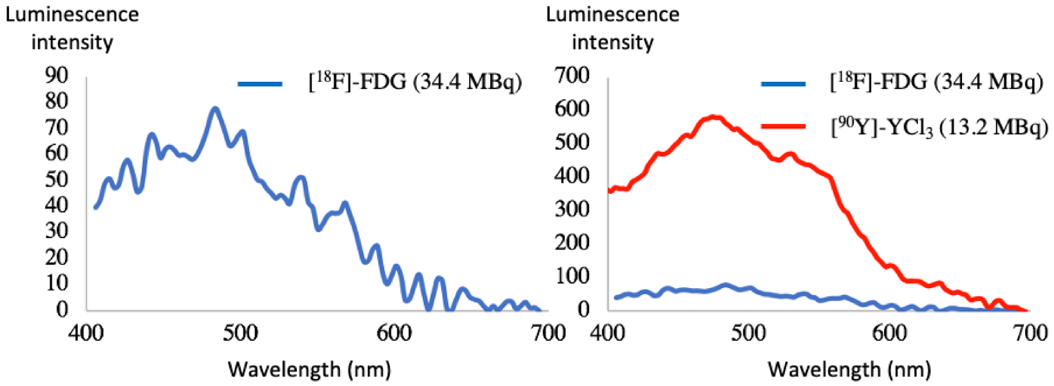

Figure 5. Cherenkov radiation emission spectra of [^{18}F]-FDG (34.5 MBq) and [^{90}Y]-YCl$_3$ (13.2 MBq) [24].

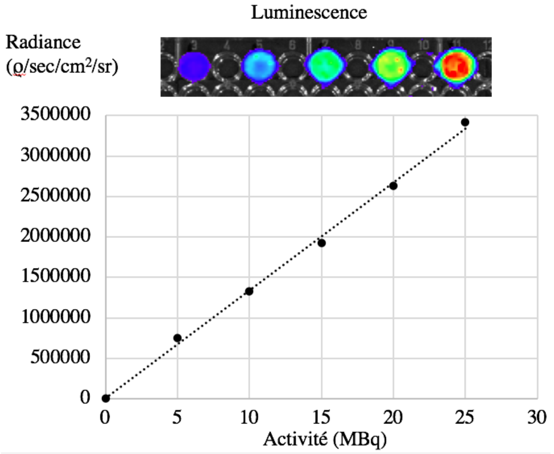

Figure 6. Measured radiance as a function of activity in [^{18}F]-FDG [1].

Experiment. It was performed in 96-well plates and consisted in mixing a solution of the CR emitter to a solution of the CR acceptor. Hence, a few microliters of a [^{18}F]-FDG solution that corresponds to approximately 10 MBq (0.270 mCi) was added to a solution of 1 mM of subphthalocyanine **SUB-PH 2** or **SUB-COUM 3**. As the radionuclide half-life has to be taken into account at all times (^{18}F half-life is 109.8 min) and because the [^{18}F]-FDG provider did not furnish the same volumetric activity (depending on multiple parameters such as the time of delivery and the starting time of the experiment), extreme care had to be taken with the volume added to a well. Hence, adding 10 MBq could vary from 15 µL up to 45 µL depending on the volumetric activity of the stock solution of the purchased radionuclide. To ensure the medium maintains the same composition (and hence the same RI), all controls were diluted the same way.

The first well was filled with [^{18}F]-FDG CR emitter (column 1), the second and third with both CR emitter and subphthalocyanine CR acceptor **SUB-PH 2** (column 2) or **SUB-COUM 3** (column 3), respectively. [^{18}F]-FDG was provided in solution in physiological serum, in which subphthalocyanines **2** and **3** are not soluble. As a result, the latter were dissolved in an organic solvent that could remain miscible with water, such as DMSO. Such a co-solvent was also added to the FDG-containing well to ensure that conditions remain comparable.

Results. A first series of radiance measurements were achieved using the **520 ± 20 nm** filter. Radiance measured in wells from column 1 that contain *only* CR emitters without **SUB** probes was 1.5-fold higher than that measured in wells from columns 2 and 3 that contain *both* CR emitters and **SUB** probes. This filter overlays a window where the CR spectral emission is significant, which explains why the radiance measured in wells from CR-emitter-only column 1 is high. Conversely, the **SUB** platform absorbs CR in this window as a result of a good spectral overlap of both while **SUB** is not yet detected in such a window. Overall, this explains such a drop in radiance from CR-only wells compared to wells containing CR-absorbing molecules.

Co-solvent used	Refractive index (RI)
Serum **(1)**	1,34
DMSO **(2)**	1,4777
CH_3OH **(3)**	1,328

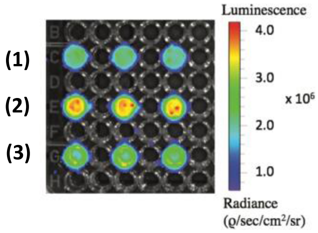

Figure 7. Measured radiance of solutions containing [^{18}F]-FDG emitter (35 µL solution) and a co-solvent (65 µL) such as serum **(1)**, DMSO **(2)**, and CH_3OH **(3)** [1]. Radiance values are also reported in a diagram depicted in Figure S2.

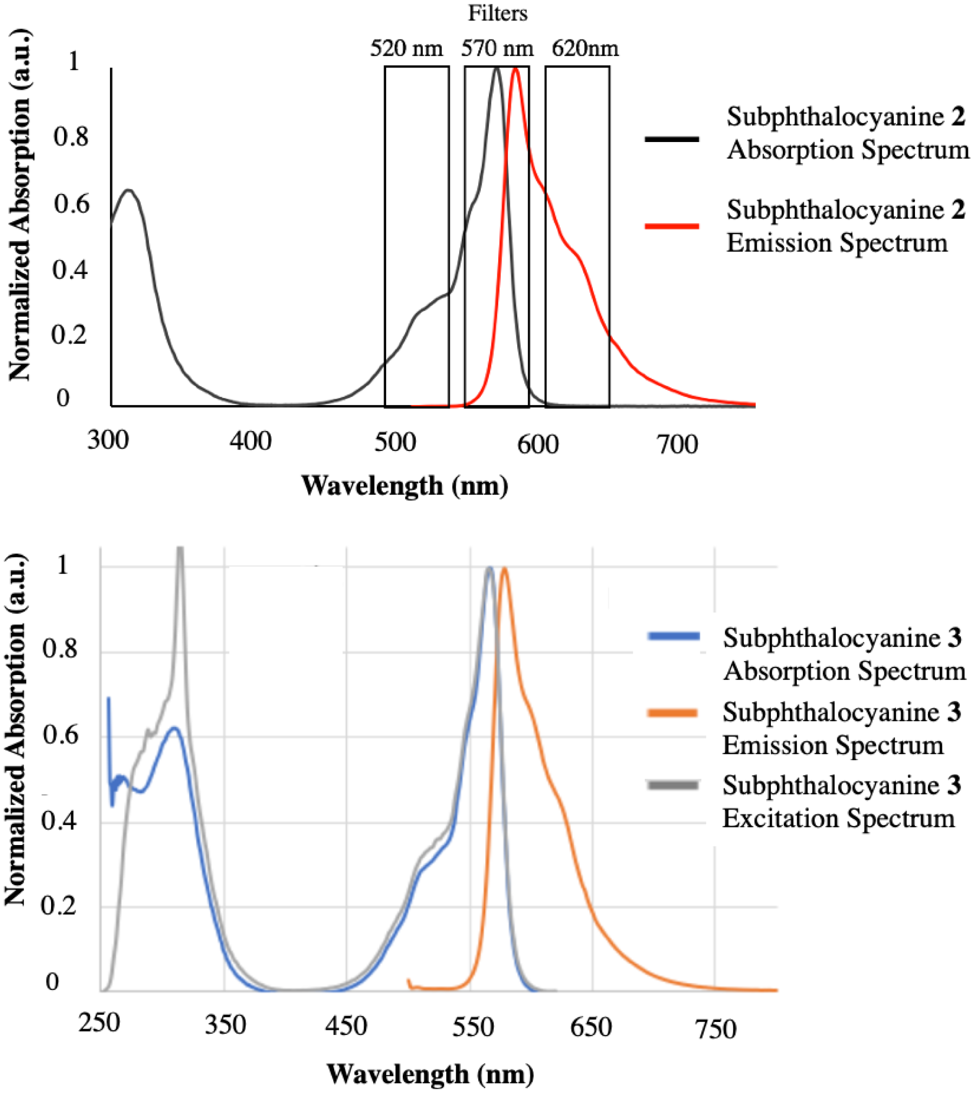

Figure 8. Top: Overlay of selected emission filters on the optical imager with subphthalocyanine **SUB-PH 2** absorption spectrum (black) and emission spectrum (red) measured in DMSO/H_2O 60/40 vol. Bottom: Subphthalocyanine **SUB-COUM 3** spectra: absorption (blue), emission (orange), and excitation (gray) spectra recorded in pure DMSO [1,32,33].

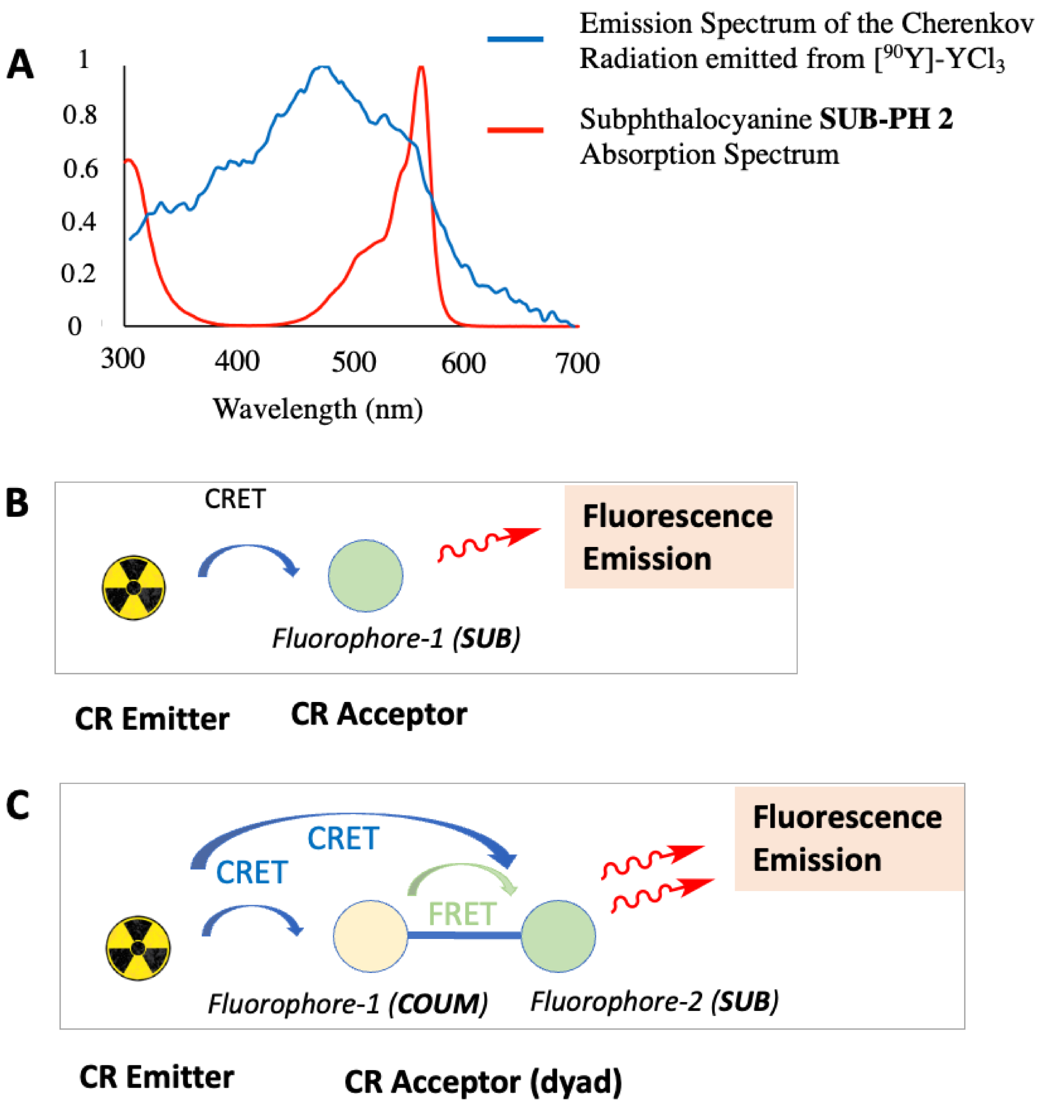

Figure 9. (A) Overlay of the Cherenkov radiation emission spectrum from [^{90}Y]-YCl$_3$ (13.2 MBq) (see Figure 5) and the absorption spectrum of subphthalocyanine **SUB-COUM 3** (measured in DMSO) (see Figure 8). (B,C) Depiction of CRET from CR emitter to CR acceptor(s) (fluorophore(s)), subsequently followed by fluorescence emission (from SUB fluorophore only), which is enhanced when COUM antenna is present and undergoes additional CRET transfer and subsequent intramolecular FRET/TBET transfers at the SUB platform (with no expected residual fluorescence emission from COUM, previous studies suggested [1,33]).

A second and third series of radiance measurements were achieved using **570** and **620 ± 20 nm** filters, respectively. Such windows shift away from the main CR emission peak. As a result, the radiance corresponding to CR emission only (column 1) keeps on dropping from 570 to 620 nm. Conversely, these filters are overlaid with **SUB** platform emission spectra, which explains why the radiance is raised in columns 2 and 3, compared to that in column 1 (control). Hence, the most spectacular result shows that the radiance corresponding to subphthalocyanine **SUB-COUM 3** emission is raised by 2.1-fold compared to the radiance to CR-only emitting well. This is because the **SUB** platform is

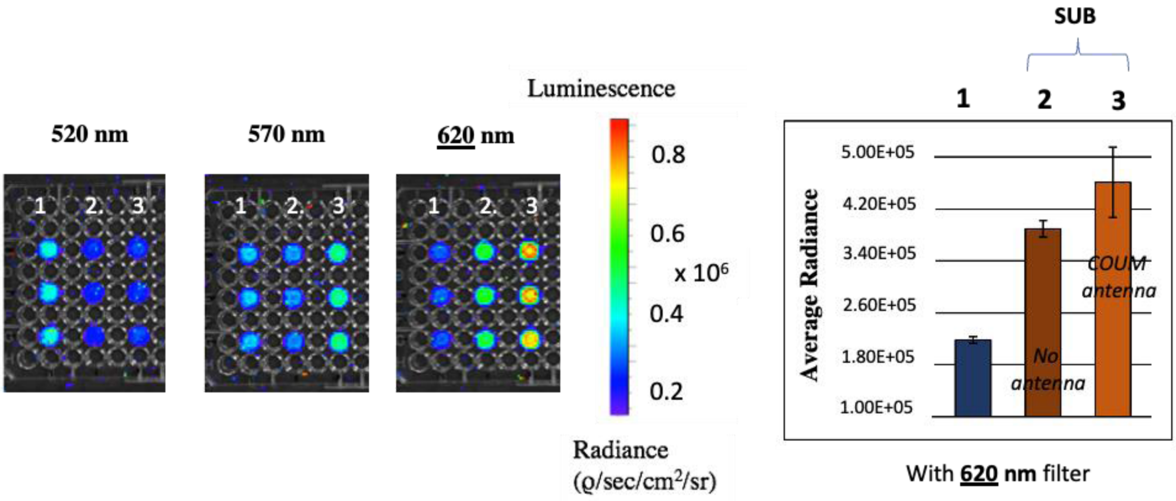

Figure 10. Cherenkov luminescence imaging studies: measured radiances of solutions containing [^{18}F]-FDG (10 MBq) CR emitter only (column 1), or CR emitter mixed with subphthalocyanines **SUB-PH 2** (column 2) and **SUB-COUM 3** (column 3). Radiances were measured with filters centered at 520, 570, and 620 nm, respectively.

equipped with a coumarin antenna. Subphthalocyanines not equipped with a **COUM** antenna do not display such a rise in radiance. Earlier results with a non-radioactive light source showed that setting the irradiation at the **COUM** antenna (360 nm) led to an emission corresponding to that of the **SUB** platform and not from that corresponding to **COUM** emission. This suggests a high energy transfer efficiency yield in the form of intramolecular Förster resonance energy transfer (FRET) or through bond energy transfer (TBET) [26,33]. It is first crucial to point out, as mentioned in the previous section, that the fluorescence quantum yields measured for all substituted subphthalocyanines remained comparable. This means that such differences in radiance measured from **SUB-PH 2** to **SUB-COUM 3** is the result of CRET and not from the subphthalocyanine Φ_F.

3. Conclusion

This proof-of-concept study showed that CR is an alternative light source to photoactivate fluorophore platforms upon CRET, and indicated that the chosen CR emitter/acceptor pair in the actual study (**^{18}F/SUB**) was relevant. Regarding the CR emitter (**^{18}F** in [^{18}F]-FDG), despite its potency to emit CR (0.8–1.4 optical photons (400–800 nm)/decay per 50 µm step size [15–18], also indicated by the energy of its emitted beta particle [E_β = 634 keV]) that appears to be not as high as that of other radionuclides (up to threefold as less as ^{90}Y), it was straightforward to perform its CLI imaging on an optical imager at 10 MBq and to record its emission spectrum on a spectrofluorometer. Moreover, **^{18}F** remains easily accessible and cheap because of its wide availability in the clinical field. Regarding the CR acceptor (**SUB**), despite its brightness (i.e., referring to Φ_F and ε) that appears to be not as high as that of other fluorophores (12,500 versus 73,000–88,000 with fluorescein), its absorption spectrum overlaps well with the CR emission spectrum while its unique conical shape makes **SUB** appealing with respect to preventing aggregation and to envisioning future molecular assemblies. Hence, such a **SUB/^{18}F** pair enabled achieving CRET and subsequent fluorescence emission from **SUB**. Furthermore, such a proof-of-concept study showed that appending an additional fluorophore onto **SUB** with a good spectral overlap with both **SUB** and CR allowed achieving additional CRET transfers at both **COUM** and **SUB** fluorophores within the dyad together with intramolecular ET transfers (FRET/TBET). This subsequently allowed further rise in radiance toward the targeted near-infrared (NIR) window. Such an approach is of significant relevance to in vivo imaging purposes for two reasons: (a) CR may be considered an alternative to exogenous lasers classically used in fluorophore photoactivation in standard optical imaging, where the radionuclide becomes an embarked (on board) light source, which has advantages with respect to signal-to-background ratios [15–18]; (b) the rationale of the study could be extended to other dyads with much larger pseudo-Stokes-shifts (than that of SUB-COUM 3) in order to achieve fluorescence emission farther in the NIR window where tissues are more transparent. Hence, fluorophores with absorption bands falling within the 300–600 nm window are a good match to CR emission spectrum (albeit residual CR emission is still detected way beyond 600 nm) [21–27]. Moreover, such a study suggests that CRET to other photoactivatable platforms other than fluorophores may potentially be envisioned [21–27].

4. Experimental section

4.1. *Materials and methods*

All spectroscopic measurements conducted to thoroughly characterize **SUB** molecules were performed on the PACSMUB (Pôle Chimie Moléculaire) platform at the University of Burgundy.

4.1.1. *Nuclear magnetic resonance spectroscopy (NMR)*

Measurements were performed on a Bruker at 300 MHz or 500 MHz (^{1}H), 75 MHz or 125 MHz (^{13}C), and 96 MHz (^{11}B) in $CDCl_3$ with the chemical shifts reported as δ in ppm relative to TMS (residual chloroform from deuterated chloroform chemical shift was set at 7.26 ppm, and coupling constants expressed in Hz). The following abbreviations were used to describe spin multiplicity: s = singlet, d = doublet, t = triplet, and m = multiplet.

4.1.2. *UV–visible spectroscopy*

UV–vis measurements were performed on a Shimadzu UV-2550 spectrophotometer in glass cuvettes of 1 × 1 × 3 cm (1 cm path) and on an Agilent Cary 50 or Cary 60.

4.1.3. *Mass spectrometry*

(a) Matrix-assisted laser desorption/ionization time of flight mass spectrometry (MALDI-TOF MS): Measurements were performed on Ultraflex II LRF 2000 (Bruker), using dithranol or DHB as a matrix or on a microflex LRF (Bruker). Solutions were prepared by dissolving 1 mg of compound in 1 mL of the appropriate solvent. (b) Electrospray ionization mass spectrometry (ESI MS). Measurements were performed on LTQ Orbitrap XL (Thermo Scientific) coupled to HPLC UltiMate 3000 (Dionex). Solutions were prepared by dissolving 1 mg compound into 1 mL of appropriate solvent and then diluted 100 times with methanol.

4.1.4. *High-pressure liquid chromatography separation and analysis (HPLC)*

System A: HPLC-MS (Hypersil C18 column, 2.6 μm, 2.1 × 50 mm) with H_2O 0.1% FA as eluent A and CH_3CN 0.1% FA as eluent B (linear gradient from 5 to 100% of B [5 min] and 100% of B [1.5 min]) at a flow rate of 0.5 mL/min. UV detection was achieved at 201, 290, 550, 690, and 750 nm. *System B*: HPLC (Hypersil C18 column, 5 μm, 10 × 250 mm) with H_2O 0.1% FA as eluent A and CH_3CN 0.1% FA as eluent B (linear gradient from 20 to 60% of B in 40 min) at a flow rate of 3.5 mL/min. UV detection was achieved at 700 and 780 nm.

4.1.5. *Fluorescence measurement and quantum yield*

Fluorescence measurements were performed on Horiba Jobin Yvon Fluorolog spectrofluorometer (software FluorEssence).

Cherenkov luminescence imaging studies: CR detection and CRET studies were performed at the CGFL Preclinical Imaging and Radiotherapy Platform (PIRP). All protocols strictly comply with standards of radioprotection and regulations of the *French Nuclear Safety Authority* (ASN). CLI studies were performed using [^{18}F]-FDG as a source of fluorine-18 radionuclide. [^{18}F]-FDG was provided by Curium (Cyclopharma), and the sample activity was measured upon reception on site. Studies were performed as follows: (a) Agilent Cary Eclipse spectrofluorometer (sensitivity: signal-to-noise measurements of Raman band of water 1/700) in quartz cuvette 1 × 1 × 3 cm (1 cm path). (b) IVIS Lumina III optical imager using 96-well plate (200 μL).

4.2. *Synthesis and radiosynthesis*

[^{18}F]-fluorodeoxyglucose (^{18}F-FDG) was purchased from Cyclopharma, which produces it on site in Dijon. Its radiosynthesis was performed on site following a reported method [28–31]. Organic syntheses of subphthalocyanines SUB-Cl, SUB-PH, and SUB-COUM were previously reported [32,33] and optimized as follows.

4.2.1. *Synthesis of B-chloro [subphthalocyaninato]boron(III):* SUB-Cl 1

A 1 M solution of BCl_3 in hexane (20 mL, 20 mmol) was slowly added under nitrogen atmosphere to a solution of phthalonitrile (1.06 g, 8.27 mmol) in dry dichlorobenzene (45 mL). Next, hexane was removed on heating the mixture at 70 °C for 30 min. A condenser was subsequently appended to the flask, and heating of the reaction mixture was raised to 180 °C and carried on for 1.5 h. The color of the mixture that was initially light milky yellow turned to dark purple on heating. On cooling, a precipitate formed, which was isolated by filtration. It was subsequently washed with methanol and pentane and then dried under reduced pressure to obtain **SUB-Cl 1** (700 mg, 58%). ^{1}H NMR (500 MHz, $CDCl_3$, 300 K, Figure S3): δ (ppm) = 7.95 (m, 6H), 8.90 (m, 6H). HR-MS ESI: m/z 431.0966 [M+H]$^+$ (calcd for $C_{24}H_{13}BClN_6^+$: 431.0978). HP-LC analysis (system A): retention time 5.83 min.

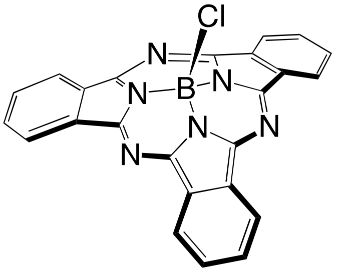

4.2.2. *Synthesis of B-(4-nitrophenoxy) [subphthalocyaninato]boron(III):* SUB-PH 2

To a solution of **SUB-Cl 1** (50 mg, 0.12 mmol) in toluene (3 mL) was added 4-nitrophenol (81 mg, 0.58 mmol). The reaction mixture was heated under reflux conditions for 3 days and monitored by LCMS. The solvent was removed under reduced pressure. Then the crude product was subjected to a short alumina gel column chromatography (eluent: dichloromethane) to remove the excess of unreacted phenol, yielding 37 mg (60%) of pure **SUB-PH 2**. ^{1}H NMR (300 MHz, $CDCl_3$, 300 K, Figure S4): δ (ppm) = 5.37 (d, ^3J = 9.2 Hz, 2H), 7.64 (d, ^3J = 9.2 Hz, 2H), 7.89 (m, 6H), 8.84 (m, 6H). ^{13}C NMR (75 MHz, $CDCl_3$, 300 K): δ (ppm) = 118.3, 122.1, 125.0, 129.9, 130.7, 141.3, 151.2, 158.5. ^{11}B NMR (96 MHz, $CDCl_3$, 300 K): δ (ppm) = −14.93 (s, 1B). UV–vis (THF), λ_{max} (nm) ($\varepsilon \times 10^3$ L·mol^{-1}·cm^{-1}) = 304 (56.7), 562 (86.0). HR-MS ESI: m/z = 533.1414 [M-e]$^+$ (calcd for $C_{30}H_{16}BN_7O_3^+$: 533.1402). Φ_F (THF) = 0.17 (reference: rhodamine 6G in solution in ethanol).

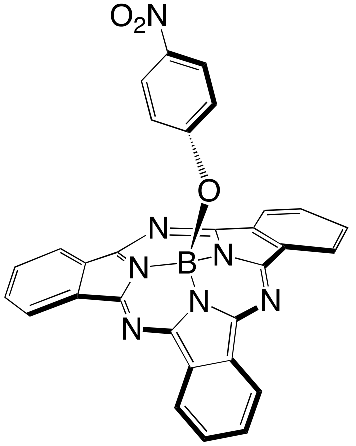

4.2.3. *Synthesis of B-(coumarinoxy) [subphthalocyaninato]boron(III):* SUB-COUM 3

To a solution of **SUB-Cl 1** (30 mg, 0.07 mmol) in toluene (4 mL) was added 7-hydroxycoumarine (57 mg, 0.35 mmol). The reaction mixture was heated under reflux conditions for 2 days and monitored by LCMS. Thereafter, the solvent was removed under reduced pressure and the crude product was subjected to alumina gel column chromatography using dichloromethane as the eluent to yield 25 mg (64%) of pure **SUB-COUM 3** as a purple solid. ^{1}H NMR (500 MHz, $CDCl_3$, 300 K, Figure S5): δ (ppm) = 5.27 (d, J = 2.2 Hz, 1H), 5.33 (dd, J = 8.5, 2.3 Hz, 1H), 6.08 (d, J = 9.4 Hz, 1H), 6.83 (d, J = 8.4 Hz, 1H), 7.36 (d, J = 9.4 Hz, 1H), 7.93 (m, 6H), 8.87 (m, 6H). ^{13}C NMR (125 MHz, $CDCl_3$, 300 K): δ (ppm) = 161.25, 156.62, 155.03, 151.61, 143.30, 131.07, 130.22, 128.29, 122.48, 116.31, 113.35, 113.11, 106.41, 77.41, 77.16, 76.91. HR-MS ESI: m/z 557.1527 [M+H]$^+$ (calcd for $C_{33}H_{18}BN_6O_3^+$: 557.1528). HP-LC analysis (system A): retention time 5.68 min, 100% MeCN, 0.1% TFA. Φ_F

(THF) = 0.19 (reference: rhodamine 6G in solution in ethanol).

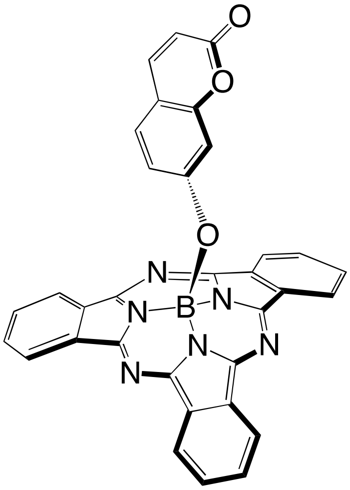

4.3. *Luminescence studies*

4.3.1. *Fluorescence*

Fluorescence measurement and quantum yield. Fluorescence measurements were performed on the Horiba Jobin Yvon Fluorolog spectrofluorometer (software FluorEssence) at 25 °C or 37 °C (using a temperature control system combined with water circulation), with standard fluorometer cells (Labbox, LB Q, light path: 10 mm, width: 10 mm, chamber volume: 3.5 mL). Fluorescence quantum yields were calculated using rhodamine 6G in ethanol ($\Phi_F = 0.96$), Nile blue in ethanol ($\Phi_F = 0.27$), and indocyanine green in DMSO ($\Phi_F = 0.11$) as reference. Excitation was performed at 488 nm (rhodamine 6G), 610 nm (Nile blue), or 725 nm (indocyanine green) for both the sample and the reference. Emission spectra were recorded upon excitation (at a given wavelength) at absorbance intensity between 0.02 and 0.09 (a.u.). Fluorescence quantum yields (Φ_F) were determined by the comparison method, using the following equation:

$$\Phi_F = \Phi_F(\text{Std}) \times \left(\frac{\eta}{\eta(\text{Std})}\right)^2 \times \left(\frac{1-10^{-\text{Abs}}}{1-10^{-\text{Abs(Std)}}}\right) \times \left(\frac{A(\text{Std})}{A}\right)$$

Here, Std corresponds to standard; Φ_F and Φ_F(Std), fluorescence quantum yields; η and η(Std), RIs of solvent; A and A(Std), areas under the fluorescence curves; Abs and Abs(Std), absorbances at excitation wavelength (488 nm).

4.3.2. *Cherenkov luminescence imaging studies: CR detection and CRET studies*

(a) On the Agilent Cary Eclipse spectrofluorometer (measurement parameters: bioluminescence mode, gate time of 10 s, 20 nm emission slit, 3 nm of data interval, Savitzky smoothing factor 5): (i) CR detection: a solution of radioactive species ([^{18}F]-FDG or [^{90}Y]-YCl_3) was mixed with saline solution (0.9% NaCl) to attain a total volume of 1 mL. (ii) CRET studies (radiofluorescence measurements): 400 μL of fluorophore (10^{-3} M in a water miscible solvent) was mixed with a solution of radioactive species ([^{18}F]-FDG or [^{90}Y]-YCl_3), the volume of which was varied because it depends on the desired level of radioactivity to introduce in the cuvette. Subsequent addition of saline solution (0.9% NaCl) was made to attain an overall volume of 1 mL. (b) On the IVIS Lumina II optical imager (measurement parameters: bioluminescence mode, on the open filter mode or with filters, with an acquisition time from 1 s to 1 min). CR detection and CRET studies: The experiment was performed in triplicate on addition of the following solution in each subphthalocyanine-containing well: 10 μL of the subphthalocyanine stock solution (1 mM in DMSO), 32 μL [^{18}F]-FDG corresponding to 10 MBq (in solution in physiological serum, the volume of which was varied because it depends on the desired level of radioactivity to introduce in wells), and 58 μL of DMSO to complete the final volume up to 100 μL. To control wells were added 10 MBq [^{18}F]-FDG and 68 μL DMSO.

Declaration of interests

The authors do not work for, advise, own shares in, or receive funds from any organization that could benefit from this article, and have declared no affiliations other than their research organizations.

Funding

CNRS “Chaire d’Excellence” (RD, 2010–2015) funds allowed to initiate the Cherenkov Luminescence Imaging (CLI) program. The following are also acknowledged: Burgundy/Burgundy Franche-Comté (BFC) Regional Councils (FABER grant (spectrofluorimeter), *3MIM* grant (optical imager), PARI Dual Regional/Université de Bourgogne Innovation Grant (through "Pharmacoimagerie et Agents Théranostiques" project), French Ministry of Higher Education, Research and Innovation for a scholarship (VL)), both ANR-EQPX-IMAPPI and European Union (PO-FEDER-FSE Bourgogne) for their contribution in purchasing radionuclides, Canceropôle Est and SATT-SAYENS for subsequent funding in subsequent development of the Cherenkov Luminescence Imaging (CLI) and Cherenkov Photodynamic Therapy (CLI-PDT) research programs.

Acknowledgments

The following are acknowledged: PACSMUB platform for access to NMR and Mass spectrometers, Preclinical (PIRP) Platform at CGFL for leaving access to their labs.

Supplementary data

Supporting information for this article is available on the journal's website under https://doi.org/10.5802/crchim.335 or from the author.

References

[1] V. Lioret, "Synthèse de molécules optimisées pour l'absorption de la radiation Cherenkov : applications à l'imagerie optique et à la thérapie photodynamique", PhD thesis, Université de Bourgogne Franche Comté, Dijon, 2019.
[2] O. Heaviside, *The Electrician*, 1888, **22**, 147-148.
[3] A. Sommerfeld, *Königliche gesellschaft der Wissenschaften zu Göttingen. Mathematisch Physikalische Klasse Nachrichten*, 1904, 363-439.
[4] E. Curie, *Madam Curie*, Heinemann, London, 1941.
[5] L. Mallet, *C. R. Acad. Sci. Paris*, 1926, **183**, 274-275.
[6] L. Mallet, *C. R. Acad. Sci. Paris*, 1928, **187**, 222-223.
[7] L. Mallet, *C. R. Acad. Sci. Paris*, 1929, **188**, 445-447.
[8] Le Monde, N. Vichney, "L'effet Cherenkov et la découverte du Docteur Mallet", 1958, 9, 4287; Ibid "Un chercheur français, le docteur Mallet, affirme avoir découvert en 1926 le phénomène baptisé "effet Cherenkov" 01/11/1958, 16, 4284.
[9] L. Mallet, *Archives d'Electricité Médicale*, 1928, **Juillet**, 285-289.
[10] P. A. Cerenkov, *C. R. Dokl. Akad. Nauk SSSR*, 1934, **2**, 451-454.
[11] P. A. Cerenkov, *Phys. Rev.*, 1937, **52**, 378-379.
[12] I. M. Franck, I. G. Tamm, *Dokl. Akad. Nauk SSR*, 1937, **14**, 109-114.
[13] J. V. Jelley, *Br. J. Appl. Phys.*, 1955, **6**, 227-232.
[14] P. A. Cherenkov, *Science*, 1960, **131**, article no. 3394, 136-142.
[15] R. Robertson, M. S. Germanos, C. Li, G. S. Mitchell, S. R. Cherry, M. D. Silva, *Phys. Med. Biol.*, 2009, **54**, N355-N365.
[16] A. Ruggiero, J. P. Holland, J. S. Lewis, J. Grimm, *J. Nucl. Med.*, 2010, **7**, 1123-1130.
[17] B. J. Beattie, D. L. J. Thorek, C. R. Schmidtlein, K. S. Pentlow, J. L. Humm, A. H. Hielscher, *PLoS One*, 2012, **7**, article no. e31402.
[18] G. S. Mitchell, R. K. Gill, D. L. Boucher, C. Li, S. R. Cherry, *Philos. Trans. R. Soc. A*, 2011, **369**, 4605-4619.
[19] A. E. Spinelli, M. Ferdeghini, C. Cavedon, E. Zivelonghi, R. Calandrino, A. Fenzi, A. Sbarbati, F. Boschi, *J. Biomed. Opt.*, 2013, **18**, article no. 20502.
[20] D. L. J. Thorek, C. C. Riedl, J. Grimm, *J. Nucl. Med.*, 2014, **55**, 95-98.
[21] M. A. Lewis, V. D. Kodibagkar, O. K. Öz, R. P. Mason, *Opt. Lett.*, 2010, **35**, 3889-3891.
[22] R. S. Dothager, R. J. Goiffon, E. Jackson, S. Harpstrite, D. Piwnica-Worms, *PLoS One*, 2010, **5**, article no. e13300.
[23] D. L. J. Thorek, A. Ogirala, B. J. Beattie, J. Grimm, *Nat. Med.*, 2013, **19**, 1345-1350.
[24] Y. Bernhard, B. Collin, R. A. Decréau, *Chem. Commun.*, 2014, **50**, 6711-6713.
[25] Y. Bernhard, B. Collin, R. A. Decréau, *Sci. Rep.*, 2017, **7**, article no. 45063.
[26] V. Lioret, P.-S. Bellaye, C. Arnould, B. Collin, R. A. Decréau, *J. Med. Chem.*, 2020, **63**, 9446-9456.
[27] V. Lioret, P. S. Bellaye, Y. Bernhard, M. Moreau, M. Guillemin, C. Drouet, B. Collin, R. A. Decréau, *Photodiagnostis Photody. Ther.*, 2023, **44**, article no. 103816.
[28] S. Yu, *Biomed. Imaging Interv. J.*, 2006, **2**, article no. e57.
[29] J. S. Fowler, T. Ido, *Semin. Nucl. Med.*, 2002, **32**, 6-12.
[30] K. Hamacher, H. H. Coenen, G. Stocklin, *J. Nucl. Med.*, 1986, **27**, 235-238.
[31] G. B. Saha, *Fundamental of Nuclear Pharmacy*, 6th ed., Springer, New-York, Heidelberg, Dordrecht, London, 2010.
[32] Y. Bernhard, P. Winckler, R. Chassagnon, P. Richard, E. Gigot, J.-M. Perrier-Cornet, R. A. Decréau, *Chem. Commun.*, 2014, **50**, 13975-13978.
[33] V. Lioret, Y. Rousselin, R. A. Decréau, *Dyes Pigm.*, 2020, **183**, article no. 108696.
[34] H. El-Kashef, *Physica B*, 2000, **279**, 295-301.

ACADÉMIE
DES SCIENCES
INSTITUT DE FRANCE

Comptes Rendus. Chimie
2024, Vol. 27, Special issue S1, p. 105-112
`https://doi.org/10.5802/crchim.264`

Research article

French/Nordic Special Issue on Materials and Coordination Chemistry

Rethinking gold(II) porphyrins: an inherent wave distortion

Abhik Ghosh [*, a] **and Jeanet Conradie** [*, a, b]

[a] Department of Chemistry, University of Tromsø, N-9037 Tromsø, Norway

[b] Department of Chemistry, University of the Free State, P.O. Box 339, Bloemfontein
9300, Republic of South Africa

E-mails: abhik.ghosh@uit.no (A. Ghosh), conradj@ufs.ac.za (J. Conradie)

Abstract. Relativistic DFT (OLYP-D3/ZORA-STO-TZ2P) calculations predict low adiabatic ionization potentials for gold(II) porphyrins, from 4.60 eV for Au[TPP] (TPP = tetraphenylporphyrin) to 5.34 eV for Au[TPFPP] [TPFPP = tetrakis(pentafluorophenyl)porphyrin]. These values are over 1 eV lower than those calculated for analogous silver(II) porphyrins, reflecting much greater relativistic destabilization of the Au 5d orbitals relative to Ag 4d orbitals. Interestingly, our calculations also place the observed structural distortion of Au[TPP] in an entirely new light. The electronic imperative of the Au(II) center to assume a pseudo-d^{10} configuration drives a wave deformation of the porphyrin core that allows for Au($d_{x^2-y^2}$)–porphyrin(π) mixing. The lateral compression–elongation of the porphyrin (unequal pairs of Au–N bonds), in contrast, appears to be a secondary effect, a *consequence* of the wave deformation. The wave distortion results in significant π spin populations on the porphyrin macrocycle, leaving behind only about 20–25% of the spin density on the gold. The effect is specific to gold: silver(II) porphyrins exhibit strictly planar cores with approximate D_{4h} local symmetry at the metal.

Keywords. Gold, Porphyrin, Nonplanar distortion, Ligand noninnocence, Relativistic effect.

Funding. Research Council of Norway (Grant agreement no. 324139) and South African National Research Foundation (Grant agreement nos. 129270 and 132504).

Manuscript received 20 July 2023, revised 11 September 2023 and 27 September 2023, accepted 27 September 2023.

1. Introduction

The consequences of Einstein's special theory of relativity [1,2] manifest themselves in virtually every aspect of the chemistry of gold [3–9]. Relativistic destabilization of the 5d orbitals allows for the existence and stability of such pentavalent Au species as the AuF_6^- anion [10,11] and Au_2F_{10} [12]. Relativistic stabilization of the 6s orbitals on the other hand allows for the existence and stability of the auride anion, a unique metal-based pseudohalide [13–15]. The latter effect is also responsible for gold having the highest electronegativity among all nonradioactive metals, essentially the same as carbon. It is worth mentioning in passing that even more dramatic relativistic effects have been postulated for roentgenium, gold's superheavy congener, notably a $6d^97s^2$ atomic ground state and a heptavalent D_{5h}-symmetric fluoride, RgF_7 [16].

Relativistic effects also explain why stable, structurally characterized Au(II) porphyrins have long remained elusive, in sharp contrast to Cu(II) and Ag(II) porphyrins [17]. The Au(III) center in por-

---

[*] Corresponding authors

ISSN (electronic): 1878-1543

phyrins was long thought to be electrochemically inert [18,19] and only in 2002 was the one-electron reduction of Au(III) porphyrins identified as metal-centered [20,21]. Only in 2017 was Au[TPP] reported as the first structurally characterized Au(II) porphyrin [22]. The structure turned out to be more than a synthetic feat: the metalloporphyrin core was found to exhibit a unique lateral distortion (Figure 1), in contrast to the usual D_{4h} geometry. The distortion, whereby the Au–N bonds in one direction are longer than those in the other direction, was also attributed to a second-order Jahn–Teller effect involving the relativistically destabilized $5d_{x^2-y^2}$ orbital and the relativistically stabilized 6s orbital. A mild wave distortion of the porphyrin was also noted, but was assumed to be incidental to the lateral distortion [22].

In this study, we have critically examined two key aspects of Au(II) porphyrins—their ionization potentials and the putative second-order Jahn–Teller distortion. Relativity was found to downshift the ionization potentials of Au(II) porphyrins by ~0.6 eV, which is severalfold that calculated for Ag(II) porphyrins. Significantly, the present study also places the unusual geometrical distortions of Au[TPP] in an entirely new light. On account of a heretofore unsuspected orbital interaction, ultimately attributable to relativity, it is the wave distortion that emerges as the preeminent stereoelectronic effect in Au(II) porphyrins; the lateral distortion appears merely incidental to the wave distortion.

2. Results and discussion

In this study, we have critically examined the role of relativity in determining two key aspects of Au(II) porphyrins, their ionization potentials and the putative Jahn–Teller distortion. Three Au(II) porphyrins were studied in this work—Au[P], Au[TPP], and Au[TPFPP]—where P, TPP, and TPFPP denote porphine, tetraphenylporphyrin, and tetrakis(pentafluorophenyl)porphyrin, respectively. For comparison purposes, the analogous Ag porphyrins were also studied. Each molecule and its corresponding cation were optimized with scalar-relativistic and two-component spin–orbit DFT as described in the *Computational methods* section.

Table 1. Adiabatic OLYP ionization potentials obtained with nonrelativistic (NR), scalar-relativistic (SR), and two-component spin–orbit (SO) ZORA calculations[a]

Molecule	NR	SR	SO
Ag[P]	6.13	5.93 (6.17)	5.93
Au[P]	5.55	4.90 (4.96)	4.87
Ag[TPP]	5.64	5.57 (5.88)	5.59
Au[TPP]	5.14	4.60 (4.57)	4.60
Ag[TPFPP]	6.50	6.34 (6.67)	–
Au[TPFPP]	5.91	5.36 (5.48)	5.34

[a] The values shown in parentheses are based on single-point B3LYP* calculations on OLYP geometries.

The relativistic calculations revealed unusually low adiabatic IPs for the Au(II) porphyrins (Table 1), which are about 1 eV lower than those of Ag(II) porphyrins and a little under 2 eV lower than those of Zn(II) porphyrins [23] (DFT has long excelled at predicting ionization potentials and photoelectron spectra of porphyrins [24–27]). Both scalar-relativistic and spin–orbit calculations yielded very similar IPs, to within 0.05 eV. For Au, the relativistic effects are large, some 0.7 eV, compared with only 0.05–0.2 eV for Ag, in line with analogous findings from our laboratory on other pairs of 4d and 5d transition metal complexes [28–33]. Substituent effects were also found to be important [25,34]: both for the Ag and Au series, the IP of the TPFPP complex is some three-quarters of an eV higher than that of the TPP complex. Electron-deficient porphyrins thus appear clearly poised to deliver more oxidatively robust Au(II) derivatives.

Turning now to the question of geometry, the Ag(II) complexes all optimized to their expected point groups: D_{4h} for Ag[P] and D_{2d} for Ag[TPP] and Ag[TPFPP] (Figures 2 and 3) [35,36]. In contrast, for the Au analogues of the three molecules, both scalar and spin–orbit relativistic calculations revealed a lateral compression–elongation, much as observed experimentally. Furthermore, like the experimental [22] structure, and DFT-optimized structures evinced a distinct wave distortion. The optimized equilibrium geometries of all the Au(II) structures, accordingly, were found to conform to only C_{2h} symmetry, with the C_2 axis passing through a pair of opposite nitrogen atoms.

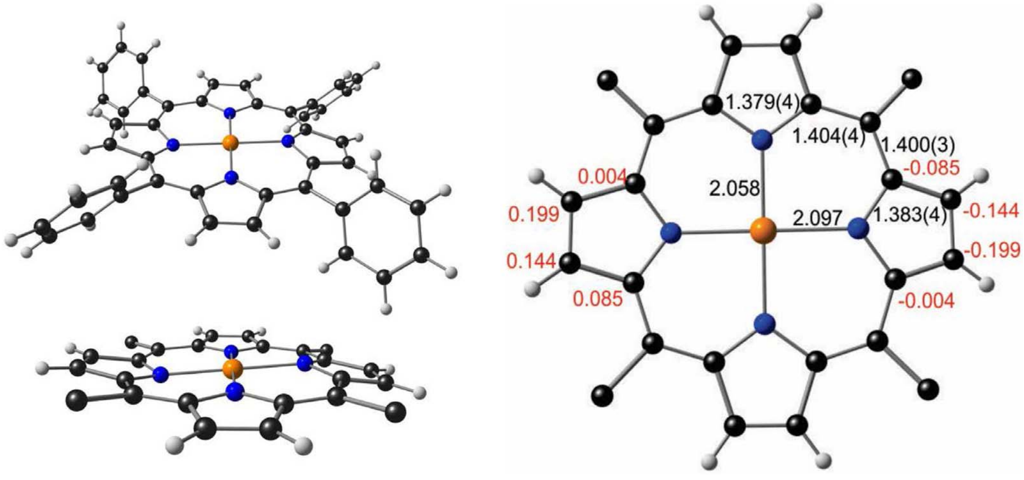

Figure 1. Top left: crystal structure of Au[TPP] (CSD: TEHZOY). Bottom left: view of porphyrin core exhibiting wave distortion. Right: selected bond distances (black) and out-of-plane deformations (red) in Å.

As of now, the unusual core geometry of Au[TPP] has been ascribed to a second-order Jahn–Teller distortion involving the Au 5$d_{x^2-y^2}$ and 6s orbitals [22]. An examination of the scalar-relativistic frontier MOs of each of the three Au(II) porphyrins studied indeed revealed varying degrees of mixing of the d_{z^2}, $d_{x^2-y^2}$, and 6s orbitals. Unlike in a simple Jahn–Teller system (but not uncommonly for second-order Jahn–Teller systems [37,38]), however, the OLYP-D3 Kohn–Sham MOs with major contributions from the three atomic orbitals were found to exhibit a remarkable 8-eV span of orbital energies in these systems. For Au[P], the orbital energies for the α or majority-spin orbitals were −7.63 eV for the primarily d_{z^2}-based HOMO-18, −3.27 eV for the primarily $d_{x^2-y^2}$-based HOMO, and 0.56 eV for the primarily 6s-based LUMO+27. Of the three MOs, it was the lower-energy, primarily d_{z^2}-based HOMO-18, not the $d_{x^2-y^2}$-based HOMO, that was found to exhibit the greatest degree of $d_{x^2-y^2}$ and 6s admixture. The HOMO, it turned out, engages in a very different orbital interaction, namely one with the porphyrin's π-HOMO. Thus, both the HOMOs and spin density profiles of the complexes exhibit surprisingly significant π-amplitudes at the *meso* positions of porphyrin (Figure 2). The Au(II) centers, as a result, carry correspondingly smaller spin populations than the Ag(II) centers in the analogous complexes (Figures 2 and 3). The latter finding greatly intrigued us, as it seemed to indicate an electronic imperative underlying the porphyrin's wave distortion: the Au(II) center appears to exploit the nonplanar wave geometry to suck electron density from the porphyrin's π-HOMO into its 5$d_{x^2-y^2}$ orbital.

To gauge the relative importance of the lateral compression–elongation and the wave distortion, we next optimized Au[P] with scalar-relativistic OLYP-D3 calculations under three different symmetry constraints, D_{4h}, D_{2h}, and C_{2h}, with all MO irreps worked out by hand. Both the D_{4h} and D_{2h} calculations led to non-aufbau orbital occupations (i.e., where LUMO is below the HOMO), an indication of the instability of the molecule under those symmetry constraints. Most interestingly, the D_{2h} optimized geometry did not exhibit the expected lateral distortion and proved essentially identical to the D_{4h} geometry. In other words, the lateral distortion does not occur in the absence of the wave distortion. We are thus led to conclude that *it is the wave distortion that is fundamental and drives the lateral distortion*, and not the other way around.

The above findings lend an entirely new complexion to the electron structure of Au(II) porphyrins. The tendency of the Au(II) center to increase its effective d-electron count parallels a recent study in which a variety of formally Au(III) complexes have been described as quasi-d^{10}, based on theoretical analyses of their bonding interactions [39]. These complexes nevertheless exhibit distinct 2p→5d XANES features,

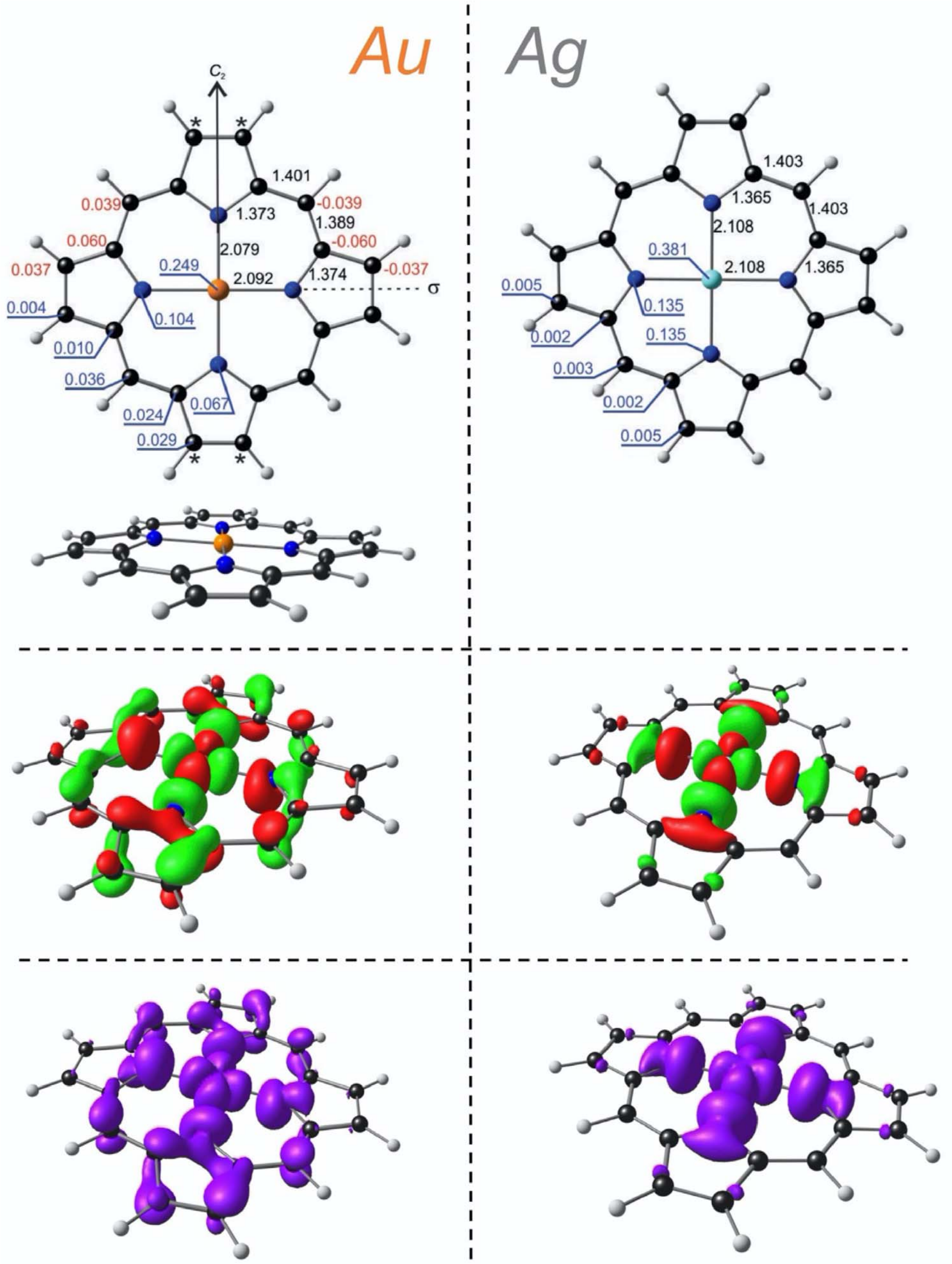

Figure 2. Top: selected OLYP-D3 optimized distances (black), out-of-plane distortions (red), and Mulliken spin populations (blue) for Au[P] (left) and Ag[P] (right). Middle row: HOMOs (SOMOs). Bottom: spin densities.

indicative of a 5d hole. Like many d^{10} complexes, on the other hand, they also exhibit weak, low-energy MLCT transitions in the near-infrared [22]. In this study, TDDFT calculations, which do a rather good job of reproducing the visible absorption spectrum of Au[TPP] (details of which are not particularly relevant), also predict two infrared absorptions with almost vanishingly small oscillator strengths. The

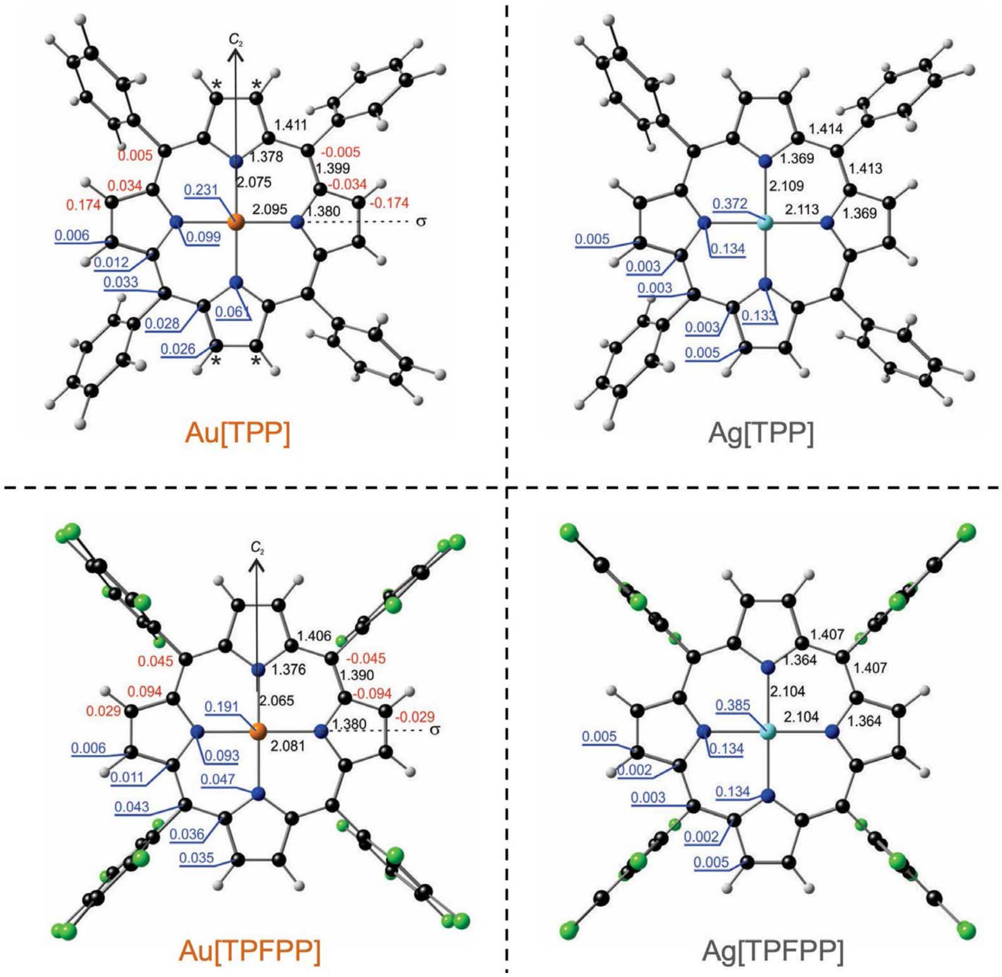

Figure 3. Selected OLYP-D3 optimized distances (black), out-of-plane distortions (red), and Mulliken spin populations (blue) for M[TPP] and M[TPFPP], where M = Ag, Au. All distances are in Å. *Note*: HOMOs (SOMOs) and spin density plots are omitted for these complexes as these are visually almost indistinguishable from those shown in Figure 2 (in spite of quantitative differences).

wavelengths of the two absorptions vary considerably with details of the computational method, such as the choice of the exchange–correlation functional and basis set, but the assignment of the two features seems stable with respect to such details. With the well-calibrated range-separated CAMY-B3LYP functional [40] and the COSMO solvation model [41], the two absorptions in dichloromethane are at 0.55 eV (2215 nm) and 0.66 eV (1863 nm, Figure 4). Given their low energies and intensities, these two features have not been experimentally detected so far, but may be viewed as computational signatures of Au[TPP]. Comfortingly, the electrochemical HOMO-LUMO gaps (defined as the algebraic difference between the oxidation and reduction potentials) of Au(II) porphyrins of ~0.6 eV, which may be inferred from the literature [20,21] are in almost perfect agreement with the CAMY-B3LYP excitation energy.

The inherent, electronically driven wave distortion of Au(II) porphyrins is reminiscent of the inherent saddling of copper corroles [42–45], which is driven by the electronic imperative of the formally empty Cu($3d_{x^2-y^2}$) orbital to accept electron density from the corrole's π-HOMO. A similar orbital in-

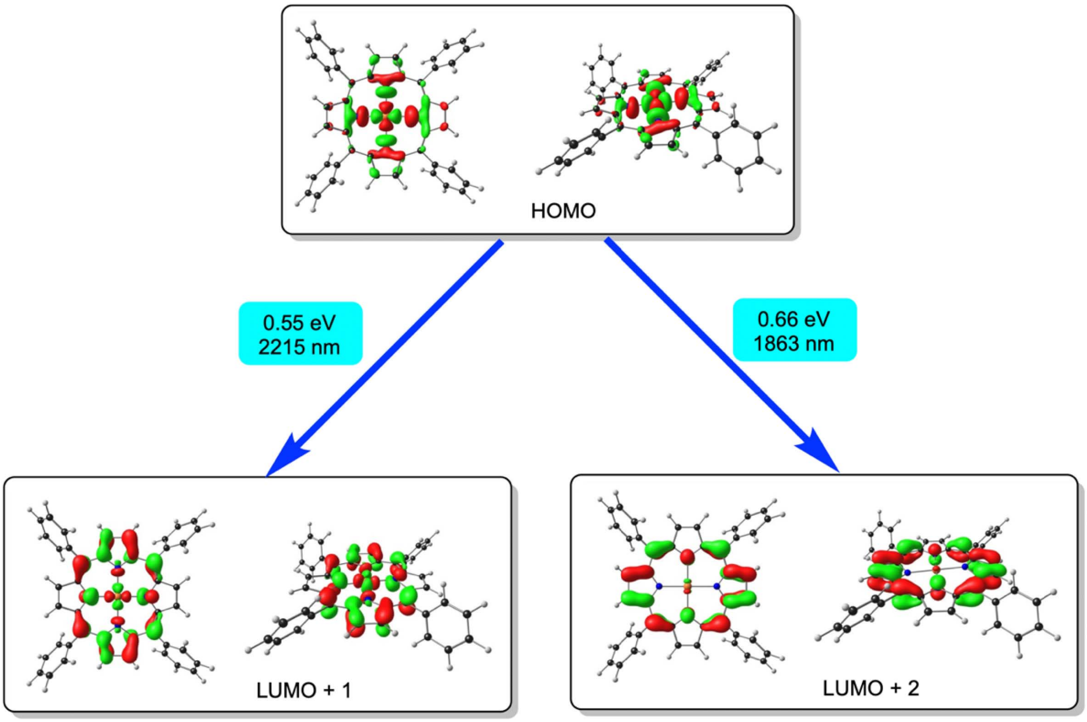

Figure 4. CAMY-B3LYP/STO-TZ2P-derived infrared transitions and their MO composition for Au[TPP].

teraction is less important for silver corroles [46,47] and not at all important for gold corroles [48–52]. The reason for the latter has to do with both relativistic destabilization of the Au(5d$_{x^2-y^2}$) orbital and the exceptionally strong σ-ligand field of the corrole [53]. Charge-neutral gold porphyrins and copper corroles provide rare examples where metal(d)–porphyrinoid(π) interactions alone suffice to engender nonplanar distortions of the macrocyclix ligands, even in the absence of sterically hindered, peripheral substituents [54].

3. Computational methods

Each Au(II) porphyrin and its corresponding cation were optimized with scalar-relativistic and two-component spin–orbit DFT (OLYP [55,56]-D3 [57]) calculations with the ZORA [58] Hamiltonian and ZORA STO-TZ2P basis sets, as well as with nonrelativistic calculations with the same basis sets, all as implemented in the ADF program system [59]. Single-point scalar-relativistic energies were also calculated using the B3LYP* [60,61] functional and found to be in excellent agreement with the OLYP-D3 results. Carefully tested, fine integration grids and tight SCF and geometry optimization criteria were used in all calculations.

4. Conclusion

The present study, in our view, has significantly deepened our electronic-structural understanding of Au(II) porphyrins.

First, the first IPs of Au(II) porphyrins have been found to be unusually low, >1 eV lower than those calculated for Ag(II) porphyrins; this difference is largely attributable to scalar relativistic effects, which are much stronger for gold than for silver. Electron-withdrawing substituents, however, are predicted to yield Au(II) derivatives such as Au[TPFPP] with higher oxidative stability.

Second, our calculations have put a whole new complexion on the experimentally observed structural distortions of Au[TPP]. The primary stereoelectronic effect appears to be a wave distortion driven by an Au(5d$_{x^2-y^2}$)–porphyrin(π) orbital interaction, which allows the formal Au(II) center to assume a pseudo-d^{10} configuration. The lateral distortion allowing for Au 5d$_{x^2-y^2}$-5d$_{z^2}$-6s mixing appears to be a secondary effect, a consequence of the wave deformation. Tellingly, in computational experiments, absent a wave formation, Au(II) porphyrins do not undergo an in-plane lateral distortion.

Declaration of interests

The authors do not work for, advise, own shares in, or receive funds from any organization that could benefit from this article, and have declared no affiliations other than their research organizations.

Data availability statement

All data generated or analyzed in this study are included in this published article and its supplementary information.

Funding

This work was supported in part by grant no. 324139 of the Research Council of Norway (AG) and grant nos. 129270 and 132504 of South African National Research Foundation (JC).

Supplementary data

Supporting information for this article is available on the journal's website under https://doi.org/10.5802/crchim.264 or from the author.

References

[1] P. Pyykkö, *Annu. Rev. Phys. Chem.*, 2012, **63**, 45-64.

[2] A. Ghosh, K. Ruud, *Am. Sci.*, 2023, **111**, 160-167.

[3] J. P. Desclaux, P. Pyykkö, *Chem. Phys. Lett.*, 1976, **39**, 300-303.

[4] P. Schwerdtfeger, *Heteroat. Chem.*, 2002, **13**, 578-584.

[5] P. Pyykkö, *Angew. Chem. Int. Ed.*, 2004, **43**, 4412-4456.

[6] P. Pyykkö, *Inorg. Chim. Acta*, 2005, **358**, 4113-4130.

[7] P. Pyykkö, *Chem. Soc. Rev.*, 2008, **37**, 1967-1997.

[8] A. Leyva-Pérez, A. Corma, *Angew. Chem. Int. Ed.*, 2012, **51**, 614-635.

[9] D. J. Gorin, F. D. Toste, *Nature*, 2007, **446**, 395-403.

[10] K. Leary, N. Bartlett, *J. Chem. Soc. Chem. Commun.*, 1972, 903-904.

[11] K. Leary, A. Zalkin, N. Bartlett, *J. Chem. Soc. Chem. Commun.*, 1973, 131-132.

[12] I.-C. Hwang, K. Seppelt, *Angew. Chem. Int. Ed.*, 2001, **40**, 3690-3693.

[13] A. Sommer, *Nature*, 1943, **152**, 215.

[14] W. E. Spicer, A. H. Sommer, J. G. White, *Phys. Rev.*, 1959, **115**, 57-62.

[15] B. Busse, K. G. Weil, *Angew. Chem. Int. Ed.*, 1979, **18**, 629-630.

[16] J. Conradie, A. Ghosh, *Inorg. Chem.*, 2019, **58**, 8735-8738.

[17] P. J. Brothers, A. Ghosh, in *Fundamentals of Porphyrin Chemistry: A 21st Century Approach* (P. J. Brothers, M. O. Senge, eds.), Wiley & Sons, Hoboken, New Jersey, 2022, 141-240.

[18] M. E. Jamin, R. T. Iwamoto, *Inorg. Chim. Acta*, 1978, **27**, 135-143.

[19] A. Antipas, D. Dolphin, M. Gouterman, E. C. Johnson, *J. Am. Chem. Soc.*, 1978, **100**, 7705-7709.

[20] K. M. Kadish, E. Wenbo, Z. Ou, J. Shao, P. J. Sintic, K. Ohkubo, S. Fukuzumi, M. J. Crossley, *Chem. Commun.*, 2002, **4**, 356-357.

[21] S. Preiß, J. Melomedov, A. W. von Leupoldt, K. Heinze, *Chem. Sci.*, 2016, **7**, 596-610.

[22] S. Preiß, C. Förster, S. Otto, M. Bauer, P. Müller, D. Hinderberger, H. Hashemi Haeri, L. Carella, K. Heinze, *Nat. Chem.*, 2017, **9**, 1249-1255.

[23] A. Ghosh, J. Conradie, *ACS Omega*, 2022, **7**, 40275-40278.

[24] A. Ghosh, *J. Am. Chem. Soc.*, 1995, **117**, 4691-4699.

[25] A. Ghosh, *J. Phys. Chem. B*, 1997, **101**, 3290-3297.

[26] A. Ghosh, T. Vangberg, *Theor. Chem. Acc.*, 1997, **97**, 143-149.

[27] A. Ghosh, *Acc. Chem. Res.*, 1998, **31**, 189-198.

[28] A. B. Alemayehu, H. Vazquez-Lima, K. J. Gagnon, A. Ghosh, *Inorg. Chem.*, 2017, **56**, 5285-5294.

[29] A. B. Alemayehu, H. Vazquez-Lima, L. J. McCormick, A. Ghosh, *Chem. Commun.*, 2017, **53**, 5830-5833.

[30] T. B. Demissie, J. Conradie, H. Vazquez-Lima, K. Ruud, A. Ghosh, *ACS Omega*, 2018, **3**, 10513-10516.

[31] A. B. Alemayehu, L. J. MCormick, H. Vazquez-Lima, A. Ghosh, *Inorg. Chem.*, 2019, **58**, 2798-2806.

[32] J. Conradie, H. Vazquez-Lima, A. B. Alemayehu, A. Ghosh, *ACS Phys. Chem. Au*, 2022, **2**, 70-78.

[33] H. Braband, M. Benz, B. Spingler, J. Conradie, R. Alberto, A. Ghosh, *Inorg. Chem.*, 2021, **60**, 11090-11097.

[34] A. Ghosh, *J. Mol. Struct. THEOCHEM*, 1996, **388**, 359-363.

[35] W. R. Scheidt, J. U. Mondal, C. W. Eigenbrot, A. Adler, L. J. Radonovich, J. L. Hoard, *Inorg. Chem.*, 1986, **25**, 795-799.

[36] W. R. Scheidt, Y. J. Lee, in *Metal Complexes with Tetrapyrrole Ligands I* (J. W. Buchler, ed.), vol. 64, Springer-Verlag, Berlin/Heidelberg, 1987, 1-70.

[37] R. G. Pearson, *Proc. Natl. Acad. Sci. USA*, 1975, **72**, 2104-2106.

[38] H. B. Wedler, P. Wendelboe, D. J. Tantillo, P. P. Power, *Dalton Trans.*, 2020, **49**, 5175-5182.

[39] E. A. Trifonova, I. F. Leach, W. B. de Haas, R. W. A. Havenith, M. Tromp, J. E. M. N. Klein, *Angew. Chem. Int. Ed.*, 2023, **62**, article no. e202215523.

[40] Y. Yakinaga, S. Ten-no, *Chem. Phys. Lett.*, 2008, **462**, 348-351.

[41] A. Klamt, G. Schüürmann, *J. Chem. Soc. Perkin Trans. 2*, 1993, **2**, 799-805.

[42] A. B. Alemayehu, E. Gonzalez, L. K. Hansen, A. Ghosh, *Inorg. Chem.*, 2009, **48**, 7794-7799.

[43] A. B. Alemayehu, L. K. Hansen, A. Ghosh, *Inorg. Chem.*, 2010, **49**, 7608-7610.

[44] K. E. Thomas, J. Conradie, L. K. Hansen, A. Ghosh, *Eur. J. Inorg. Chem.*, 2011, 1865-1870.

[45] H. Lim, K. E. Thomas, B. Hedman, K. O. Hodgson, A. Ghosh, E. I. Solomon, *Inorg. Chem.*, 2019, **58**, 6722-6730.

[46] K. E. Thomas, H. Vazquez-Lima, Y. Fang, Y. Song, K. J. Gagnon, C. M. Beavers, K. M. Kadish, A. Ghosh, *Chem. Eur. J.*, 2015, **21**, 16839-16847.

[47] R. Sarangi, L. J. Giles, K. E. Thomas, A. Ghosh, *Eur. J. Inorg. Chem.*, 2016, 3225-3227.

[48] K. E. Thomas, A. B. Alemayehu, J. Conradie, C. Beavers, A. Ghosh, *Inorg. Chem.*, 2011, **50**, 12844-12851.

[49] E. Rabinovich, I. Goldberg, Z. Gross, *Chem. Eur. J.*, 2011, **17**, 12294-12301.

[50] K. E. Thomas, C. M. Beavers, A. Ghosh, *Mol. Phys.*, 2012, **110**, 2439-2444.

[51] J. Capar, J. Zonneveld, S. Berg, J. Isaksson, K. J. Gagnon, K. E. Thomas, A. Ghosh, *J. Inorg. Biochem.*, 2016, **162**, 146-153.

[52] K. E. Thomas, K. J. Gagnon, L. J. McCormick, A. Ghosh, *J. Porphyr. Phthalocyan.*, 2018, **22**, 596-601.

[53] A. B. Alemayehu, K. E. Thomas, R. F. Einrem, A. Ghosh, *Acc. Chem. Res.*, 2021, **54**, 3095-3107.

[54] S. Ganguly, A. Ghosh, *Acc. Chem. Res.*, 2019, **52**, 2003-2014.

[55] N. C. Handy, A. J. Cohen, *Mol. Phys.*, 2001, **99**, 403-412.

[56] C. Lee, W. Yang, R. G. Parr, *Phys. Rev. B*, 1988, **37**, 785-789.

[57] S. Grimme, J. Antony, S. Ehrlich, H. Krieg, *J. Chem. Phys.*, 2010, **132**, article no. 154104.

[58] E. van Lenthe, E. J. Baerends, J. G. Snijders, *J. Chem. Phys.*, 1993, **99**, 4597-4610.

[59] G. te Velde, F. M. Bickelhaupt, E. J. Baerends, C. Fonseca Guerra, S. J. A. van Gisbergen, J. G. Snijders, T. Ziegler, *J. Comput. Chem.*, 2001, **22**, 931-967.

[60] M. Reiher, O. Salomon, B. Artur Hess, *Theor. Chem. Acc.*, 2001, **107**, 48-55.

[61] O. Salomon, M. Reiher, B. A. Hess, *J. Chem. Phys.*, 2002, **117**, 4729-4737.

ACADÉMIE
DES SCIENCES
INSTITUT DE FRANCE

Comptes Rendus. Chimie
2024, Vol. 27, Special issue S1, p. 113-123
`https://doi.org/10.5802/crchim.328`

Research article

French/Nordic Special Issue on Materials and Coordination Chemistry

Synthesis and characterization of *cis*-bisdiphenylphosphinoethene gold(I) complexes

Océane Yvonne Odette Fayet [a], **Stefano Crespi** [a] and **Andreas Orthaber** [*, a]

[a] Department of Chemistry Ångström Laboratories – Synthetic Molecular Chemistry,
BOX 523 Uppsala (75120), Sweden
E-mail: andreas.orthaber@kemi.uu.se (A. Orthaber)

Océane Yvonne Odette Fayette dedicates this manuscript to her grandmother who never had the opportunity to finish her chemistry degree

Abstract. A series of solid-state structures of gold(I) complexes using the semi-rigid *cis*-1,2-bis(diphenylphosphino)ethene (= *cis*-**bdppe**) ligand are reported. The proximity of the phosphine donor atoms of the bidentate ligand framework greatly favors formation of mononuclear over dinuclear complexes. Structural analysis and theoretical studies shed further light on counter intermolecular packing motifs in the solid state including interactions of solvent, ligand and counterion fragments.

Keywords. Aurophilic interactions, Gold(I) complex, Single crystal X-ray diffraction.

Funding. Swedish Research Council (grant nos. 2017-03727, 2021-05414, and 2022-06725), ERASMUS program.

Manuscript received 31 August 2023, revised 29 April 2024, accepted 23 July 2024.

1. Introduction

Coinage metals are well known for their versatile coordination chemistry, yielding a large variety of structural motifs, which are strongly influenced by ligating donor atoms, denticity and geometry of ligands [1–4]. Importantly, secondary interactions like van der Waals, dipole, dispersive, metallophilic interactions often play decisive roles in supramolecular arrangements and solid state-packing. In particular, gold(I) is prone to form simple linear coordination compounds with coordination number two ($CN = 2$), where the gold(I) ion can further engage in moderate to strong metallophilic, i.e. aurophilic, interactions [5]. These exhibit strengths comparable to strong hydrogen bonding and allow stabilization of inter- and intramolecular arrangements alike. The former often leads to preferred conformations, while the latter can lead to extended supramolecular structures observable in the solid-state and solution [6,7]. Observation of these effects in multinuclear clusters can also be interpreted using the premise of cooperativity to further increase their strength, and importance.

Chelating effects are well understood for a variety of ligands possessing energetically favorable binding to a single metal (cation). Nonetheless, multidentate phosphine ligands are also well known to stabilize high nuclearity gold cluster compounds balancing the benefits of aurophilic/metallophilic and chelating effects [8,9]. However, subtle steric effects of the chelating ligand may have large repercussions on the nuclearity and coordination environment [10,11], the latter also playing important roles in catalytic applications [12]. Other non-classical interactions such as halogen or hydrogen bonding involving donors and acceptors other than oxygen and nitrogen are of great

---

[*] Corresponding author

ISSN (electronic): 1878-1543

interest. Halide interactions with acidic hydrogen atoms of "non-coordinating" solvents such as chlorinated alkanes offer a variety of possibilities. In particular, chloroform and DCM have been subject to extensive studies revealing their importance in intermolecular stabilization and packing effects in the solid-state [13]. For example, chloride (and other halide) ions are often found in a hexacoordinated environment stabilized by chloroform X···H–C hydrogen bonding interactions [14,15]. Similar chloroform halide interactions are found in a variety of organic and inorganic molecular systems [16–20]. Spectroscopic and theoretical analyses of such chloroform and bromoform–chloride interactions clearly showed their affinity towards secondary solid-state interactions [18,21,22].

We detail the different aspects of primary and secondary factors that govern the formation of mono- and dinuclear gold clusters based on the rigid bidentate *cis*-1,2-bis(diphenylphosphino)ethene (= *cis*-**bdppe**) ligand. In this combined theoretical and experimental/structural investigation of selected complexes, we elucidate the structural diversity of these deceivingly simple coordination compounds [23].

2. Results

Synthesis of linear phosphine gold halide complexes is typically achieved by the straightforward ligand substitution reaction starting from chloridotetrahydrothiophene gold(I), [AuCl(tht)], or similar thioether precursors with phosphine ligands in a suitable solvent such as DCM, chloroform or THF [24,25]. Our initial attempts to prepare a dinuclear gold complex based on *cis*-1,2-bis(diphenylphosphino)ethene (= *cis*-**bdppe**) in a 2:1 gold:ligand ratio were unsuccessful. Reactions in concentrated chloroform solutions resulted in the formation of a mononuclear complex along with unreacted gold precursor (Scheme 1).

Single crystals of this complex have been obtained by slow evaporation of the solvent, revealing the molecular structure of the complex as a gold(I) center tetrahedrally coordinated by two *cis*-**bdppe** ligands. (Figure 1) Complex **1-Cl** crystallizes in the monoclinic space group *C2/2* with half of the molecule present in the asymmetric unit. The two ligands form a slightly distorted tetrahedral arrangement around the gold center (twist of the least squares planes 104.25(5)°). The gold–phosphorus distances are in the expected range of gold(I) phosphine complexes (P1–Au1 2.375(1) Å and P2–Au1 2.372(1) Å). Notably, the chloride counterion is stabilized by four chloroform molecules illustrating the ability of the acidic solvent proton to engage in hydrogen bonded interactions (C–H···Cl donor acceptor distance and angles of 3.294(3)/3.354(2) Å) and 149.1(2)°/144.3(1)°, respectively. Moreover, slightly longer hydrogen bonding interactions with the ethene bridge of the ligands are also observed (C21···Cl 3.574(2) Å and C1···Cl 3.639(2) Å). A Hirshfeld surface analysis of the chloride fragment (Figure 1b) illustrates the hydrogen bonding interactions of the solvent molecules and the ligand backbone. Notably, the yellow single crystals of **1-Cl** show discoloration and lose their crystallinity over time, presumably due to solvent loss.

We utilized the geometry obtained from X-ray diffraction as the starting point of computational analysis. We preoptimized the geometry using the semiempirical tight-binding GFN2-xTB method, which is known to provide optimal molecular geometries for gold complexes [26], followed by a second geometry optimization at the r^{2}SCAN-3c level. As for the tight-binding approach, this composite method is reported to provide fast and reliable geometries for organo-gold species [27]. The structure was characterized as a true minimum, with no relevant imaginary frequencies.

We studied the orbital contributions governing the intermolecular interactions in the metal complex by applying Weinhold's Natural Bond Orbital (NBO) analysis. In particular, we studied the second-order energy terms ($E(2)$) that arise from the interaction of two unperturbed NBOs, which provide a quantitative value for the stereoelectronic stabilization associated with that specific orbital interaction. As expected, one source of intermolecular stabilization comes from the negative hyperconjugation of the lone pairs of the chloride anion with the C–H σ* orbitals of chloroform. We found an analogous negative hyperconjugative effect affording $n_{\mathrm{Cl}} \rightarrow \sigma^*_{\mathrm{CH}}$ values ranging between 2–4 kcal·mol^{-1} (see Table 1 and Figure 2). Most interestingly, we found a hyperconjugative effect between the halide and the C–H bonds of the *cis*-**bdppe** ligand (see Figure 2). The stabilization associated with these perturbations is minimal (1–1.3 kcal·mol^{-1}), but still relevant to explain

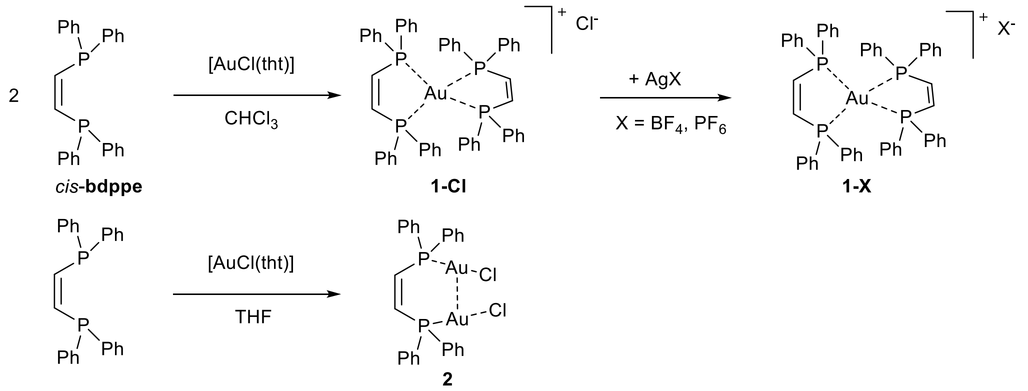

Scheme 1. Synthesis of mono- and dinuclear gold complexes of diphosphine ligand *cis*-**bdppe**.

the peculiar apical position that the halide assumes in the geometry of the complex.

Exclusive formation of this complex can be improved by maintaining a strict 1:1 ratio of metal precursor to ligand and performing the reactions in chloroform (Scheme 1). The crude product was purified by washing with cold ethanol yielding 96% of analytically pure compound **1-Cl**. We hypothesized that the poor solubility of the gold precursor and the chloride-stabilizing nature of chloroform are the main reasons for the formation of this product. Hence further reactions were conducted in different coordinating solvents. Reactions in THF at higher concentrations (>0.1 M) gave a product mixture, while reactions in THF at lower concentrations (1–2 mM) exclusively resulted in formation of dinuclear complex **2** in good yields. Upon removal of all volatiles and washing with ethanol, the THF insoluble portion contained mainly **1-Cl**, and the soluble fraction left for crystallization provided analytically pure material of complex **2** (yield 78%). The complex crystallized in the monoclinic space group *Cc* with one molecule in the asymmetric unit (Figure 4). The dinuclear complex **2** showed a slight decrease of the gold phosphine distance to 2.231(1) Å and 2.237(1) Å for P1–Au1 and P2–Au2, respectively. The spatial arrangement of the diphosphine and moderate aurophilic interactions led to an intramolecular Au1–Au2 distance of 3.0313(3) Å—below the sum of their van der Walls radii (3.32 Å)—which indicates moderate aurophilic interactions. While the ligand backbone is essentially co-planar, the diphenylphosphine-C single bond rotation creates a twisted arrangement of the nearly linear phosphine gold(I) chloride fragments (Cl–Au···Cu–Cl torsion angle of 51.96(6)°).

Removing the coordinating chloride ions from the dinuclear complex **2** by non- or weakly coordinating anions using suitable silver(I) salts proved to be difficult and led to complex mixtures of products, including a tetrahedrally coordinated gold ion, determined by ^{31}P-NMR spectroscopy. Unambiguous identification of this species was obtained by single crystal X-ray diffraction of crystal directly obtained by slow evaporation of the crude reaction mixture. Targeted synthesis of these tetrahedral coordination compounds **1-X** by treating **1-Cl** with suitable silver(I) salts gave essentially quantitative conversions. Compound **1-BF$_4$** and **1-PF$_6$** crystallized in the triclinic space group *P-1* and monoclinic space group *P2*$_1$ with one and two molecules in the asymmetric unit, respectively. The solid-state structure of **1-PF$_6$** also contained disordered solvent molecules which were treated as diffuse scattering using solvent masking. Substituting the chloride of complex **1-Cl** with a tetrafluoroborate (**1-BF$_4$**) or hexafluorophosphate (**1-PF$_6$**) barely affected the direct gold(I) coordination (P–Au distances ranging from 2.3859(4) Å to 2.3996(3) Å) and 2.356(6) Å to 2.394(6) Å, respectively. However the folding angle of the P2Au planes varied significantly: 98.1(1)° (**1-BF$_4$**) and 110.2(2)° (**1-PF$_6$**) compared to 104.7(4)° (**1-Cl**). The tetrafluoroborate anion is positioned in between the diphenylphoshine groups from the two ligands. Weak hydrogen bonding interactions of the tetrafluoroborate and intermolecular π-stacking (centroid distances 3.373(1) Å) contribute to the solid-state packing of **1-BF$_4$**. Similarly, π-interactions **1-PF$_6$**

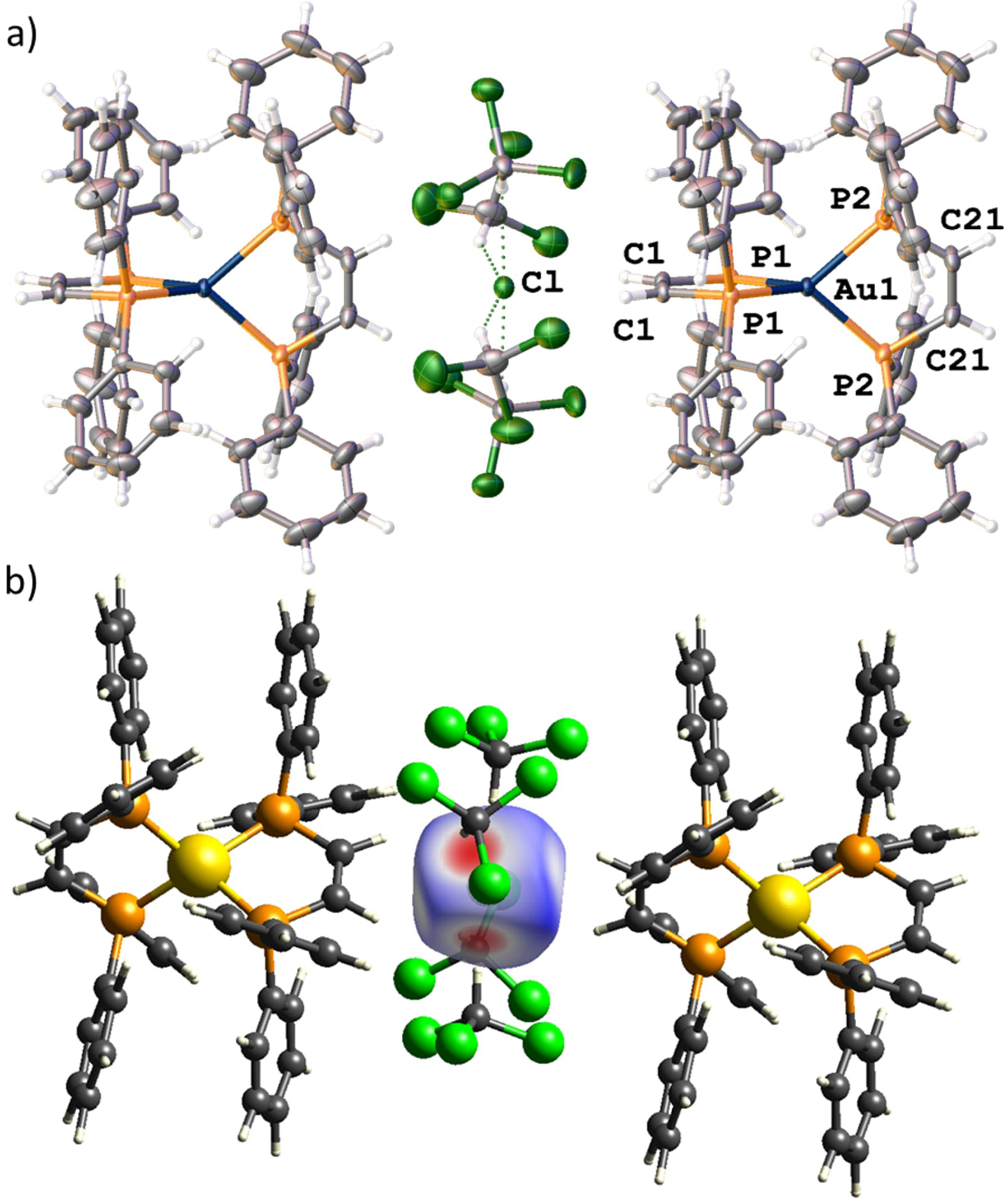

Figure 1. (a) Solid-state structure of mononuclear complex **1**. ORTEP style representation with ellipsoids drawn at a 50% probability level. Further crystallographic details are elaborated in the experimental section. (b) Hirshfeld surface analysis highlighting the hydrogen bonded interactions of the chloride fragment.

(for details, see Supporting Information Figures S1–S2) dominate the solid-state packing. In contrast to **1**-BF_4, **1**-PF_6 and **1**-Cl have the counterions and solvent molecules (THF and $CHCl_3$, respectively) in close proximity to the ethylene bridge. The differences of the counterion position and additional solvation effects provide a rationale for the large differences observed in the discussed folding angles. The gold (coinage metal) coordination environment is in good agreement with previously reported [M(I)(*cis*-**bdppe**)$_2$]PF_6 complexes (M = Au and Cu) [28]. In a slight variation of this ligand, the diphosphine

Table 1. Relevant $E(2)$ values associated with selected hyperconjugative interactions in one of the orbitals depicted in Figure 3

NBO number (Donor orbital)	Donor orbital	NBO number (Acceptor orbital)	Acceptor orbital	$E(2)$ (kcal·mol^{-1})
156	LP Cl_{102}	350	BD* C_4–H_5	1.25
156	LP Cl_{102}	447	BD* C_{78}–H_{79}	1.03
157	LP Cl_{102}	350	BD* C_4–H_5	0.25
157	LP Cl_{102}	447	BD* C_{78}–H_{79}	0.46
158	LP Cl_{102}	350	BD* C_4–H_5	0.28
158	LP Cl_{102}	447	BD* C_{78}–H_{79}	0.13
155	LP Cl_{102}	479	BD* C_{106}–H_{107}	1.64
157	LP Cl_{102}	479	BD* C_{106}–H_{107}	2.48
158	LP Cl_{102}	479	BD* C_{106}–H_{107}	4.32
155	LP Cl_{102}	483	BD* C_{111}–H_{112}	0.71
156	LP Cl_{102}	483	BD* C_{111}–H_{112}	1.86
157	LP Cl_{102}	483	BD* C_{111}–H_{112}	3.11
158	LP Cl_{102}	483	BD* C_{111}–H_{112}	2.98
155	LP Cl_{102}	487	BD* C_{116}–H_{117}	0.79
156	LP Cl_{102}	487	BD* C_{116}–H_{117}	1.21
157	LP Cl_{102}	487	BD* C_{116}–H_{117}	3.51
158	LP Cl_{102}	487	BD* C_{116}–H_{117}	3.00
155	LP Cl_{102}	491	BD* C_{121}–H_{122}	1.59
157	LP Cl_{102}	491	BD* C_{121}–H_{122}	1.92
158	LP Cl_{102}	491	BD* C_{121}–H_{122}	4.46

LP: lone pair; BD*: antibonding orbital; the index as a subscript for the atoms of each bond corresponds to the atom index in the cartesian coordinate file.

2,3-bis(diphenylphosphino)maleic acid (*dpmaa*) could also be targeted to form either a mononuclear tetrahedral or a dinuclear gold complex. In view of the high solubility in water, cytotoxicity tests revealed potential applications as anti-tumor agents [29]. The related 2,3-bis(diphenylphosphino)maleic-N-phenylimide ligand showed similar coordination behavior forming both mono- and dinuclear complexes [30,31].

Despite the easy of formation of the mononuclear complex, treatment of **2** with silver triflate and excess of ligand partially suppressed its formation and a dinuclear complex **3** (Scheme 2 containing two ligands was formed in an inseparable mixture with **1-OTf**. Similarly, treatment of **2** with silver tetrafluoroborate led to the identification of **1-BF$_4$**. The mononuclear cations **1**$^+$ have been identified by their characteristic ^{31}P NMR resonance, as well as their crystal structure (see Supporting Information). Unambiguous identification of the molecular structure of compound **3** was provided by single crystal X-ray diffraction of colorless blocks that crystallized directly from the reaction mixture (Figure 5). Dinuclear complex **3** crystallized in the centrosymmetric space group *P-1* with half of a molecule in the asymmetric unit. The gold atoms are modeled with a positional disorder having site occupancy factors of 89.5% and 10.5%. Two gold atoms bridge the ligands with an Au···Au distance of 2.9908(4) Å and 3.051(4) for the major and minor component respectively, which is comparable to that observed in **2**, despite the shorter intraligand P1···P2 distance (3.525(2) Å). In addition,

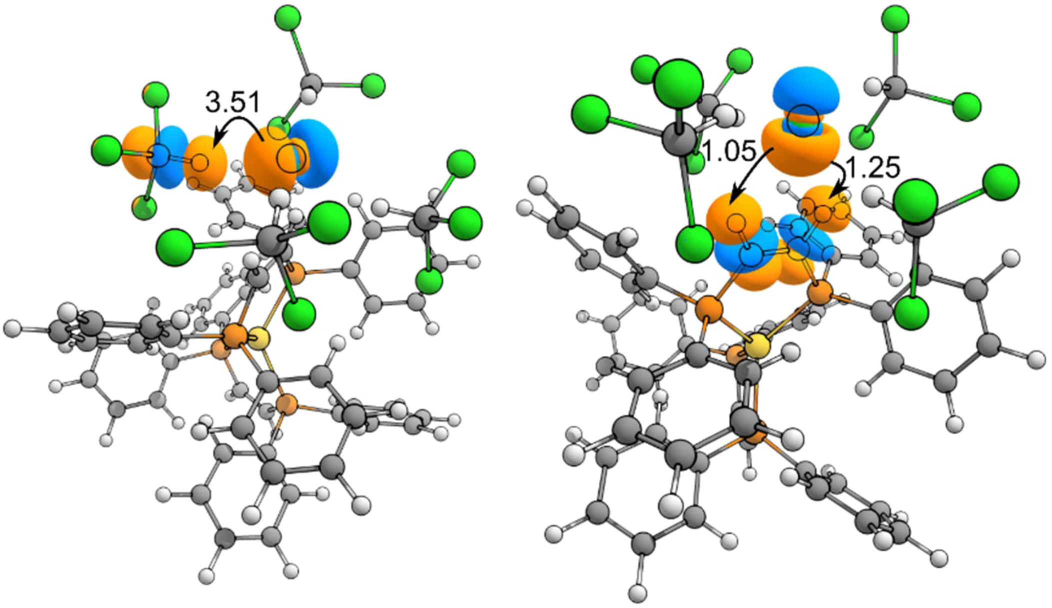

Figure 2. Geometry of the gold complex obtained at r^{2}SCAN-3c level of theory. The main $n_{\mathrm{Cl}} \rightarrow \sigma^*_{\mathrm{CH}}$ NBO interactions (in kcal·mol^{-1}) are depicted: the chloride-chloroform (left) and chloride-ligand (right) ones.

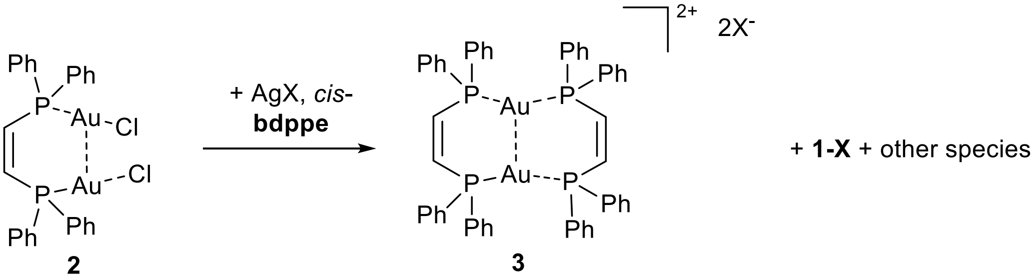

Scheme 2. Attempted synthesis of **3**, under the formation of various side products including **1** and unidentified species.

π–π-interactions (centroid distances 3.435(8) Å) result in a partially rigidified diphenylphosphine backbone. The inter-ligand P···Au···P arrangement is slightly contorted (162.3(1)°), forming a near ideal plane *plane1* (P1Au1P1′P2′Au1′P2) with an average deviation of 0.1 Å, while the planes spanned by the ligand backbone *plane2* (P1C1C21P2) form an overall chair like arrangement and a fold angle 48.8(3)°between *plane1* and *plane2*. In a similar approach, **2** was treated with silver trifluoroacetic acid (2.5 equiv) and subsequently added to a solution of 4,4′-bipyridine; however predominant formation of tetrahedrally coordinated mono-nuclear gold complex was observed.

Neither the mononuclear nor the dinuclear complexes show any appreciable emission with UV irradiation in solution and solid state. This is, in particular, surprising given the short intramolecular Au···Au distances of the dinuclear complexes, which is indicative of aurophilic interactions and contrasts the observed emission of higher nuclearity clusters using this and similar ligand systems [32].

3. Conclusions

The chemistry of these rigid diphosphine ligands having an unsaturated spacer is dominated by the balance of chelating and aurophilic effects that lead

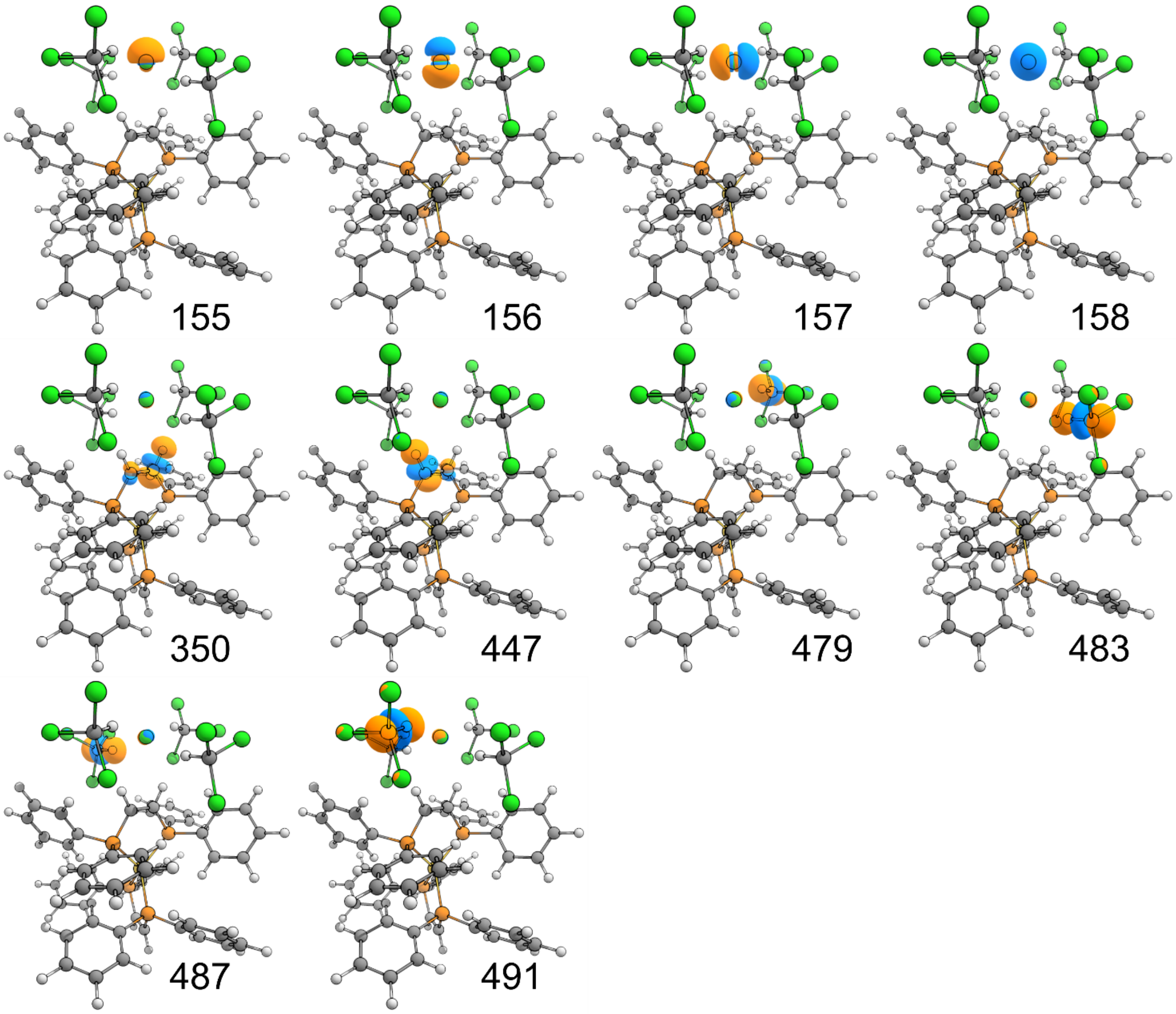

Figure 3. Depiction of the relevant NBOs (isovalue 0.05) listed in Table 1. Each number corresponds to the index value of the NBO.

to mono and dinuclear complexes. Primarily, reaction conditions such as ligand:gold ratio, solvent and concentration of reagents also lead to different products. Further, non-covalent interactions play decisive roles in the solid-state packing and may impact their solution behavior. Notably, the prepared dinuclear gold(I) complexes are non-emissive, which hints at dominating non-radiative decay pathways. With this study we have elucidated few of the factors that direct the coordination behavior, the simple bidentate phosphine ligand towards Au(I) centers, and provide more insights into the rational synthesis of related derivatives.

4. Experimental Section

4.1. *General*

All chemicals were obtained from commercial suppliers and used as received. All reactions and products were protected from prolonged exposure to sunlight using aluminum foil or amberized glass.

4.2. *X-ray crystallography*

Crystallographic data sets were collected from single crystal samples mounted on a loop fiber and

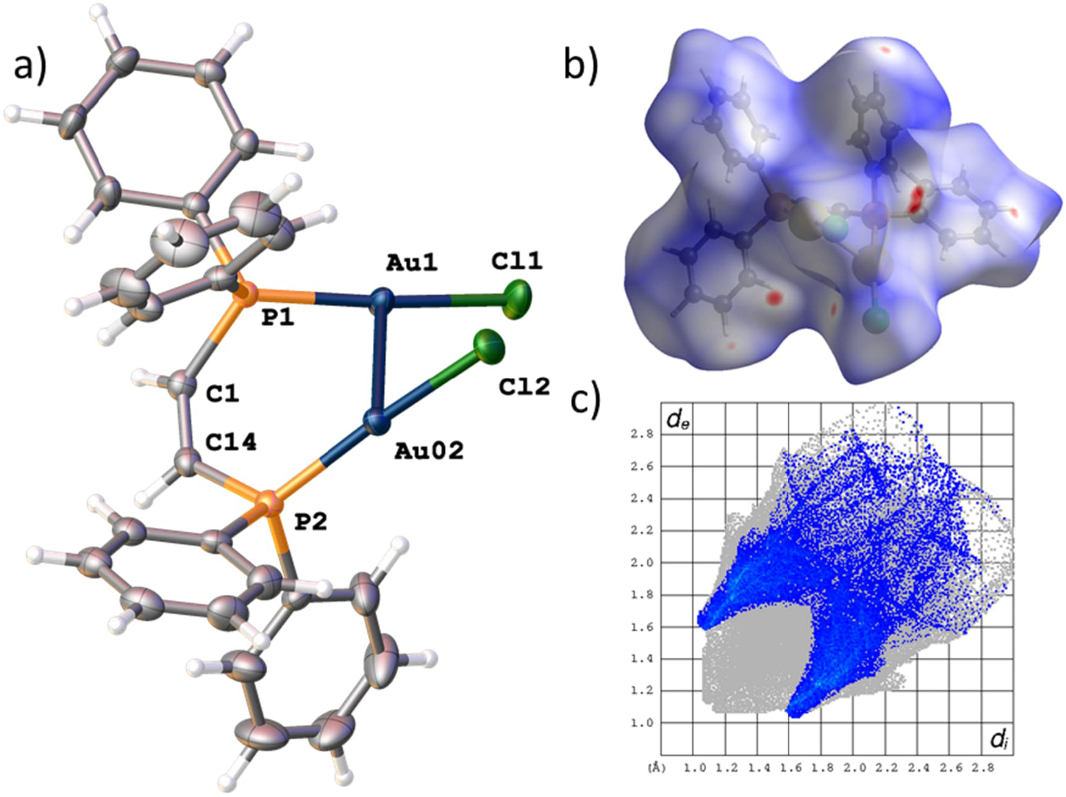

Figure 4. Solid-state structure of mononuclear complex **2** and Hirshfeld surface analysis. (a) ORTEP style representation with ellipsoids drawn at a 50% probability level. Further crystallographic details are elaborated in the experimental section. Red areas indicate dominating intermolecular CH···π interactions. (b) Hirshfeld surface plot. (c) Short intermolecular contacts; highlighted in blue H···C interactions.

coated with high viscosity Fomblin PFPE (Hampton Research). Collection was performed using a Bruker SMART APEX diffractometer equipped with an APEXII CCD detector, a 3-circles goniometer, and a MoK_α-microfus sealed tube. The crystal-to-detector distance was 5.0 cm, and the data collection was carried out in 512 × 512-pixel mode. Cell refinement and data reduction were performed with SAINT (Bruker AXS), absorption correction was done by multi-scan methods using SADABS [33,34]. The structure was solved by direct methods and refined using SHELX suite of programs [35,36] using OLEX2 [37]. Full details concerning the data sets and crystal resolutions can be found in the respective CIF files stored at the Cambridge Crystallographic Data Centre under the allocated deposition numbers CCDC: 2291875-2291879.

4.3. *Computational methods*

Preliminary optimizations of the geometries were obtained using xTB 6.6.0 [38] at GFN2-xTB level002E. Optimization and frequency analysis at the DFT level were performed using ORCA 5.0.3 [39] with r^2SCAN-3c method [40]. Finally, NBO analysis was performed using NBO 7.0.9 software package [41]. The cartesian coordinates of the optimized geometry, the Molden file with the NBOs and the ORCA output of the NBO analysis can be found in a figshare repository [42].

4.4. *Synthesis*

4.4.1. *Synthesis of [AuCl(tht)]*

Tetrahydrothiophene gold(I) chloride was prepared in a slightly modified way than reported in

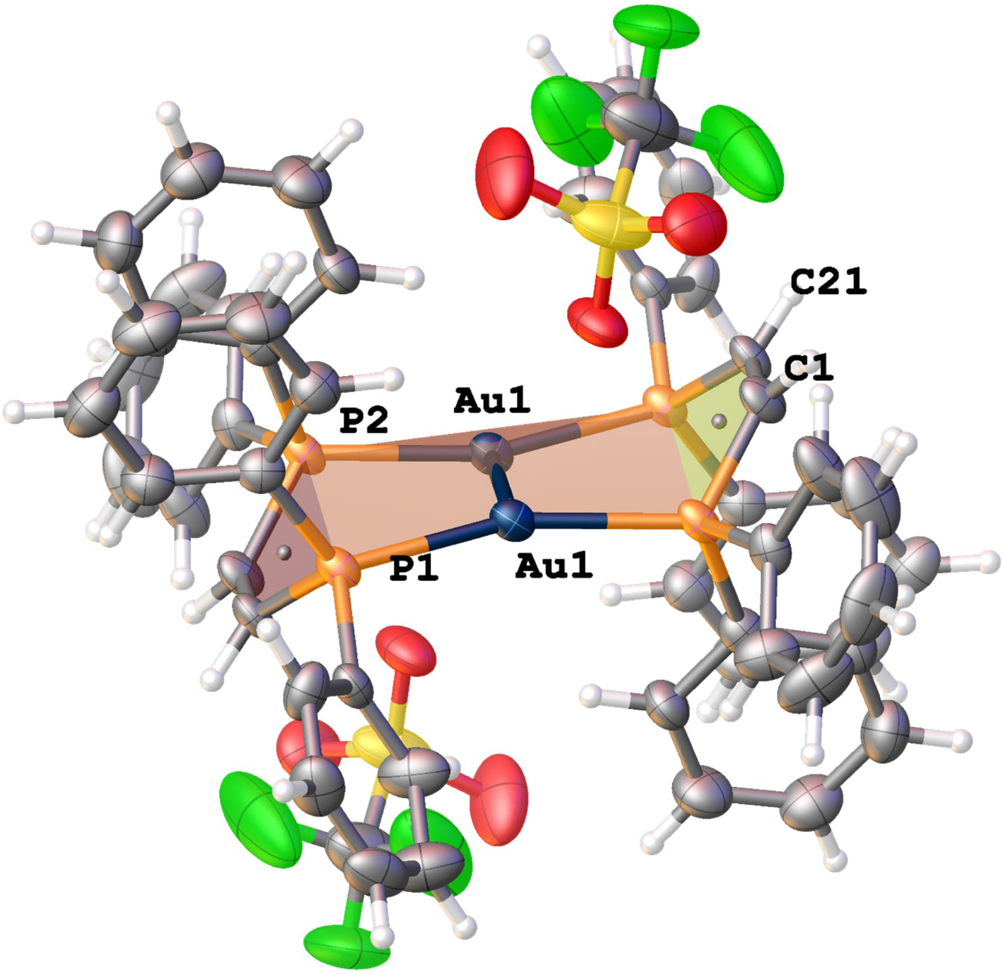

Figure 5. Solid-state structure of dinuclear complex **3**. ORTEP style representation with ellipsoids drawn at a 50% probability level. Further crystallographic details in the experimental section.

literature [43]. Tetrahydrothiophene (C_4H_8S, 45 µL, 0.51 mmol, 1.4 eq) was added to a suspension of tetrachloroauric acid ($H[AuCl_4]$, 123 mg, 0.36 mmol, 1 eq) in water (1 mL)/EtOH (5 mL). The initial yellow precipitate changed to a white precipitate within 15 min. The precipitate was filtered and washed twice with cold EtOH (10 mL) to yield 94% of analytically pure product. The solution was filtered and subjected to slow evaporation of the solvent protected from light, giving the corresponding complexes in good yields (95% and 92%, respectively) as microcrystalline powders. Single crystals suitable for X-ray diffraction were obtained by slowing down the evaporation of THF.

4.4.2. *Synthesis of **1-Cl***

Tetrahydrothiophene gold(I) chloride (44 mg, 0.14 mmol, 1 eq) and $Ph_2P–C=C–PPh_2$ (*cis*-**bdppe**, 108 mg, 0.27 mmol, 2 eq) were dissolved in chloroform (5 mL) and stirred with protection from light for 24 h. Filtration, followed by slow evaporation of all solvents gave **1-Cl** in 96% yield as large yellow crystalline material suitable for single crystal diffraction. Upon further drying of the material under reduced pressure, removal of residual tht also results in complete discoloration of the material which is ascribed to the loss of chloroform solvate molecules. NMR spectroscopic data is in agreement with previously reported data of the cationic complex **1-OTf** and **1-PF$_6$**:[32] ^{1}H NMR (400 MHz, CD_2Cl_2) δ 7.53–7.40 (m, 4H), 7.33 (dd, *J* = 10.1, 7.9 Hz, 8H), 7.15 (td, *J* = 8.0, 6.6 Hz, 25H) ppm. ^{31}P NMR (161.8 MHz, CD_2Cl_2) δ 23.1 ppm.

4.4.3. *Synthesis of **1-BF$_4$** and **1-PF$_6$***

A solution of **1-Cl** (40 mg) in THF (10 ml) is treated with 1 equivalent of $[Ag(MeCN)_4)]BF_4$ or $[Ag(MeCN)_4)]PF_6$ for 24 h. The solution is filtered and slow evaporation of the solvent protected from light gives the corresponding complexes in good yield (95% and 92%) containing single crystals suitable for X-ray diffraction.

4.4.4. *Synthesis of **2***

Importantly, [AuCl(tht)] (70 mg, 0.22 mmol, 2 eq) must be fully dissolved in THF (ca. 80–100 ml) before *cis*-**bdppe** (43 mg, 0.11 mmol, 1 eq in 5 mL THF) is added. The reaction is stirred overnight, followed by slow evaporation of the solvent (at all time protect from light), upon which small colourless crystals suitable for x-ray diffraction are obtained. Residual tht is removed under reduced pressure, while impurities arising from formation of **1-Cl** can be easily removed by extracting **2** using a minimal amount of THF, which upon solvent removal gives 78% of **2**, while the THF insoluble fraction consists mainly of **1-Cl**. 1H NMR (400 MHz, CD_2Cl_2) δ 7.59 (m, 16H) 7.52 (d, *J* = 7.3 Hz, 8H), 7.47–7.38 (m, 20H) ppm. ^{31}P NMR (161.8 MHz, CD_2Cl_2) δ 13.6 ppm.

4.4.5. *Attempted synthesis of **3***

In an attempt to remove the coordinating chloride complex **2** (50 mg, 0.06 mmol) was stirred for 24 h with a silver salt, [Ag(OTf)], in THF (36 mg, 2.5 equiv.) in the presence of excess ligand (24 mg, 1.1 equiv.). The reaction mixture was filtered, and after removal of all volatiles the crude was crystallized from THF and chloroform, giving a product mixture containing **3** (crystalline) and **1-X** (where X is either OTf or Cl). Satisfactory spectroscopic data could not be obtained. ^{31}P NMR (THF): −22.6 ppm.

Declaration of interests

The authors do not work for, advise, own shares in, or receive funds from any organization that could benefit from this article, and have declared no affiliations other than their research organizations.

Funding

The authors would like to thank the Swedish Research Council (Vetenskapsrådet project grant 2017-03727 to AO, and 2021-05414 to SC) for financial support. OYOF would like to thank the ERASMUS program for funding their exchange. The computations were made possible by resources provided by the National Academic Infrastructure for Supercomputing in Sweden (NAISS) at the National Supercomputer Centre (Linköping University, project NAISS 2023/22-567) partially funded by the Swedish Research Council through grant agreement no. 2022-06725.

Supplementary data

Supporting information for this article is available on the journal's website under https://doi.org/10.5802/crchim.328 or from the author.

References

[1] V. R. Naina, F. Krätschmer, P. W. Roesky, *Chem. Commun.*, 2022, **58**, 5332-5346.
[2] A. V. Paderina, I. O. Koshevoy, E. V. Grachova, *Dalton Trans.*, 2021, **50**, 6003-6033.
[3] T. Agou, N. Wada, K. Fujisawa, T. Hosoya, Y. Mizuhata, N. Tokitoh, H. Fukumoto, T. Kubota, *Inorg. Chem.*, 2018, **57**, 9105-9114.
[4] A. K. Gupta, A. Orthaber, *Chem. Eur. J.*, 2018, **24**, 7536-7559.
[5] P. Pyykkö, *Chem. Rev.*, 1997, **97**, 597-636.
[6] A. Deák, T. Megyes, G. Tárkányi, P. Király, L. Biczók, G. Pálinkás, P. J. Stang, *J. Am. Chem. Soc.*, 2006, **128**, 12668-12670.
[7] E. Öberg, *Phosphorus Centers in π-conjugated Systems*, Uppsala University, Uppsala, 2013.
[8] M. T. Dau, J. R. Shakirova, A. J. Karttunen, E. V. Grachova, S. P. Tunik, A. S. Melnikov, T. A. Pakkanen, I. O. Koshevoy, *Inorg. Chem.*, 2014, **53**, 4705-4715.
[9] L.-Y. Yao, T. K.-M. Lee, V. W.-W. Yam, *J. Am. Chem. Soc.*, 2016, **138**, 7260-7263.
[10] G. E. Johnson, J. Laskin, *Analyst*, 2016, **141**, 3573-3589.
[11] S.-S. Zhang, L. Feng, R. D. Senanayake, C. M. Aikens, X.-P. Wang, Q.-Q. Zhao, C.-H. Tung, D. Sun, *Chem. Sci.*, 2018, **9**, 1251-1258.
[12] T.-A. Nguyen, J. Roger, H. Nasrallah, V. Rampazzi, S. Fournier, H. Cattey, E. D. Sosa Carrizo, P. Fleurat-Lessard, C. H. Devillers, N. Pirio *et al.*, *Chem. – Asian J.*, 2020, **15**, 2879-2885.

[13] F. H. Allen, P. A. Wood, P. T. A. Galek, *Acta Crystallogr. B*, 2013, **69**, 379-388.

[14] Z. Lai, A. Li, S. Peng, J. L. Sessler, Q. He, *Chem. Sci.*, 2021, **12**, 11647-11651.

[15] X. Xie, R. E. McCarley, *Inorg. Chem.*, 1997, **36**, 4011-4016.

[16] G. Bresciani, M. Bortoluzzi, S. Zacchini, F. Marchetti, G. Pampaloni, *Eur. J. Inorg. Chem.*, 2018, **2018**, 999-1006.

[17] V. N. Khrustalev, I. A. Portnyagin, I. V. Borisova, N. N. Zemlyansky, Y. A. Ustynyuk, M. Y. Antipin, M. S. Nechaev, *Organometallics*, 2006, **25**, 2501-2504.

[18] P. V. Gushchin, G. L. Starova, M. Haukka, M. L. Kuznetsov, I. L. Eremenko, V. Y. Kukushkin, *Cryst. Growth Des.*, 2010, **10**, 4839-4846.

[19] M. S. Abdelbassit, O. J. Curnow, M. R. Waterland, *Helv. Chim. Acta*, 2023, **106**, article no. e202200163.

[20] D. M. Ivanov, A. S. Novikov, G. L. Starova, M. Haukka, V. Y. Kukushkin, *CrystEngComm*, 2016, **18**, 5278-5286.

[21] T. V. Serebryanskaya, A. S. Novikov, P. V. Gushchin, M. Haukka, R. E. Asfin, P. M. Tolstoy, V. Y. Kukushkin, *Phys. Chem. Chem. Phys.*, 2016, **18**, 14104-14112.

[22] P. Botschwina, R. Oswald, V. Dyczmons, *Int. J. Mass Spectrom.*, 2007, **267**, 308-314.

[23] Y. Wang, M. Liu, R. Cao, W. Zhang, M. Yin, X. Xiao, Q. Liu, N. Huang, *J. Med. Chem.*, 2013, **56**, 1455-1466.

[24] D. Morales Salazar, E. Mijangos, S. Pullen, M. Gao, A. Orthaber, *Chem. Commun.*, 2017, **53**, 1120-1123.

[25] A. El Nahhas, M. A. Shameem, P. Chabera, J. Uhlig, A. Orthaber, *Chem. Eur. J.*, 2017, **23**, 5673-5677.

[26] I. F. Leach, L. Belpassi, P. Belanzoni, R. W. A. Havenith, J. E. M. N. Klein, *ChemPhysChem*, 2021, **22**, 1262-1268.

[27] N. Fleck, R. M. Thomas, M. Müller, S. Grimme, B. H. Lipshutz, *Green Chem.*, 2022, **24**, 6517-6523.

[28] S. J. Berners-Price, L. A. Colquhoun, P. C. Healy, K. A. Byriel, J. V. Hanna, *J. Chem. Soc., Dalton Trans.*, 1992, **23**, 3357-3363.

[29] S. J. Berners-Price, R. J. Bowen, M. A. Fernandes, M. Layh, W. J. Lesueur, S. Mahepal, M. M. Mtotywa, R. E. Sue, C. E. J. van Rensburg, *Inorg. Chim. Acta*, 2005, **358**, 4237-4246.

[30] Y. Wang, A. Eichhöfer, F. Weigend, D. Fenske, O. Fuhr, *Dalton Trans.*, 2019, **48**, 6863-6871.

[31] R. Nyamwihura, L. Yang, V. N. Nesterov, M. G. Richmond, *J. Mol. Struct.*, 2017, **1129**, 188-194.

[32] S. Bhargava, K. Kitadai, T. Masashi, D. W. Drumm, S. P. Russo, V. W.-W. Yam, T. K.-M. Lee, J. Wagler, N. Mirzadeh, *Dalton Trans.*, 2012, **41**, 4789-4798.

[33] SAINT, 2007, Bruker AXS Inc.: Madison, Wisconsin, USA (accessed).

[34] SADABS, 2001, Bruker AXS Inc.: Madison, Wisconsin, USA (accessed).

[35] G. Sheldrick, *Acta Crystallogr. Sect. A: Found. Crystallogr.*, 2008, **A64**, 112-122.

[36] G. Sheldrick, *Acta Crystallogr. Sect. C: Cryst. Struct. Commun.*, 2015, **71**, 3-8.

[37] O. V. Dolomanov, L. J. Bourhis, R. J. Gildea, J. A. K. Howard, H. Puschmann, *J. Appl. Crystallogr.*, 2009, **42**, 339-341.

[38] C. Bannwarth, E. Caldeweyher, S. Ehlert, A. Hansen, P. Pracht, J. Seibert, S. Spicher, S. Grimme, *WIREs Comput. Mol. Sci.*, 2021, **11**, e1493.

[39] F. Neese, *WIREs Comput. Mol. Sci.*, 2022, **12**, article no. e1606.

[40] S. Grimme, A. Hansen, S. Ehlert, J.-M. Mewes, *J. Chem. Phys.*, 2021, **154**, article no. 064103.

[41] NBO 7.0, 2018, Theoretical Chemistry Institute, University of Wisconsin, Madison WI (accessed).

[42] https://doi.org/10.6084/m9.figshare.23578899.

[43] R. Uson, A. Laguna, M. Laguna, D. A. Briggs, H. H. Murray, J. P. Fackler, *Inorganic Syntheses*, John Wiley & Sons, Inc., Hoboken, NJ, 2007, 85-91 pages.

ACADÉMIE
DES SCIENCES
INSTITUT DE FRANCE

Comptes Rendus. Chimie
2024, Vol. 27, Special issue S1, p. 125-132
`https://doi.org/10.5802/crchim.299`

Preliminary communication

French/Nordic Special Issue on Materials and Coordination Chemistry

Hypsochlorins

Simon Larsen [a], **Jeanet Conradie** [a, b], **Nicolas Desbois** [c], **Claude P. Gros** [*, c] and **Abhik Ghosh** [*, a]

[a] Department of Chemistry, UiT – The Arctic University of Norway, Tromsø N-9037, Norway

[b] Department of Chemistry, University of the Free State, Bloemfontein 9300, Republic of South Africa

[c] Institut de Chimie Moléculaire de l'Université de Bourgogne (ICMUB), UMR CNRS 6302, Université de Bourgogne, 9 Avenue Alain Savary, BP 47870, 21078 Dijon Cedex, France

E-mails: claude.gros@u-bourgogne.fr (C. P. Gros), abhik.ghosh@uit.no (A. Ghosh)

Abstract. Both the Soret and Q bands of chlorin e6 complexes blueshift on going from Zn to Pd to Pt as the coordinated metal, establishing the latter two complexes as hypsochlorins. DFT/TDDFT calculations indicate that the blueshifts appear to be related to the presence of the electronegative metal ion, which lowers the orbital energies of the HOMO and HOMO-1, while leaving the LUMOs relatively unaffected.

Keywords. Chlorin, Hypsochlorin, Hypso, Hypsoporphyrin, TDDFT.

Funding. Research Council of Norway (Grant no. 262229), CNRS (Grant no. UMR UBCNRS 6302), South African National Research Foundation (Grant nos. 129270 and 132504).

Manuscript received 29 September 2023, revised 10 January 2024, accepted 8 February 2024.

1. Introduction

Over a half-century ago, Martin Gouterman [1] devised his eponymous four-orbital model of porphyrin spectra, and thereby was able to classify them as belonging to three broad classes, normal, hyper and hypso [2,3]. Briefly, hyper spectra exhibit redshifted features and/or extra features relative to normal spectra, while hypso spectra are blueshifted relative to normal spectra. Although the variety of porphyrinoid compounds is vastly greater today, Gouterman's classification remains useful. Thus, the hyperporphyrin concept has emerged as a design principle for photosensitizers for photodynamic therapy and related applications [4]. Many hypsoporphyrins are phosphorescent and potentially useful as triplet photosensitizers, in such applications as oxygen sensing and photodynamic and related therapies [5–7]. The hypso effect had long been attributed to an increase in the HOMO–LUMO gap in certain late transition porphyrins as a result of antibonding interactions between occupied metal d_π orbitals and the porphyrin's e_g LUMOs. A recent DFT investigation, however, has indicated a different origin for the hypso effect, namely, a lowering of the a_{2u} HOMOs in metalloporphyrins with relatively electronegative metal ions such as Pd(II) and Pt(II) [8].

Many years ago, we showed that Gouterman's four-orbital model also applies to corroles [9,10]. Unsurprisingly, many metallocorroles exhibit hyper spectra [11–13] and quite a few also exhibit hypso

---

[*] Corresponding authors

ISSN (electronic): 1878-1543

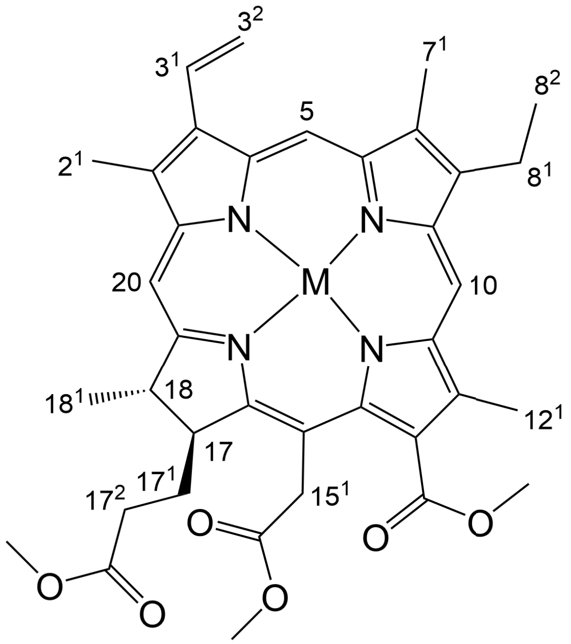

Scheme 1. A chlorin e6 trimethyl ester metal complex with partial atom numbering.

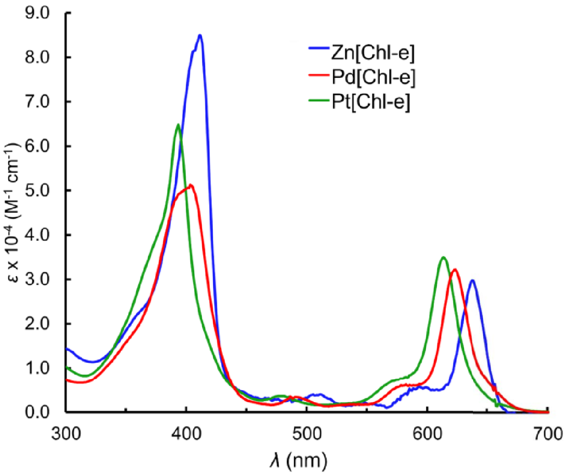

Figure 1. UV–visible spectra of M[Chl-e], where M = Zn, Pd, and Pt, in CH_2Cl_2 at ambient temperature.

spectra [8]. Herein we show that the hypso effect also applies to chlorins [14,15], with both the Soret and Q band maxima of chlorins blueshifting, going from Zn to Pd to Pt as the coordinated metal (Scheme 1). The finding is surprising in that the HOMO of closed-shell chlorins is invariably an a_{1u}-type MO (in terms of D_{4h} irreps) [3,16–19] which has no amplitude on the central nitrogen atoms and is, therefore, likely to be unaffected by the electronegativity of the central metal. Gratifyingly, the spectral data proved consistent with electrochemical cyclic voltammetry measurements and DFT/TDDFT calculations, leading to a coherent picture of hypsochlorins, as described below.

2. Results and discussion

Table 1 lists the UV–vis absorption maxima and redox potentials (V versus SCE) of the Zn, Pd, and Pt complexes of chlorin e6 trimethyl ester, M[Chl-e], where M = Zn, Pd, and Pt; the UV–vis spectra and cyclic voltammograms are depicted in Figures 1 and 2, respectively. From Zn to Pd and from Pd to Pt, the Q band blueshifts by 14 and 10 nm, respectively, and the Soret by 8 and 10 nm, respectively. The two minor features between the Soret and Q bands also blueshift in the same order. All complexes exhibit reversible 1st oxidations and 1st reductions. While there are small variations in the 1st reduction potentials there are greater variations in the 1st oxidation potentials and a clear trend of increasing oxidation potentials in the order of Zn < Pd < Pt, which in turn results in an increasing electrochemical HOMO–LUMO gap for the same series. The electrochemical data thus suggests that the hypso effect in chlorins stems primarily from a lowering of the HOMO energy in the presence of an electronegative coordinated metal.

To obtain a qualitative understanding of the above findings, DFT and TDDFT calculations were carried out using simple unsubstituted chlorin models of the complexes studied. The OLYP [20,21]-D3 [22]/ZORA-STO-TZ2P optimized geometries of M[Chl] (M = Zn, Pd, Pt; Chl = unsubstituted chlorin; Figure 3) revealed essentially planar (as opposed to ruffled) geometries so differences in macrocycle conformation appear unlikely to be a significant contributor to the observed spectral differences [23]. Single-point CAMY-B3LYP [24] calculations were then carried out on the OLYP-D3 geometries. Figure 4 depicts selected CAMY-B3LYP frontier MOs along with the corresponding orbital energies, while Figure 5

Table 1. Redox potentials (V versus SCE) and UV–vis absorption maxima of the compounds studied

Compound	$E_{1/2\mathrm{ox}2}$	$E_{1/2\mathrm{ox}1}$	$E_{1/2\mathrm{red}1}$	$E_{1/2\mathrm{red}2}$	$E_{\mathrm{red}2}$	ΔE	Soret band (nm)	Q band (nm)
Zn[Chl-e]	0.96	0.55	−1.29	–	−1.79	1.84	411	637
Pd[Chl-e]	–	0.77	−1.17	−1.69	–	1.94	403	623
Pt[Chl-e]	–	0.81	−1.22	−1.73	–	2.03	393	613

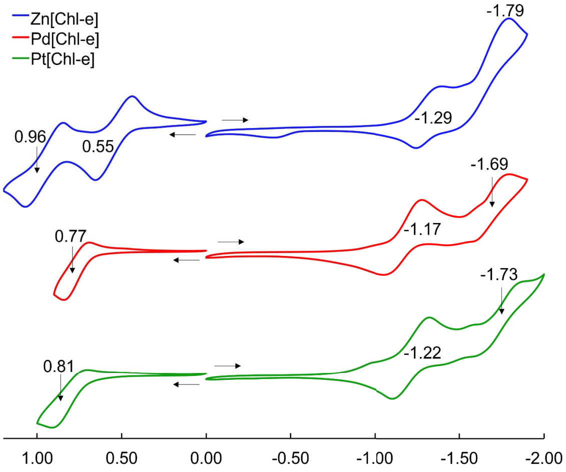

Figure 2. Cyclic voltammograms (V versus SCE) of M[Chl-e], where M = Zn, Pd, and Pt, in CH_2Cl_2 containing 0.1 M tetrabutylammonium perchlorate at ambient temperature; scan rate 100 mV·s^{-1}.

presents the orbital energy levels in a graphical manner. Figure 6 depicts the simulated TD-CAMY-B3LYP-D3/Q4 STO-TZ2P-COSMO optical spectra in dichloromethane of the three M[Chl] derivatives. The key result is that, while the LUMO and LUMO+1 energies are essentially constant across all three M[Chl] derivatives, both the HOMO and HOMO-1 energies downshift going from Zn to Pd to Pt. Understandably, the downshifts for the a_{1u}-type HOMO are smaller than those for the a_{2u}-type HOMO-1, given that only the latter has substantial amplitudes on the central nitrogen atoms. In spite of the simplicity of our models, these computational results appear to nicely, if qualitatively, capture the essence of both the UV–vis and electrochemical measurements.

Finally, the calculated absorption maxima from CAMY-B3LYP TDDFT calculations on M[Chl] in dichloromethane (Figure 6) were found to be in surprisingly good agreement with the experimental absorption maxima for M[Chl-e]. Thus, for instance, the calculations correctly captured the larger hypsochromic shifts for the Q band relative to the Soret band. In all three cases, the Q band consists of approximately 95% HOMO → LUMO character, with the remainder made up of HOMO-1 → LUMO+1 character (Table 2). The Soret band, by comparison, consists of a mixture of HOMO-1 → LUMO and HOMO → LUMO+1 character. Since both the HOMO and HOMO-1 downshift from Zn through Pd to Pt, it makes sense that both the Q and Soret absorption maxima blueshift in the same order.

In summary, a combined experimental and theoretical study indicates the plausible occurrence of a hypso effect in chlorins. Thus, both the Soret and Q bands blueshift going from Zn to Pd to Pt as the coordinated metal. As in the case of porphyrins, the blueshifts appear to be largely attributable to the presence of an electronegative coordinated atom, which lowers the orbital energies of the HOMO and HOMO-1, while leaving the LUMOs relatively unaffected.

3. Experimental section

3.1. *Materials*

All reagents were purchased from Sigma-Aldrich and used as received except chlorin e6 trimethyl ester (CAS 35038-32-5) which was purchased from PorphyChem. Silica gel 60 (0.04–0.063 mm particle size, 230–400 mesh, Merck) was employed for flash chromatography. Silica gel 60 preparative thin-layer chromatographic plates (20 cm × 20 cm × 0.5 mm, Merck) were used for final purification of all compounds.

3.2. *General instrumental methods*

UV–visible spectra were recorded on an HP 8454 spectrophotometer. ^{1}H NMR spectra were recorded

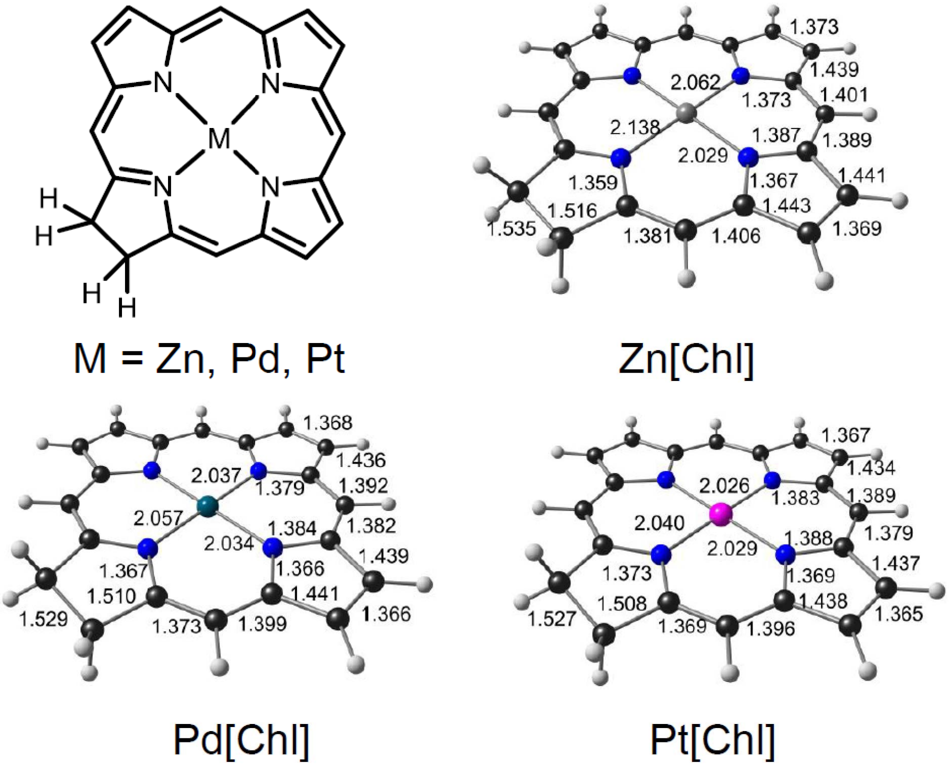

Figure 3. Selected skeletal bond distances for M[Chl], where M = Zn, Pd, and Pt and Chl = unsubstituted chlorin.

on a 400 MHz Bruker Avance III HD spectrometer equipped with a 5 mm BB/1H SmartProbe and referenced to either residual C_6H_6 at 7.16 ppm or residual $CHCl_3$ at 7.26 ppm. High-resolution electrospray-ionization mass spectra were recorded on an Orbitrap Exploris 120 spectrometer using methanolic solutions. Cyclic voltammetry was carried out at ambient temperature with a Gamry Reference 620 potentiostat equipped with a three-electrode system: a 3 mm disc glassy carbon working electrode, a platinum wire counter-electrode, and a saturated calomel reference electrode (SCE). Tetra(n-butyl)ammonium perchlorate (*CAUTION!*) was used as the supporting electrolyte. Anhydrous CH_2Cl_2 (Sigma-Aldrich) was used as solvent. The electrolyte solution was purged with argon for at least 2 min prior to all measurements, which were carried out under an argon blanket. The glassy carbon working electrode was polished using a polishing pad and 0.05 micrometer polishing alumina from ALS Japan. All potentials were referenced to the SCE.

3.3. *Synthesis*

The Zn complex was made by adding a solution of $Zn(OAc)_2 \bullet 2H_2O$ (29.5 mg, 4 eq.) in 1 mL MeOH to a solution of chlorin e6 trimethyl ester (21.9 mg) in 5 mL chloroform. The resulting solution was refluxed for 1 h. The Pd complex was made by dissolving chlorin e6 trimethyl ester (17.3 mg) and $Pd(OAc)_2$ (19.7 mg, 3 eq.) in 5 mL pyridine and refluxing the resulting solution for 4 h. The Pt complex was made by dissolving chlorin e6 trimethyl ester (18.0 mg) and $Pt(OAc)_2$ (26.3 mg, 3 eq.) in 5 mL benzonitrile and refluxing the resulting solution for 10 h. Following reflux, each mixture was rotary-evaporated to dryness and the residue dissolved in DCM and placed on a silica column. Dichloromethane/ethyl acetate 20:1 eluted a blue fraction which was evaporated to

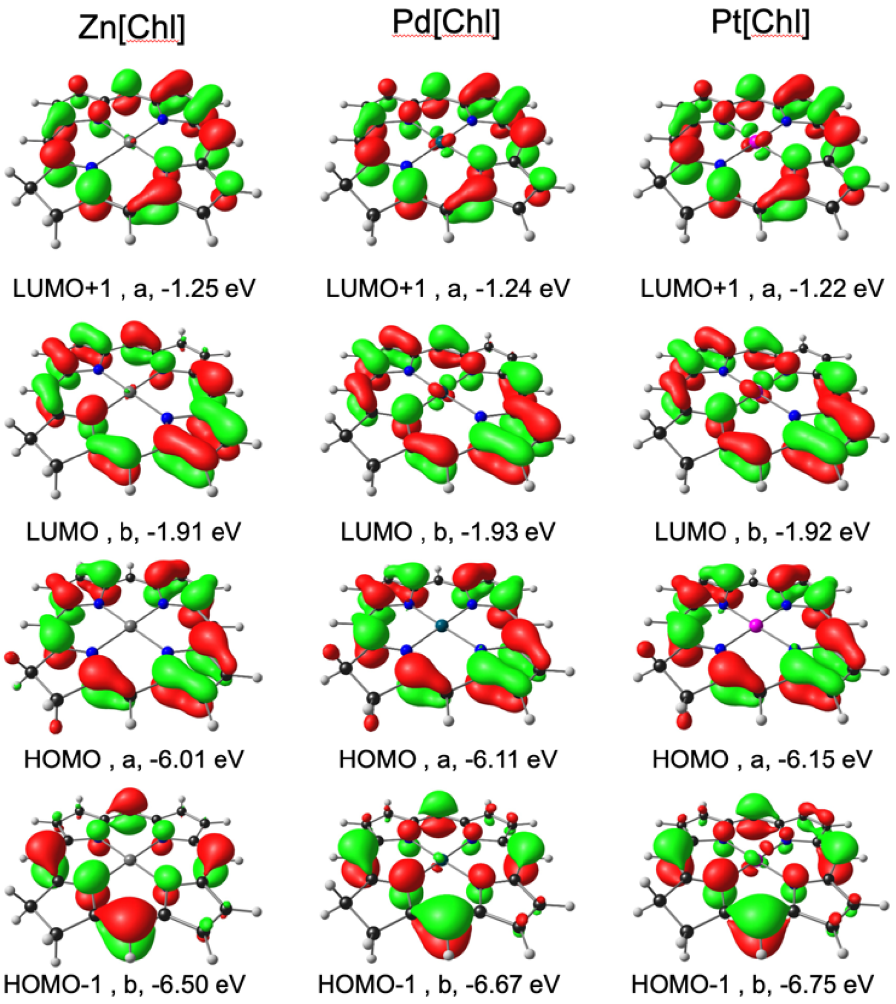

Figure 4. CAMY-B3LYP frontier MOs of M[Chl] (M = Zn, Pd, Pt), with C2 irreps (a and b) and orbital energies.

dryness and further purified by preparative TLC using *n*-hexane/ethyl acetate 1:1 as solvent. Yields and analytical details are as follows:

3.3.1. *Zn[Chl-e]*

Yield 16.8 mg, 70%. UV–Vis (CH_2Cl_2) λ_{max} (nm) [$\epsilon \times 10^{-4}$ ($M^{-1}\cdot cm^{-1}$)]: 411 (8.50), 505 (0.40), 593 (0.58), 637 (2.98). ^{1}H NMR (400 MHz, C_6D_6, δ in ppm): 9.54 (s, 1H, **5**), 9.41 (s, 1H, **10**), 8.50 (s, 1H, **20**), 8.05 (dd, J = 17.8, 11.5 Hz, 1H, **3^1**), 6.18 (d, J = 18.0 Hz, 1H, **3^2 *trans***), 5.91 (d, J = 1.8 Hz, 1H, **3^2 *cis***), 5.45 (d, J = 19.0 Hz, 1H, **15^1**), 5.28 (d, J = 19.0 Hz, 1H, **15^1**), 4.28 (d, J = 10.2 Hz, 1H, **17**), 4.01 (t, J = 7.1 Hz, 1H, **18**), 3.95 (s, 3H, **OCH_3**), 3.59 (s, 3H, **OCH_3**), 3.47 (q, J = 7.5 Hz, 2H, **8^1**), 3.38 (s, 3H, **OCH_3**), 3.26 (s, 3H, **12^1**), 3.25 (s, 3H, **2^1**), 3.01 (s, 3H, **7^1**), 2.30 (dt, J = 15.9, 7.9 Hz, 1H, **17^1**), 2.07 (d, J = 10.0 Hz, 1H, **17^1**), 2.00–1.91 (m, 1H, **17^2**), 1.67 (d, J = 7.2 Hz, 3H, **18^1**), 1.60 (t, J = 7.6 Hz, 3H, **8^2**), ~1.55 (1H, **17^2** concealed by overlapping peaks). MS (ESI, positive mode): m/z calcd for $C_{37}H_{40}N_4O_5ZnH$ 701.2312; [$M+H^+$] found 701.2307.

3.3.2. *Pd[Chl-e]*

Yield 1.9 mg, 9.4%. UV–Vis (CH_2Cl_2) λ_{max} (nm) [$\epsilon \times 10^{-4}$ ($M^{-1}\cdot cm^{-1}$)]: 403 (5.14), 486 (0.35), 582 (0.62), 623 (3.22). ^{1}H NMR (400 MHz, $CDCl_3$, δ in ppm): 9.57 (s, 1H, **5/10**), 9.56 (s, 1H, **5/10**), 8.62

Table 2. CAMY-B3LYP-D3/STO-TZ2P TDDFT results, including transition energies (E) and wavelengths (λ), oscillator strengths (f), MO compositions, and symmetries

Molecule	Peak	E (eV)	λ (nm)	f	MO composition			State symmetry
					From	To	Weight (%)	
Zn[Chl]	Q	2.12	584.6	0.45	HOMO	LUMO	92.6	B
					HOMO-1	LUMO+1	6.3	B
	Soret	3.04	408.4	1.80	HOMO	LUMO+1	62.3	A
					HOMO-1	LUMO	35.8	A
		3.33	372.3	1.23	HOMO-1	LUMO+1	91.4	B
					HOMO	LUMO	6.4	B
Pd[Chl]	Q	2.18	568.4	0.48	HOMO	LUMO	94.3	B
					HOMO-1	LUMO+1	4.5	B
	Soret	3.11	398.7	1.60	HOMO-1	LUMO	59.8	A
					HOMO	LUMO+1	38.2	A
		3.47	356.9	1.10	HOMO-1	LUMO+1	92.5	B
					HOMO	LUMO	4.5	B
Pt[Chl]	Q	2.23	556.1	0.50	HOMO	LUMO	94.8	B
					HOMO-1	LUMO+1	3.9	B
	Soret	3.18	390.1	1.58	HOMO	LUMO+1	56.5	A
					HOMO-1	LUMO	40.9	A
		3.56	348.4	1.14	HOMO-1	LUMO+1	92.6	B
					HOMO	LUMO	3.8	B

(s, 1H, **20**), 7.98 (dd, J = 17.8, 11.5 Hz, 1H, $\mathbf{3^1}$), 6.16 (dd, J = 17.8, 1.7 Hz, 1H, $\mathbf{3^2}$ ***trans***), 6.03 (dd, J = 11.5, 1.7 Hz, 1H, $\mathbf{3^2}$ ***cis***), 5.14 (d, J = 19.1 Hz, 1H, $\mathbf{15^1}$), 4.93 (d, J = 19.0 Hz, 1H, $\mathbf{15^1}$), 4.48–4.35 (m, 2H, overlapping **17** and **18**), 4.19 (s, 3H, **OCH$_3$**), 3.86 (s, 3H, **OCH$_3$**), 3.75 (q, J = 7.6 Hz, 2H, $\mathbf{8^1}$), 3.62 (s, 3H, **OCH$_3$**), 3.44 (s, 3H, $\mathbf{12^1}$), 3.33 (s, 3H, $\mathbf{2^1}$), 3.29 (s, 3H, $\mathbf{7^1}$), 2.58–2.46 (m, 1H, $\mathbf{17^1}$), 2.24–2.11 (m, 1H, $\mathbf{17^1}$), 2.07–1.95 (m, 1H, $\mathbf{17^2}$), 1.75 (d, J = 7.1 Hz, 3H, $\mathbf{18^1}$), 1.69 (t, J = 7.6 Hz, 3H, $\mathbf{8^2}$) ~1.69 (1H, $\mathbf{17^2}$ concealed by overlapping peaks). MS (APCI, positive mode): m/z calcd for $C_{37}H_{40}N_4O_5PdH$ 743.2055; [M + H$^+$] found 743.2065.

3.3.3. *Pt[Chl-e]*

Yield 5.8 mg, 24.7%. UV–Vis (CH_2Cl_2) λ_{max} (nm) [$\epsilon \times 10^{-4}$ ($M^{-1}\cdot cm^{-1}$)]: 393 (6.49), 478 (0.36), 613 (3.49). ^{1}H NMR (400 MHz, $CDCl_3$, δ in ppm): 9.56 (s, 1H, **5**), 9.52 (s, 1H, **10**), 8.70 (s, 1H, **20**), 7.98 (dd, J = 17.8, 11.5 Hz, 1H, $\mathbf{3^1}$), 6.14 (dd, J = 17.8, 1.7 Hz, 1H, $\mathbf{3^2}$ ***trans***), 6.02 (dd, J = 11.4, 1.6 Hz, 1H, $\mathbf{3^2}$ ***cis***), 5.13 (d, J = 19.1 Hz, 1H, $\mathbf{15^1}$), 4.93 (d, J = 19.1 Hz, 1H, $\mathbf{15^1}$), 4.46–4.34 (m, 2H, overlapping **17** and **18**), 4.20 (s, 3H, **OCH$_3$**), 3.87 (s, 3H, **OCH$_3$**), 3.71 (q, J = 7.6 Hz, 2H, $\mathbf{8^1}$), 3.63 (s, 3H, **OCH$_3$**), 3.50 (s, 3H, $\mathbf{12^1}$), 3.31 (s, 3H, $\mathbf{2^1}$), 3.24 (s, 3H, $\mathbf{7^1}$), 2.54 (ddd, J = 16.1, 9.0, 7.0 Hz, 1H, $\mathbf{17^1}$), 2.20 (ddd, J = 16.2, 7.2, 4.8 Hz, 1H, $\mathbf{17^1}$), 2.09–1.97 (m, 1H, $\mathbf{17^2}$), 1.76 (d, J = 7.1 Hz, 3H, $\mathbf{18^1}$), 1.68 (t, J = 7.6 Hz, 3H, $\mathbf{8^2}$), ~1.71 (1H, $\mathbf{17^2}$ concealed by overlapping peaks). MS (APCI, positive mode): m/z calcd for $C_{37}H_{40}N_4O_5PtH$ 832.2668; [M + H$^+$] found 832.2670.

3.4. *Computational method*

The three M[Chl] (M = Zn, Pd, Pt] complexes were optimized with scalar-relativistic DFT calculations, with the OLYP [20,21] functional augmented with Grimme's D3 [22] dispersion correction, all-electron ZORA STO-TZ2P basis sets, fine integration grids,

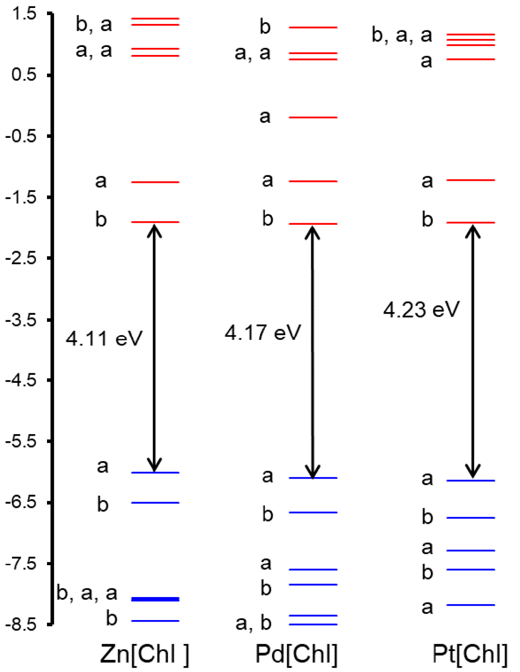

Figure 5. CAMY-B3LYP-D3/STO-TZ2P-COSMO frontier MO energy levels along with C_2 irreps (a and b).

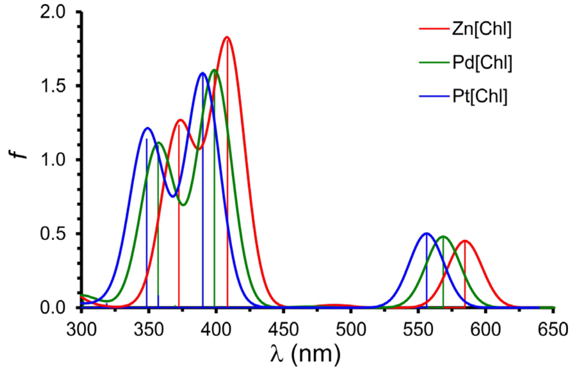

Figure 6. Simulated TD-CAMY-B3LYP-D3/STO-TZ2P-COSMO optical spectra in dichloromethane. The vertical lines represent calculated transitions which have then been broadened with Gaussians to generate the simulated spectra.

and tight criteria for both SCF cycles and geometry optimizations, as implemented in the ADF 2019 program system [25]. All the optimizations were carried out with a C_2 symmetry constraint and the COSMO (Conductor like Screening Model) [26] solvation model with dichloromethane as solvent. TDDFT calculations were performed on the OLYP-D3 optimized geometries using the CAMY-B3LYP [24] range-separated functional (which has been extensively calibrated for calculations of porphyrin spectra [4,7,27]), with basis set and other parameters the same as in the ground-state calculations).

Declaration of interests

The authors do not work for, advise, own shares in, or receive funds from any organization that could benefit from this article, and have declared no affiliations other than their research organizations.

Funding

This research was supported by the Research Council of Norway (grant no. 262229 to AG), the CNRS (grant UMR UBCNRS 6302), and the South African National Research Foundation (grant nos. 129270 and 132504 to JC).

Acknowledgment

The authors also warmly thank Mrs. Sandrine Pacquelet for technical assistance.

Supplementary data

Supporting information for this article is available on the journal's website under https://doi.org/10.5802/crchim.299 or from the author.

References

[1] A. Ghosh, *Angew. Chem. Int. Ed.*, 2021, **60**, 9760-9770.
[2] M. Gouterman, G. H. Wagniére, L. C. Snyder, *J. Mol. Spectrosc.*, 1963, **11**, 108-115.
[3] M. Gouterman, in *The Porphyrins* (D. Dolphin, ed.), vol. III, Part A, Academic Press, New York, 1978, 1-165.
[4] C. C. Wamser, A. Ghosh, *JACS Au*, 2022, **2**, 1543-1560.
[5] Y. Lin, T. Zhou, R. Bai, Y. Xie, *J. Enzyme Inhib. Med.*, 2020, **35**, 1080-1099.
[6] K. C. Tong, D. Hu, P. K. Wan, C. N. Lok, C. M. Che, *Adv. Inorg. Chem.*, 2020, **75**, 87-119.
[7] A. B. Alemayehu, K. E. Thomas, R. F. Einrem, A. Ghosh, *Acc. Chem. Res.*, 2021, **54**, 3095-3107.
[8] A. Ghosh, J. Conradie, *J. Phys. Chem. A*, 2021, **125**, 9962-9968.

[9] A. Ghosh, T. Wondimagegn, A. B. Parusel, *J. Am. Chem. Soc.*, 2000, **122**, 5100-5104.

[10] A. Ghosh, *Chem. Rev.*, 2017, **117**, 3798-3881.

[11] A. Alemayehu, J. Conradie, A. Ghosh, *Eur. J. Inorg. Chem.*, 2011, **12**, 1857-1864.

[12] S. Ganguly, A. Ghosh, *Acc. Chem. Res.*, 2019, **52**, 2003-2014.

[13] I. K. Thomassen, A. Ghosh, *ACS Omega*, 2020, **5**, 9023-9030.

[14] A. J. McHugh, M. Gouterman, C. Weiss, *Theor. Chim. Acta*, 1972, **24**, 346-370.

[15] A. Zhang, M. J. Stillman, *Phys. Chem. Chem. Phys.*, 2018, **20**, 12470-12482.

[16] E. Fujita, C. K. Chang, J. Fajer, *J. Am. Chem. Soc.*, 1985, **107**, 7665-7669.

[17] S. Licoccia, M. J. Chatfield, G. N. La Mar, K. M. Smith, K. E. Mansfield, R. R. Anderson, *J. Am. Chem. Soc.*, 1989, **111**, 6087-6093.

[18] A. Ghosh, *J. Phys. Chem. B*, 1997, **101**, 3290-3297.

[19] A. B. Parusel, A. Ghosh, *J. Phys. Chem. A*, 2000, **104**, 2504-2507.

[20] N. C. Handy, A. J. Cohen, *Mol. Phys.*, 2001, **99**, 403-412.

[21] C. Lee, W. Yang, R. G. Parr, *Phys. Rev. B*, 1988, **37**, 785-789.

[22] S. Grimme, J. Antony, S. Ehrlich, H. Krieg, *J. Chem. Phys.*, 2010, **132**, article no. 154104.

[23] H. Ryeng, E. Gonzalez, A. Ghosh, *J. Phys. Chem. B*, 2008, **112**, 15158-15173.

[24] Y. Yakinaga, S. Ten-no, *Chem. Phys. Lett.*, 2008, **462**, 348-351.

[25] G. te Velde, F. M. Bickelhaupt, S. J. A. van Gisbergen, C. F. Guerra, E. J. Baerends, J. G. Snijders, T. Ziegler, *J. Comp. Chem.*, 2001, **22**, 931-967.

[26] A. Klamt, G. Schüürmann, *J. Chem. Soc., Perkin Trans.*, 1993, **2**, 799-805.

[27] J. Conradie, C. C. Wamser, A. Ghosh, *J. Phys. Chem. A*, 2021, **125**, 9953-9961.

Comptes Rendus

Chimie

Objectif de la revue

Les *Comptes Rendus Chimie* sont une revue électronique évaluée par les pairs de niveau international, qui couvre l'ensemble des domaines des sciences chimiques.

Ils publient des numéros thématiques, des articles originaux de recherche, des articles de synthèse, des mises au point, des mises en perspective historiques, des textes à visée pédagogique, ou encore des actes de colloque, en anglais ou en français, sans limite de longueur et dans un format aussi souple que possible (figures, données associées, etc.).

Depuis 2020, les *Comptes Rendus Chimie* sont publiés avec le centre Mersenne pour l'édition scientifique ouverte, selon une politique vertueuse de libre accès diamant, gratuit pour les auteurs (pas de frais de publication) comme pour les lecteurs (accès libre, immédiat et pérenne).

À propos de la revue

Les *Comptes Rendus Chimie* sont exclusivement publiés au format électronique.

Toutes les informations sur la revue, ainsi que le texte intégral de l'ensemble des articles, sont disponibles sur son site internet, à l'adresse https://comptes-rendus.academie-sciences.fr/chimie/.

Informations pour les auteurs

Pour toute question relative à la soumission d'un manuscrit, merci de consulter le site internet de la revue : https://comptes-rendus.academie-sciences.fr/chimie/.

Contact

Académie des sciences
23 quai de Conti
75006 Paris (France)
cr-chimie@academie-sciences.fr

COMPTES RENDUS
DE L'ACADÉMIE DES SCIENCES

Chimie

Volume 27, nº S1, 2024

Special issue / *Numéro spécial*

French/Nordic Special Issue on Materials and Coordination Chemistry / *Numéro spécial franco-nordique sur les matériaux et la chimie de coordination*

Guest editors / *Rédacteurs en chef invités*

Claude P. Gros (Université de Bourgogne, Dijon, France) and Abhik Ghosh (The Arctic University, UiT, Tromsø, Norway)

Cover illustration / *Illustration de couverture*

© Crédits Photo : W. Ryan Osterloh, Claude P. Gros & Jeanet Conradie.

Contents / *Sommaire*

1878-1543 (electronic)

Académie des sciences — Paris

COMPTES RENDUS
DE L'ACADÉMIE DES SCIENCES

Chimie

Volume 27, nº S1, 2024